# Cavity Optomechanics with High-Stress Silicon Nitride Films

Thesis by

Dalziel Joseph Wilson

In Partial Fulfillment of the Requirements

for the Degree of

Doctor of Philosophy
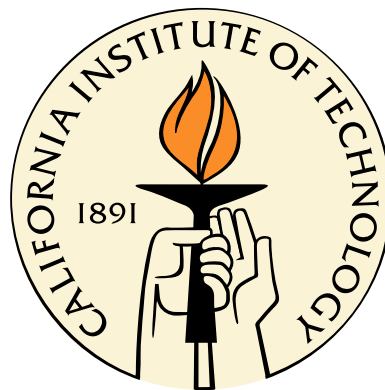
California Institute of Technology

Pasadena, California

2012

(Defended December 15, 2011)

For Nona, who taught my brothers and me how to wander the hills

Acknowledgements

I'd like to acknowledge with deepest gratitude the friends and colleagues who have made my experience at Caltech so meaningful: Jeff Kimble, our tireless mentor and a true "gentleman cowboy"; Cindy Regal, who spearheaded our optomechanics project and nurtured it with characteristic grace; Scott Papp, whose burden is to have a solution to every technical problem; Scott Curtis, who makes the basement of East Bridge feel like an ivory tower; Kang-Kuen Ni, a fearless experimentalist, a kindred spirit, and a decent sailor; Yi Zhao, whose patience and professionalism inspires me; Jon Hood, whose success seems inevitable; Richard Norte, who continues to reinvent the wheel; Tracy Northup, who taught me the Zen of cavity construction; Russ Miller and Andreea Boca, who humored me in the CQED lab; Dave Boozer and Kyung Soo Choi, two gentle giants in their own way; Dan Alton, Aki Goban, and Ding Ding, our able-bodied new generation; Eric Tai and Jetson-Leder Louis, who represent all that is good about Caltech undergrads in my book; Terry-Ann Suer, whose honesty and passion I rely on; Morgan Charles Putnam, with whom I share the secret handshake; and Hardy, Ernie, Ang, Ma, and Pops, whose love and support I daily take for granted.

Abstract

There has been a barrage of interest in recent years to marry the fields of nanomechanics and quantum optics. Mechanical systems provide sensitive and scalable architectures for sensing applications ranging from atomic force microscopy to gravity wave interferometry. Optical resonators driven by low noise lasers provide a quiet and well-understood means to read-out and manipulate mechanical motion, by way of the radiation pressure force. Taken to an extreme, a device consisting of a high-Q nanomechanical oscillator coupled to a high-finesse optical cavity may enable ground-state preparation of the mechanical element, thus paving the way for a new class of quantum technology based on chip-scale phononic devices coupled to optical photons. By way of mutual coupling to the optical field, this architecture may enable coupling of single phonons to real or artificial atoms, an enticing prospect because of the vast "quantum optics toolbox" already developed for cavity quantum electrodynamics.

The first step towards these goals — ground-state cooling of the mechanical element in a "cavity optomechanical" system — has very recently been realized in a cryogenic setup. The work presented in this thesis describes an effort to extend this capability to a room temperature apparatus, so that the usual panoply of table-top optical/atomic physics tools can be brought to bear. This requires a mechanical oscillator with exceptionally low dissipation, as well as careful attention to extraneous sources of noise in both the optical and mechanical componentry. Our particular system is based on a high-Q, high-stress silicon nitride membrane coupled to a high-finesse Fabry-Perot cavity. The purpose of this thesis is to record in detail the procedure for characterizing/modeling the physical properties of the membrane resonator, the optical cavity, and their mutual interaction, as well as extraneous sources of noise related to multimode thermal motion of the oscillator, thermal motion of the cavity apparatus, optical absorption, and laser phase fluctuations. Our principle experimental result is the radiation pressure-based cooling of a high order, $\simeq 4.8$ MHz drum mode of the membrane from room temperature to $\simeq 100$ mK ($\simeq 500$ phonons). Secondary results include an investigation of the Q-factor of membrane oscillators with various geometries, some of which exhibit state-of-the-art $Q \times$frequency products of 3×10^{13} Hz, and a novel technique to suppress extraneous radiation pressure noise using electro-optic feedback.

Contents

Chapter 1

Introduction

1.1   Background

The field of cavity optomechanics [1] has experienced remarkable progress in recent years [2, 3], owing much to the integration of micro- and nanomechanical resonator technology [4, 5, 6, 7]. Using a combination of cryogenic pre-cooling [8, 9, 10] and improved fabrication techniques [11, 12, 13], it is now possible to realize systems wherein the mechanical frequency of the resonator is larger than both the energy decay rate of the cavity and the rethermalization rate of the resonator [4, 14, 15, 6]. These represent two basic requirements for ground-state cooling using cavity light forces [2, 16, 17], an advance that would help to establish a new class of quantum technology based on chip-scale phononic devices [18].

Very recently the field has reached a milestone. The use of radiation pressure in an optomechanical system combined with cryogenic pre-cooling has made possible the ground-state preparation of a solid-state microwave-frequency mechanical resonator [6]. This result closely followed the successful ground-state cooling of a micro-resonator in a microwave cavity system [15] and a system based solely on conventional cryogenics [10]. A variety of systems have also demonstrated phonon occupations of $\bar{n} < 10$ [19, 4]. Essential to these efforts has been the development of ultra-high-Q mechanical resonators that are compatible with low-loss optical (or microwave) cavities where radiation pressure dominates over photothermal effects.

Looking forward, an enabling advance would be to push capabilities of optomechanics to an extreme where quantum limits could be achieved in the presence of a room-temperature thermal bath. Cryogen-free operation at optical wavelengths would greatly facilitate the integration of mesoscopic quantum mechanical oscillators into hybrid quantum systems. For example, using cold atoms, mechanical oscillators could be coupled to atomic motional states or spin thus linking to a rich quantum optics toolbox [20, 21]. Via projective measurements utilizing atomic ensembles, quantum effects could also be recognized without achieving full ground-state cooling [22].

It is with these goals in mind that the Quantum Optics group at Caltech, under the guidance

of post-docs Cindy Regal and Scott Papp, began a first series of optomechanics experiments in the summer of 2008. We adopted a promising optomechanical platform introduced at Yale, in which a flexible SiN membrane with exceptional mechanical properties is coupled to a standard high-finesse Fabry-Perot cavity [13, 7, 23]. We first demonstrated [14] that SiN membranes could be optimized to realize one of the key minimum requirements for ground-state cooling from room temperature, namely a mechanical quality factor Q_m larger than the number of room-temperature thermal phonons, i.e., $Q_m > \bar{n}_{room} \equiv k_B T_{room}/(\hbar \Omega_m)$ [24]. We then developed an optomechanical system [14] in which cavity cooling could be applied to multiple higher-order modes of these films, with negligible optical absorption and scattering at a wavelength of interest for cold-atom systems [20, 21, 22]. Using this system, we have been able to cool a radio-frequency ($\Omega_m/2\pi = 4.8$ MHz) vibrational mode of the membrane from room temperature to an occupation number of $\bar{n} \approx 500$.

In this dissertation, I will elaborate on the development of our first-generation "membrane-in-the-middle" experiment in the Kimble group. A pictorial outline is provided in Figure 1.1. A short summary of each chapter is given below.

1.2 Outline

In Chapter 2 we provide a basic theoretical description of mechanical oscillators, optical cavities, and their interaction via the radiation pressure force. The treatment is fully classical, which is suitable for the description of all of the experimental results presented in later chapters. Our main objective is to derive coupled equations of motion for the amplitude of the resonator and the intracavity field using a language amenable to the standard input-output formalism for optical cavities. Towards this end, we use as a model the "canonical" 1D optomechanical system in which one end-mirror in a planar Fabry-Perot resonator has been replaced by a compliant micro-mirror.

In Chapter 3 we introduce the MIM system, using a transfer matrix formalism to describe its steady-state, linear optical properties. We take a ground-up approach, first obtaining a model for a thin dielectric film, then a dielectric mirror, then a Fabry-Perot cavity constructed from two dielectric mirrors. We then study the effect of inserting a thin dielectric film between the cavity mirrors. The transfer matrix formalism is used to analytically and numerically model the dispersive coupling between the position of the film and the cavity resonance. We also model the finesse and transmission/reflection coefficients of the compound cavity as a function of the position of the film and the reflection and loss coefficients of the film and the mirrors.

In Chapter 4 we discuss the mechanical properties of high-stress silicon nitride films — in particular, the square "membrane" resonators we have purchased commercially from Norcada, Inc. We outline the construction and material properties of these membranes, the shape and spectrum of their vibrational modes, and their dynamic mechanical properties. We then describe a simple experimen-

Chapter 2-3
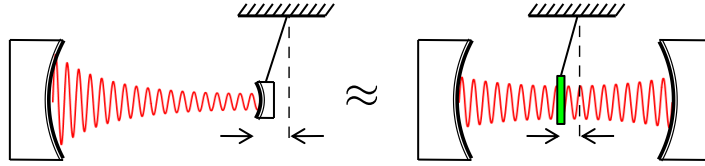
Chapter 4
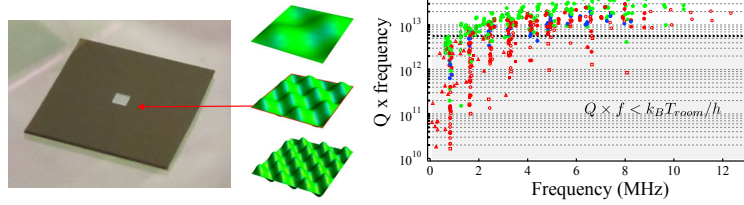
Chapters 5-6
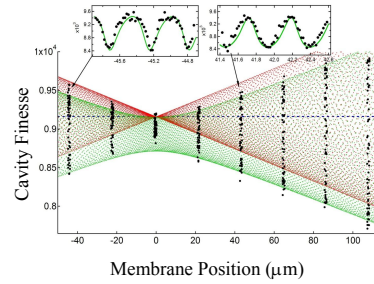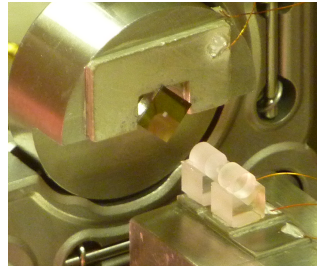
Chapters 7-8
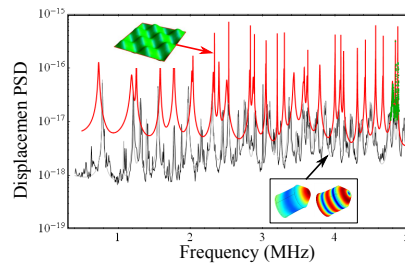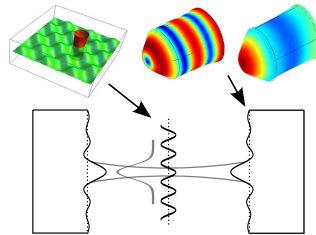
Chapter 9
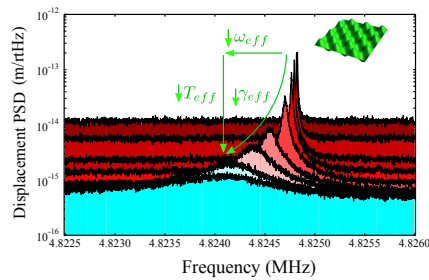
Chapter 10
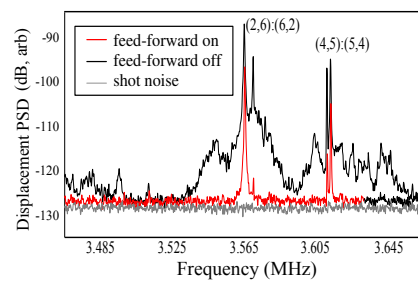
Figure 1.1: Illustrated thesis outline. In Chapters 2–3 we discuss the basic dynamic properties of optomechanical systems and the peculiar steady-state properties of the "membrane-in-the-middle" (MIM) system. In Chapter 4 we elaborate on the membrane resonator and characterization of its mechanical properties. In Chapters 5–6 we describe the design and characterization of a high-finesse cavity interfaced with a membrane resonator. In Chapters 7–8 we discuss aspects of modeling and measuring thermal vibrations of a multimode MIM system. In Chapter 9 we demonstrate optomechanical cooling of a high-order membrane mode. In Chapter 10 we investigate a fundamental roadblock to ground-state cooling associated with Brownian motion of the mirror substrates.

tal apparatus used to characterize their mechanical properties. Using this apparatus, we conduct a phenomenological study of the role of membrane geometry and mounting conditions on mechanical quality. We demonstrate that quality $\times$ frequency factors in excess of 10^{13} Hz are attainable for the higher harmonics of a 500-μm-wide by 30-nm-thick membrane oscillating at a frequency of several MHz. Significantly, this represents a key minimum requirement for ground-state optomechanical cooling from room temperature [24].

In Chapter 5 we present a top-down description of the MIM apparatus currently in operation in our lab, discussing design criteria and construction of the cavity, the system for nano-positioning the membrane between the cavity mirrors, the vacuum chamber, the vibration isolation system, and the optical circuit used to lock and probe the cavity.

In Chapter 6 we discuss measurements of the linear optical properties of our MIM cavity, walking step-by-step through the predictions of Chapter 3. We first individually characterize the optical properties of the membrane and the mirrors. We then characterize the transfer function of the cavity (output/input power vs. laser detuning) with and without the membrane, using the membrane position and the laser frequency as variable parameters. We infer, for example, the optomechanical coupling of the membrane. Comparing the transfer function to the numerical matrix model also gives information about the absorption and reflection of the mirrors and membrane.

In Chapter 7 we discuss two important departures from the 1D model presented in Chapters 2–3. First we include the transverse spatial profile of both the cavity mode and mechanical vibration in our computation of the optomechanical coupling. Then we consider the full multi-mode spectrum of vibration modes in our model for the Brownian displacement noise spectrum of the membrane resonator. As an important corollary, we model the Brownian displacement noise spectrum of the cavity mirror substrates, using finite element analysis to compute their vibrational eigenmodes and eigenfrequencies.

In Chapter 8 we discuss two methods used to characterize Brownian motion of the membrane. These include directly monitoring the transmitted power of the detuned cooling beam and monitoring the phase of a resonant probe via the Pound-Drever-Hall technique. We describe the sensitivity of these measurements and how they may be calibrated. We then step through an example measurement of the membrane's effective temperature. Finally, we use these techniques to characterize laser phase noise and Brownian motion of the mirror substrates — a result revisited in Chapter 10.

In Chapter 9 we investigate optical spring and damping forces in our MIM system. Using ~ 1 W of circulating power and a cavity finesse of $\approx 10^4$, we are able to optically damp the $(6,6)$ drum mode of a square $500\,\mu$m-wide by 50-nm-thick membrane (oscillating at 4.8 MHz) from room temperature to ≈ 500 phonons, representing a temperature compression of $\approx 10^4$. We compare our results to a simple multimode cooling model.

In Chapter 10 we investigate a fundamental roadblock to ground-state cooling associated with

Brownian motion of the mirror substrates. This motion produces extra intensity noise on the cavity field, which can result in radiation pressure heating of the low-mass membrane. We analyze this "substrate noise" in the context of the MIM system and discuss the role of spatial mode overlap between the mechanical and optical modes in determining its relative magnitude. We show that by simultaneously driving two separate spatial modes of the cavity, it is possible to exploit this overlap to measure the substrate noise background independent of the membrane. We then develop a method to suppress substrate noise by applying open loop feedback to the frequency of the input field.

Chapter 2

Basic Theory

The purpose of this chapter is to establish a formal language that will be used in the rest of this thesis to describe mechanical resonators, electric fields in optical cavities, and their interaction in a typical cavity-optomechanical system. As a model for the latter, we consider the "canonical" arrangement shown in Figure 2.1, in which one of the end-mirrors in a rigid Fabry-Perot cavity is replaced by a compliant micro-mirror. The fields inside and outside the cavity will be modeled as plane waves and the mechanical resonator as a rigid plate on the end of a pendulum spring. With this simple model, we will classically derive the coupled equations of motion for the cavity field and the end-mirror. We will then use the coupled equations of motion to derive expressions for the optical spring and damping forces experienced by the micro-mirror, in a "weak" limit that is appropriate for modeling
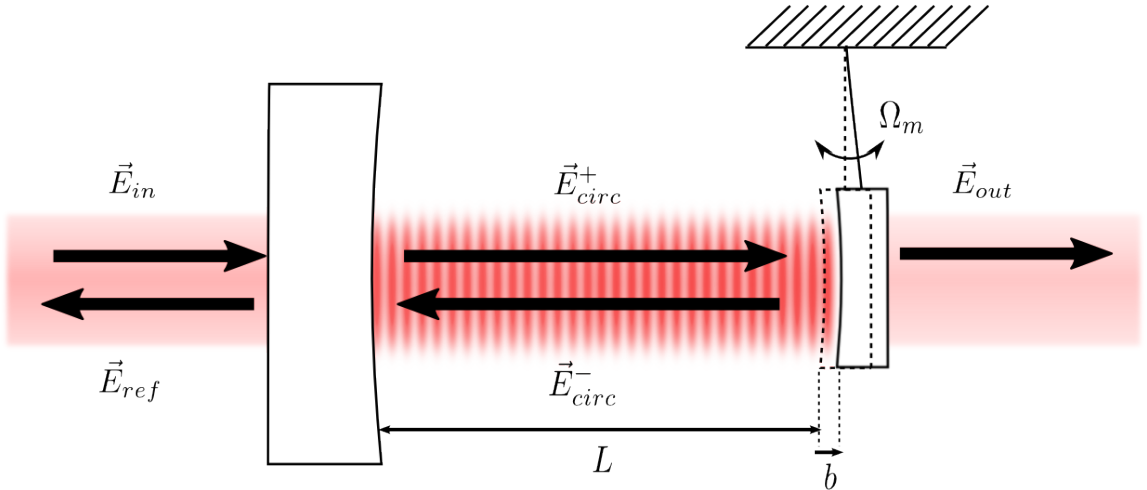
Figure 2.1: Schematic of the "canonical" 1D optomechanical system: a planar Fabry-Perot resonator with a compliant end-mirror. $\{E_{in}, E_{ref}, E_{circ}^+, E_{circ}^-, E_{out}\}$ represent the traveling waves incident on, reflected from, circulating inside, and transmitted from the cavity, respectively. Variable b represents the displacement of the mirror face from its equilibrium position in the absence of cavity light forces.

the experimental results in later chapters.

Parts of this section will rely on mathematical tools developed for the Fourier analysis of periodic and noisy signals. In the next section we briefly outline these tools.

2.1 Mathematical Tools: Fourier Analysis

We here establish conventions that will be used to describe the spectral content of periodic and noisy signals. For good references see, for example [25, 26, 27].

Let $x(t)$ be a possibly complex function of time that describes a physical process. The Fourier transform (FT) and inverse Fourier transform (IFT) will be *formally* defined:

$$x(\Omega) = \int_{-\infty}^{\infty} x(t)e^{-i\Omega t}dt, \tag{2.1a}$$

$$x(t) = \int_{-\infty}^{\infty} x(\Omega)e^{i\Omega t}d\Omega/2\pi, \tag{2.1b}$$

respectively, where $\Omega = 2\pi f$ is the angular counterpart to Fourier frequency f.

By *formally*, we mean to suggest that for some functions, the FT does formally exist. An important condition for existence is that the function have a finite "energy" or zero "power":

$$\text{"energy"} \equiv E_x \equiv \int_{-\infty}^{\infty} |x(t)|^2 dt < \infty, \tag{2.2a}$$

$$\text{"power"} \equiv \langle x(t)^2 \rangle \equiv \lim_{T \to \infty} \frac{1}{T} \int_{-T/2}^{T/2} |x(t)|^2 dt = 0. \tag{2.2b}$$

Unfortunately, many useful functions do not have zero power. A sinusoidal function is an important example. To get around this particular case, we introduce the Dirac-delta function, $\delta(\Omega)$, which has the property:

$$\delta(\Omega - \Omega_0) = \int_{-\infty}^{\infty} e^{i\Omega_0 t}e^{-i\Omega t}dt, \tag{2.3a}$$

$$e^{i\Omega_0 t} = \int_{-\infty}^{\infty} \delta(\Omega - \Omega_0)e^{i\Omega t}d\Omega/2\pi. \tag{2.3b}$$

Thus we have, for a common sinusoidal function:

$$x(t) = x_0 \cos(\Omega_0 t) = \frac{x_0}{2}\left(e^{i\Omega_0 t} + e^{-i\Omega_0 t}\right), \tag{2.4a}$$

$$x(\Omega) = \frac{x_0}{2}(\delta(\Omega - \Omega_0) + \delta(\Omega + \Omega_0)). \tag{2.4b}$$

Fourier transform $x(\Omega)$ has units of $[x]/$Hz and is related to the energy of $x(t)$ by Parseval's

theorem:

$$E_x = \int_{-\infty}^{\infty} |x(\Omega)|^2 d\Omega/2\pi. \tag{2.5}$$

The quantity $|x(\Omega)|^2$ has units of $[x]^2/\text{Hz}^2$ and is referred to as the "double-sided energy spectral density" of x. "Double-sided" refers to the fact that both positive and negative frequencies are included in the normalization of the density function. Importantly, note that although $|x(\Omega)|^2$ has been expressed as an explicit function of *angular* Fourier frequency Ω, it is normalized like a density function in the domain of non-angular Fourier frequencies, $f = \Omega/2\pi$. This notational convention will greatly simplify later expressions.

A random function $x(t)$ is a second important example of a function with non-zero power. $x(t)$ might describe a "noisy" physical process like the flux of electrons through a resistor or the amplitude of a cantilever undergoing Brownian motion. In this situation the spectral content of $x(t)$ is defined relative to one of its statistical measures.

For the following we consider only functions $x(t)$ which are real-valued and "stationary" in the (loose) sense that statistical properties of $x(t)$ and time-shifted value $x(t+\tau)$ are the same (see [27] for details). An important statistical measure is the autocorrelation of $x(t)$, defined:

$$\langle x(t)x(t+\tau)\rangle = \lim_{T\to\infty} \int_{-T/2}^{T/2} x(t)x(t+\tau)dt; \ x \in \Re. \tag{2.6}$$

The Fourier transform of the autocorrelation of $x(t)$ is referred to as the "double-sided power spectral density"

$$S_{xx}(\Omega) \equiv \int_{-\infty}^{\infty} \langle x(t)x(t+\tau)\rangle e^{-i\Omega\tau} d\tau, \tag{2.7}$$

and has the property

$$\langle x^2(t)\rangle = \int_{-\infty}^{\infty} S_{xx}(\Omega)d\Omega/2\pi. \tag{2.8}$$

It can be shown that if $x(t)$ is real-valued, then $S_{xx}(\Omega) = S_{xx}(-\Omega)$. This property can be used to define a "single-sided" power spectral density,

$$S_x(\Omega) \equiv 2S_{xx}(\Omega), \tag{2.9}$$

on the domain of positive angular Fourier frequencies ($\Omega > 0$), which has the property:

$$\langle x^2(t)\rangle = \int_0^{\infty} S_x(\Omega)d\Omega/2\pi. \tag{2.10}$$

Note again that although $S_x(\Omega)$ is here expressed an an explicit function of Ω, it is defined by Eqs. 2.7– 2.9 to represent a density in the domain of *non-angular*, positive Fourier frequencies $f = \Omega/2\pi > 0$.

An important utility of the power spectral density is that it can be used to used predict the outcome of passing a noisy signal through a linear system. A linear system is an input-output model of a physical system based on a linear transformation, $\mathcal{G} : x(t) \mapsto y(t)$. Let $x(t)$ describe the input signal and $y(t) = \mathcal{G}(x(t))$ the output signal. Functions $x(t)$ and $y(t)$ might represent voltages at the input and output of an electronic filter, for example. They might also represent a driving force $x(t)$ applied to a damped harmonic oscillator to produce a displacement $y(t)$. In any case, when the system's behavior is time-invariant, the transformation can be written as the convolution of $x(t)$ with a function $g(t)$, the "step-response function" of the system (here assumed to be real):

$$y(t) = \int_{-\infty}^{\infty} x(t')g(t - t')dt'. \tag{2.11}$$

The step-response function possesses a Fourier transform, $g(\Omega)$, called the "frequency response function" of the system. Importantly, it can be shown that [26, 27]:

$$y(\Omega) = g(\Omega)x(\Omega), \tag{2.12a}$$

$$S_y(\Omega) = |g(\Omega)|^2 S_x(\Omega). \tag{2.12b}$$

Function $|g(\Omega)|^2$ is called the transfer function of the system.

Eq. 2.12 suggests that if we know the response of the system to a sinusoidal input, then we can predict the response of the system to a noisy input. Thus we will often invoke the Fourier transform as an analytical tool to obtain $g(\Omega)$, even if the inputs and outputs of the system can only be described by spectral densities.

2.2   Mechanical Oscillator: 1D Model

In our model system, shown in Figure 2.1, the compliant mirror is treated like a rigid plate attached to a pendulum spring. The mirror is contrained to move along the cavity axis. $b(t)$ represents the time-varying displacement of the mirror face from its equilibrium position when the intracavity field is not excited. Small displacements of the mirror along the cavity axis are modeled by the equation of motion for a driven, velocity-damped harmonic oscillator:

$$m\ddot{b}(t) + m\Gamma_m \dot{b}(t) + m\Omega_m^2 b(t) = F(t), \tag{2.13}$$

where Γ_m is the energy damping rate of the spring in angular units, Ω_m is the mechanical resonance frequency in angular units, and F is an external driving force. The effective mass, m, of displacement amplitude b is defined so that the potential energy of the mass-spring system is $U(t) = \frac{1}{2}m\Omega_m^2 b(t)^2$. For a massless pendulum spring, m is equivalent to the physical mass m_{phys}.

The mass-spring system can be thought of as a linear system which transforms a small sinusoidal force into small sinusoidal position change. The frequency response function (Eq. 2.12) describing this process, $\chi(\Omega) \equiv b(\Omega)/F(\Omega)$, is referred to as the mechanical susceptibility of the system; here $b(\Omega)$ and $F(\Omega)$ are the Fourier transforms (Eq. 2.1) of $b(t)$ and $F(t)$.

An expression for $\chi(\Omega)$ can be obtained by formally applying the Fourier transform to both sides of Eq. 2.13. This gives:

$$-m\Omega^2 b(\Omega) + im\Omega\Gamma_m b(\Omega) + m\Omega_m^2 b(\Omega) = F(\Omega), \tag{2.14a}$$

$$\chi(\Omega) \equiv \frac{b(\Omega)}{F(\Omega)} = \frac{m^{-1}}{\Omega_m^2 - \Omega^2 + i\Omega\Gamma_m}. \tag{2.14b}$$

Note that for most real-world resonators, velocity damping is only suitable for describing fluctuations near resonance. Damping of internal vibrations in bulk resonators has been found to obey a more complicated equation of motion consistent with a frequency-dependent damping term, $\Gamma_m \to \Gamma_m(\Omega)$ in Eq. 2.14a. This subject will be revisited in Chapter 7. It's worth mentioning here a common form of internal damping, "structural" damping, that has the property $\Gamma_m(\Omega) = \Gamma_m(\Omega_m) \times \Omega_m/\Omega$. This form of damping is characteristic of elastic bodies whose various internal modes (at different frequencies) all share similar quality factors, where the quality factor is defined:

$$Q_m \equiv \frac{\Omega_m}{\Gamma_m(\Omega_m)}. \tag{2.15}$$

In the absence of external forces, Eqs. 2.13–2.14 suggest that a damped oscillator decays to a steady-state amplitude of zero. In reality, the mean vibrational energy of the system is non-zero, since it is energetically coupled to an environment with a finite temperature, T_{bath}. The effect of this coupling is described by introducing a random driving force with a power spectral density (Eq. 2.9) given by the Fluctuation-Dissipation Theorem [28, 29]:

$$S_F(\Omega) = \frac{4k_B T_{bath}}{\Omega} \, \mathrm{Im}\left[\chi(\Omega)^{-1}\right] = 4k_B T_{bath}\Gamma_m(\Omega)m. \tag{2.16}$$

Fluctuations of b are related to fluctuations of F by the mechanical transfer function, $|\chi(\Omega)|^2$:

$$S_b(\Omega) = |\chi(\Omega)|^2 S_F(\Omega) = \frac{4k_B T_{bath}\Gamma_m(\Omega)}{m} \frac{1}{(\Omega_m^2 - \Omega^2)^2 + \Omega^2\Gamma_m^2(\Omega)}. \tag{2.17}$$

For structural and velocity damping we have, using the shorthand notation $\Gamma_m(\Omega_m) \equiv \Gamma_m$:

$$S_b(\Omega)|_{velocity} = \frac{4k_B T_{bath}\Gamma_m}{m} \frac{1}{(\Omega_m^2 - \Omega^2)^2 + \Omega^2\Gamma_m^2}, \tag{2.18a}$$

$$S_b(\Omega)|_{structural} = \frac{4k_B T_{bath}\Gamma_m}{m} \frac{\Omega_m/\Omega}{(\Omega_m^2 - \Omega^2)^2 + \Omega_m^2\Gamma_m^2}. \tag{2.18b}$$
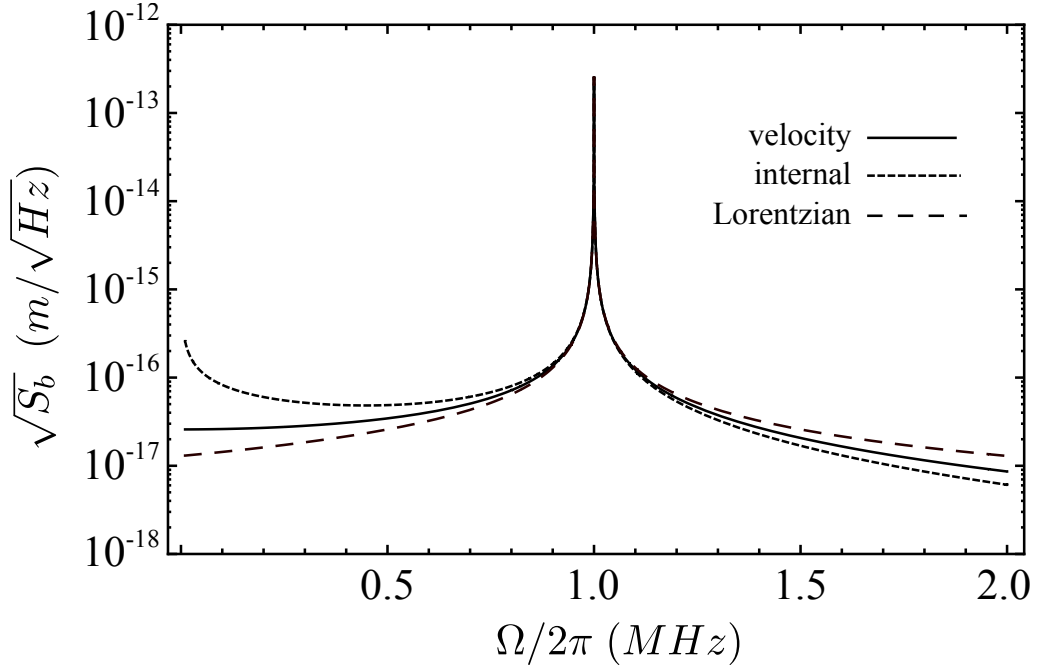
Figure 2.2: Power spectral density of displacement fluctuations for a Brownian oscillator with parameters $\{m, Q_m, \Omega_m, T_{bath}\} = \{10\,\text{ng}, 10^4, 2\pi \times 1\,\text{MHz}, 300\,\text{K}\}$. Models for velocity (Eq. 2.18a) and internal (Eq. 2.18b) damping are compared to the Lorentzian approximation (Eq. 2.19).

In both cases, the fluctuations of a weakly damped oscillator ($\Gamma_m \ll \Omega_m$) near resonance are approximated by a Lorentzian with FWHM $= \Gamma_m$:

$$S_b(\Omega) \approx \frac{4k_B T_{bath}}{m\Omega_m^2 \Gamma_m} \frac{1}{1 + 4(\Omega_m - \Omega)^2/\Gamma_m^2}. \tag{2.19}$$

One can also check that for both cases in Eq. 2.18, summing the power spectral density over all positive Fourier frequencies gives a mean potential energy,

$$\langle U \rangle = \frac{1}{2}m \int_0^\infty \Omega^2 S_b(\Omega) d\Omega/2\pi = \frac{1}{2}k_B T_{bath}, \tag{2.20}$$

that is consistent with the principle of energy equipartition.

A representative plot of structural damping and velocity damping for a weakly damped system is given in Figure 2.2. We give the plot for values which will be of relevance in the experiment: $\{m, Q_m, \Omega_m, T_{bath}\} = \{10\,\text{ng}, 10^4, 2\pi \times 1\,\text{MHz}, 300\,\text{K}\}$. Only a small fraction of energy ($\sim 1/Q_m$) is contributed by the off-resonant frequencies where the models differ. Thus we often use velocity damping and/or the Lorentzian approximation to describe a weakly damped system.

2.3   Optical Cavity: 1D Model

In our model (Figure 2.1) we consider an optical cavity consisting of two weakly transmissive mirrors separated by a vacuum gap of length L. The cavity is driven by an electric field incident on the left (input) mirror. The task is to determine the magnitude of the electric field in the cavity. As a departure from the usual steady-state treatment (see [30]), we will allow the amplitude of all fields to vary on a timescale $\sim 2\pi/\Omega_m$, much slower than both an optical cycle and the cavity round trip time, $T_{rt} = 2L/c$. This will allow us to characterize the slow buildup and decay of the cavity field in response to a perturbation.

For simplicity, we assume that the mirrors are flat and that the fields entering, exiting, and circulating between the cavity mirrors are described by uniform plane waves with a single carrier frequency, ω_0, and a common polarization perpendicular to the cavity axis, z. The mirrors are modeled as thin, lossless dielectric plates with reflection coefficients $r_{1,2}$ and $it_{1,2}$ ($r_{1,2}$ and $t_{1,2}$ are real), where $r_{1,2}^2 + t_{1,2}^2 = 1$. This "transmission line" model is discussed in detail in [31, 32].

A diagram of the transmission line model is shown in Figure 2.3. Let $E_{in}(t)e^{i\omega_0 t}$ and $E_{ref}(t)e^{i\omega_0 t}$ be the complex amplitude of the incident and reflected traveling waves at the outer surface of the left mirror. Let $E_{out}(t)e^{i\omega_0 t}$ be the complex amplitude of the transmitted field at the outer surface of the right mirror. The total intracavity field $E_{circ}(z,t)e^{i\omega_0 t}$ is given by the superposition of a plane wave propagating in the right direction $E_{circ}^+(t)e^{i(\omega_0 t - kz)}$ and a plane wave propogating in the left direction, $E_{circ}^-(t)e^{i(\omega_0 t + kz)} = r_2 E_{circ}^+(t)e^{i(\omega_0 t + kz)}$. Letting $z = 0$ be the inner surface of the left
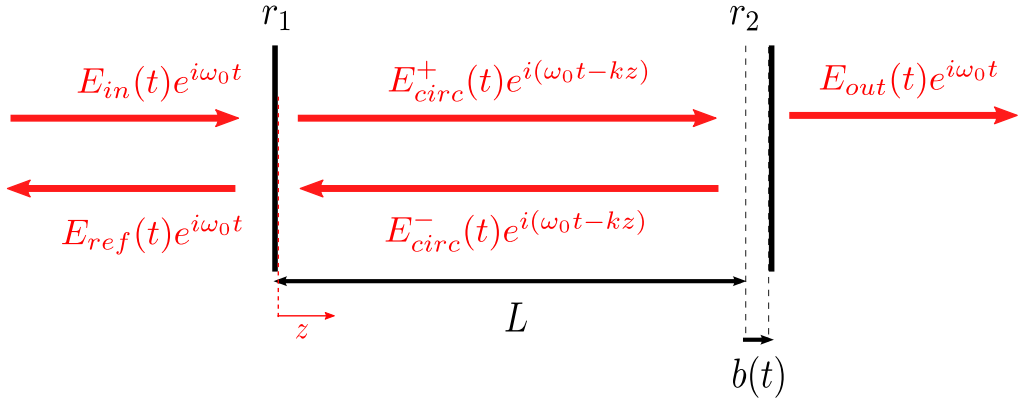
Figure 2.3: Schematic of the "canonical" 1D optomechanical system: a planar Fabry-Perot resonator with a compliant end-mirror. $\{E_{in}(t), E_{ref}(t), E_{circ}^+(t), E_{circ}^-(t), E_{out}(t)\}$ represent the slowly varying complex amplitudes of the traveling waves incident on, reflected from, circulating inside, and transmitted from the cavity, respectively.

mirror, we have:

$$E_{circ}(z,t) = E_{circ}^+(t)e^{-ikz} + r_2 E_{circ}^+(t)e^{ikz} \tag{2.21a}$$

$$= E_{circ}^+(t)(e^{-ikz} + r_2 e^{ikz}), \tag{2.21b}$$

$$E_{out}(t) = it_2 E_{circ}^+(t)e^{-ikL}, \tag{2.21c}$$

$$E_{ref}(t) = r_1 E_{in}(t) + it_1 r_2 E_{circ}^+(t). \tag{2.21d}$$

One more equation is needed to solve for the fields. For this, note that a forward propagating plane wave originating at $z = 0$ and traversing one round trip to its origin position will acquire a complex amplitude of $r_1 r_2 e^{-2ikL}$. This property defines a recursion relation between the total forward propagating field inside the cavity at time t and the forward propagating field at a later time $t + T_{rt}$ [31, 32]:

$$E_{circ}^+(t + T_{rt}) \approx it_1 E_{in}(t) + r_1 r_2 e^{-2ikL} E_{circ}^+(t). \tag{2.22}$$

The recursion relation can be used to obtain a differential equation for $E_{circ}^+(t)$:

$$\frac{dE_{circ}^+(t)}{dt} \approx \frac{E_{circ}^+(t + T_{rt}) - E_{circ}^+(t)}{T_{rt}} = \frac{it_1}{T_{rt}} E_{in}(t) + \frac{1}{T_{rt}}(r_1 r_2 e^{-2ikL} - 1)E_{circ}^+(t). \tag{2.23}$$

We now consider some approximations relevant to cavities with low internal losses and highly reflectivity mirrors, $r_{1,2} \approx -1$. In this case we can write

$$r_1 r_2 \approx 1 - \frac{t_1^2}{2} - \frac{t_2^2}{2}. \tag{2.24}$$

Internal losses can be modeled as a small imaginary component added to k:

$$e^{-2ikL} \approx e^{-2i\omega_0 L/c}(1 - \delta_L). \tag{2.25}$$

Near resonance, the round trip phase becomes

$$e^{-2i\omega_0 L/c} \approx 1 - i\left(\frac{\omega_0 - \omega_c}{FSR}\right), \tag{2.26}$$

where $FSR = c/2L$ is the cavity free spectral range (in non-angular units) and $\omega_c = 2\pi \times nFSR$ is one of the cavity resonance frequencies with $n > 0$ a positive integer.

For highly reflective mirrors ($r_{1,2} \approx -1$), the magnitude of the forward and backward propagating

waves are nearly equal. This gives rise to an intracavity standing wave:

$$E_{circ}(z,t) = -2iE_{circ}^{+}(t)e^{i\omega_0 t}\sin(kz)\vec{x} \tag{2.27a}$$

$$\equiv 2E_{circ}(t)e^{i\omega_0 t}\sin(kz)\vec{x}. \tag{2.27b}$$

We can now recast Eq. 2.23 in terms of the slowly varying envelope of the standing wave field, $E_{circ}(t) \equiv -iE_{circ}^{+}(t)$ (Eq. 2.27b). Near resonance and for $r_{1,2} \approx -1$:

$$\frac{dE_{circ}(t)}{dt} \approx -\left(\frac{t_1^2/2 + t_2^2/2 + \delta_L}{T_{rt}} + i(\omega_0 - \omega_c)\right)E_{circ}(t) + \frac{t_1}{T_{rt}}E_{in}(t), \tag{2.28a}$$

$$E_{out}(t) = t_2 E_{circ}(t), \tag{2.28b}$$

$$E_{ref}(t) = t_1 E_{circ}(t) - E_{in}(t). \tag{2.28c}$$

In actuality, the fields circulating inside the cavity are not plane waves. Both of the mirrors will have a large spherical radius of curvature, $R_m >> L$. In the paraxial approximation, this results in cavity modes with a transverse profile $|\psi(x,y)|$ and a nearly planar wavefront [31] (see Section 7.1.2):

$$E_{circ}(x,y,z,t) \approx 2E_{circ}(t)e^{i\omega_0 t}|\psi(x,y)|\sin(kz). \tag{2.29}$$

The tranvserse profile defines an effective cross-sectional are of the beam:

$$\iint |\psi(x,y)|^2 dxdy \equiv A. \tag{2.30}$$

In SI units, the energy in the cavity fields, the power "circulating" in the cavity, and the power supplied by the input beam ($E_{in}(t)$ now denotes that fraction which is spatially mode matched to the cavity) each have slowly varying envelopes with magnitude:

$$U_c(t) = \iiint \left(\epsilon_0 \langle \text{Re}[E_{circ}(x,y,z,t)]^2\rangle\right)dxdydz = \epsilon_0|E_{circ}(t)|^2 \times AL, \tag{2.31a}$$

$$P_{circ}(t) = \iint \left(\epsilon_0 c \langle \text{Re}[E_{circ}^{+}(x,y,z,t)]^2\rangle\right)dxdy = \frac{1}{2}\epsilon_0 c|E_{circ}(t)|^2 \times A = \frac{U_c(t)}{T_{rt}}, \tag{2.31b}$$

$$P_{in}(t) = \iint \left(\epsilon_0 c \langle \text{Re}[E_{in}(x,y,z,t)]^2\rangle\right)dxdy = \frac{1}{2}\epsilon_0 c|E_{in}(t)|^2 \times A. \tag{2.31c}$$

Setting $E_{in}(t) = 0$ in (2.28), we see that the energy in the cavity decays at a rate

$$U_c(t) = U(0)e^{-(t_1^2 + t_2^2 + 2\delta_L)t/T_{rt}} \equiv U(0)e^{-(\gamma_1 + \gamma_2 + \gamma_L)t} \equiv U(0)e^{-\gamma t} \tag{2.32a}$$

$$\equiv U(0)e^{-2(\kappa_1 + \kappa_2 + \kappa_L)t} \equiv U(0)e^{-2\kappa t}, \tag{2.32b}$$

where $\{\gamma_1, \gamma_2, \gamma_L\} \equiv \{t_1^2, t_2^2, 2\delta_L\}/T_{rt}$ are the rates of energy decay through the input mirror, output mirror, and into internal loss channels, respectively, and $\gamma \equiv \gamma_1 + \gamma_2 + \gamma_L$ is the total energy decay rate. Likewise $\{\kappa_1, \kappa_2, \kappa_L\} \equiv \{t_1^2/2, t_2^2/2, \delta_L\}/T_{rt}$ represent the rates of amplitude decay through the input mirror, output mirror, and into internal loss channels, respectively, and $\kappa \equiv \kappa_1 + \kappa_2 + \kappa_L$ is the total amplitude decay rate.

To deal with energy and power, it is useful to rewrite Eq. 2.23 using units such that $|E(t)|^2 = P(t)$. We can then multiply both sides of Eq. 2.23 by $\sqrt{T_{rt}}$ and define a new variable on the left-hand side, $a(t) = \sqrt{T_{rt}}E_{circ}(t)$, which is normalized to give the energy in the fields: $|a(t)|^2 = U_c(t) = T_{rt}P_{circ}(t)$. Near resonance, we have:

$$\dot{a}(t) = -\left(\kappa + i(\omega_0 - \omega_c)\right)a(t) + \sqrt{2\kappa_1}E_{in}(t), \tag{2.33a}$$

$$E_{out}(t) = \sqrt{2\kappa_2}a(t), \tag{2.33b}$$

$$E_{ref}(t) = \sqrt{2\kappa_1}a(t) - E_{in}(t) = \sqrt{\frac{\kappa_1}{\kappa_2}}E_{out}(t) - E_{in}(t). \tag{2.33c}$$

To solve Eq. 2.33, it is useful to rewrite each slowly varying envelope in terms of its Fourier transform Eq. 2.1. This gives

$$a(\Omega) = \frac{\sqrt{2\kappa_1}}{\kappa + i(\omega_0 + \Omega - \omega_c)}E_{in}(\Omega) \left(= \int_{-\infty}^{\infty} a(t)e^{-i\Omega t}dt\right), \tag{2.34a}$$

$$E_{out}(\Omega) = \sqrt{2\kappa_2}a(\Omega), \tag{2.34b}$$

$$E_{ref}(\Omega) = \sqrt{2\kappa_1}a(\Omega) - E_{in}(\Omega) = \sqrt{\frac{\kappa_1}{\kappa_2}}E_{out}(\Omega) - E_{in}(\Omega). \tag{2.34c}$$

Now consider the special case for which the envelope function of the input field has a constant value, corresponding to a monochromatic input field with frequency ω_0. In this case $E_{in}(\Omega) =$

$E_0\delta(\Omega)$ where $\delta(\Omega)$ is a delta function (Eq. 2.3). The rest of the fields also take on constant values:

$$\langle E_{in}\rangle = \int_{-\infty}^{\infty} E_0\delta(\Omega)d\Omega/2\pi = E_0, \tag{2.35a}$$

$$\langle P_{in}\rangle = |E_0|^2, \tag{2.35b}$$

$$\langle E_{out}\rangle = \frac{\sqrt{4\kappa_1\kappa_2}}{\kappa}\frac{1}{1+i(\omega_0-\omega_c)/\kappa}\langle E_{in}\rangle, \tag{2.35c}$$

$$\langle P_{out}\rangle = \frac{4\kappa_1\kappa_2}{\kappa^2}\frac{1}{1+(\omega_0-\omega_c)^2/\kappa^2}\langle P_{in}\rangle, \tag{2.35d}$$

$$\langle E_{ref}\rangle = \frac{2\kappa_1-\kappa-i(\omega_0-\omega_c)}{\kappa+i(\omega_0-\omega_c)}\langle E_{in}\rangle, \tag{2.35e}$$

$$\langle P_{ref}\rangle = \frac{(2\kappa_1-\kappa)^2+(\omega_0-\omega_c)^2}{\kappa^2+(\omega_0-\omega_c)^2}\langle P_{in}\rangle. \tag{2.35f}$$

We can measure $\{\kappa_1,\kappa_2,\kappa_L,\kappa\}$ by slowly sweeping the detuning of the input field $\omega_c-\omega_0$. In practice we do this by changing the cavity length or the laser wavelength at a rate $\ll \kappa$, while monitoring $\{P_{in}, P_{out}, P_{ref}\}$ on separate photodetectors. The curve swept out in either transmission or reflection is a Lorentzian with a HWHM of κ and a FWHM of γ.

Note also the conventional "finesse" notation:

$$\langle P_{circ}\rangle = \frac{c}{2L}\langle U_{circ}\rangle \equiv \frac{\mathcal{F}}{\pi}\frac{2\kappa_1}{\kappa}\frac{1}{1+(\omega_0-\omega_c)^2/\kappa^2}\langle P_{in}\rangle = \frac{\mathcal{F}}{\pi}\frac{\kappa}{2\kappa_2}\langle P_{out}\rangle. \tag{2.36}$$

The quantity $\mathcal{F} \equiv \pi c/(2\kappa L) = FSR/(2\kappa/2\pi) = FSR/(\gamma/2\pi)$ is the cavity "finesse" and gives a measure of the resonant power buildup inside the cavity.

In the next section, we will use Eq. 2.33 to treat the dynamics of a cavity with a moving boundary.

2.4 Optomechanical Interaction: 1D Model

We now wish to couple the motion of the mirror to the amplitude of the intracavity field. This coupling is mediated by the radiation force experienced by the mirror, which in the simple 1D model is given by

$$F_{rad} = \frac{2P_{circ}}{c} = \frac{U_c}{L}. \tag{2.37}$$

The dynamics of the system also depend critically on the "optomechanical coupling", g, between the mirror position and the cavity resonance frequency:

$$g \equiv \frac{d\omega_c}{db}. \tag{2.38}$$

To see this, it is useful to recast the radiation pressure force in terms of the work done on the cavity by a small displacement of coordinate b. Using Eq. 2.31a and noting that the actual cavity length at any particular time is $L + b$:

$$F_{rad} = -\frac{dU_{mech}}{db} = \frac{dU_c}{db} = \frac{d\omega_c}{db}\frac{dL}{d\omega_c}\frac{dU_c}{dL} = -\frac{g}{\omega_c}U_c. \tag{2.39}$$

Eq. 2.37 is reproduced by setting $g = -\omega_c/L$ for a simple Fabry-Perot resonator. Note that the negative sign of g is unconventional, and relates to the choice of sign for b. Here we equate positive b with a longer cavity, so the average radiation pressure force is positive.

Coupled equations of motion for the cavity field and the mirror are obtained by replacing ω_c in Eq. 2.33 by $\omega_c + gb(t)$ and by including a radiation pressure force as well as an additional driving term in the equation of motion for b, Eq. 2.13. This gives:

$$m\ddot{b}(t) + m\Gamma_m\dot{b}(t) + m\Omega_m^2 b(t) = F(t) + F_{rad}(t) = F(t) - \frac{g}{\omega_c}|a(t)|^2, \tag{2.40a}$$

$$\dot{a}(t) = -\left(\kappa + i(\omega_0 - \omega_c - gb(t))\right)a(t) + \sqrt{2\kappa_1}E_{in}(t). \tag{2.40b}$$

It's important to note that $b(t)$ is the *real-valued* amplitude of the mirror, whereas $a(t)$ is the slowly varying *complex* amplitude of the intracavity standing wave, in units such that $|a(t)|^2 = U_c(t)$.

An approximate solution to Eq. 2.40 can be obtained by linearizing each variable around its steady-state value:

$$\{b(t), a(t), E(t), U(t), F(t)\} = \{\langle b\rangle, \langle a\rangle, \langle E\rangle, \langle U\rangle, \langle F\rangle\} + \{\delta b(t), \delta a(t), \delta E(t), \delta U(t), \delta F(t)\}. \tag{2.41}$$

If the input field is monochromatic ($\langle E_{in}\rangle = E_0$, $\delta E_{in}(t) = 0$) and the mirror motion only changes the cavity resonance frequency by a small fraction of the cavity linewidth ($g_0\delta b/\kappa \equiv \epsilon << 1$), then the intracavity field is modulated by only a small fraction of its average value. In this case the coupled equations of motion become, to first order in $\delta a/\langle a\rangle$ and $\delta b/\langle b\rangle$:

$$m\delta\ddot{b}(t) + m\Gamma_m\delta\dot{b}(t) + m\Omega_m^2\delta b(t) = \delta F(t) + \delta F_{rad}(t) \tag{2.42a}$$

$$\delta\dot{a}(t) \approx -\left(\kappa + i\Delta\right)\delta a(t) + ig\delta b(t)\langle a\rangle, \tag{2.42b}$$

where $\Delta \equiv \omega_0 - \omega_c - g\langle b\rangle$ is the shifted detuning between the cavity and the input field and

$$\langle a\rangle = \frac{\sqrt{2\kappa_1}}{\kappa + i\Delta} E_0, \tag{2.43a}$$

$$\langle b\rangle = \frac{\langle F_{rad}\rangle}{m\Omega_m^2} \tag{2.43b}$$

$$\langle F_{rad}\rangle = -\frac{g\langle U_c\rangle}{\omega_c} \tag{2.43c}$$

$$\langle U_c\rangle = |\langle a\rangle|^2 = \frac{2\kappa_1}{\kappa^2 + \Delta^2}|E_0|^2 \tag{2.43d}$$

are the steady-state values obtained by taking the time average of both sides of Eqs. 2.40a–2.40b.

The fluctuating part of the radiation pressure force is given to first order in $\delta a/\langle a\rangle$ by:

$$\delta F_{rad}(t) = F_{rad}(t) - \langle F_{rad}\rangle = -\frac{g}{\omega_c}\left(\langle a\rangle \delta a^*(t) + \langle a\rangle^* \delta a(t)\right) \tag{2.44}$$

where $\delta a^*(t)$ obeys an equation of motion given by the complex conjugate of Eq. 2.42b.

To elucidate the effect of F_{rad} on the dynamics of b, it is useful to recast Eq. 2.42a in the Fourier domain:

$$-m\Omega^2 \delta b(\Omega) + im\Gamma_m\Omega\delta b(\Omega) + m\Omega_m^2\delta b(\Omega) = \delta F(\Omega) + \delta F_{rad}(\Omega). \tag{2.45}$$

$\delta F_{rad}(\Omega)$ can be computed by taking the Fourier transform of both sides of Eq. 2.44 and Eq. 2.42b. Letting $[\delta a^*](\Omega)$ represent the Fourier transform of $\delta a^*(t)$, we obtain:

$$\delta F_{rad}(\Omega) = -\frac{g}{\omega_c}\left(\langle a\rangle [\delta a^*](\Omega) + \langle a\rangle^* \delta a(\Omega)\right) \tag{2.46a}$$

$$= -\frac{g^2\langle U_c\rangle}{\omega_c}\left(A_+(\Omega) - A_-(\Omega)\right)\delta b(\Omega), \tag{2.46b}$$

where

$$A_\pm(\Omega) \equiv \frac{i}{\kappa \pm i(\Delta \pm \Omega)} \tag{2.47}$$

characterizes the strength of the $\pm\Omega$ sideband on the intracavity field generated by the moving mirror.

According to Eq. 2.46, the magnitude of the radiation pressure force fluctuations, $\delta F_{rad}(\Omega)$, depends on the magnitude of the static radiation pressure force, $\langle F_{rad}\rangle$, the magnitude of the cavity resonance frequency fluctuations produced by the mirror, $g\delta b(\Omega)$, and the dynamic response of the the intracavity energy to resonance frequency fluctuations, characterized by $(A_+(\Omega) - A_-(\Omega))$. The response term contains an imaginary component related to the finite build-up time of the intracavity field. Consequently, $\delta F_{rad}(\Omega)$ contains a component oscillating in phase with mirror's position, $\propto b(\Omega)$, and a component oscillating in phase with the mirror's velocity, $\propto \dot{b}(\Omega) = i\Omega b(\Omega)$. These correspond to an optical spring/anti-spring force and an optical damping/anti-damping force,

respectively.

The effect of δF_{rad} on the dynamics of δb can be expressed as an "effective" mechanical susceptibility, $\chi_{eff}(\Omega) \equiv \delta b(\Omega)/\delta F(\Omega)$, obtained by isolating the external force $\delta F(\Omega)$ on the right-hand side of Eq. 2.45:

$$\chi_{eff}(\Omega)^{-1} = \chi(\Omega)^{-1} - \frac{\delta F_{rad}(\Omega)}{\delta b(\Omega)} \tag{2.48a}$$

$$= (\Omega_m^2 - \Omega^2 + i\Omega\Gamma_m(\Omega))m + \frac{g^2\langle U_c\rangle}{\omega_c}\left(A_+(\Omega) - A_-(\Omega)\right). \tag{2.48b}$$

The effective susceptibility can be expressed in terms of an optical spring constant $k_{opt}(\Omega)$ (approximated by an "optical spring shift" of the mechanical frequency $\Delta\Omega_{opt}(\Omega) \approx k_{opt}(\Omega)/2m\Omega_m$), and an optical damping rate, $\Gamma_{opt}(\Omega)$:

$$\chi_{eff}(\Omega)^{-1} = (\Omega_m^2 + k_{opt}(\Omega)/m - \Omega^2 + i\Omega(\Gamma_m(\Omega) + \Gamma_{opt}(\Omega))m, \tag{2.49a}$$

$$\approx ((\Omega_m + \Delta\Omega_{opt}(\Omega))^2 - \Omega^2 + i\Omega(\Gamma_m(\Omega) + \Gamma_{opt}(\Omega))m, \tag{2.49b}$$

$$k_{opt}(\Omega) \approx 2m\Omega_m\Delta\Omega_{opt}(\Omega) \equiv -\text{Re}\left[\frac{\delta F_{rad}(\Omega)}{\delta b(\Omega)}\right] = \frac{g^2\langle U_c\rangle}{\omega_c}\text{Re}\left[A_+(\Omega) - A_-(\Omega)\right], \tag{2.49c}$$

$$m\Omega\Gamma_{opt}(\Omega) \equiv -\text{Im}\left[\frac{\delta F_{rad}(\Omega)}{\delta b(\Omega)}\right] = \frac{g^2\langle U_c\rangle}{\omega_c}\text{Im}\left[A_+(\Omega) - A_-(\Omega)\right]. \tag{2.49d}$$

For sufficiently weak radiation pressure, i.e., $\Delta\Omega_{opt} \ll \kappa$ and $\Gamma_{opt} \ll \kappa$, the mechanical susceptibility near resonance reduces to that of a velocity-damping oscillator with a shifted resonance frequency and damping rate:

$$\chi_{eff}(\Omega)^{-1} \approx ((\Omega_m + \Delta\Omega_{opt}(\Omega_m))^2 - \Omega^2 + i\Omega(\Gamma_m(\Omega_m) + \Gamma_{opt}(\Omega_m))m. \tag{2.50a}$$

It is convenient to express the "weak" optical spring shift an damping rate in fundamental units of intracavity photon number, $\langle n_c\rangle \equiv \langle U_c\rangle/\hbar\omega_c$, and the zero-point displacement, $b_{zp}^2 \equiv \hbar/2m\Omega_m$:

$$\Delta\Omega_m(\Omega_m) = \frac{g^2\langle U_c\rangle}{\omega_c}\frac{1}{2m\Omega_m}\text{Re}[A_+(\Omega_m) - A_-(\Omega_m)] \tag{2.51a}$$

$$= \langle n_c\rangle\frac{g^2 b_{zp}^2}{\kappa}\left(\frac{(\Delta + \Omega_m)/\kappa}{1 + (\Delta + \Omega_m)^2/\kappa^2} + \frac{(\Delta - \Omega_m)/\kappa}{1 + (\Delta - \Omega_m)^2/\kappa^2}\right) \tag{2.51b}$$

$$\Gamma_{opt}(\Omega_m) = \frac{g^2\langle U_c\rangle}{\omega_c}\frac{1}{m\Omega_m}\text{Im}[A_+(\Omega_m) - A_-(\Omega_m)] \tag{2.51c}$$

$$= 2\langle n_c\rangle\frac{g^2 b_{zp}^2}{\kappa}\left(\frac{1}{1 + (\Delta + \Omega_m)^2/\kappa^2} - \frac{1}{1 + (\Delta - \Omega_m)^2/\kappa^2}\right). \tag{2.51d}$$

Note that positive damping and negative spring shifts correspond to red detuning of the drive beam from cavity resonance and vice versa.

As a result of this modified susceptibility, the mirror responds differently to the thermal force

(Eq. 2.16). The modified power spectrum of thermal fluctuations is given by:

$$S_b(\Omega) = |\chi_{eff}(\Omega)|^2 S_F(\Omega) = 4k_B T_{bath}\Gamma_m(\Omega)|\chi_{eff}(\Omega)|^2 \tag{2.52a}$$

$$= \frac{4k_B T_{bath}\Gamma_m(\Omega)}{m} \frac{1}{\left((\Omega_m + \Delta\Omega_{opt}(\Omega))^2 - \Omega^2\right)^2 + \Omega^2(\Gamma_m(\Omega) + \Gamma_{opt}(\Omega))^2}. \tag{2.52b}$$

Note that the expression for the thermal force fluctuations, $S_F(\Omega) = 4k_B T_{bath}\Gamma_m(\Omega)$, is obtained by applying the Fluctuation Dissipation Theorem (Eq. 2.16) to the *intrinsic* mechanical susceptibility rather than the effective susceptibility. This choice reflects the fact that $\Gamma_{opt}(\Omega)$, the rate of transfer of mechanical energy into the electromagnetic energy, introduces negligible thermal excitation (due the low thermal occupation of optical photons at typical ambient temperatures, i.e., $\hbar\omega_0 >> k_B T_{bath}$).

If the intrinsic and optical springs are weak and underdamped, the thermal noise spectrum near resonance reduces to (using the shorthand notation $\Gamma_m(\Omega_m) \equiv \Gamma_m$ and $\Gamma_{opt}(\Omega_m) \equiv \Gamma_{opt}$):

$$S_b(\Omega) \approx \frac{4k_B T_{bath}\Gamma_m}{m} \frac{1}{((\Omega_m + \Delta\Omega_{opt})^2 - \Omega^2)^2 + \Omega^2(\Gamma_m + \Gamma_{opt})^2}. \tag{2.53}$$

Dissipation of mechanical energy into electromagnetic energy ($\Gamma_{opt} > 0$) without added thermal noise leads to "optical cooling", characterized by a reduced vibrational energy. Expressed as an effective temperature, the vibrational energy of the oscillator in the "weak" damping limit (Eq 2.53), is given by:

$$T_{eff} = \frac{m}{k_B}\int_0^\infty \Omega^2 S_b(\Omega) \approx \frac{\Gamma_m}{\Gamma_m + \Gamma_{opt}}T_{bath}. \tag{2.54}$$

Or in terms of the mean thermal phonon occupation number:

$$\bar{n} \approx \frac{k_B T_{eff}}{\hbar\Omega_m} \approx \frac{\Gamma_m}{\Gamma_m + \Gamma_{opt}}\bar{n}_{bath}, \tag{2.55}$$

where $\bar{n}_{bath} \equiv k_B T_{bath}/\hbar\Omega_m$ is the occupation when in equilibrium with the surrounding thermal bath.

Chapter 3

Membrane-in-the-Middle System: Transfer Matrix Treatment

In this chapter we investigate a compound cavity consisting of two mirrors divided by a thin dielectric plate. The physics of compound interferometers has been studied in various modern contexts, notably for gravity wave detection. Only recently was the concept extended to "micro"-optomechanical systems by the Harris group at Yale, whose idea was to place an ultra-thin dielectric film between two mirrors of a high finesse optical cavity [13, 7, 23]. This so-called "membrane-in-the-middle" (MIM) system has various attractive features, chief among them the possibility of integrating small-
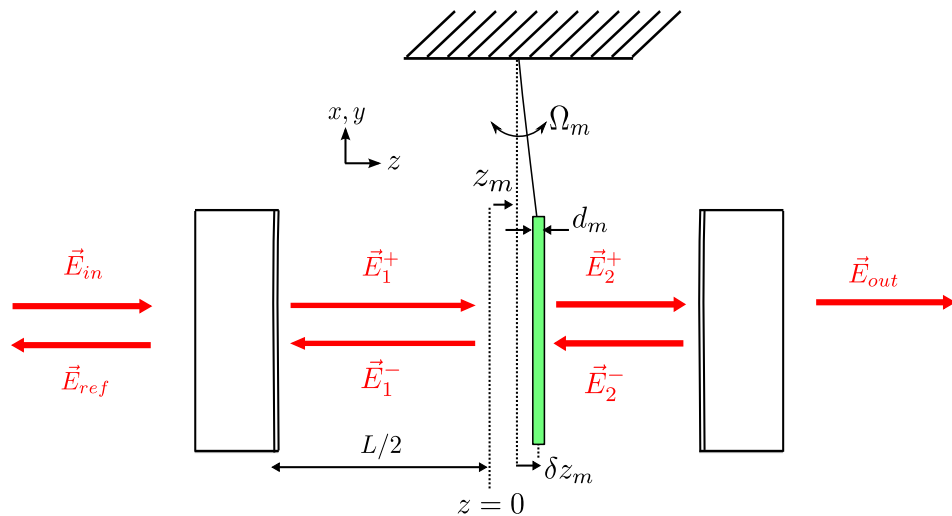
Figure 3.1: Linear (plane-wave) model of the membrane-in-the-middle system. Here a thin film of thickness d_m has been placed between two mirrors comprising a Fabry-Perot cavity with length L in the absence of the film. The equilibrium position of the membrane is displaced a distance z_m relative to the midpoint of the cavity. The membrane undergoes small displacements of amplitude $\delta z_m \ll \lambda$ around this equilibrium position with frequency Ω_m. In this chapter we consider only static properties of the cavity — such as the cavity transmission, resonance frequency, and internal losses — as a function of the membrane position and the reflection/absorption coefficients of the membrane and mirrors.

mass, high- mechanical-quality membrane resonators (see chapter 4) that have exceptionally low optical loss at near-infrared wavelengths. The cavity resonance frequency shift produced by a small displacement of the membrane's position (the "optomechanical coupling" (Eq. 2.38), an important figure of merit for optomechanical studies) depends on the membrane's position with respect to the intracavity standing wave. Remarkably, a 50 nm film with index of refraction of $n_m = 2.0$ can exhibit a linear optomechanical coupling strength nearly as high as the end-mirrors when positioned appropriately with respect to the intracavity standing wave. The coupling can also be quadratic when the membrane is positioned at a node or antinode, which has led to proposals for QND readout of the membrane's vibrational energy [23].

Here we focus on characterizing the steady-state linear optical properties of the MIM system. Towards this end, another attractive feature of the MIM system is the simplicity of its geometry. When the cavity length (L) is much shorter than the Rayleigh length (z_R) set by its spot size (w_c) and operating wavelength (λ), i.e., $L \ll z_R = \pi w_c^2 / \lambda$, then the arrangement shown in Figure 3.1 can be modeled as a plane wave propagating at normal incidence through a periodic dielectric. The apparatus we have developed (introduced in Chapter 5) is one such system, consisting of a 50 nm film bisecting a cavity with length $L = 0.742$ mm and spot-size $w_c = 35.6$ μm, giving $L/z_R = 0.17$. It seems inevitable and highly desirable, furthermore, that optomechanics with thin films will move to shorter, fiber-based cavities or fully integrated Bragg mirror cavities on a chip. In ours and especially the latter systems, the steady-state fields may be obtained by a simple and highly extensible transfer matrix method described in many standard optics texts [31, 30]. Solving the static boundary-value problem gives a wealth of useful information, including the optomechanical coupling coefficient for the membrane, the cavity eigenspectrum, transmission, reflection, linewidth, and finesse, as well the steady-state radiation pressure at each boundary. The problem is also numerically tractable when the refractive index of the film is made complex to include the effect of optical absorption. More complicated systems — for instance, including a second membrane or a realistic multilayer dielectric mirror — are also straightforward to model numerically with the transfer matrix technique. In this chapter we show how this method has be applied to our short-cavity MIM system. The framework for this treatment in our group was first laid out by Jeff Kimble in the fall of 2008. We will use it to derive several of the results mentioned above in addition to basic properties of the film and the Fabry-Perot (FP) resonator. This chapter is intended to provide a basic toolbox for the experiments described in later sections.

3.1 Characteristic Matrix

Consider the scenario illustrated in Figure 3.2: a plane, traveling EM wave is scattered at normal incidence from a dielectric plate. The incident field is assumed to be linearly polarized and

$$n_1 \qquad n_2 \qquad n_3$$

Basic relationships in $\mu \approx \mu_0$ media

$$\vec{B} = (n/c)\hat{k} \times \vec{E}$$
$$n = \sqrt{\mu\epsilon/\mu_0\epsilon_0} \approx \sqrt{\epsilon/\epsilon_0}$$
$$c = \sqrt{1/\mu_0\epsilon_0}$$

Continuity of $E_\perp$ at boundaries I/II

$$E_I = E_{i,I} + E_{r,I} = E_{t,1} + E'_{r,II}$$
$$E_{II} = E_{i,II} + E_{r,II} = E_{t,II}$$

Continuity of $B_\perp/\mu$ at boundaries I/II

$$E_{i,I} - E_{r,I} \approx \frac{n_2}{n_1}\left(E_{t,I} - E'_{r,II}\right)$$
$$E_{i,II} - E_{r,II} \approx \frac{n_3}{n_2} E_{t,II}$$

Phase relationships $\quad k_0 = \frac{2\pi}{\lambda}$

$$E_{i,II} = E_{t,I} e^{-in_2 k_0 d}$$
$$E_{r,II} = E'_{r,II} e^{in_2 k_0 d}$$
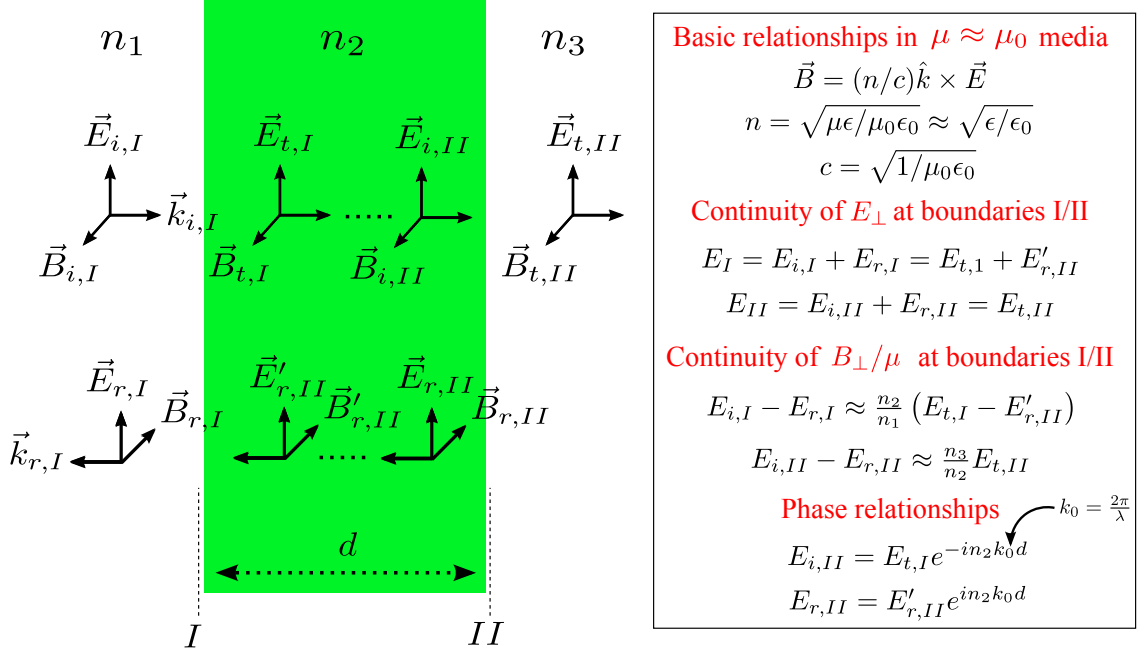
Figure 3.2: Schematic of the boundary-value problem for propagation of a plane EM wave through a dielectric plate at normal incidence. For all media we assume $\mu \approx \mu_0$. The wave enters the plate (medium with refractive index n_2) from the left medium with index n_1 and exits into the right medium with index n_3. Note that the continuity relations apply to fields just to the right or left of interfaces I and II.

monochromatic. The relationship between the total (sum of left- and right-going traveling waves) fields $E_{I(II)}$ and $B_{I(II)}$ are obtained by solving the boundary-value problem outlined in the box at right in Figure 3.2. Continuity relationships between the total fields immediately to the left and right of each boundary are set by Maxwell's equations, while traveling waves propagating in the same direction within a common medium are related by a phase shift. The relationship between the total fields at adjacent boundaries is described by a characteristic matrix, M. In the following we let $c = 1$ and assume that materials discussed are "non-magnetic" in the sense that their magnetic susceptibility is nearly that of vacuum ($\mu \approx \mu_0$). This gives:

$$\begin{pmatrix} E_I \\ B_I \end{pmatrix} \equiv \begin{pmatrix} E_{i,I} + E_{r,I} \\ B_{i,I} - B_{r,I} \end{pmatrix} = M \cdot \begin{pmatrix} E_{II} \\ B_{II} \end{pmatrix} = M \cdot \begin{pmatrix} E_{t,II} \\ B_{t,II} \end{pmatrix}. \tag{3.1}$$

The characteristic matrix for plane-wave propagation through vacuum, a thin dielectric membrane, a planar dielectric mirror, a planar FP resonator, and a planar FP resonator divided by a thin dielectric membrane (Figure 3.1) can all be written in the form $M_{tot} = \prod_i M_i$. We can use this basic property to derive a host of useful results. Our fundamental building block will be the characteristic matrix for propagation at normal incidence through a single-layer, non-magnetic dielectric plate with thickness d and index n_2, representing the central medium in Figure 3.2. This matrix

has the form:

$$M = \begin{pmatrix} \cos\phi_2 & in_2{}^{-1}\sin\phi_2 \\ in_2\sin\phi_2 & \cos\phi_2 \end{pmatrix} : \phi_2 = \frac{2\pi n_2 d}{\lambda}. \tag{3.2}$$

3.1.1 Reflection/Transmission Coefficient for a Dielectric Plate

Amplitude reflection ($r \equiv E_{r,I}/E_{i,I}$) and transmission ($t \equiv E_{t,I}/E_{i,I}$) coefficients associated with characteristic matrix M for a dieliectric plate (Eq. 3.2) follow from the defining relation given in Eq. 3.1 and the boundary conditions given in the box at right in Figure 3.2. Assuming that $\mu = \mu_0$ gives:

$$t = \frac{E_{t,II}}{E_{i,I}} = \frac{2n_1}{n_1 M_{11} + n_1 n_3 M_{12} + M_{21} + n_3 M_{22}} \tag{3.3a}$$

$$r = \frac{E_{r,I}}{E_{i,I}} = \frac{n_1 M_{11} + n_1 n_3 M_{12} - M_{21} - n_3 M_{22}}{n_1 M_{11} + n_1 n_3 M_{12} + M_{21} + n_3 M_{22}}. \tag{3.3b}$$

In our system we will frequently be interested in the case for which the dielectric plate (e.g., the film inside our optical cavity) is embedded in air or vacuum: $n_1 = n_3 \approx 1$. We will also assume that absorption in the plate is small. Following [33], we can model this loss as an imaginary component to the index of refraction (hereafter we drop the indexed notation) $n_2 \equiv n \approx |n| - i\,\text{Im}[n]$. Using the formula for the transfer matrix of a dielectric plate (Eq. 3.2) with $\phi_2 \equiv \phi = 2\pi d/\lambda$ and $\text{Im}[n] \ll |n|$, we obtain [30]

$$r = \frac{\left(1 - |n|^2\right)\sin\phi}{(|n|^2 + 1)\sin\phi - 2i|n|\cos\phi} \tag{3.4}$$

$$t = \frac{-2i|n|}{(|n|^2 + 1)\sin\phi - 2i|n|\cos\phi}. \tag{3.5}$$

The associated power transmission (T) and reflection (R) coefficients associated with t and r are given by:

$$T \equiv \frac{|E_{t,II}|^2}{|E_{i,I}|^2} = |t|^2, \tag{3.6a}$$

$$R \equiv \frac{|E_{r,II}|^2}{|E_{i,I}|^2} = |t|^2. \tag{3.6b}$$
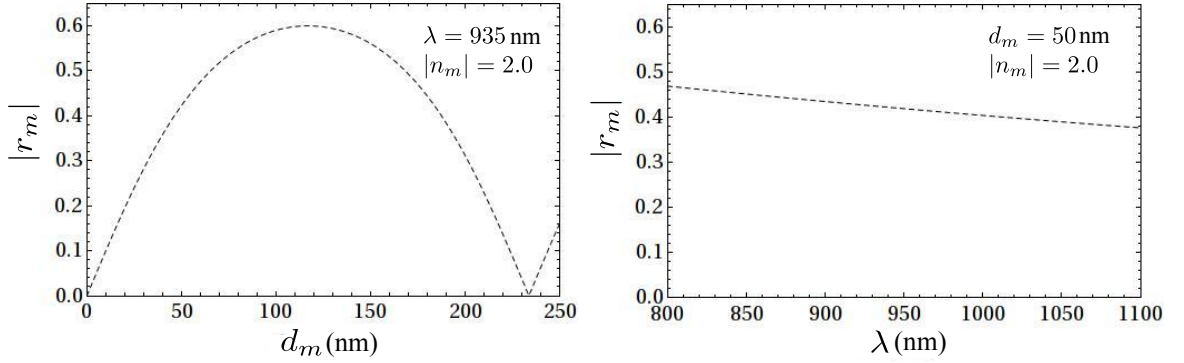
Figure 3.3: Amplitude reflectivity of a Si_3N_4 thin film with thickness d_m and real index $|n_m|$. For $|n_m| = 2.0$, the maximum reflection coefficient is achieved at $d_m = \lambda/8$: $|r_m|_{max} = 0.6$. At 935 nm, the amplitude reflection coefficient of a 50 nm film is $|r_m| = 0.42$.

For $\text{Im}[n] \ll 1$, the power loss due to absorption in the plate is given by

$$\delta \equiv 1 - (R + T) \approx 4\text{Im}[n] \left(\frac{(|n|^2 + 1)\phi + (|n|^2 - 1)\sin\phi\cos\phi}{(1 - |n|^2)^2 \sin^2\phi + 4|n|^2} \right). \tag{3.7}$$

In the experiment we divide the cavity with a 50-nm-thick by 500-μm-square window of LPCVD stoichiometric Si_3N_4. We will refer to properties of this "membrane" with index m, such as refractive index n_m and reflection coefficient r_m. We will be interested in the optical properties of the membrane in the near-infrared, particularly between 800 and 1064 nm, where it is assumed that $\text{Im}[n_m] \ll 1$. LPCVD Si_3N_4 has a real index of $|n_m| \approx 2.0$ at these wavelengths [34, 35] and exceptionally low absorption consistent with $\text{Im}[n_m] \approx 10^{-5} - 10^{-7}$ [36, 14, 13]. We have made our own measurements of n_m in Chapter 6, and found them to be consistent with $|n_m| = 1.98$ and $\text{Im}[n_m] \leq 0.8 \times 10^{-5}$. For a 50-nm-thick film and $\lambda = 935$ nm, this gives $|r_m| = 0.42$ and $\delta_m \leq 8$ ppm . Both quantities will have important consequences when trying to incorporate such a film into a high-finesse cavity. Here, it is worth noting that for $|n_m| = 2.0$, the maximum value of $|r_m|$ is obtained for a $\lambda/4$ plate ($\cos\phi_m = 0$), which at 935 nm is ≈ 117 nm. At this thickness, $|r_m| = (|n_m|^2 - 1)/(|n_m|^2 + 1) = 0.6$. A plot of $|r_m|$ vs. λ and film thickness d_m for typical experimental parameters is shown in Figure 3.3.

3.1.2 Reflection/Transmission Coefficient for a Dielectric Mirror Coating

The dielectric mirrors in our cavity are constructed by depositing a sequence of $\lambda/4$ ($\phi = \pi/2$ at operating wavelength) plates onto a glass substrate. The $\lambda/4$ plates have alternating "high" and "low" index values of n_H and n_L, respectively (Figure 3.4), each pair behaving like a band-stop filter for light entering from the low-index side. The glass substrate has a slightly wedged and AR-coated face opposite the coated face; this enables us to ignore back reflections, so we instead focus on transmission from air through the coating into the glass. At the center wavelength of the coating,

the characteristic matrix for each mirror is given by [37, 30]

$$M_{mirror} = (M_H M_L)^q M_H \tag{3.8a}$$

$$= \left(\begin{pmatrix} 0 & in_H^{-1} \\ in_H & 0 \end{pmatrix} \begin{pmatrix} 0 & in_L^{-1} \\ in_L & 0 \end{pmatrix} \right)^q \begin{pmatrix} 0 & in_H^{-1} \\ in_H & 0 \end{pmatrix} \tag{3.8b}$$

$$= \begin{pmatrix} 0 & in_{eff}^{-1} \\ in_{eff} & 0 \end{pmatrix} ; \quad n_{eff} = n_H (n_H/n_L)^q. \tag{3.8c}$$

For a field which enters the dielectric stack from air and exits into the substrate (Figure 3.4), the amplitude transmission and reflection coefficients for the stack are given by

$$r_{mirror} = \frac{n_0 n_S - n_{eff}^2}{n_0 n_S + n_{eff}^2} \tag{3.9}$$

$$t_{mirror} = \sqrt{\frac{n_S}{n_0}} \frac{-2in_0 n_{eff}}{n_S n_0 + n_{eff}^2} = \frac{-2i\sqrt{n_0 n_S} n_{eff}}{n_S n_0 + n_{eff}^2}, \tag{3.10}$$

where n_0 and n_S are the index of air and the mirror substrate and the pre-factor of $\sqrt{n_S/n_0}$ accounts for the reduced field amplitude in the mirror substrate, thus preserving the relation $|r_{mirror}|^2 + |t_{mirror}|^2 \equiv R_{mirror} + T_{mirror} = 1$.

The effect of the substrate can be absorbed into the effective index by defining $n'_{eff} = n_{eff}/\sqrt{n_0 n_S}$ in Eq. 3.8. By this convention, the mirror behaves like a thin plate of birefringent material with $\phi = \lambda/4$ and an enhanced index of refraction, $n'_{eff} \approx 2/|t_{mirror}| = 2/\sqrt{T_{mirror}} \gg 1$. Based on Eq. 3.2, the characteristic matrix of this lossless mirror coating is given by

$$M_{mirror+no\ loss} = \begin{pmatrix} 0 & i\sqrt{T_{mirror}}/2 \\ 2i/\sqrt{T_{mirror}} & 0 \end{pmatrix}. \tag{3.11}$$

To include the effect of small scattering/absorption loss on the mirror coatings while maintaining the correct reflection phase shift, we can concatenate the mirror with a thin plate of material with an index of $1 + i\delta_{loss}/8\pi$ and a phase angle of $\phi = 0$, where $\delta_{loss} \ll 1$ (Figure 3.4). For a field entering from the "air side" of the lossy plate, one obtains

$$M_{mirror+loss} \approx \begin{pmatrix} 1 & \delta_{loss}/4 \\ \delta_{loss}/4 & 1 \end{pmatrix} \begin{pmatrix} 0 & i\sqrt{T_{mirror}}/2 \\ 2i/\sqrt{T_{mirror}} & 0 \end{pmatrix}. \tag{3.12}$$

One can verify that the amplitude reflection coefficient $r_{mirror+loss}$ associated with $M_{mirror+loss}$ (Eq. 3.3) introduces a phase-shift $arg(r_{mirror+loss}) \approx \pi$ and the the power reflection coefficient ($R_{mirror+loss}$) and transmission coefficient ($T_{mirror+loss}$) associated with $M_{mirror+loss}$ (Eq. 3.6)

ΔL_M

mirror penetration depth (at coating center)

$$\Delta L_M \approx \frac{1}{n_H - n_L} \frac{\lambda_c}{2} << L_c$$

effective mirror matrix (at coating center)

no loss: $\begin{pmatrix} 0 & i\sqrt{T}/2 \\ 2i/\sqrt{T} & 0 \end{pmatrix}$

add loss: $\begin{pmatrix} 1 & \delta/4 \\ \delta/4 & 1 \end{pmatrix} \begin{pmatrix} 0 & i\sqrt{T}/2 \\ 2i/\sqrt{T} & 0 \end{pmatrix}$

wedge

n_0
(air)

n_s
(Bk7 glass)

n_0
(air)

$$T = 1 - R = 1 - \left| \frac{E_r}{E_i} \right|^2$$
$$= \frac{n_s}{n_0} \left| \frac{E_t}{E_i} \right|^2 = \frac{4 n_0 n_s}{n_H^2} \left(\frac{n_L}{n_H} \right)^q$$

$\phi = 2\pi$ $\frac{\pi}{2}$ $\frac{\pi}{2}$ $\frac{\pi}{2}$ $\frac{\pi}{2}$ $\frac{\pi}{2}$ $\frac{\pi}{2}$ $\frac{\pi}{2}$ $>> 2\pi$

n_0 | $1 + i\frac{\delta}{8\pi}$ $\delta << 1$ | n_H | n_L | n_H | n_L | n_H | .... | n_L | n_H | n_s | n_0

(loss) 1 2 .... q
(dielectric stack)

Figure 3.4: Outline of the model used in Section 3.1.2 to transform a super-mirror built on a thick, possibly lossy dielectric coating to a slightly displaced (by the coating penetration depth), infinitely thin mirror. To simplify notation we have written $\{\delta_{mirror}, R_{mirror}, T_{mirror}\} \equiv \{\delta, R, T\}$.

give rise to a loss coefficient of $1 - (R_{mirror+loss} + T_{mirror+loss}) \approx \delta_{loss}$.

To further check that our assumptions are reasonable, we quickly review the details of our cavity mirrors as described in [37]. The mirrors consist of a 35-layer stack of alternating high-index Ta_2O_5 ($n_H = 2.0411$) and low-index SiO_2 ($n_L = 1.455$) deposited on a BK7 ($n_S = 1.5098$) substrate. At coating center, $\lambda \approx 852$ nm, the mirror transmission is $T_{mirror} = 4n_S n_0 (n_L)^{34}/(n_H)^{36} = 14.6$ ppm ($t_{mirror} = 0.0038$). Scattering/absorption loss from the mirror coatings is typically $\delta_{loss,SA} \approx 3$ ppm, which is not an insignificant fraction. However, in the experiment, we operate near the edge of the coating curve, 935 nm; this results in a substantially higher transmission $T_{mirror} \approx 300$ ppm

($t_{mirror} \approx 0.017$) relative to SA loss.

We must also account for the finite penetration of the field into the coatings. In [38] and [37], it was shown that near the center of the coating, the cavity length inferred from the resonance frequencies of a Fabry-Perot cavity formed between the two mirrors is greater than the physically measured gap (e.g., by a ruler) by an amount $\Delta L_{coating}$. On resonance, this extra cavity length is roughly $\Delta L_{coating} = \lambda/2/(n_H - n_L)$, which for our mirrors centered at 850 nm is roughly $\Delta L_{coating} \approx 0.85 \times 1.63/2 = 0.67\,\mu\text{m} \ll L = 742\,\mu\text{m}$. The penetration away from the center of the coating curve is even greater (at 935 nm, it and turns out to penetrate several hundred nanometer deeper for the D1306 coating). In modeling the mirror as an infinitely thin reflector, we absorb this $\sim 1\,\mu\text{m}$ adjustment into L, so that L corresponds to the slightly larger "experimental" length associated with cavity parameters like the free spectral range described in the next section.

3.2   Fabry-Perot Cavity

A Fabry-Perot (FP) cavity is obtained by cascading two mirrors with amplitude transmission coefficients t_1 and t_2 separated by a dielectric spacer with index of refraction n_c and thickness L (defined here to include the coating penetration depth). For a vacuum spacer ($n_c = 1$), the characteristic matrix for this system can be written

$$M_{FP} = \begin{pmatrix} 0 & i\sqrt{T_1}/2 \\ 2i/\sqrt{T_1} & 0 \end{pmatrix} \begin{pmatrix} 1 & \delta_1/4 \\ \delta_1/4 & 1 \end{pmatrix} \begin{pmatrix} \cos\phi_L & i\sin\phi_L \\ i\sin\phi_L & \cos\phi_L \end{pmatrix} \begin{pmatrix} 1 & \delta_2/4 \\ \delta_2/4 & 1 \end{pmatrix} \tag{3.13a}$$

$$\times \begin{pmatrix} 0 & i\sqrt{T_1}/2 \\ 2i/\sqrt{T_1} & 0 \end{pmatrix}, \tag{3.13b}$$

where $\phi_L = 2\pi L/\lambda$, $T_{1,2} = |t_{1,2}|^2$, and $\delta_{1,2} = 1 - R_{1,2} - T_{1,2}$ are the losses of mirror 1 and 2, as defined in the previous section.

Amplitude reflection (r_{FP}) and transmission (t_{FP}) coefficients for a planar FP cavity are obtained from Eq. 3.3. For a high-finesse cavity cavity ($T_{1,2}, \delta_{1,2} \ll 1$) driven from the left side of mirror 1:

$$t_{FP} = \frac{2\sqrt{T_1 T_2}}{(T_1 + T_2 + \delta_1 + \delta_2)\cos\phi_L + 4i\sin\phi_L}. \tag{3.14}$$

FP cavity resonances occur at frequencies ω_c for which t_{FP} is maximum. Absorbing mirror penetration depth into the cavity length, the condition for resonance is given by $\phi_L = \omega_c L/c = m\pi$ or $\omega_c/2\pi = mFSR$, where m is an integer and $FSR = c/2L$ is the free-spectral range of the cavity

in non-angular units. Near resonance, we can write

$$t_{FP} \approx \frac{t_{max}}{1 + i\Delta_c/\kappa}, \tag{3.15a}$$

$$t_{max} = \frac{2\sqrt{T_1 T_2}}{T_1 + T_2 + \delta_1 + \delta_2}, \quad \kappa = FSR \times \frac{T_1 + T_2 + \delta_1 + \delta_2}{2}, \tag{3.15b}$$

where $\Delta_c = \omega - \omega_c$ is the cavity detuning from the input field with frequency $\omega/2\pi = c/\lambda$ and κ is the cavity linewidth (intensity HWHM) in angular units.

The transmission coefficient of the cavity plays a central role in various aspects of the experiment. We often measure the power transmission $T_{FP} = |t_{FP}|^2 = t_{max}^2/(1 + \Delta_c^2/\kappa^2)$ vs. detuning in order to obtain information about the dynamics of the intracavity field. We will also often use the quantity known as the "finesse", $\mathcal{F}$ to describe the cavity:

$$\mathcal{F} \equiv \frac{FSR}{2(\kappa/2\pi)} = \frac{2\pi}{T_1 + T_2 + \delta_1 + \delta_2}. \tag{3.16}$$

The finesse is a measure of frequency and length resolving power of the resonator. To see the latter, we can express the free spectral range and linewidth of the cavity in units of equivalent cavity length change: $FSR_L = \lambda/2$ and $\kappa_L \equiv \lambda/4\mathcal{F}$ (HWHM), respectively. By definition, the finesse also gives information about internal losses $\delta_{1,2}$ if T_1 and T_2 are known. We will use this notion to characterize the membrane absorption coefficient in Section 3.3.2. The finesse is also a measure of the resonant build-up of the circulating power in the cavity. On resonance:

$$\frac{P_{circ}}{P_{in}}(\Delta = 0) = \frac{|t_{max}|^2}{T_2} = \frac{2T_1}{T_1 + T_2 + \delta_1 + \delta_2} \times \frac{\mathcal{F}}{\pi}. \tag{3.17}$$

3.3 Dielectric Film inside a Fabry-Perot Cavity

The MIM system is achieved by placing a thin dielectric film (our Si_3N_4 "membrane") into the gap between two FP end-mirrors, as pictured in Figure 3.1. We will be interested in the case of a nearly lossless ($|t_{1,2}|^2 = T_{1,2} >> \delta_{1,2}$), symmetric ($t_1 = t_2 \equiv t_{mirror}$) cavity. This system is described by the characteristic matrix:

$$M_{mim} = \begin{pmatrix} 0 & i|t_{mirror}|/2 \\ i2/|t_{mirror}| & 0 \end{pmatrix} \begin{pmatrix} \cos\phi_1 & i\sin\phi_1 \\ i\sin\phi_1 & \cos\phi_1 \end{pmatrix} \begin{pmatrix} \cos\phi_m & i\sin\phi_m/n_m \\ in_m\sin\phi_m & \cos\phi_m \end{pmatrix} \tag{3.18a}$$

$$\times \begin{pmatrix} \cos\phi_2 & i\sin\phi_2 \\ i\sin\phi_2 & \cos\phi_2 \end{pmatrix} \begin{pmatrix} 0 & i|t_{mirror}|/2 \\ i2/|t_{mirror}| & 0 \end{pmatrix}, \tag{3.18b}$$

where $\phi_1 = \pi(L + 2z_m - d_m)/\lambda$, $\phi_2 = \pi(L - 2z_m - d_m)/\lambda$ and $\phi_m = 2\pi d_m/\lambda$. L, d_m, and z_m are the cavity length, membrane thickness, and the membrane position, respectively. z_m is defined as the position of the center of the membrane relative to midpoint between the two mirrors. We assume for this analysis that the membrane is stationary ($\delta z_m = 0$ in Figure 3.1).

Intuitively, the system behaves like a FP with one end-mirror (say, the exit mirror) replaced by an etalon formed between that end-mirror and the membrane. Because the transmission coefficient of the mirror is much smaller than that of the membrane, the etalon is nearly one-sided, and the main effect of the membrane is to alter the phase shift of the reflected light. A traveling wave that traverses from $z_m = 0$ to the end-mirror and back experiences an extra phase shift due to multiple reflections from the membrane. The magnitude of the phase shift depends on the position of the membrane with respect to both the antinode and the end-mirror in a non-linear fashion. Minimum/maximum phase shifts occur when the membrane is at a node/antinode of the intracavity standing wave. This non-linear phase-shift gives rise to a dispersive optomechanical coupling between the membrane position and the resonance frequency of the compound cavity.

Several properties of the MIM cavity are straightforward to measure in the lab, in particular: the MIM cavity resonance frequency, transmission coefficient, and linewidth. We can use the matrix method to compute these variables as functions of the position, z_m, of the membrane. Importantly, this gives information about the optomechanical coupling of the membrane and the effect of membrane absorption on cavity finesse.

3.3.1 MIM Cavity Resonance Condition, Optomechanical Coupling

A standard Fabry-Perot resonator possesses resonance frequencies corresponding to a round-trip phase of $m\pi$ or $f_c = \omega_c/2\pi = mc/2L$, where $m = 0, 1, 2....$ We can determine this condition analytically by using the fact that on resonance, the phase of the transmitted field is a multiple of π. The resonance condition then becomes

$$Im[M_{11} + M_{12} + M_{21} + M_{22}] = 0. \tag{3.19}$$

Applying this condition to the characteristic matrix for a FP cavity (Eq. 3.2), we can check that resonance condition is indeed $\sin(\phi_L) = 0 \rightarrow \phi_L = m\pi$.

The resonance condition for the membrane-in-the-middle cavity is more complicated to derive by this algebraic method. With some effort, and assuming all refractive indexes are purely real (no absorption), that the effective index of each mirror is much larger than that of the membrane, and
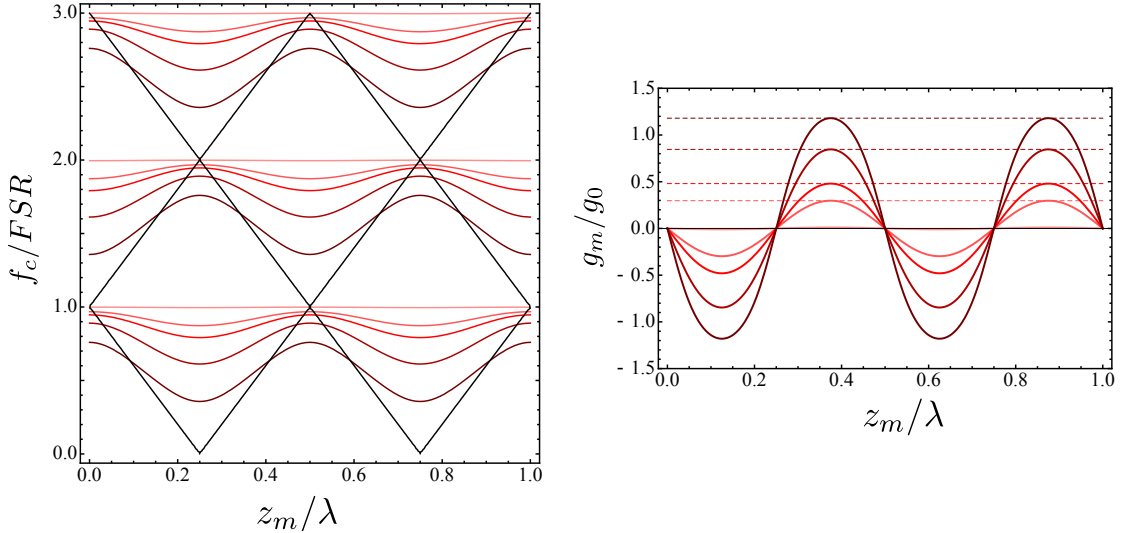
Figure 3.5: Resonance frequency structure of the "membrane-in-the-middle" system. Plotted on the left are resonance frequencies (in units of the bare cavity FSR) vs. membrane position for $|n_m| = 2$, d_m (nm) = {0 (lightest), 30, 50, 100, 200 (darkest)}, and assuming that the membrane is located near cavity center ($z_m \approx 0$). Differentiating with respect to z_m gives the optomechanical coupling, $g_m = d\omega_c/dz_m$, as shown on the right. Extrema of g_m correspond to $2|r_m|g_0$, where $g_0 = \omega_c/L$ is the optomechanical coupling of the bare cavity operating at frequency $f_c = \omega_c/2\pi$ and r_m is the reflection coefficient of the membrane. For membrane index $|n_m| = 2$ and thicknesses d_m as above, the corresponding set of reflection coefficients are $|r_m| = \{0, 0.15, 0.24, 0.42, 0.59\}$ (lightest to darkest).

calling $|r_m|$ the reflectivity of the membrane with thickness d_m, we obtain, in agreement with [23],

$$|r_m| \cos[2k_c z_m] = \cos(k_c(L - d_m) - arg(r_m)) \tag{3.20}$$

where $k_c = 2\pi f_c/c$ denotes a resonant wave vector. To solve this transcendental equation, we can first assume that the membrane is near the center of the cavity, $z_m = 0$. In this case the argument $2k_c z_m$ remains approximately constant while k_c is varied by π/L (a free spectral range of the bare cavity). To find an approximate solution, we can let $k_c \to k_0 = 2\pi/\lambda_0$ on the left-hand side, where k_0 is the resonant wave vector when $z_m = 0$, and absorb d_m into the cavity length, i.e., $L + d_m \to L$. We then obtain

$$k_c L = 2\pi f_c/FSR = \cos^{-1}\left(|r_m| \cos(2k_0 z_m)\right) + arg(r_m), \tag{3.21}$$

where f_c is now the resonance frequency of the MIM cavity.

Eq. 3.21 describes how the resonance frequency of the cavity depends on the reflectivity of the membrane and its position with respect to the intracavity standing wave. A plot of f_c/FSR vs. z_m is shown in Figure 3.5. Two features stand out. First, the optomechanical coupling of the membrane, $g_m \equiv d\omega_c/dz_m$, is non-linear. At a node ($2k_0 z_m = m\pi$) or antinode ($2k_0 z_m = (2m + 1)\pi$) of the intracavity field, the optomechanical coupling vanishes. Second, the magnitude of the coupling scales
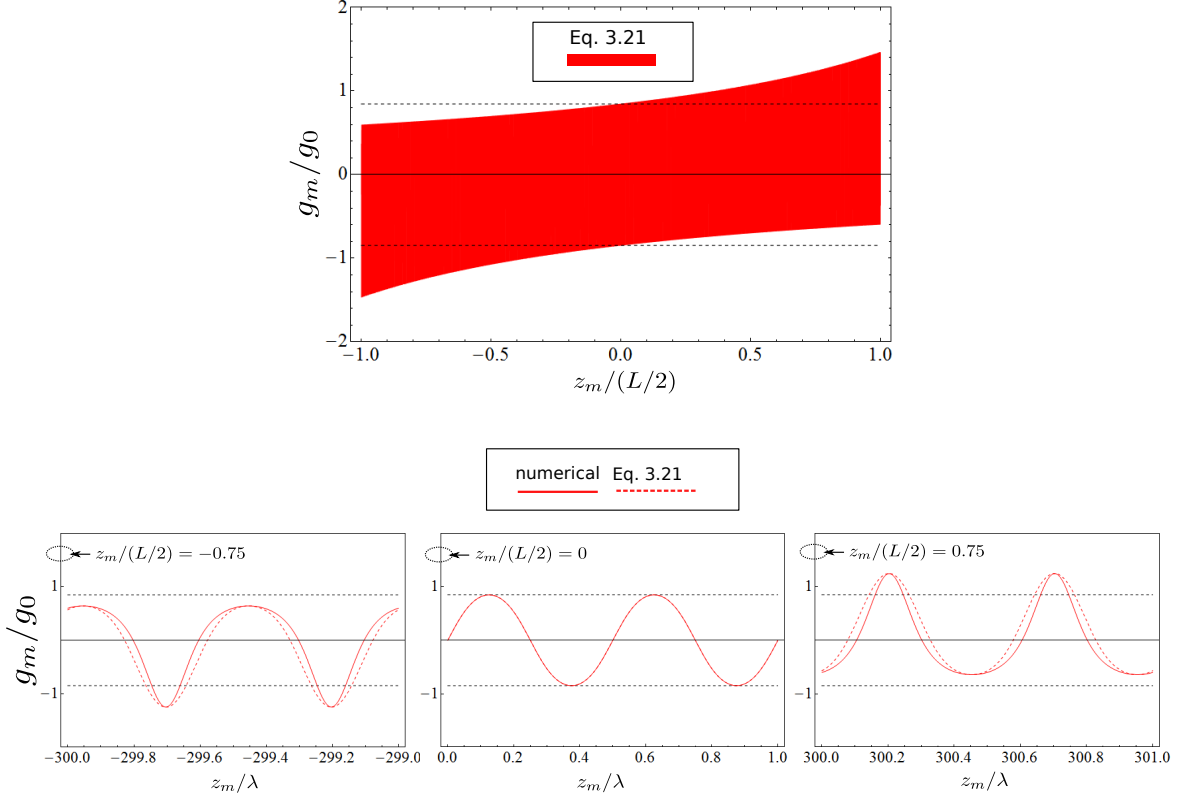
Figure 3.6: Optomechanical coupling of the membrane, $g_m \equiv d\omega_c/dz_m$, vs. membrane position relative to cavity center, z_m. Upper plot shows the range of values taken by g_m/g_0 for z_m ranging from the position of mirror 1 ($z_m = -L/2$) to the position of mirror 2 ($z_m = L/2$), calulated using the approximate analytical expression, Eq. 3.22. Lower plots show the detailed variation of g_m/g_0 vs. z_m as the membrane is translated along the intracavity standing wave (with periodicity $\lambda/2$). We show the detailed variation for three starting positions relative to the midpoint of the cavity, $z_m = \{-0.75L/2, 0, 0.75L/2\}$. Solid lines correspond to a numerical calculation of g_m/g_0. Dashed lines correspond to the values given by Eq. 3.22.

linearly with membrane reflectivity. Maximum coupling occurs at positions halfway between a node and an antinode, in which case $d\omega_c/dz_m = 2|r_m|g_0$, where $g_0 = \omega_c/L$ is the optomechanical coupling of an end-mirror. These features are summarized in the following formula for the optomechanical coupling [23]:

$$\frac{d\omega_c}{dz_m} \equiv g_m(z_m) = -g_0 \frac{2|r_m|\sin(2k_0 z_m)}{\sqrt{1 - |r_m|^2 \cos^2(2k_0 z_m)}} \equiv -2|r_m|g_0\xi(k_0, z_m). \tag{3.22}$$

A plot of $g_m(z_m)/g_0 = 2|r_m|\xi(k_0, z_m)$ vs. z_m for various values of $|r_m|$ is also given in Figure 3.5. The optomechanical coupling reaches a maximum when the membrane is located halfway between a node and antinode of the intracavity field. This is consistent with the picture in which round-trip phase acquired by the circulating field varies roughly sinusoidally with membrane position (maximum and minimum at an antinode and node, respectively).

The above formula is valid when the membrane is near the cavity center. For our short cavity, however, we have found that the result is qualitatively different for $z_m/L > 0$. This might be predicted in the limit that $|r_m| \to 1$, in which case the system driven from the left behaves like a cavity with length $L/2 + z_m$. For $z_m \ll L$, the optomechanical coupling of this cavity is $2g_0$, as predicted by Eq. 3.22. In general, however, the optomechanical coupling for this extreme case goes as $2g_0/(1 - 2z_m/L)$. To include the effect of $|r_m| < 1$, we differentiate both sides of Eq. 3.21 with respect to z_m while leaving $k_0 \to k_c(z_m)$ a function of z_m on the right-hand side (resonance frequency of the cavity changes as the membrane moves). This gives

$$g_m(z_m) = g_0 \frac{-2|r_m|\xi(k_c(z_m), z_m)}{1 - 2|r_m|\xi(k_c(z_m), z_m) \times (z_m/L)} \approx g_0 \frac{-2|r_m|\xi(k_0, z_m)}{1 - 2|r_m|\xi(k_0, z_m) \times (z_m/L)}. \qquad (3.23)$$

For $|r_m| < 1$, the extrema of $g_m(z_m)$ varies within the envelope $1/(1 - 2|r_m|(z_m/L))$. In Figure 3.6, we check this result against the solution obtained by numerically solving $\arg[t_{mim}] = 0$ as a function of frequency using Eqs. 3.18 and 3.3. The computation is made for the parameters used in the experiment ($L = 742\ \mu$m, $\lambda = 935$ nm). The envelope is seen to match. The discrepancy in the sub-structure is explained by the the fact that $(k_c(z_m) - k_0)z_m \sim |r_m|\pi z_m/L$ is non-negligible for $z_m \sim L$.

3.3.2   Linewidth and "Finesse" of the MIM Cavity

An analytical formula for the linewidth of the MIM cavity may be obtained by linearizing $T_{mim} = |t_{mim}|^2$ (where t_{mim} is the amplitude transmission coefficient associated with M_{mim}) around solutions to the resonance condition, Eq. 3.20. We have not identified a simple expression for the case in which the absorption of the membrane is finite ($\text{Im}[n_m] > 0$). In this case we have found it useful to numerically calculate $|t_{mim}|^2$ via the characteristic matrix given in Eq. 3.18. Results are discussed below.

First we can try to predict an expression for the linewidth of the MIM cavity for the case of negligible membrane absorption ($\text{Im}[n_m] = 0$) using the results obtained in the previous section. For $|r_m| \to 1$ and $\text{Im}[n_m] = 0$, the left-driven cavity has an effective length of $L/2 + z_m$ and a vanishing transmission (since $t_m \to 0$). The circulating field is shielded from the exit mirror and experiences only half of the internal losses; it also traverses the cavity in less time due to the reduced cavity length. This results in a cavity decay rate of $\kappa = \kappa_0/(1 + 2z_m/L)$, where κ_0 is the linewidth (HWHM) of the cavity with membrane removed. For $|r_m| < 1$ and $\text{Im}[n_m] = 0$, we draw an analogy
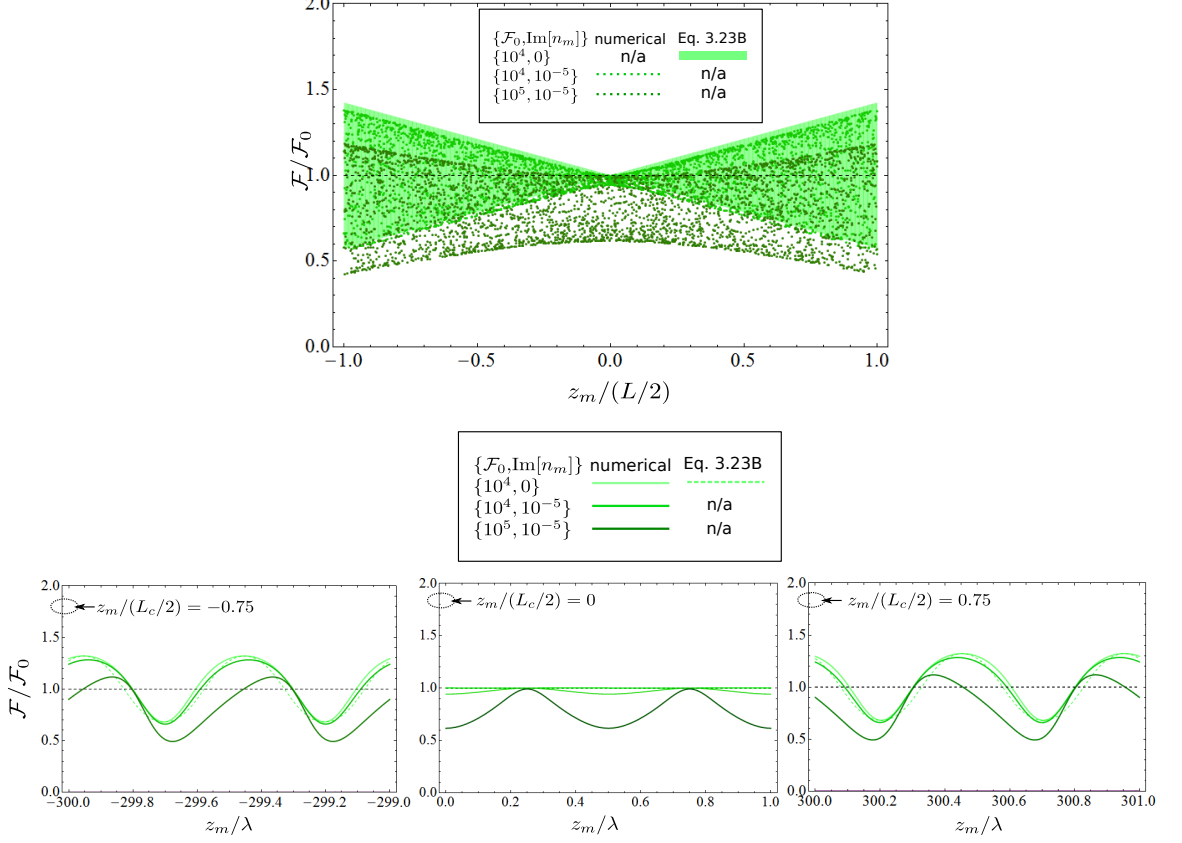
Figure 3.7: Finesse of the of the MIM cavity, $\mathcal{F} \equiv \pi c/2L\kappa$ (κ is the amplitude decay rate of the cavity in angular units) vs. membrane position with respect to cavity center, z_m. Upper plot shows the range of values taken by $\mathcal{F}/\mathcal{F}_0$ ($\mathcal{F}_0$ corresponds to the cavity finesse with the membrane removed) for z_m ranging from the position of mirror 1 ($z_m = -L/2$) to the position of mirror 2 ($z_m = L/2$). In the upper plot, the solid curve is obtained using the analytical expression for a lossless membrane, Eq. 3.24, and the dotted curves correspond to numerically computed values for $\{\mathcal{F}_0, \mathrm{Im}[n_m]\} = \{10^4, 10^{-5}\}$ (green) and $\{10^5, 10^{-5}\}$ (dark green). Lower plots show the detailed variation of $\mathcal{F}/\mathcal{F}_0$ vs. z_m as the membrane is translated along the intracavity standing wave (with periodicity $\lambda/2$). We show the detailed variation for three starting positions relative to the midpoint of the cavity, $z_m = \{-0.75L/2, 0, 0.75L/2\}$. Solid lines correspond to numerically computed values for $\{\mathcal{F}_0, \mathrm{Im}[n_m]\} = \{10^4, 0\}$ (light green), and $\{10^4, 10^{-5}\}$ (green), $\{10^5, 10^{-5}\}$ (dark green). The single, dashed, light green line corresponds to the analytical expression for a lossless membrane (Eq. 3.24). This line overlaps well with light green solid line, and is difficult to see.

to the expression obtained for g_m (Eq. 3.23) to predict:

$$\kappa = \kappa_0 \frac{1}{1 - \xi(k_c(z_m), z_m) \times (z_m/L)} \approx \kappa_0 \frac{1}{1 - \xi(k_c(z_m), z_m) \times (z_m/L)} \tag{3.24a}$$

$$\mathcal{F} \equiv \frac{\pi c}{2L\kappa} = \mathcal{F}_0(1 - \xi(k_c(z_m), z_m) \times (z_m/L)) \approx \mathcal{F}_0(1 - \xi(k_0, z_m) \times (z_m/L)). \tag{3.24b}$$

In Figure 3.7 we compare Eq. 3.24 to the solution obtained by numerically computing $|t_{mim}|^2$ vs.

f_c using Eqs. 3.3 and 3.18 and fitting the solution near $\arg[t_{mim}] = 0$ to a Lorentzian to obtain κ. The computation is made for parameters relevant to the experiment: $L = 742$ μm and $\lambda = 935$ nm. Two bare cavity finesse values, $\mathcal{F}_0 = 10^4$ and 10^5, and two membrane absorption values, $\text{Im}[n_{mem}]$ $= 10^{-5}$ and 0, are compared. We find that in the absence of absorption, the cavity finesse is indeed modulated according to the envelope function predicted in Eq. 3.24b. The effect of absorption is an increased cavity linewidth and therefore a drop in finesse compared to the lossless case. The reduction is most pronounced when the membrane is positioned near an antinode of the intracavity field. When the membrane is positioned near the center of the cavity, the variation in finesse is purely due to absorption. The fractional change in finesse when the membrane is positioned at an antinode is $\approx 6\%$ and 38%, respectively, for the case of $\mathcal{F}_0 = 10^4$ and 10^5 ($T_{mirror} \approx 310$ and 31 ppm) and $\text{Im}[n_m] = 10^{-5}$. Though not necessarily obvious, the same result is obtained by using a round-trip loss of $2\delta_m = 20$ ppm predicted by Eq. 3.7 along with the following formula for the fractional change in finesse: $\Delta\mathcal{F}/\mathcal{F}_0 \approx 2\delta_m/(2\delta_m + T_{mirror})$.

3.4   Power Transmission/Reflection for the MIM Cavity

We conclude by numerically computing the resonant values of R_{mim}, T_{mim}, and $1-(R_{mim}+T_{mim})$ as a function of z_m for a symmetric cavity ($t_1 = t_2$). Cavity length, wavelength, bare cavity finesse, and $\text{Im}[n_m]$ values are chosen as in the Figure 3.7. Results of the computation are shown in Figure 8.6.

A number of interesting features are apparent. First of all, the resonant transmission of the MIM cavity varies as a function of membrane position relative to the intracavity standing wave (denoted z_m/λ in the figure) even in the absence of absorption. We may understand this in the limit of $\text{Im}[n_m]=0$, $d_m \ll \lambda$, and $z_m \ll L$ by first placing the membrane at a node near cavity center. In this case the intracavity field is unaffected and the cavity transmission is the same as the bare symmetric cavity (transmission = 1 on resonance). If the membrane is then translated away from the node, each subcavity becomes detuned with opposite sign from the resonance frequency of the bare cavity. The detuning is equal in magnitude from the bare cavity resonance but unequal in magnitude from the resonance frequency of the MIM cavity (shifted lower because of the finite storage time of the mirror-membrane etalon). As a consequence, the power build-up in the two subcavities is different.

A second feature is that the extrema of R_{mim} and T_{mim} for local translation of membrane position relative to the intracavity standing wave does not vary as a function the membrane's coarse positioning relative to the end-mirror (denoted z_m/L in the figure). This can be reasoned from the limit $r_m \to 1$, in which case — unlike the optomechanical coupling and the cavity linewidth — the transmission and reflection coefficient of the cavity does not vary as a function of coarse positioning relative to the cavity end-mirror.
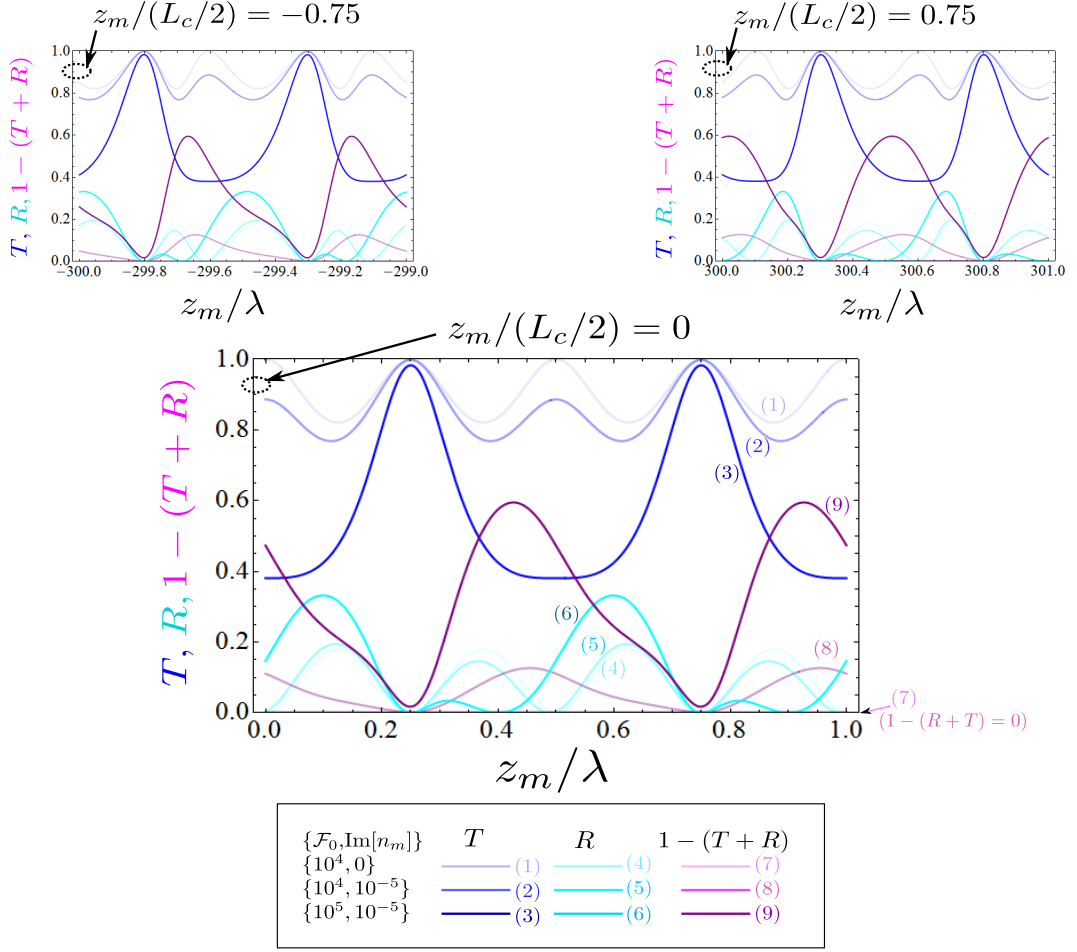
Figure 3.8: Resonant power transmission (T, blue), reflection (R, cyan), and absorption loss ($1-(R+T)$, purple) of the MIM cavity vs. membrane position, z_m, calculated numerically. Light, medium, and dark lines correspond to $\{\mathcal{F}_0, \mathrm{Im}[n_m]\} = \{10^4, 0\}$, $\{10^4, 10^{-5}\}$, and $\{10^5, 10^{-5}\}$, respectively. Variation occurs as the membrane is translated along the intracavity standing wave (with periodicity $\lambda/2$). We show this detailed variation with the membrane placed at three starting positions relative to the midpoint of the cavity, $z_m = \{-0.75L/2, 0, 0.75L/2\}$

A third, important feature pertains to the effect of membrane absorption. As expected, absorption decreases the transmission of the cavity when the membrane is positioned away from a cavity node. The effect is most pronounced when the membrane is positioned near an antinode of the intracavity field. We may compare the reduction in this case to the reduction in power transmission observed for a symmetric Fabry-Perot with round-trip internal losses δ_{RT}: $P_{out}/P_{in} = T^2_{mirror}/(T_{mirror} + \delta_{RT})^2$ (3.15). For the case of $\mathcal{F}_0 = \{10^4, 10^5\}$ and $\delta_{RT} = 2\delta_m$ = 20ppm, we obtain $P_{out}/P_{in} = \{39\%, 89\%\}$, in agreement with the numerical results. In analogy to the lossy symmetric Fabry-Perot, we can also compare the round-trip losses to the the expression $1 - (R_{FP} + T_{FP}) = 1 - T^2_{mirror}/(T_{mirror} + \delta_{RT})^2$ [31]. We obtain $\{11\%, 61\%\}$, which agrees with the numerical result. For the membrane located near an antinode, therefore, we may conveniently

ignore $\text{Re}[n_m]$ when computing the effect of absorption on cavity transmission and linewidth.

3.5   Conclusion

The purpose of this chapter was to establish some basic steady-state optical properties of dielectric films, dielectric mirrors, two-mirror optical cavities, and the compound "membrane-in-the-middle" cavity. We have alluded to an apparatus described in Chapter 5, in which a short, high-finesse cavity ($\mathcal{F} = 10^3 - 10^4$) is integrated with a thin (50 nm) dielectric film with low optical loss ($\text{Im}[n_m] \sim 10^{-5}$). In the next chapter we will discuss the mechanical properties of these films. In Chapters 5 and 6 we'll describe design/construction of the apparatus and its characterization using the numerical models developed above.

Chapter 4

Mechanical Properties of High-Stress Silicon Nitride Membranes

Mechanical dissipation poses a critical impediment to observing quantum behavior in optomechanical systems. The task is made more challenging by confining the parameter space to MEMS/NEMS structures which can be coupled strongly to a light field while introducing minimal optical loss. A significant breakthrough was introduced by the Harris group at Yale [23]. In their optomechanical system, a flexible, $\sim$ nanogram mass, *commercially* available SiN membrane with exceptional mechanical properties is coupled to a standard high-finesse Fabry-Perot cavity [13, 7, 23], thereby separating the task of fabricating the oscillator from integrating it into an optical system. Our group's point of entry into the field in 2008 was a demonstration that these SiN membranes could be optimized to realize one of the key minimum requirements for optomechanical cooling to the ground state from *room temperature*, namely a mechanical quality factor Q_m larger than the number of room temperature thermal phonons: $Q_m > \bar{n}_m = k_B T_{room}/\hbar\Omega_m$ [14, 24]. In this chapter I elaborate on those results, providing an overview of the membrane resonator and its mechanical description as well as a detailed description of the apparatus for characterizing mechanical quality factors. I will also summarize an ongoing investigation into clamping-related losses, which we believe limit the mechanical quality of the resonators we've studied.

Broadly speaking, the approach we've taken is to extend the work done at Yale [23] to include films with high tensile stress. SiN under tensile stress has been recognized for some time for its unusually low mechanical dissipation, particularly among amorphous materials [7, 39, 40, 41]. Initial optomechanical experiments with SiN membranes used the fundamental mode of a 1-mm-square film with $Q_m = 1.1 \times 10^6$ at $\Omega_m/2\pi = 130$ kHz [7], corresponding to a relatively low tensile stress of $\mathcal{T} \approx 100$ MPa . In our experiments [14] we use a SiN film in its stoichiometric form, Si_3N_4, which when deposited by low-pressure chemical vapor deposition (LPCVD) on silicon has a large tensile

Norcada Membrane Chip
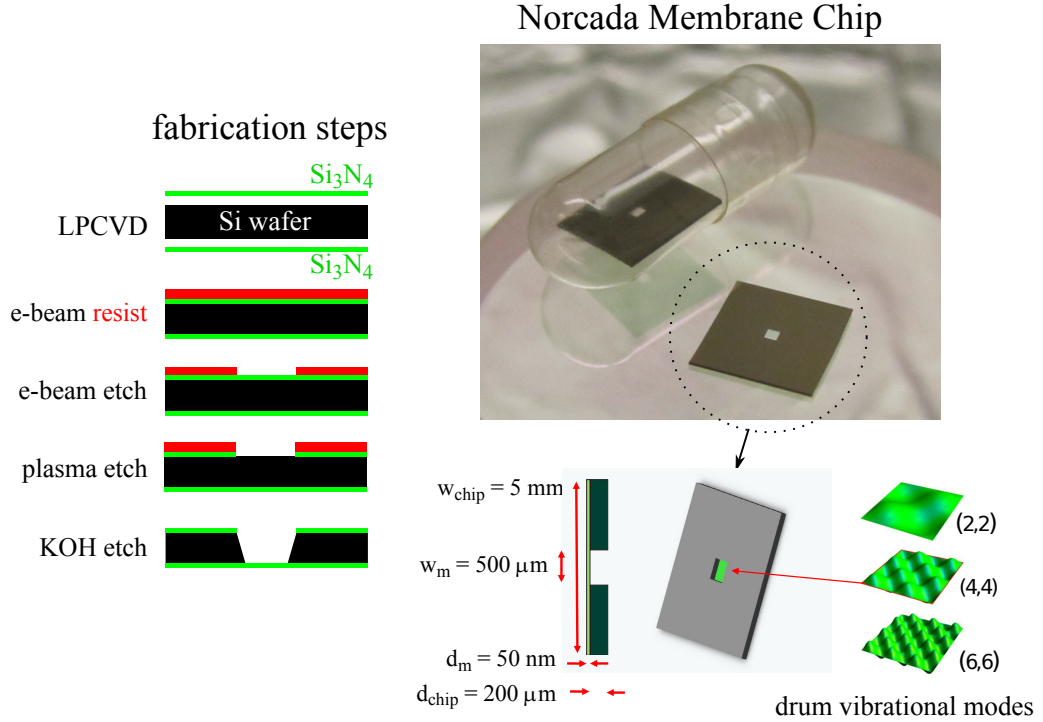
fabrication steps

Figure 4.1: Overview of the mechanical element: a membrane resonator constructed from a thin film of silicon nitride deposited a silicon wafer. Basic fabrication procedure is shown at left. At top right, we show a photograph of a "membrane chip" purchased commercially from Norcada, Inc. Dimensions of this device are shown at bottom left. This particular membrane chip consists of a 50 nm layer of stoichiometric Si_3N_4 deposited on a square silicon substrate with dimensions 5 mm $\times$ 5 mm $\times$ 200 μm. A 500-μm-square window of thin film is exposed. This window is what we refer to as the "membrane" — it exhibits transverse (drum) vibrations, a subset of which are shown at bottom right.

stress of $\mathcal{T} \sim 1$ GPa. In addition, we use sub-mm membranes and focus on the high-order modes (as illustrated in Figure 4.1); this along with the increased tension has allowed us to increase the resonant frequency of our mechanical mode by more than an order of magnitude over the mode cooled in [7], while simultaneously realizing improved room-temperature quality factors. The method of using tension to increase the frequency of mechanical modes while maintaining low dissipation has been recognized as an important tool for seeing quantum effects in a variety of mechanical systems [7, 39, 42, 43].

4.1 SiN Membranes: Architecture and Material Properties

The mechanical element in our optomechanical system is a silicon nitride membrane. As pictured in Figure 4.1, each membrane consists of a square "window" of thin-film silicon nitride deposited on a

silicon wafer (a.k.a. "chip"). The thickness d and width w of the window and chip shown in the figure are $\{d_m, w_m\} = \{50 \text{ nm}, 0.5 \text{ mm}\}$ and $\{d_{chip}, w_{chip}\} = \{200\,\mu\text{m}, 5 \text{ mm}\}$, respectively. We purchase these devices commercially from a Canadian MEMs company — Norcada, Inc. [34] — which develops them for use as sample holders for transmission electron microscopy and as vacuum windows for X-ray spectroscopy. Their utility for these applications inherits from the exceptional surface quality of LPCVD SiN thin films and because these films offer unparalleled optical transparency in the soft X-ray band. Typically SiN membranes are manufactured with low tensile stress ($\mathcal{T} \sim 100$ MPa) to improve yield and overall mechanical robustness. Our focus has been on high-stress films ($\mathcal{T} \sim 1$ GPa), the product of a slightly modified fabrication process.

4.1.1 Fabrication

The mechanical properties of silicon nitride films are closely related to the LPCVD process [35, 41]. LPCVD occurs at high temperature (700 – 800 K) and low pressure (~ 200 mTorr); under these conditions, the procedure consists of exposing a combination of volatile compounds — ammonia and dichlorosilane — to a bare silicon wafer. The volatiles react to create a thin film of silicon nitride on the wafer. Upon cooling the device to room temperature, the film acquires tensile stress due to the thermal expansion mismatch between silicon and silicon nitride. The absolute magnitude of the tension can be controlled via the deposition temperature and the ratio and flow rate of the volatile chemicals. Low stress is desirable for many commercial applications. This is accomplished by using a LPCVD recipe which dopes the film with extra nitride. High-stress silicon nitride is produced using a slightly modified recipe [41] which results in a stoichiometric Si_3N_4 chemistry. Whereas low-stress films exhibit a tensile stress of $\mathcal{T} \sim 100$ MPa, high-stress stoichiometric films obtain a tensile stress as high as $\mathcal{T} \approx 1.2$ GPa. This has been routinely achieved in the academic NEMs community, for instance in the context of high-stress nano-strings [41, 40]. By contrast, the included stress in our commercial high-stress films is closer to $\mathcal{T} \approx 900$ MPa. To date, we have not been able to find a vendor for higher stress films.

To expose the membrane window, a standard sequence of e-beam, plasma, and chemical etching is followed. We usually have Norcada perform this procedure, but have recently had success developing our own membranes in the KNI facility at Caltech using raw LPCVD-coated wafers (also purchased from Norcada). Oskar Painter's graduate student Richard Norte and our post-doc Kang-Kuen Ni have helmed this effort. As illustrated in Figure 4.1, the procedure consists of (1) depositing an e-beam resist atop the silicon nitride film (the substrate is coated on both sides but polished on only one; we operate on the unpolished surface); (2) using the e-beam to write square holes in the resist (oriented along the (111) crystal planes of the silicon wafer), thus exposing square regions of Si_3N_4; (3) plasma-etching through the exposed Si_3N_4 until the underlying Si is exposed; (4) washing away the excess resist; and (5) dipping the wafer into KOH, which etches away at the exposed Si at an

Material Property	LPCVD Si$_3$N$_4$	Silicon (111 crystal)
Young's Modulus, E (GPa)	270-290 (210 [39])	160-190
Poisson Ratio, ν	0.27	0.26 ($\parallel$ to 111 plane)
		0.18 ($\perp$ to 111 plane)
density, ρ (kg/m^3)	2700-3200	2330
specific heat per unit volume, c_V (J/kg/K)	540-700	700
thermal conductivity, κ_c (W/m/K)	3-35	14
thermal expansion coefficient, α (m/K)	2.3$\times10^{-6}$ @ 300K	2.6$\times10^{-6}$ @ 300K

Table 4.1: Table of material properties for high stress LPCVD Si$_3$N$_4$ film and the underlying silicon (111 crystal) substrate. Spread reflects a survey of values cited in [35, 44, 39, 45, 46, 47] and [35, 44], respectively.

angle of 54.7^o with respect to both crystal planes, until it reaches the opposite Si$_3$N$_4$ surface. The wafer is then dried, cleaned, and diced into the square chips pictured.

4.1.2 Material Properties

As a quick reference for this chapter, in Table 4.1 we present a collection of material properties for high-stress LPCVD silicon nitride films and the silicon wafer substrate. Values for LPCVD silicon nitride films do not generally coincide with bulk properties; nor do values for low-stress and high-stress LPCVD films coincide with one another. Properties such as the thermal conductivity appear to vary substantially between these three cases and depend on the detail of the fabrication process or geometry (e.g., film thickness) and measurement procedure. As comprehensive resources, we've found the textbooks [35, 44] and the website *www.memsnet.org* to be useful. For comparative purposes, we often assume the properties cited in [39].

4.2 SiN Membranes: Mechanical Description

4.2.1 Transverse Vibrational Modes

A thin, flexible membrane under high tensile stress is the two-dimensional analog of thin, flexible string under high tensile stress. "Thin" means that the thickness d_m of the membrane is much smaller than the square dimensions $w_m \times w_m$, so that the volume change associated with transverse vibration contributes negligibly to the potential energy. "High tension" refers to the situation in which the work done to deform the surface of the membrane is dominated by tensile rather than internal elastic stress. In general, the transverse vibrations of a thin plate [48, 49, 50] under tension satisfy an elastic wave equation of the form

$$-\frac{D}{d}\nabla^4 u + \mathcal{T}\nabla^2 u = \rho\frac{\partial^2}{\partial t^2}u \tag{4.1}$$

where $u(x, y, t)$ describes the transverse (z) displacement of mass element $\rho(x,y)dxdy$ on the surface of the plate residing in the $x - y$ plane, d is the plate thickness, $\mathcal{T}$ is the in-plane tension, ∇ is the two-dimensional gradient operator $\frac{\partial^2}{\partial x^2} + \frac{\partial^2}{\partial y^2}$, and $D \equiv Ed^3/12(1 - \sigma^2)$ is the flexural rigidity of the plate with Young's modulus E and Poisson ratio σ. The right- and left-hand sides of the elastic wave equation (Eq. 4.1) compare the kinetic energy to the potential energy of deformation due to flexural rigidity and tension, respectively. Solutions to the wave equation may be obtained by the method of separation of variables. We assume that the tension and density are uniformly distributed across the square region $\{x \in [-d_m, d_m], y \in [-d_m, d_m]\}$ and that at the boundary the membrane is simply supported: $u = \partial^2 u/\partial n^2 = 0$, where n is the coordinate normal the boundary. In this case, a set of solutions of the form

$$u_{ij}(x, y, t) = b_{ij}(t) \sin(k_x x) \sin(k_y y) \tag{4.2a}$$

$$b_{ij}(t) = b_0 \sin(\Omega_{ij} t + \phi) \tag{4.2b}$$

$$\{k_x, k_y\} = \{i\pi/w_m, j\pi/w_m\}, \ \{i, j\} \in \{\mathbb{Z}^+, \mathbb{Z}^+\} \tag{4.2c}$$

satisfies (4.1). These vibrational modes of a square drum are given by the product of two sinusoids with an overall amplitude that fluctuates harmonically in the absence of dissipation. The first several vibrational modeshapes of this form shown in the bottom right of Figure 4.1.

To compare the roles of tension and elasticity, we can examine the dispersion relation for the mechanical frequency Ω_{ij} in the case of $D = 0$ and $\mathcal{T} = 0$. For the membrane with thickness d_m and square width w_m, they are

$$\Omega_{ij}|_{\mathcal{T}=0} = \sqrt{\frac{D}{d_m \rho}} \left(k_x^2 + k_y^2 \right) = \sqrt{\frac{D}{d_m \rho}} \left(\frac{\pi\sqrt{2}}{w_m} \right)^2 \left(\frac{i^2 + j^2}{2} \right) \tag{4.3a}$$

$$\Omega_{ij}|_{\mathcal{D}=0} = \sqrt{\frac{\mathcal{T}}{\rho}} \sqrt{k_x^2 + k_y^2} = \sqrt{\frac{\mathcal{T}}{\rho}} \left(\frac{\pi\sqrt{2}}{w_m} \right) \sqrt{\frac{i^2 + j^2}{2}}. \tag{4.3b}$$

For a high-stress LPCVD silicon nitride membrane with density $\rho = 2.7$ g/cm^3, Young's modulus $E = 270$ GPa, Poisson ratio $\sigma = 0.27$, tension $\mathcal{T} = 900$ MPa, thickness $d_m = 50$ nm, and square width $w_m = 500\,\mu$m, the fundamenal frequency ($i = j = 1$) in these two extremes is $\Omega_{1,1}|_{\mathcal{T}=0} = 1.9$ kHz and $\Omega_{1,1}|_{\mathcal{D}=0} = 816.5$ kHz. For these dimensions, the tension at which the fundamental frequencies would be equal is $\mathcal{T} = D \times (2\pi^2/w_m^2 d_m) = 4.8$ kPa. Owing to this large disparity, we use the frequency and dispersion relation for $D = 0$ in our description of both "low-stress" (~ 100 MPa) and "high-stress" (~ 1 GPa) membranes. Measurements made on our samples from Norcada are in good agreement with this model, as shown in Section 4.6.1.

4.2.2 Dynamical Equation of Motion

Near resonance, forced vibrations of a single membrane mode (i, j) can be modeled by letting the generalized amplitude $b_{ij}(t)$ obey the equation of motion for a damped harmonic oscillator [50]

$$\ddot{b}_{ij}(t) + \Gamma_{ij}\dot{b}_{ij}(t) + \Omega_{ij}^2 b_{ij}(t) = F_{ij}^{ext}(t)/m_{ij}. \tag{4.4}$$

The physical magnitude of the amplitude, damping rate Γ_{ij}, effective mass m_{ij}m and driving force F_{ij}^{ext} depends on the distribution of the force relative to the mechanical mode and the choice of definition for the amplitude (e.g., the maximum amplitude or the rms average of $u_{ij}(x, y)$). A description of m_{ij} and b_{ij} which is germane to the radiation pressure force applied in an optical cavity is discussed in Chapter 6. For a thorough description in this context, we also refer the reader to [51] and [52].

By defining b_{ij} as the maximum amplitude of the vibrational mode (i.e., the amplitude of an antinode for a square drum mode) and noting that the potential energy of the vibrational mode is $U_{ij}(t) = (1/2)\int_S u_{ij}^2(x, y, t)\Omega_{ij}^2 \rho dx dy dz = (1/2)\Omega_{ij}^2 \rho d_{mem}^2 t_{film} b_{ij}(t)^2/2$ (the sum of the potential energy of each mass element in the vibrating film), we are led to identify $m_{ij} = m_{physical}/4$ for all modes in order to retain the form $U_{ij}(t) = (1/2)m_{ij}\Omega_{ij}^2 b_{ij}^2(t)$ of a harmonic oscillator [52]. Hereafter, we drop the subscripts and implicitly refer $\{b, \Gamma_m, \Omega_m, m, F_{ext}\}$ to the amplitude, damping rate, frequency, effective mass, and generalized driving force for a single vibrational mode:

$$\ddot{b}(t) + \Gamma_m \dot{b}(t) + \Omega_m^2 b(t) = F_{ext}(t)/m. \tag{4.5}$$

4.3 Characterizing Mechanical Dissipation: Concept of Q

Dissipation in oscillatory mechanical systems is frequently characterized by a dimensionless "quality factor", Q_m. For an under-damped system, Q_m is defined as the cycle-averaged energy W_m of the oscillator divided by the energy dissipated over a cycle ΔW_m,

$$Q_m = 2\pi \times \frac{W_m}{\Delta W_m}. \tag{4.6}$$

For an under-damped harmonic oscillator obeying 4.5 ($\Gamma_m << \Omega_m$) one can show that Q_m is equivalent to the ratio of the mechanical frequency and the damping rate as defined in the equation of motion (4.4). To see this, we assume that amplitude $b(t)$ describes harmonic motion, $b(t) = b_0 \sin(\Omega_m t + \phi_m)$, and identify ΔW_m as the work done by the oscillator on the environment over a single cycle:

$$\Delta W_m = \oint m\Gamma_m \dot{b}\, db = m\Gamma_m \int_0^{2\pi/\Omega_m} \dot{b}^2 dt = \frac{2\pi}{\Omega_m}\Gamma_m \times \frac{1}{2}m\Omega_m^2 = 2\pi\frac{\Gamma_m}{\Omega_m}W_m \tag{4.7}$$

$$\rightarrow Q_m = \frac{\Omega_m}{\Gamma_m}. \tag{4.8}$$

Note that Γ_m is the rate of mechanical energy dissipation in angular units.

We now consider two approaches to characterizing Q_m in the lab. The first approach consists of measuring the steady-state response of the system to an external driving force. The second, a transient ("ringdown") approach, consists of perturbing the system out of equilibrium and directly monitoring its decay back to steady state.

4.3.1 Steady-State Approach

4.3.1.1 Driven Vibration

Mechanical quality may be inferred by monitoring the steady-state response of the system to an applied external force. A simple case to consider is that of a sinusoidal drive force $F_{ext}(t) = F_0 \sin(\Omega_0 t)$, which may, for example, be applied by a piezo shaker attached to the membrane chip. For an under-damped ($\Gamma_m \ll \Omega_m$) harmonic oscillator driven near resonance, the steady-state solution to Eq. 4.5 is a vibration $b(t) = b_0 \sin(\Omega_0 t + \phi_0)$ with an amplitude b_0 well-approximated by a Lorentzian function of the drive detuning $\Omega_m - \Omega_0$ (see Section 2.2):

$$b_0^2 = \frac{F_0^2/m}{(\Omega_m^2 - \Omega_0^2)^2 + \Omega_0^2 \Omega_m^2/Q_m^2} \approx \frac{(\Omega_m/2Q_m)^2}{(\Omega_m - \Omega_0)^2 + (\Omega_m/2Q_m)^2} \frac{F_0^2 Q_m^2}{m\Omega_m^4}. \tag{4.9}$$

Since in practice it is often difficult to measure F_0 or b_0 directly, it is customary to sweep Ω_0 (for example using a network analyzer to drive the piezo shaker) and fit the response curve to a Lorentzian to obtain Q_m.

4.3.1.2 Brownian Vibration

We can also directly monitor Brownian vibration [29] of the membrane (the steady-state response to thermal force fluctuations). This is a viable option because of the low mass of the membrane. To wit, a silicon nitride membrane with dimensions $\{d_m, w_m\} = \{50 \text{ nm}, 500 \ \mu\text{m}\}$ and a tension of $\mathcal{T} = 900$ MPa has an effective mass of $m = m_{phys}/4 \approx 8.4$ ng, a fundamental vibrational frequency of ≈ 800 kHz, and an rms thermal amplitude fluctuation of $\sqrt{\langle b^2 \rangle} = \sqrt{k_B T_{room}/m\Omega_m^2} \approx 4.4$ pm. Amplitude fluctuations of this magnitude are straightforward to measure by integrating the membrane into a low-finesse interferometer, as discussed in the next section.

Thermal fluctuations of the membrane are characterized by their power spectral density (Eq. 2.7), as described in Section 2.2 (see also [29]). Using the convention of a single-sided power spectral density and making the Lorentzian approximation near resonance gives:

$$S_b(\Omega) \approx \frac{4k_B T_{room}}{m\Omega_m^2} \frac{Q_m}{\Omega_m} \frac{(\Omega_m/2Q_m)^2}{(\Omega_m - \Omega)^2 + (\Omega_m/2Q_m)^2} \ \frac{\text{m}^2}{\text{Hz}}; \ \ \Omega = 2\pi f, \tag{4.10}$$

Please note that although S_b is always expressed in this thesis as an explicit function of Ω, it is defined to represent a density function in the domain of non-angular Fourier frequencies, $f = \Omega/2\pi$. By this convention, we have $\int_0^\infty S_b(\Omega)d\Omega/2\pi = \langle b^2 \rangle = \frac{k_B T_{room}}{m\Omega_m^2}$.

The power spectral density can be measured with a spectrum analyzer and fit to a Lorentzian, which requires that the resolution bandwidth of the analyzer be smaller than Γ_m. As discussed below, we've found this method difficult for high-quality mechanical resonances ($Q_m > 10^6$, $\Omega_m > 2\pi \cdot 1$ MHz) because of slow drift of the mechanical frequency.

4.3.2 Transient Approach: Ringdown Technique

It's possible to directly monitor energy dissipation by perturbing the system and watching it evolve back to equilibrium. For a weakly damped harmonic oscillator, this evolution is characterized by a cycle-averaged energy that decays like an exponential. The slope of this "ringdown" decay curve gives a direct measure of Q_m.

Consider again a damped harmonic oscillator (4.5) driven by external force $F_0 \sin(\Omega_0 t)$ until a steady energy $W_0 = (1/2)mb_0^2$ is reached, as in (4.9). The force is then instantaneously shut off at time t_0. For an underdamped oscillator ($\Gamma_m \ll \Omega_m$) the time evolution of the cycle averaged energy is directly related to the work done on the environment (4.7) over an oscillatory period, $\tau_m = 2\pi/\Omega_m$:

$$\frac{dW_m}{dt} \approx \frac{\Delta W_m}{\tau_m} = \Gamma_m W_m \tag{4.11a}$$

$$\rightarrow W_m = W_0 e^{-\Gamma_m(t-t_0)} = W_0 e^{-\Omega_m(t-t_0)/Q}. \tag{4.11b}$$

In the lab we perform an interferometric measurement that records the membrane's amplitude rather than its energy. An expression for the amplitude ringdown can be obtained by solving (4.5) with $F_{ext} = 0$ and initial condition $b(t=0) = b_0$ with the assumption $\Gamma_m \ll \Omega_m$. The solution is a sinusoid with a slowly varying envelope that decays with time constant is $2Q_m/\Omega_m$:

$$b(t) = b_0 \cos(\Omega_m t + \phi_0)e^{-\Gamma_m(t-t_0)/2} = b_0 \cos(\Omega_m t + \phi_0)e^{-\Omega_m(t-t_0)/2Q_m}. \tag{4.12}$$

We can measure the envelope function using a network analyzer in zero-span mode, as described below.
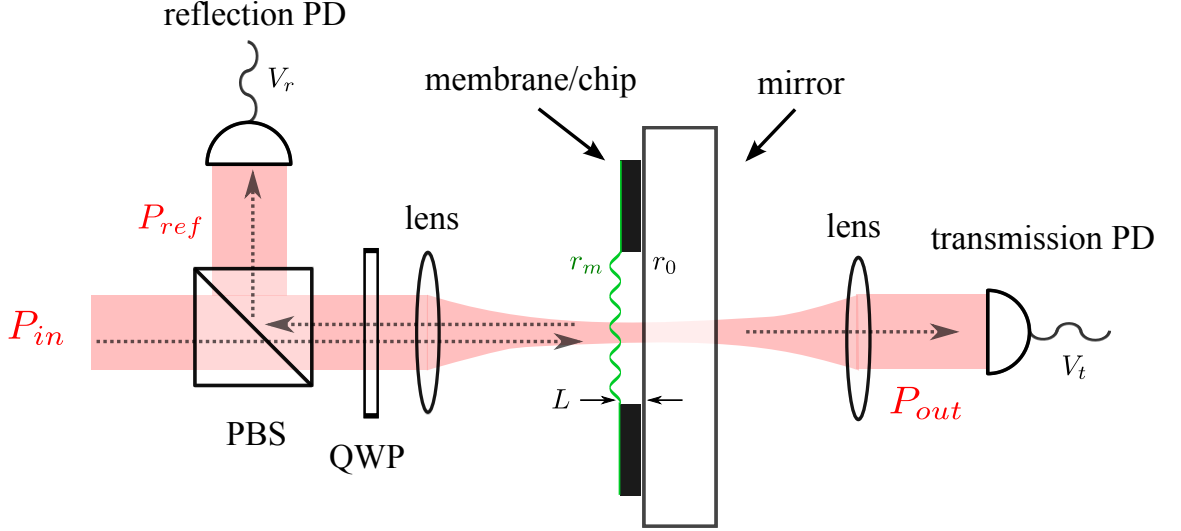
Figure 4.2: Schematic of the apparatus for displacement readout. A low-finesse etalon is formed between the membrane and a partially reflecting mirror. The amplitude of the transmitted and/or reflected field is monitored on a photodetector.

4.4 Displacement Readout

The geometry of the membrane and membrane chip enables an exceptionally simple device for displacement readout. As illustrated in Figure 4.2, we brace the chip against a partially reflecting mirror to form a low-finesse etalon between the membrane (reflectivity r_m) and mirror (reflectivity r_0) surface. The etalon is probed with a focused laser beam. Both the amplitude and phase of the reflected and transmitted field depend on the etalon spacing, L, which depends on the amplitude of the vibrating membrane surface.

The steady-state power transmitted and reflected from a lossless, asymmetric etalon may be found in many standard optics texts [30], with a particularly thorough treatment given in Chapter 3 of [31]. The relevant formulas are given by

$$P_{out} = \frac{T_{max}}{1 + (2\mathcal{F}/\pi)^2 \sin^2(2\pi L/\lambda)} \times P_{in} \tag{4.13a}$$

$$P_{ref} = P_{in} - P_{out} \tag{4.13b}$$

$$T_{max} = \left(\frac{t_m t_0}{1 - r_m r_0}\right)^2 \tag{4.13c}$$

$$\mathcal{F} \equiv \frac{\pi \sqrt{r_m r_0}}{1 - r_m r_0}, \tag{4.13d}$$

where L is the etalon spacing and $\mathcal{F}$ is the etalon "finesse".

For the 50-nm-thick membrane and the probe wavelength of ≈ 850 nm used for the bulk of our studies, the membrane's reflection coefficient is $r_m = 0.42$ (corresponding to a real index of ≈ 2.0).

We typically use a $r_0^2 \approx 50\%$ beamsplitter as the reflector. The finesse $\mathcal{F}$ of an etalon thus formed is $\mathcal{F} \approx 2.4$, producing (ideally) a fringe with a visibility of $V(\mathcal{F}) \equiv (P_{max} - P_{min})/(P_{max} + P_{min}) = \mathcal{F}^2/(\pi^2/2 + \mathcal{F}^2) \approx 0.54$. The maximum transmission in this case is $T_{max} \approx 0.99$.

To measure small displacements, we monitor either the power transmitted or reflected from the etalon while positioned on the slope of this fringe. The length-to-power transduction provided by the fringe, dP/dL, can be estimated by differentiating the expression for the transmitted power (Eq. 4.13a) at the position half-way between the maximum and minimum value of the fringe. In this case it can be shown that

$$\frac{dP_{out}}{dL} = -P_{out} \times \frac{4\mathcal{F}}{\lambda}C_T(\mathcal{F}) \tag{4.14a}$$

$$\frac{dP_{ref}}{dL} = -P_{ref} \times \frac{4\mathcal{F}}{\lambda}C_R(\mathcal{F}) \tag{4.14b}$$

where P_{out} and P_{ref} are the average transmitted and reflected power half-way up the fringe and the correction factors $C_{T,R}(\mathcal{F})$ are $\mathcal{O}(1)$ for $T_{max} \approx 1$ and $\mathcal{F} > 1$. For $T_{max} = 1$ and $\mathcal{F} = 2.4$, we have $C_T(\mathcal{F}) = \sqrt{\mathcal{F}^2/(\pi^2/4 + \mathcal{F}^2)} = 0.76$ and $C_R(\mathcal{F}) \approx C_T(\mathcal{F})/V(\mathcal{F}) = 1.41$.

4.4.1 Measurement Sensitivity

The optical field is collected on a photodiode, which produces a photocurrent $i(t) = \mathcal{R}P_{out}$, where $\mathcal{R}$ is the responsivity of the detector. To quantify the sensitivity of the displacement measurement, we can compare the power spectral density $S_i(\Omega)$ of photocurrent fluctuations produced by etalon length fluctuations $S_L(\Omega)$ to the spectral density of photocurrent shot noise fluctuations $S_i^{shot}(\Omega)$ [53, 54]. For the transmitted field:

$$S_i(\Omega) = \left(\mathcal{R}\frac{dP_{out}}{dL}\right)^2 S_L(\Omega) = \mathcal{R}^2 \left(\frac{4\mathcal{F}}{\lambda}\right)^2 P_{out}^2 C_T^2(\mathcal{F})S_L(\Omega) \ \frac{A^2}{Hz} \tag{4.15a}$$

$$S_i^{shot}(\Omega) = 2e\langle i \rangle = 2e\mathcal{R}P_{out} \ \frac{A^2}{Hz}. \tag{4.15b}$$

Comparison of Eq. 4.15a and Eq. 4.15b gives the shot-noise-limited length sensitivity of the interferometer, S_L^{shot}, defined as the displacement power spectral density necessary to give a signal-to-shot-noise of one. In amplitude units:

$$\sqrt{S_L^{shot}} \equiv \frac{\lambda}{4\mathcal{F}}\sqrt{\frac{2e}{\mathcal{R}}}\sqrt{\frac{1}{P_{out}}}\frac{1}{C_T(\mathcal{F})} \tag{4.16a}$$

$$\approx 7\frac{fm}{\sqrt{Hz}} \times \sqrt{\left(\frac{\lambda}{850\,nm}\right)\left(\frac{0.5\,A/W}{\mathcal{R}}\right)\left(\frac{100\,\mu W}{P_{out}}\right)}\left(\frac{2.4}{\mathcal{F}}\right)\frac{1}{C_T(\mathcal{F})}. \tag{4.16b}$$

As an example, consider the expected thermal displacement amplitude of the fundamental vibration mode of a membrane with typical values $\{d_m, w_m, \rho, \Omega_m/2\pi, Q_m\} = \{50 \text{ nm}, 500 \text{ } \mu\text{m}, 2.7$ g/cm^3, 800 kHz, $10^6\}$. The effective mass of the membrane is $m = \rho t_{film} d_{mem}^2/4 \approx 8.4$ ng. The rms vibrational amplitude due to thermal agitation with energy $k_B T_{room}$ is $\sqrt{k_B T_{room}/m\Omega_m^2} = 4.4$ pm for $T_{room} = 298$ K. Half of this displacement is contained in a bandwidth of $\Omega_m/Q_m/2\pi = 0.8$ Hz, corresponding to a noise amplitude of $\approx 4.9 \text{ pm}/\sqrt{Hz}$. Equation 4.16 suggests that the necessary probe power to achieve shot-noise-limited sensitivity at this level would be < 1 μW. In practice we use a commercial photodetector, New Focus 1801, with a shot noise equivalent power of ≈ 100 μW at 850 nm. Operating at this power, the signal-to-noise in a bandwidth of 1 Hz should ideally be > 50 dB (in power units). The best we've achieved is ~ 30 dB, which we attribute mainly to imperfections in alignment, fringe detuning, and mode-overlap between the optical beam and the membrane. We are however tolerant of less sensitivity when the membrane is driven resonantly to amplitudes $>>$ pm.

4.5 Apparatus for Characterizing Membrane Mechanics

An overview of the experimental apparatus is given in Figure 4.3. The low-finesse etalon described in the previous section resides in a vacuum chamber operating at $< 10^{-6}$ Torr. A piezoelectric shaker is added either behind the mirror or between the mirror and the chip in order to excite vibrational modes of the membrane. The etalon is probed with a laser beam that has been focused to a spot size small enough to transect the local displacement of higher order vibrational modes of the membrane. Vibrations are monitored by directing the reflection from the etalon to a photodetector. The output of the photodetector's transimpedance amplifier is directed to a spectrum and a network analyzer, the latter of which is used for ringdown measurements using the piezo as a vibration transducer. We elaborate on these components below.

4.5.1 Etalon

Displacement readout is performed by interrogating an etalon formed by securing the membrane chip face-up against a partially reflecting mirror. A reflection based setup is depicted in Figure 4.3. We place a piezo-electric shaker either below the mirror or between the mirror and chip, depending on the manner in which the chip is secured. The piezo we typically use is a 1-mm-thick plate of "Pz27" material from Ferroperm, Inc. (similar to Navy II), which has a unloaded resonance of ~ 1 MHz and a static response of ~ 0.1 nm/V. The specifics of how the chip is secured to the mirror has varied widely in practice, because we have found that the quality factor of the membrane vibrational modes depend sensitively on the manner in which the chip is secured. We have tried a large variety of adhesives and mechanical fasteners to secure the chip, some of which are outlined in Section 4.7.1.
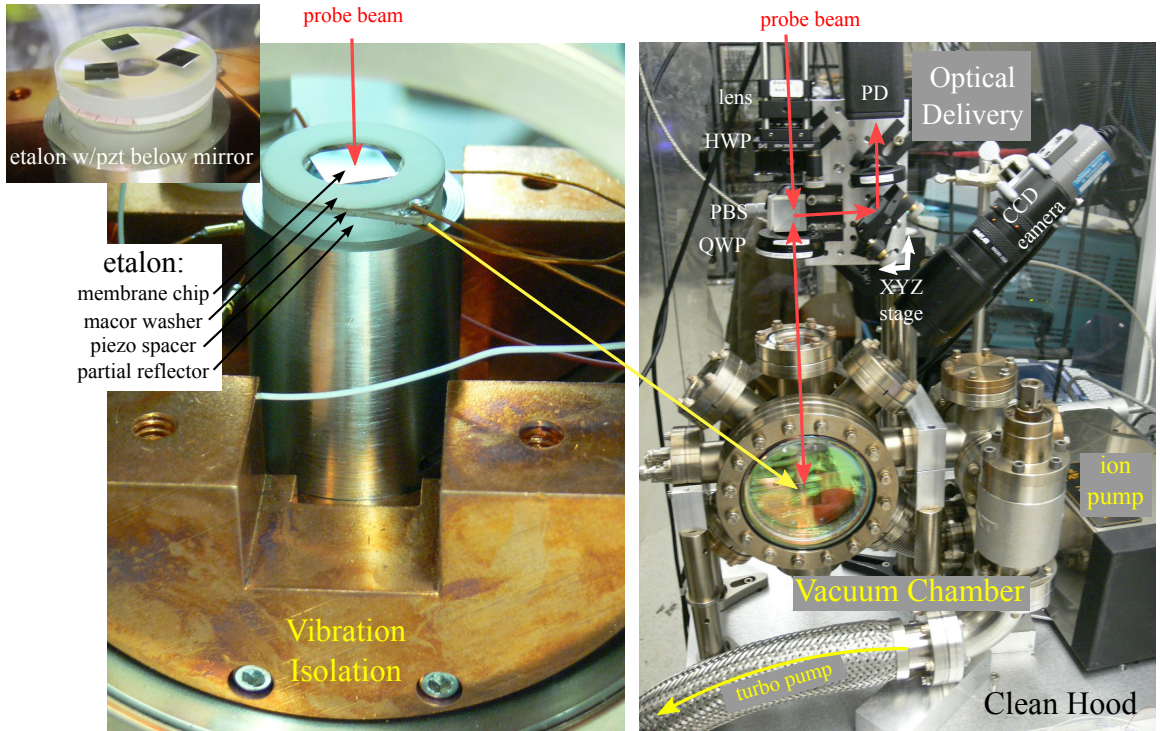
Figure 4.3: Overview of the apparatus used to characterize membrane mechanics. A low-finesse etalon is formed between the membrane and a partially reflecting mirror. The etalon resides in a vacuum chamber at $< 10^{-6}$ mbar. A laser beam is focused onto the membrane and the reflection from the etalon is directed to a photodetector. The resulting photocurrent is processed on a network/spectrum analyzer

However, to minimize "clamping losses" we have found no better solution than to simply rest the chip on the device under its own gravity. To reduce the contact area, we often rest the chip on a curved mirror substrate or on a washer with inner diameter just smaller than the diagonal size of the chip. A design we frequently use is shown in the main photo at left in Figure 4.3. It consists of a 1" plano partial reflector (a Thorlabs near-infrared 50/50 beamsplitter), a 1-mm-thick piezoelectric spacer (Ferroperm Pz27), and a Macor washer to prevent the membrane chip from sliding. The jig shown is made to accommodate 10 mm chips. The piezo-electric spacer has been machined on a diamond band saw to remove a rectangular area slightly smaller than the chip dimensions so that it may rest on its edges. Three small dabs of Krazy Glue secure the piezo to the mirror. To achieve good sensitivity to thermal noise, on the other hand, the simplified arrangement shown in the upper left inset is preferred. In this case a piezo is placed beneath the mirror — usually in this case it must be driven significantly harder to drive the membrane.

4.5.2   Vacuum Chamber

The etalon sits in a vacuum chamber which has been evacuated to $< 10^{-6}$ mbar. The chamber inherits from an retired CQED experiment in our lab [55] and consists of a 6" stainless steel octagon from Kimball Physics with Conflat fittings, as shown in Figure 4.3. The chamber is supplied with AR-coated viewports from Larson Electronics, nominally centered at 852 nm with $\sim 0.1\%$ reflectivity at that wavelength. A dedicated vibration isolation system sits inside the chamber; however, we have found that this is not critical. The chamber in fact sits on a table in rigid contact with the floor inside of a clean hood.

It is important to evacuate the chamber to high vacuum to eliminate air damping (Eq. 4.21); however, at the same time we desire the ability to cycle the chamber rapidly, so some effort was made to minimize conduction paths. The chamber is attached to a 55 liter/sec turbo pump station (Varian Turbo-V60) which can be used to rough the apparatus to $\sim 10^{-6}$ mbar in approximately 15 minutes. This would be sufficient, however, vibration of the turbo pump tends to place a 70 kRPM ripple on the time domain ringdown measurement, so for this measurement we transfer the vacuum load to a 55 liter/sec ion pump (Varian Diode 55 Starcell). The vacuum pressure is inferred from the ion pump current. Fully recycling the chamber to atmosphere, replacing the membrane(s), and pumping back down to $\sim 10^{-6}$ mbar with the load transferred to the ion pump takes roughly 30 minutes.

4.5.3   Optical Layout

The optics used to probe the etalon can be seen in the upper-right-hand corner of Figure 4.3. A clean Gaussian beam is provided by a $5\,\mu$m-core single-mode optical fiber (Oz Optics, not shown). The field radiating from the fiber is expanded and re-focused onto a focal plane coinciding with the membrane using a pair of achromatic lenses. A knife-edge measurement was used to determine a $1/e^2$ waist size of $\approx 50\,\mu$m. The beam passes through a half waveplate (HWP), a polarization beam splitter (PBS), and a quarter wave plate (QWP) enroute to the etalon. The HWP/PBS pair enables power adjustments. The QWP is oriented at ≈ 22.5 degrees to the polarization axis so as to direct the light reflected from the etalon onto a path terminating in a low-noise photodetector (New Focus model 1801).

To facilitate alignment of the etalon, the input/output optics described in the preceding paragraph are placed on a small breadboard secured to a three-axis translation stage. The fiber coupler is also affixed to a kinematic mirror mount for small tip/tilt adjustments. Retro-reflection from the etalon is fine tuned by iterating between these five degrees of freedom. Rough transverse alignment is achieved by monitoring scatter from the chip surface on a CCD camera mounted to the side of the chamber. The retro-reflection may be fine tuned by symmetrizing the airy rings on the retro-

reflected beam. These rings are formed because the focused laser beam diffracts slightly over the gap between the membrane and mirror surface. For small membranes, one also observes a Fraunhaufer diffraction pattern formed by the hard square aperture. The central lobe of the Airy/Fraunhaufer diffraction pattern should be isolated with an aperture for improved signal to noise.

The reflected beam is directed to a New Focus 1801 photodetector with a responsivity of ≈ 0.5 A/W. The internal transmipedance amplifier has a bandwidth of 100 MHz and gain of of 20V/mW into a load of 50 Ohm.

4.5.4 Spectrum/Network Analyzer

The output of the photodetector's transimpedance amplifier is directed to one of two devices: an analog network analyzer (HP 4395A) and/or an FFT-based spectrum analyzer (Tektronix 5103A). The network analyzer (NA) is used for swept response (Section 4.3.1.1) and ringdown (Section 4.3.2) measurements. The spectrum analyzer (SA) is used for measuring thermal noise power spectra (Section 4.3.1.2). We will not review here the details of how network and spectrum analyzers work but rather provide an operational description.

4.5.4.1 Spectrum Analyzer Measurement

Operationally, the spectrum analyzer takes as its input a voltage $V(t)$ and outputs a voltage power spectrum. The power spectrum is defined as the integral of the voltage power spectral density, $S_V(\Omega)$, over an effective bandwidth B (defined in non-angular frequency units):

$$\langle V^2(\Omega)\rangle_B \equiv \int_{\Omega-(2\pi)B/2}^{\Omega+(2\pi)B/2} S_V(\Omega')d\Omega'/2\pi. \tag{4.17}$$

The effective bandwidth of the spectrum analyzer can be defined relative to its output when supplied with a signal having a known, constant power spectral density $S_V(\Omega) = C_0$. In this special case:

$$B = \langle V^2(\Omega)\rangle_B/S_V(\Omega). \tag{4.18}$$

The SA is used to approximate power spectral densities by normalizing the measured power spectrum by its effective bandwidth. We denote this approximate power spectral density as $S_V^B(\Omega)$:

$$S_V^B(\Omega) \equiv \langle V^2(\Omega)\rangle_B/B \approx S_V(\Omega). \tag{4.19}$$

This approximation is valid when the power spectral density of the underlying signal varies slowly on a scale set by B. If, on the other hand, the signal $V(t)$ has all of its spectral content inside the

window $\Omega_0 \pm (2\pi)B/2$, then the analyzer produces a value:

$$S_V^B(\Omega_0) = \langle V^2 \rangle / B \tag{4.20}$$

where $\langle V^2 \rangle = \int_0^\infty S_V(\Omega) d\Omega / 2\pi$, is the rms^2 amplitude of the signal.

We have verified that when operating the Tektronix 5103A in the "PSD units" mode, the effective bandwidth is indeed given by Eq. 4.18. This was done by supplying the RSA input with calibrated white noise generated by a SRS DS345 function generator in "noise" mode. To obtain the effective bandwidth directly, we have the analyzer compute the power spectral density of a calibrated sinusoidal input signal $V(t) = V_0 \sin(\Omega_0 t)$, which gives the value $S_V^B(\Omega_0) = V_0^2/(2B)$. A last issue worth noting is that for noisy signals, a consistent outcome for $S_V^B(\Omega_0)$ is only obtained after averaging numerous measurements; this averaging must take place in power units (a setting that must be specified — some analyzers by default average the logarithm of the power [56, 57]).

4.5.4.2 Network Analyzer Measurement

The HP 4395A network analyzer is based on a superheterodyne architecture. Internal to the network analyzer is a tunable local oscillator which produces a reference sinusoidal voltage (the "source signal") at angular frequency Ω_s, i.e., $V_s(t) = V_s^0 \sin(\Omega_s t)$. The source signal $V_s(t)$ is used to drive a piezo shaker coupled to the membrane. The signal produced by the etalon reflection photodetector's transimpedance amplifier is $V(t) = V_0 \sin(\Omega_s t + \phi_0)$. If the piezo is shaken near the resonance frequency of the membrane ($\Omega_s \approx \Omega_m$) and then abruptly shot off, the resulting "ringdown" signal is predicted to have the form $V(t) = V_0 e^{-\Omega_m t/2Q_m} \sin(\Omega_m t + \phi_0)$ according to Eq. 4.12. We denote the slowly varying envelope at carrier frequency Ω by $V_\Omega(t)$. For the ringdown, $V_{\Omega_m}(t) = V_0 e^{-\Omega_m t/2Q_m}$.

The network analyzer is simultaneously used to measure $V_{\Omega_s}(t)$, the slowly varying amplitude of $V(t)$ in the frame rotating at Ω_s. It does this by mixing $V(t)$ against a local oscillator $V_{LO}(t) = V_{LO}^0 \sin(\Omega_{LO} t)$ into the passband of a narrow bandpass (IF) filter centered at intermediate frequency $\Omega_s - \Omega_{LO}$, and then passing the output of this filter to an rms detector (digitally implemented by the HP4395A). If $V(t) = V_0 \sin(\Omega_s t + \phi_0)$, then the output of the rms detector is proportional to $V_{\Omega_s}(t) = V_0$. If $V(t) = V_0 e^{-\Omega_m t/2Q_m} \sin(\Omega_m t + \phi_0)$, and if the bandwith of the IF filter (B_{IF}) satisfies $\Omega_m/Q_m \ll 2\pi B_{IF} \ll |\Omega_m - \Omega_s|$, then the output of the rms detector for sufficiently short times (set by $2\pi/(\Omega_m - \Omega_s)$) is proportional to $V_{\Omega_m}(t) \approx V_0 e^{-\Omega_m t/2Q_m}$. We use the network analyzer in this single frequency ("zero span") mode to perform ringdown measurements.
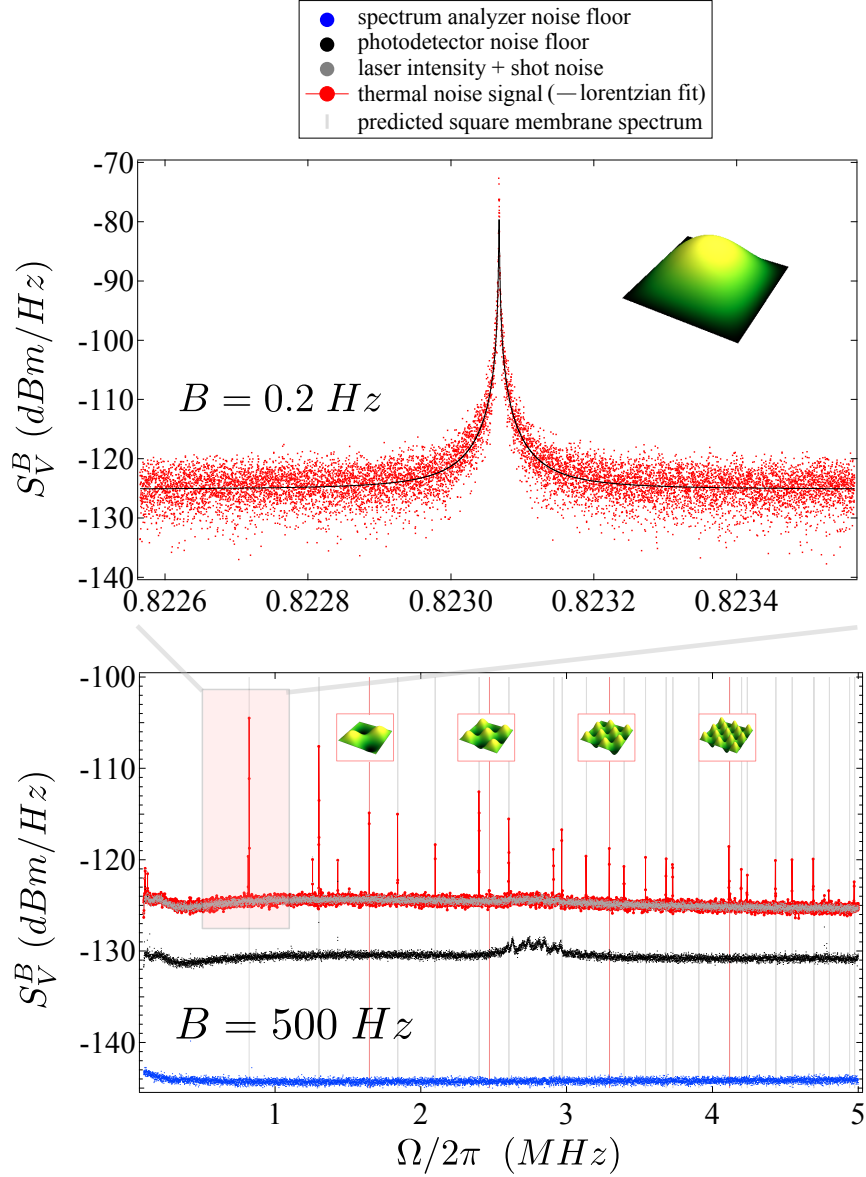
Figure 4.4: Thermally induced vibrations of a membrane with dimensions $\{d_m, w_m\}$ = $\{50\,\text{nm}, 500\,\mu\text{m}\}$. Lower plot: broadband thermal noise power spectrum obtained using an effective bandwidth of $B = 500$ Hz $>> \Gamma_m/2\pi$. Units are in logarithmic power dissipated by the output of the photodetector transimpedance amplifier into 50 Ohm: $10\text{Log}[S_V^B(\Omega)/50\text{Ohm/mW}]$ dBm/Hz. Noise peaks are located at eigenfrequencies of a the square membrane resonator, with vertical lines representing the model $\Omega_{ij} = \Omega_{11}\sqrt{(i^2 + j^2)/2}$. Diagonal modes are highlighted in pink. From the value of the fundamental frequency, $\Omega_{11}/2\pi = 823.5\,\text{kHz}$, we infer a film tension of $\mathcal{T} = 935$ MPa. Upper plot: a high-resolution measurement of the fundamental mode. For this measurement, an effective bandwidth of $B = 0.2$ Hz is used and 3 scans are averaged. Becuase in this case $B < \Gamma_m/2\pi$, the shape of the power spectrum is proportional to the underlying thermal noise power spectral density, given by Eq. 4.10. A Lorentzian fit is shown, where the linewidth is constrained to the value obtained from a separate ringdown measurement, shown in Figure 4.6, for which $Q_m = \Omega_m/\Gamma_m = 1.4 \times 10^6$.

4.6   Measurements

4.6.1   Thermal Noise Spectrum: Static Mechanical Properties

An example of a thermal noise measurement in shown in Figure 4.4. For this measurement we use the arrangement shown at upper left in Figure 4.3, in which the membrane chip rests flush atop a $r_0^2 \approx 50\%$ reflector. The membrane used has dimensions $\{d_m, w_m\} = \{50 \text{ nm}, 0.5 \text{ mm}\}$ and a factory specified tension of $\mathcal{T} \approx 900$ MPa. The etalon is probed with a beam focused to a spot size of $\approx 50 \,\mu$m. Approximately $120 \,\mu$W of the light reflected from the etalon is collected onto the reflection photodetector (New Focus 1801). The output of its transimpedance amplifier is directed to the spectrum analyzer (Section 4.5.4).

On the bottom half of Figure 4.4 we display the power spectral density of the photodetector signal in logarithmic power units: $10\text{Log}[S_V^B(\Omega)/50 \text{ Ohm/mW}]$ dBm/Hz. An effective bandwidth of $B = 500 \gg \Gamma_m/2\pi$ Hz is used and a range from $\Omega/2\pi = 100$ kHz to 5 MHz is displayed. With this span and bandwidth, a broad spectrum of thermal noise peaks are apparent, but none are resolved. For the fundamental mode near 820 kHz, we observe a signal to noise of ≈ 20 dB relative to the -125 dBm/Hz noise floor produced by a combination of shot noise and detector noise. This compares favorably to the signal to noise of $10\log[(k_B T_{room}/m\Omega_m^2)/\langle L^2(\Omega_m)\rangle_{B=500 \text{ Hz}}^{shot}] \approx 22$ dB predicted by comparing the predicted rms^2 displacement of the fundamental mode, $k_B T_{room}/m\Omega_m^2 = 4.4$ pm^2, to the effective length noise S_L^{shot} associated with shot noise integrated over a bandwidth of $B = 500 Hz$, according to Eq. 4.16: i.e., $\langle L^2(\Omega_m)\rangle_{B=500 \text{ Hz}}^{shot} \approx 2.5 \times 10^{-2}$ pm^2.

Information about static mechanical properties of the membrane can be inferred from this multimode thermal noise spectrum. The measured value of the fundamental frequency, $\Omega_{11}/2\pi = 0.823$ MHz, can be used to estimate the tension. Using a value for the density supplied by Norcada and literature on LPCVD SiN films, $\rho = 2.7$ g/cm^3 [39], and assuming window dimensions of $w_m = 500$ μm , (which have been independently verified to within 1% using an SEM), the tension inferred from the eigenfrequency formula, $\Omega_{11}/2\pi = \sqrt{\mathcal{T}/(2\rho w_m^2)}$, is $\mathcal{T} = 935$ MPa. This value is within 5% of the factory specified value of 900 MPa. We have found the tension as inferred from the fundamental frequency (assuming fixed dimensions) to vary by a few % between chips in the same processing run from Norcada and by as much as 5% from order to order with identical specifications.

To gauge the precision of the chip geometry and/or uniformity of the tensile stress, we can examine the deviation of the multimode vibrational spectrum from the model dispersion relation: $\Omega_{i,j} = \Omega_{1,1}\sqrt{(i^2 + j^2)/2}$. A plot of the difference between the measured and predicted values $\Delta(i,j) \equiv (\Omega_{ij} - \Omega_{ij}^{meas})/2\pi$ for all modes with frequencies $\Omega_{ij}/2\pi < 5$ MHz is shown in Figure 4.5. We observe that the spectrum does not deviate by more than 0.1% from the model prediction. In the figure, we compare the measured deviation to a model in which the membrane is allowed a small rect-
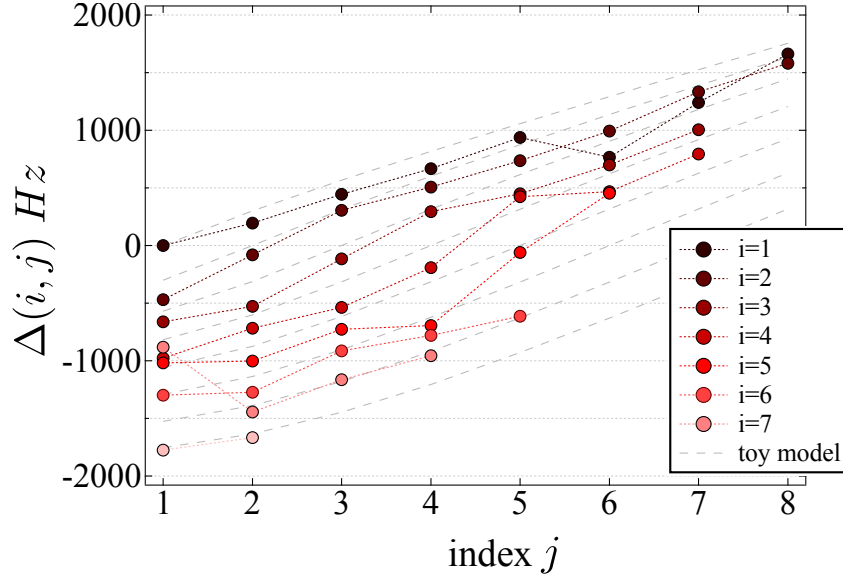
Figure 4.5: Difference $\Delta(i,j) \equiv (\Omega_{i,j} - \Omega_{i,j}^{meas})/2\pi$ between the measured frequency spectrum in Figure 4.4 and the ideal model $\Omega_{ij} = \Omega_{11}\sqrt{(i^2+j^2)/2}$, where Ω_{11} is the measured value. The trend is roughly consistent with a toy model in which the membrane is allowed to be rectangular with one dimension $\approx 0.077\%$ larger than the other (model shown in light gray).

angularity, in which case the model dispersion relation becomes $\Omega_{i,j} = 2\pi\sqrt{\frac{\mathcal{T}}{2\rho}\left(\left(\frac{i}{d_x}\right)^2 + \left(\frac{j}{d_y}\right)^2\right)}$. From this model we infer an effective rectangularity of $|1 - d_y/d_x| \approx 8 \times 10^{-4}$.

In the upper frame of Figure 4.4, we hone in on the fundamental drum mode of the membrane. An effective bandwidth of $B = 200$ mHz is used and three measurements are averaged. We have found it difficult to obtain a good linear least-squares fit of this peak to a Lorentzian because the sub-Hz-wide feature tends to drift by more than a linewidth during the coarse of a single measurement (taking $\Delta t = 2/B = 10$ seconds). In the figure we show a fit to a Lorentzian whose linewidth is obtained using a ringdown measurement, as described in the next section.

4.6.2 Ringdown Measurement of Q_m

An example of a ringdown measurement is shown in Figure 4.6. This measurement was made with the same membrane, optical probe, and etalon configuration described in the previous section. For ringdown measurements, however, the photodetector signal is directed to the input of the HP 4395A network analyzer (Section 4.5.4.2).

The ringdown procedure begins by exciting the membrane. To do this, the network analyzer source is connected to the piezo beneath the etalon mirror and the source frequency is centered at the mechanical frequency, $\Omega_s \approx \Omega_m$. The resulting vibration of the piezo resonantly excites the membrane to an energy $W_0 >> k_B T_{room}$. After a steady-state amplitude is reached (in practice this
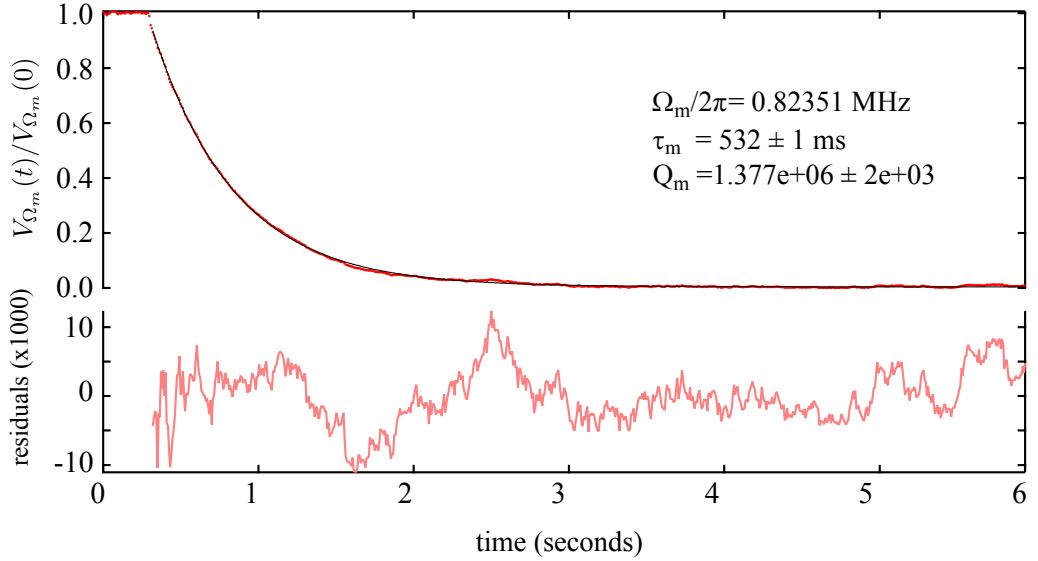
Figure 4.6: Example of a ringdown measurement for the $(1,1)$ mode of the $\{d_m, w_m\}$ = $\{50\,\text{nm}, 500\,\mu\text{m}\}$ membrane characterized in Figure 4.4. Here we use a piezo shaker to excite the fundamental mode of the membrane to an energy $W_0 >> k_B T_{room}$. After switching off the resonant drive, we monitor the amplitude of the oscillator decay. The amplitude inferred from the power reflected from the etalon incorporating the membrane, producing a photodetector signal $V(t)$. $V_{\Omega_m}(t)$, the slowly varying amplitude of V at carrier frequency $\Omega_m/2\pi = 823$ kHz, is monitored using a network analyzer in zero span mode. The measurement is fit to a decaying exponential (black curve). Amplitude residuals are shown in pink. A value of $Q_m \approx 1.38 \times 10^6$ is obtained from the formula $Q_m = \Omega_m/2\tau_m$, where τ_m is the amplitude e-folding time inferred from the fit.

involves patiently tuning Ω_s to track slow drift in Ω_m), we abruptly disconnect the network analyzer source from the piezo. We monitor $V_{\Omega_m}(t)$, the slowly decaying envelope of the oscillation at carrier frequency Ω_m, using the network analyzer in "zero-span" mode, as described in Section 4.5.4.2. To obtain a sufficiently sampled decay curve, we choose an IF bandwidth $2\pi B_{IF} \sim 100 \times \Omega_m/Q_m$, with typical values between $\sim 100 - -1000$Hz for the measurements discussed here and in later sections.

A ringdown measurement of the 823 kHz fundamental mode corresponding to the thermal noise peak in Figure 4.4 is shown in Figure 4.6. We use an IF bandwidth of $B_{IF} = 300$ Hz. The decaying magnitude of $V_{\Omega_m}(t)$ is fit by linear least-squares to an exponential. Residuals of this fit (defined as the difference between the measured and fitted values) are shown in the lower, pink trace, and are less than 1% of the starting value of the decay curve. From the fit, we infer a quality factor of $Q_m = 1.380 \pm 0.005 \times 10^6$, where the error bar is computed from the chi-square value of the fit. The repeatability of this measurement, however, is closer to 10%, for reasons we don't understand. The noise in the measurement at long times is due to Brownian motion of the membrane. For this measurement, the initial amplitude of the membrane is ~ 100 times larger than thermally driven amplitude, corresponding to an initial amplitude of ~ 1 nm. Because the starting energy for the
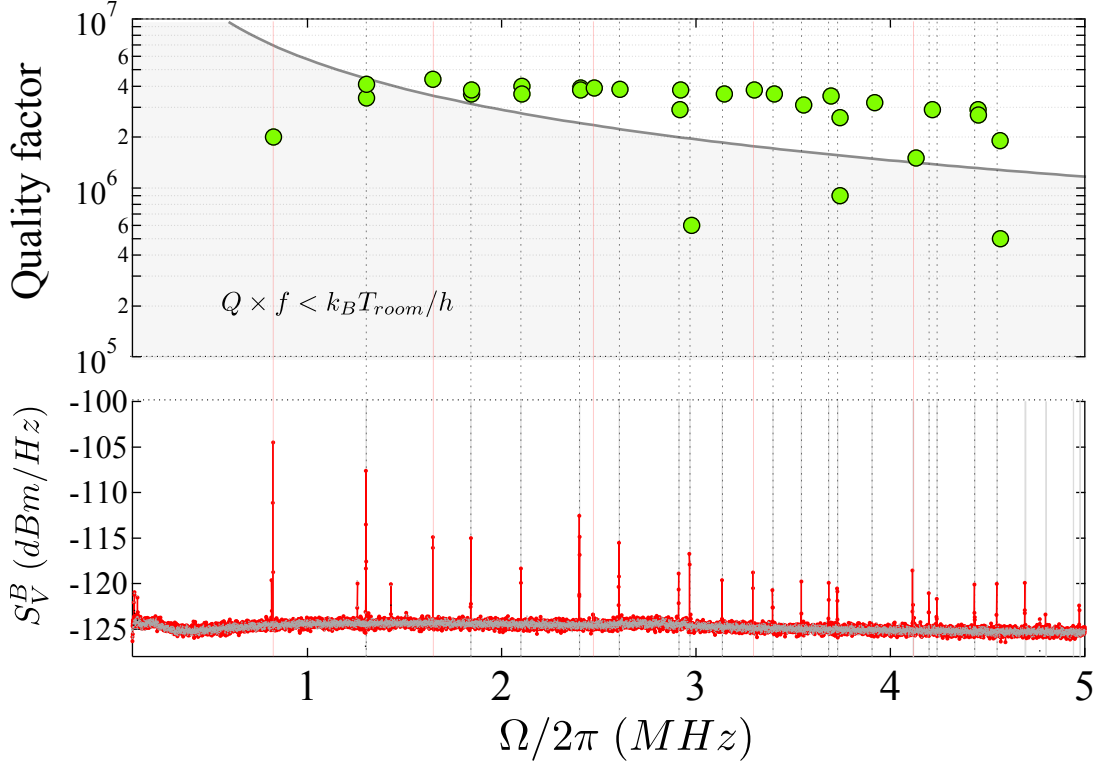
Figure 4.7: Set of ringdown measurements for all membrane modes (i,j) such that $\Omega_{ij}/2\pi < 4.6$ MHz, using the same membrane with dimensions $\{d_m, w_m\} = \{50\,\text{nm}, 500\,\mu\text{m}\}$ as in Figure 4.4. The reduced mechanical quality for the fundamental mode relative to Figure 4.4 is due to a slight modification of the chip mounting. For higher order membrane modes, the value of Q_m is roughly constant at $\sim 4 \times 10^6$, corresponding to a monotonically increasing $Q \times f$ product ($f = \Omega/2\pi$) which surpasses the critical value of 6×10^{12} Hz (shaded gray).

ringdown is substantially larger than the thermal energy, it is worth comparing the result to a more careful measurement of the linewidth of the thermal response. This is done in the next section.

4.6.2.1 Q-factors of Higher-Harmonics — A Single Trial

In Figure 4.7, we have carried out the ringdown measurement for all internal modes of a $\{d_m, w_m\} = \{50\,\text{nm}, 0.5\,\text{mm}\}$ Norcada membrane from 800 kHz to 4.6 MHz, using the etalon configuration shown in the upper left inset of Figure 4.3. We separate vibrational resonances of the piezo and membrane chip (some of which have quality factors in excess of 10^4) from vibrations of the membrane by examining the thermal noise spectrum, as shown in the lower plot. Remarkably, for higher harmonics the $Q \times f$ product exceeds $1.5 \times 10^{13} > k_B T_{room}/h$ (several years ago this was believed to be unique among NEM/MEMs oscillators at room temperature [14]). Roughly a factor of two variation in quality factor is observed between higher order drum modes. We have yet to systematically investigate the role of mode order in determining of mechanical Q_m, but note that a recent study

has been performed at Cornell in which it was found that different mode shapes may experience different support-related clamping losses [58]. What we have found is that the result shown in Figure 4.7 varies widely depending on the details of the membrane window and membrane chip geometry, as well as the way that the chip is attached to the etalon. A large collection of measurements of the sort shown in Figure 4.7 was taken in order to sort out this behavior phenomenologically. We discuss this study in the next section.

4.7 Compilation of Mechanical Q Measurements

Over the course of three years, we have compiled a large database of Q_m measurements for chips and membranes of various geometries. We have varied the chip dimensions, membrane dimensions, and the manner in which the membrane is secured to the chip. More recently, we have also begun developing our own membranes along with Richard Norte (graduate student from the Painter group) and Kang-Kuen Ni (our postdoc) using the facilities at the Painter group clean room and the Caltech KNI—these include circular membranes and more exotic, tethered structures. It has long been appreciated in the nanomechanics community that the size of the resonator and its substrate and their mechanical attachment plays a critical role in determining mechanical dissipation. In particular, smaller structures tend to have smaller Q_m, and structures with high aspect ratios exhibit Q_m-dependence on the thin dimension, which may be attributed to surface-related, thermo-elastic, and "clamping"-type loss mechanisms. "Clamping" loss, which pertains to acoustic coupling to the mechanical support, has been extensively studied for cantilever type structures [59] and also depends on the "large" dimensions of the resonator. A recent treatment of clamping loss in high-stress films has also been carried out, in which it has been shown both experimentally and theoretically that the geometry of the mechanical mode can enhance or suppress coupling to the support structure [58]. Variations on this subject abound. In order to limit our search space, we have focused on measuring the mechanical quality of square Norcada membranes with stoichiometric chemistry and tension $\mathcal{T} \approx 900$ MPa. We have varied the thickness of the membrane from 30 nm to 100 nm and the square dimensions of the membrane from 250 μm to 1 mm. Likewise, we have varied the thickness of the membrane chip from 200 μm to 500 μm and the square dimensions from 5 mm to 10 mm. We have also tried various methods of mounting the membrane chip, including adhesive bonding, rigid mechanical clamping, and resting under its own gravity. Results vary widely, but show a definite trend towards improved Q with smaller membrane thickness, larger window size, larger substrate dimensions, and minimal clamping of the membrane chip. We summarize these results below.
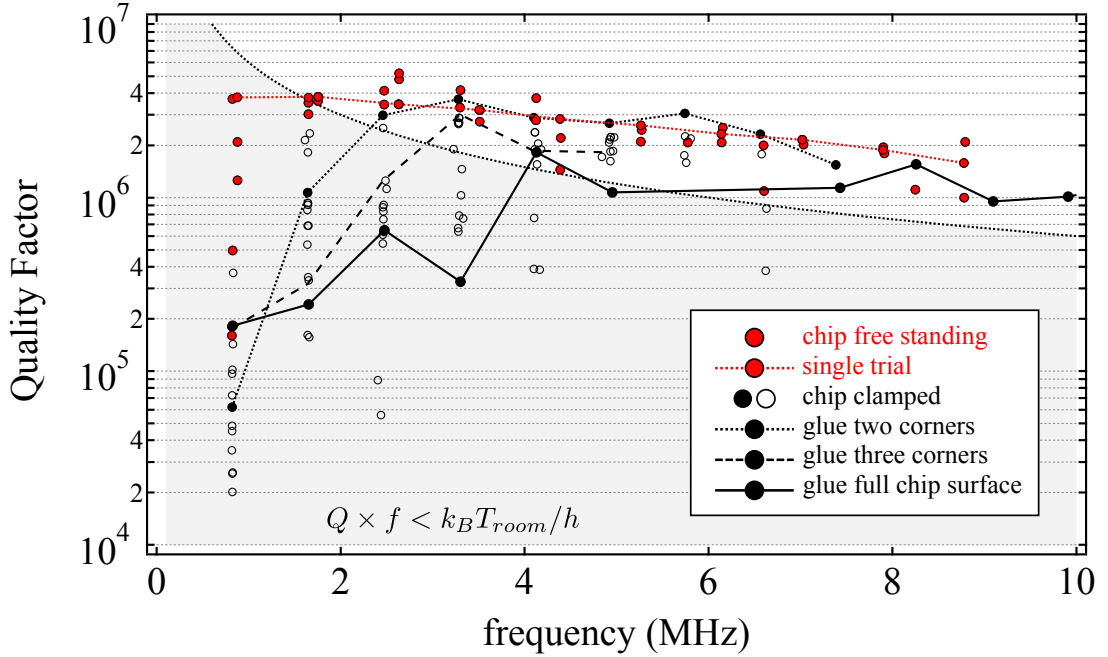
Figure 4.8: Compilation of mechanical Q measurements for different chip mounting methods. Here we have fixed the chip and membrane dimension at $\{d_m, w_{mem}\} = \{50\,\text{nm}, 500\,\mu\text{m}\}$ and $\{d_{chip}, w_{chip}\} = \{0.2\,\text{mm}, 5\,\text{mm}\}$, respectively. A variety of methods were investigated, including adhesive bonding and rigid mechanical clamping, denoted as open or closed black circles. Three examples are illustrated with black lines. These consist of adhesively bonding the entire chip surface to a planar surface, bonding three corners, and bonding two corners, respectively. We compare these results to the case for which the membrane rests "free standing" under its own weight on a planar surface, corresponding to red points.

4.7.1 Influence of Chip Mounting

Practically speaking, we must somehow attach the membrane chip to a separate device (e.g., a mirror) in order to conduct simple tests or to perform the more complicated optomechanics experiment described in the rest of this dissertation. We at first did not anticipate that this would have a substantial effect on the membrane mechanics. We were wrong. For the measurements described in this chapter, we had to somehow attach the chip to the etalon mirror substrate. Originally the entire setup was oriented vertically rather than horizontally (membrane surface normal to gravity); for these earlier iterations we used a small dab of glue or carbon sticky tape to secure the membrane chip against the mirror. Those initial trials were performed on large (1 mm), low-stress (~ 100 MPa) films, which exhibited $Q_m \sim 10^5 - -10^6$, as large as we expected from the work done at Yale and Cornell [13, 40]. When we started studying high-stress Norcada films of nominal dimensions $\{d_m, w_{mem}\} = \{50\,\text{nm}, 500\,\mu\text{m}\}$, we discovered a trend whereby the lower order membrane modes, particularly the fundamental, exhibited significantly deteriorated Q-values relative to higher order membrane modes, and that the quality factor of the lower order modes varied widely from chip

to chip. We made various attempts at alleviating the problem. We tried varying the type of glue from soft silicon adhesive (VacSeal, RTV) to hard epoxy (Masterbond EPLTE-LO) to hard-ceramic (Ceramabond 835). We tried bonding the chip rigidly over its entire surface using a flowable UV epoxy (Norland 81). We tried using minuscule dabs of cyanoacrylic adhesive (Krazy Glue) at the corners. We also tried mechanically clamping the chip between two flat metal surfaces. More recently, we've investigated optical contacting of the chip to the mirror. Without exception, the best results we've observed are for a vertically oriented setup in which the chip simply rests under its own gravity ("free-standing") on the surface of a smooth mirror, or on three points provided by resting on a curved mirror or a washer ring (see left side of Figure 4.3, each geometry gives similar results). We've found the "next best" alternative to be a single dab of adhesive at one corner, then two corners, three corners, and so on. The extent to which the Q is affected depends on the size of the chip and the membrane, being more sensitive for thin membranes and chips. In Figure 4.8, we focus on the results of testing a batch of chips with the nominal membrane/substrate dimensions given above for different mounting techniques. These results illustrate the qualitative behavior described in this paragraph.

4.7.2 Influence of Membrane Thickness and Substrate Thickness

We have purchased chips from Norcada with varying film thickness ($d_m = 30$ nm, 50 nm, and 100 nm) and chip thickness ($d_{chip} = 200$ μm and 500 μm). By fixing the square dimensions of the membrane ($w_m = 500$ μm) and chip ($w_{chip} = 5$ mm), we were able to study the role of d_m and d_{chip} on Q_m. An exhaustive set of measurements was carried out by one of our SURF students, Jetson-Leder-Louis, in the summer of 2010. Those results are shown in Figure 4.9. For each measurement, the membrane was allowed to rest on four corners under its own weight atop a piezo-electric spacer, as shown at top left in Figure 4.3. Jetson's results suggest that the quality factors of low-order membrane modes increase roughly linearly with decreasing membrane thickness, and that for each membrane thickness, the Qs obtained for a $500 - \mu$m-thick substrate are $\sim 25 - -50\%$ better than the results obtained for a $200 - \mu$m-thick substrate.

4.7.3 Influence of Membrane Window Size

We have for some time been interested in using smaller membranes with larger fundamental resonance frequencies, lower effective masses, and larger thermal displacement amplitudes for our optomechanics experiment. To date, we have tested high-stress membranes with square dimensions varying from 1 mm to 200 μm, the latter having been developed at the KNI facility at Caltech by Richard Norte and Kang-Kuen Ni. When all other membrane and chip dimensions are fixed, we have found evidence that suggests that membranes with smaller square dimensions exhibit lower $Q \times f$
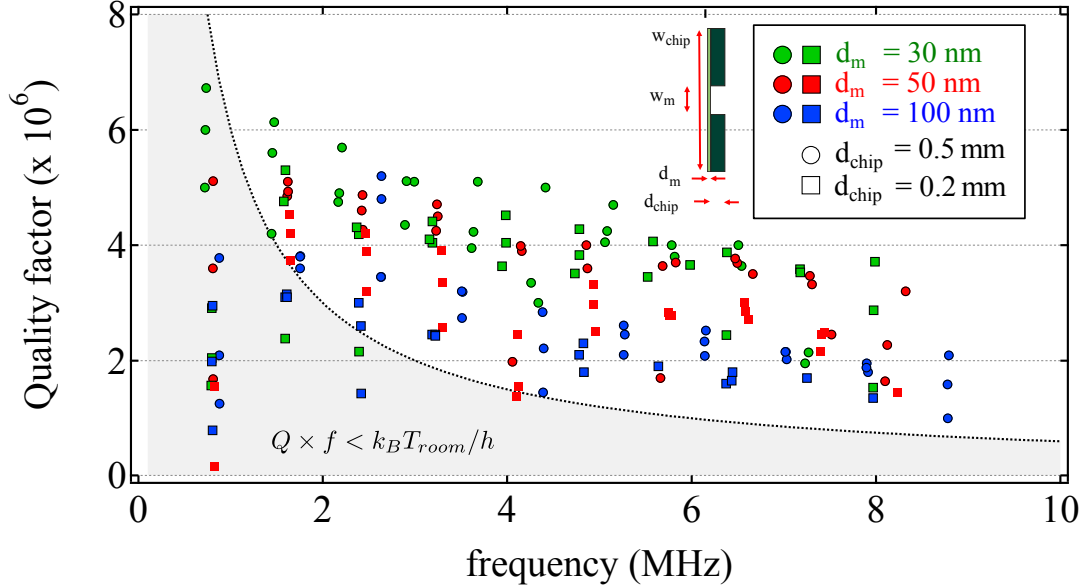
Figure 4.9: Compilation of Q measurements for different membrane and chip thicknesses. Here we have fixed the square chip and membrane dimensions at $w_m = 500\,\mu$m and $w_{chip} = 5$ mm, respectively. The thickness of the film is varied between $d_m = 30$ nm, 50 nm, and 100 nm. The thickness of the chip is varied between $d_{chip} = 200\ \mu$m and 500 μm. For a given membrane mode, the quality factor scales roughly inversely with membrane thickness. Marginal improvement is also seen for thicker chips. In all cases, the membrane is mounted by resting on a planar surface under its own weight.

products. For free-standing chips, most of our study as been limited to $w_m = 0.25$ mm and 0.5 mm membrane windows. We have found that at similar mechanical frequencies, Q_m for the modes of the $w_m = 0.25$ mm membrane are roughly half that of the $w_m = 0.5$ mm membrane. A subset of results for $d_m = 50$ nm membranes in which the chip dimensions has been fixed at $d_{chip} = 0.2$ mm thick and $w_{chip} = 5$ mm wide is shown in Figure 4.10.

4.8   Summary of Q Measurements, Comparison to Clamping Models

A summary of results culled from three years of measurements on high-stress Norcada membranes of various geometries is shown in Figure 4.11. Here we have plotted the results in terms of the $Q \times f$ product, which may be compared to the critical value of $k_B T_{room}/h = 6 \times 10^{12}$ Hz denoted by gray shading. The results are categorized in terms of membrane thickness d_m, membrane square dimensions w_m, and chip thickness d_{chip} (though we have also varied chip size w_{chip} from 5 mm to 10 mm, we have noticed only a marginal improvement from this change). The manner in which the chip has been secured is broadly categorized as "clamped" (e.g., using adhesive at the boundary)
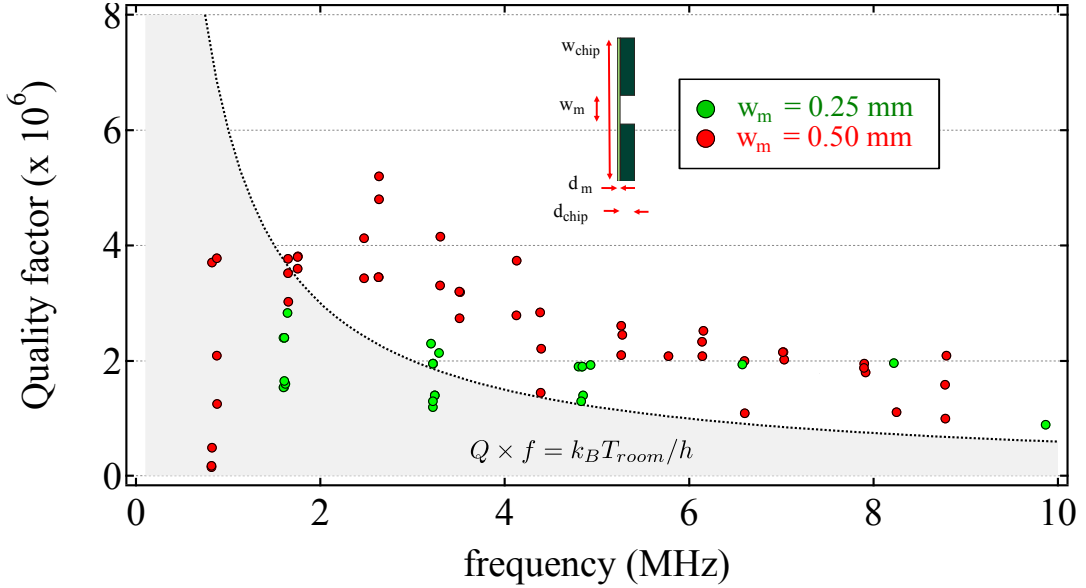
Figure 4.10: Compilation of Q measurements for different membrane sizes. Here we have membrane thickness at at $d_m = 50$ nm and the chip dimensions at $\{d_{chip}, w_{chip}\} = \{0.2$ mm, 5 mm$\}$. The width w_m of the square membrane is varied between 0.25 mm, 0.5 mm, and 1 mm. As an important caveat, for 1 mm membranes we have only made measurements for rigidly mounted chips— we believe this explains the discrepancy from the trend inferred from the 250 μm and 500 μm trials. For these two cases the membrane chip was allowed to rest on a planar surface under its own weight.

vs. "free-standing" under its own weight. Note that the best results are obtained for the thinnest (30 nm) membranes deposited on the thickest (500 μm) chips. The scatter in measured Q_m values extends two orders of magnitude and is predominantly associated with lower order modes of rigidly mounted membrane chips. This scatter is diminished for higher order membrane modes, which we may interpret as having weaker coupling to the substrate. At high frequencies, these quality factors appear to asymptotically approach a $Q \times f$ product of several 10^{13} Hz. Higher frequencies were not measured for lack of ability to drive them with the piezo.

It is interesting to compare these qualitative trends to loss mechanisms often quoted in NEMs and MEMs literature. A tremendous amount of work has been dedicated to this subject, so we confine ourselves to the loss mechanisms that have been suggested for transverse vibrations of structures based on thin films. Surprisingly little is understood physically about the role of tensile stress in these types of resonators [41]. For doubly clamped nano-beam type geometries at room temperature, for example, it has been suggested that primary loss mechanisms include viscous air damping, thermoelastic loss, and external (clamping) loss due to surface layers and acoustic coupling to the support [39, 59]. We touch on these subjects below.
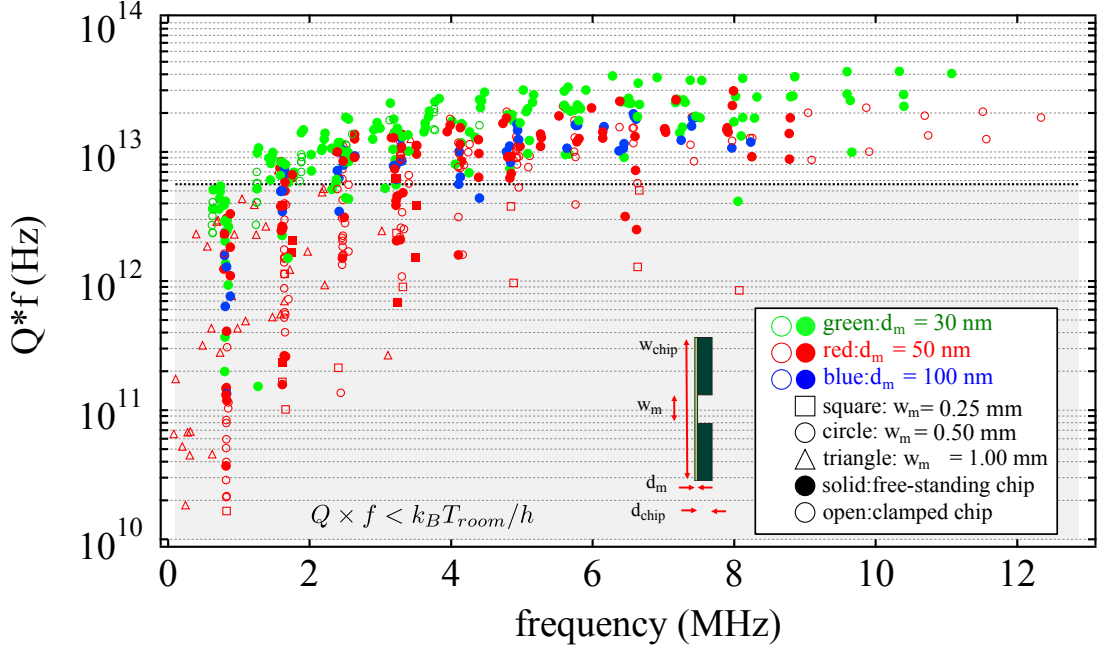
Figure 4.11: Summary of Q measurements. Here we highlight the results for differing membrane thickness d_m, membrane size w_m, and mounting technique ("clamped" vs. free-standing). Different chip size and thicknesses are lumped together, though we note that moderately improved quality factors are recorded for thicker chips. The highest $Q \times f$ products were obtained for d_m =30-nm-thick, $w_m = 500$-μm-wide membranes on a $d_{chip} = 500$-μm-thick, $w_{chip} = 5$-mm-wide chip resting on three corners under its own weight. Membranes with different dimensions appear to exhibit $Q \times f$ with scaling roughly w_m/d_m.

4.8.1 Clamping Mechanisms

Air damping for a thin beam of thickness t obeys a relation [40]

$$Q_{air} = \frac{\rho t \Omega_m}{4} \sqrt{\frac{\pi}{2}} \sqrt{\frac{RT}{M}} \frac{1}{P} \approx 6 \times 10^8 \times \left(\frac{t}{50 \text{ nm}} \right) \left(\frac{\Omega_m/2\pi}{1 \text{ MHz}} \right) \left(\frac{10^{-6} \text{ mbar}}{P} \right) \sqrt{\frac{T}{298 \text{ K}}} \quad (4.21)$$

in the molecular flow regime, characterized by a mean free path ℓ between gas particles (with diameter d_0) that is greater than the largest dimension of the oscillator. For an ideal gas, $\ell = k_B T_{room}/\sqrt{2}\pi d_0^2 P > 1$ mm implies $P < 6 \times 10^{-2}$ mbar for this condition to hold for 50-nm-thick films at room temperature with $d_0 \approx 0.4$ (typical for gas particles in air). For our operating pressure of $P \sim 10^{-6}$ mbar neither the absolute value nor the thickness dependence associated with air damping seems to match the measured Q_m data.

A second candidate is thermoelastic loss, which arises when elastic strain produced by vibration induces local temperature gradients. Equilibration of these gradients draws energy from the vibration. This form of loss can dominate in room temperature NEMS/MEMs systems, where the small dimension of the oscillator can lead to thermal relaxation rates as fast or faster than the vibrational

frequency. A formula which is often applied to resonators under tensile stress but which is derived for purely bending-type resonators in is [60]

$$Q_{TED} = \frac{c_v}{E\alpha^2 T} \left(\frac{6}{\xi^2} - \frac{6}{\xi^3} \frac{\sinh\xi + \sin\xi}{\cosh\xi + \cos\xi} \right)^{-1} ; \; \xi = d\sqrt{\frac{\Omega_m \rho c_m}{2\kappa_c}} \qquad (4.22)$$

where d is the thickness of the structure. c_v is the specific heat per unit volume, E is the Young's modulus, α is the linear thermal expansion coefficient, c_m is the specific heat per unit mass, κ_c is the thermal conductivity, and T is the ambient temperature. For parameters $\{d, \rho, E, \kappa_c, \alpha, c_m, c_v\}$ = $\{50 \text{ nm}, 2.7 \text{g/cm}^3, 210 \text{ GPa}, 30 \text{ W/m/K}, 2.3 \times 10^{-6} \text{ m/K}, 710.6 \text{ J/kg/K}\}$, one predicts $Q \times f \approx$ 6×10^{13} Hz (the second term in (4.22) is negligible in our case, since $\xi \ll 1$). The main uncertainty in this number comes from the value of κ_c, which varies by as much as a factor of ten in the literature (see [39] and references in Table 4.1). This result suggests that thermoelastic losses may explain the highest $Q \times f$ products we've achieved. However, we have several reasons to believe that this is not the case. First of all, $\xi \ll 1$ suggests $Q_{TED} \propto d_m^{-2}$; if this were the case and 30 nm membranes were thought to be limited by thermoelastic losses, then results for our 100-nm-thick membranes would exceed the predicted thermoelastic limit. More importantly, our resonators are decidedly far from "bending"-type resonators. The derivation of Q_{TED} in [60] assumes a relationship between internal strain and mechanical frequency which significantly overestimates the curvature of the transverse vibrations associated with a given mechanical frequency (it is this curvature which leads to volume change and thermoelastic heating for a thick 1D or 2D string). A more rigorous calculation which takes into account tension has been carried out by our colleague Darrick Chang. He predicts that the thermoelastic $Q_{TED} \times f$ limit for our square drum resonators can be as high as $\sim 10^{19}$ Hz. This prediction is in qualitative agreement with the results of a calculation we've been told has been independently carried out by the Yale group [61].

We have yet to identify a smoking gun from among the various clamping loss mechanisms normally cited for NEMs structures. Phenomenologically, what we observe is a quality factor that scales roughly inversely with membrane thickness d_m, roughly linearly with membrane square dimensions w_m, roughly linearly with chip thickness d_{chip}, and roughly independent of frequency for higher harmonics. By contrast, models for surface loss [59] in planar resonators predict that thicker films should exhibit higher Q_m, since fractionally less of the vibrational energy is shared with the lossy surface layer. Models for acoustic coupling of doubly clamped beams and cantilevers to their support substrates generally predict that Q should scale as a power law greater than or equal to linear in the length of the resonator, depending on the geometry of the substrate [39]. These models assume, however, that $\mathcal{T} = 0$, that the beam width is much smaller than its length (in our case the two are equal), and that the wavelength of an acoustic phonon propagating in the substrate material at the vibrational frequency of the resonator is much different than relevant dimensions of either

the resonator or the substrate. In our case, a 1–10 MHz frequency phonon propagating in silicon with elastic wave speed $\approx$ 5000 m/s has a wavelength of 0.5 - 5 mm, which is of the same order as the square dimensions of the membrane (w_m = 0.25–1 mm), the thickness of the chip (d_{chip} = 0.2–0.5 mm), and the square dimensions of the chip (w_{chip} = 5 mm–10 mm)! Recent work by the Cornell group with Ignacio Wilson-Rae [58] has taken some of these considerations into account. They predict that for square and circular membrane geometries similar to ours, the quality factor limit due to acoustic coupling to the support should indeed scale as w_m/d_m. They compare their prediction to measurements made on d_m = 112.5 nm, w_m = 250-μm-square membranes developed in-house with $\mathcal{T}$ = 1200 MPa and using a somewhat different processing method than Norcada. Their Q prediction is a factor 10–100 higher than measured. Accounting for this discrepancy by adding an ad-hoc internal loss term, they are able to predict to within factor of $\sim$ 2 the differences in the quality factors of different higher harmonics for the same square membrane. It is interesting to note that the quality factors they observe agree to within a factor of $\sim$ 2 with the value of $Q \approx 10^6$ that our results would phenomenologically predict for a membrane of their dimensions.

4.9   Concluding Remarks

Extending the work begun at Yale [13], we have found that commercial high-stress Si_3N_4 membranes can exhibit exceptionally high quality factors at room temperature, even exceeding the basic condition for ground-state optomechanical cooling from room temperature ($Q \times f > k_B T_{room}/h > 6 \times 10^{12}$ Hz) for higher harmonics of sub-mm membranes. We have characterized the static and dynamic mechanical properties of these films using a simple optical setup. This setup allows for the study of both the steady state response to thermal excitation and the ringdown response to a resonant piezo-electric driving force. A comprehensive set of measurements has been made with regards to what we believe to be predominantly clamping-type losses. We have found that thinner, larger membranes on thicker substrates produce the best results, and that straining the substrate can have substantial effects on the measured Q_m. In our case the effect of adding strain is deleterious, in contrast for example to [62] . Our findings suggests that a compromise must still be made to keep the resonator "small" and at the same time of high quality. A metric for the "smallness" of the resonator may be given in terms of the product of its quality factor and its surface-to-volume ratio (R). It has been noted in the past [13] that silicon nitride membranes exhibit a marked advantage over other geometries in this respect. In our case, $Q \times R = 3 \times 10^5$ nm^{-1} and $Q \times f > 2 \times 10^{13} Hz$ for the higher order mode of a 30-nm-thick square membrane with sum-mm dimension. Both numbers currently appear to be among the best achieved at room-temperature for mescoscopic oscillators used in opto/electromechanical studies, as well as in the broader MEMs/NEMS community.

Chapter 5

Membrane-in-the-Middle Apparatus

In this chapter I present a top-down description of our first-generation "membrane-in-the-middle" apparatus, including the cavity, nanopositioning system, vacuum chamber, vibration isolation, and optical layout. The description herein is intended to furnish the backdrop for the experiments described in later chapters. Most of the hardware in the system described here was developed in the autumn and winter of 2008. At the time, the "mechanics" project in the Kimble group was unfunded but heavily resourced, having recently decommissioned two laboratories ("lab 11" and "lab 9") dedicated to our Fabry-Perot-based CQED project. By dint of my familiarity with those projects, Cindy Regal, Scott Papp, and I were able to carve out an exclusive claim to a hodge-podge of valuable equipment. In particular, we decided to construct the new experiment around in-house diode and titanium-sapphire lasers operating at NIR (800 – 950 nm) wavelengths, along with a warehouse of optics at those wavelengths, including the supermirrors used for the optical cavity. We also gathered vacuum components, a nanopositioning stage, vibration isolation material, servo electronics, RF synthesizers and spectrum analyzers, computers — you name it. Much of the lore and technology that has been inherited, particularly with regards to the development of high-finesse Fabry-Perot cavities (a craft with a long history in the Kimble group), will be lifted out of historical context here. I begin, rather, where the dust has settled, referring to former theses as needed.

5.1   Design Criteria

In the previous chapter it was shown that high-stress, stoichiometric Si_3N_4 membranes could exhibit exceptionally high quality factors. They also have small mass (~ 10 ng) and a geometry that enables them to be integrated into an an optical cavity [7], making them an attractive candidates for optomechanical studies [13]. Coupled with preliminary data (Section 6.4) and documented evidence [36, 13] that Si_3N_4 could exhibit low optical absorption in the NIR, and drawing from the seminal
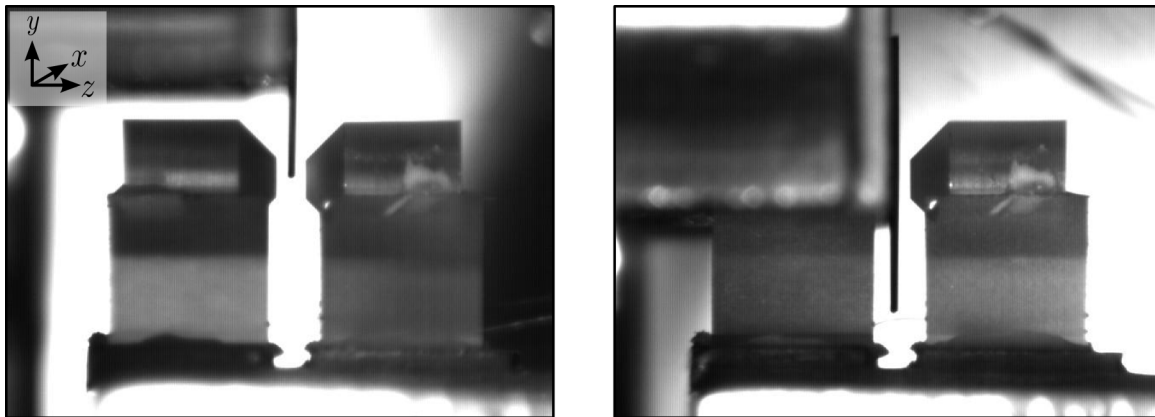
Figure 5.1: Initial nanopositioning of the membrane between the cavity mirrors (the cameraman is holding his breath). In this chapter we explain the architecture and operation of the "membrane-in-the-middle" apparatus pictured here.

work of the Harris group [7], we set about constructing our own "membrane-in-the-middle" (MIM) cavity apparatus in October of 2008. Our design criteria deviated in some respects from the Harris group's, and can be summarized as follows:

1. The cavity mirrors should support a finesse of $\mathcal{F} > 10^5$, as we anticipated the extinction coefficient for our films to be $< 10^{-5}$ in the NIR. To provide some leeway, we also anticipated the need to "tune" the cavity finesse by operating on the side of the mirror coating curve.

2. The cavity length should be long enough to enable operation in the good cavity limit, but short enough to support a spot size smaller than the (6,6) mode of a 500-μm-square membrane (deemed a sweet spot based on our mechanical Q measurements at the time, see Chapter 4). To obtain $\kappa(HWHM) \sim 1$ MHz, this compromise would require a $L \sim 1$ mm cavity with the smallest radius of curvature mirror substrates we had available at the time, $R_c = 5$ cm.

3. The cavity length must be tunable to enable referencing/locking to the laser. This would be necessary since, for a ~ 1 mm cavity, the free spectral range, $FSR \equiv c/2L \sim 100$ GHz, is much larger than the mode-hop free range of our diode and ti-sapph lasers.

4. The membrane should be separate from the cavity and attached to a nanopositioning stage with five alignment degrees of freedom. We had little idea how difficult alignment would be, so we required a positioning system with both fine and coarse tuning capability. Fine resolution along the cavity (z) axis should be sub-nm $(<< \lambda)$. Fine resolution along perpendicular (x, y) axes should be sub-μm (much smaller than the nodal spacing for the 6,6 mode of a 500-μm-square membrane). Fine tip/tilt resolution should be $<< L/(R_c \cdot \mathcal{F}) \sim 1$ μrad. Coarse

resolution along the cavity axis should be longer than the cavity length, > 1 mm. Coarse resolution in the x and y direction should enable complete removal of the membrane from the cavity, and hence be larger than the 5 mm chip dimensions.

5. The membrane should be attached to a stiff, short-range piezo shaker for ringdown measurements and in order to provide a dither at the mechanical frequency for displacement calibration.

6. The membrane chip should be mounted in a fashion which does not appreciably reduce the quality factor of the membrane.

7. The MIM cavity should be supplied with dedicated vibration isolation. Isolation should ideally limit vibration of the membrane with respect to the cavity mirrors to $\sim \lambda/\mathcal{F} \sim 100$ pm at seismic frequencies (< 100 Hz).

8. The MIM cavity should be enclosed inside a vacuum chamber. It must be large enough to accommodate the cavity, membrane nanopositioning system, and a vibration-isolation stack. It must also be able to achieve a moderately high vacuum of $\sim 10^{-6}$ mbar in order to eliminate the possibility of air damping on mechanical quality of the membrane.

We now discuss how these challenges were met by the various components.

5.2 Cavity Design

Short, small-waist, high-finesse Fabry-Perot cavities are the mainstay of a decades-old CQED project in the Kimble group [63, 64]. Consequently, we have borrowed a great deal from the design of our CQED system in the development of the cavity for our MIM system. The marriage has been fruitful because, as it turns out, the task of loading into and trapping an atom inside of a short Fabry-Perot cavity places similar geometric constraints on the system as the criteria listed above. In particular, both systems benefit from a design which permits optical axis to the volume between the two cavity mirrors over a large solid angle. In the atomic physics experiment, this optical access has enabled us to efficiently load and interrogate a trapped atom using laser beams transverse to the cavity axis. In the optomechanics experiment, we take advantage of this optical axis to maneuver a dielectric thin film between the mirrors. In both cases, a large solid angle requires that the ratio of the mirror diameter to the cavity length be small. The design therefore centers around a pair of dielectric supermirrors with $\sim$ mm dimensions [37].

A schematic of the cavity is shown in Figure 5.2, corresponding to the photo in Figure 5.1 and the schematic in Figure 5.3. Its design represents the culmination of many years of meticulous tweaking, and includes only several minor modifications specific to my own prejudices and the (for the most part relaxed) demands of the optomechanics project. Basic elements of the design have been

y

x

z

L = 0.743 mm

superpolished mirror, 5 cm radius of curvature

1mm

1mm

3 mm

3 mm

3 mm

mirror substrate (BK7)

v-block (BK7)

4 mm

0.5 mm

5 mm

4 mm

shear mode pzt (ferroperm Pz27)
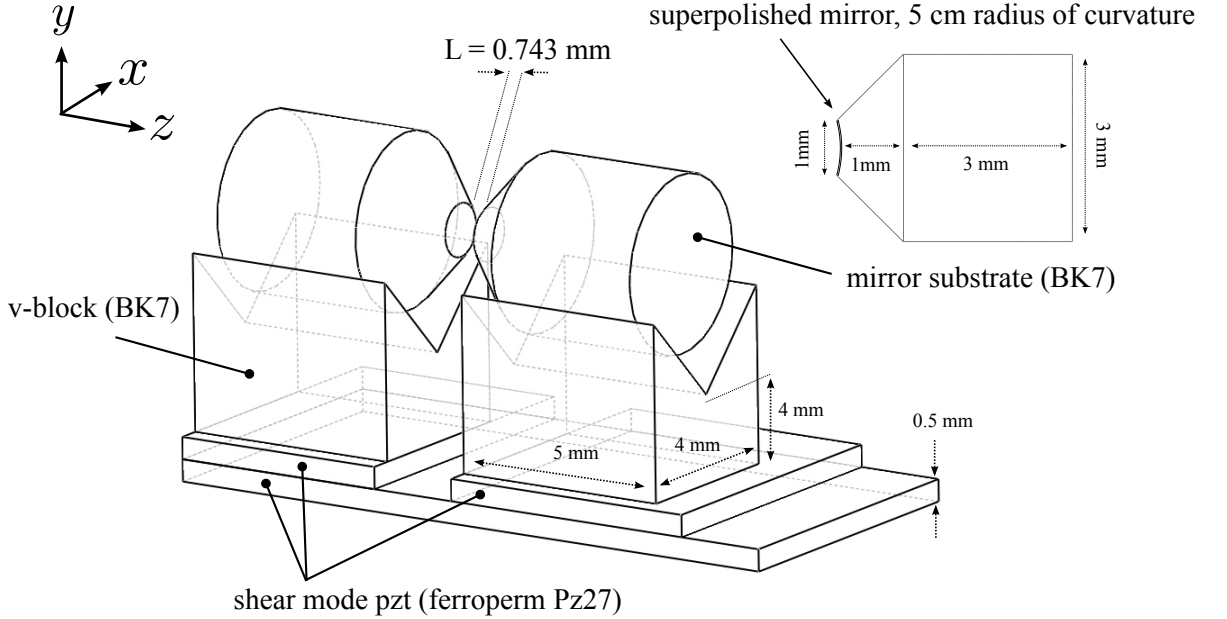
Figure 5.2: Schematic of the optical cavity, including mounting components and mirror substrates

described in detail in the dissertations of no less than seven generations of CQED experimentalists in the Kimble group, includeing Russ Miller [63], Tracy Northup [65], Andreea Boca [66], Kevin Birnbaum [67], Jason McKeever [68], Joe Buck [69], Teresa Lynn [70], Christina Hood [71], Dave Vernooy [72], and Quentin Turchette [73]. In particular, we refer the reader to Tracy and Christina's theses for a detailed description of the mirrors, to Kevin and Christina's thesis for a manual to cavity construction, and to Joe Buck's thesis for an in-depth discussion of the mirror substrates.

We here elaborate on the mirrors, the cavity assembly, and choice of cavity parameters:

5.2.1 Mirrors: Coating and Substrate

The mirror coatings used in this experiment are described analytically in Chapter 3 and characterized experimentally in Chapter 6. They were drawn from a batch of dielectric "supermirrors" developed by Advanced Thin Films in 2005 for use in our Cesium CQED experiment [37, 65]. At the center of the coating curve, roughly $\lambda_c \approx 850$ nm, the reflectivity of the mirrors is $R_{mirror} \approx 0.999985$. The scattering/absorption probability δ_{SA} for a photon incident upon the mirror is designed to be better than $\delta_{SA} = 1 - R_{mirror} - T_{mirror} = 3$ ppm. However, as is typical, handling of the mirrors has resulted in a marginally higher loss of ≈ 5 ppm. For a symmetric cavity, this enables a loss limited finesse of $\mathcal{F} = \pi/(T_{mirror} + \delta_{SA}) \approx 1.5 \times 10^5$ at coating center. The mirrors were also designed so that a reasonably high-finesse may still be obtained at the "magic" trapping wavelength for cesium, 935 nm. For this particular batch of mirrors, the transmission at 935 nm is ≈ 300 ppm, allowing

for a relatively less lossy symmetric cavity with a finesse of $\approx 10^4$. We have taken advantage of the wavelength dependence of the coating curve to operate the MIM cavity at a variety of finesse values.

Physically, each mirror consists of a 35-layer dielectric stack deposited on a superpolished BK7 glass substrate. The substrates arrive from the factory with cylindrical dimensions of $\{D_s, L_s\} = \{7.75 \text{ mm}, 4 \text{ mm}\}$. The superpolished face has been ground against a convex blank with a spherical radius of $R_c = 2.5$ cm - ∞(plano). In our case the radius is $R_c = 5$ cm. The other, plano face of the substrate has a slight wedge to prevent back-reflection; this surface has received an AR coating ($< 0.1\%$) centered at a wavelength of 850 nm. After coating, the substrates used in our experiment were honed to dimensions of $\{D_s, L_s\} = \{3 \text{ mm}, 4 \text{ mm}\}$ on a glass lathe. The edge of the superpolished face was then chamfered at 45 degrees to reduce the diameter of the mirror face to 1 mm.

5.2.2   Cavity Construction

To form a cavity, two mirrors are placed face to face and aligned in the customary fashion — so that the coated surfaces are pierced by the line joining their centers of curvature (see [37] for a thorough description). A geometrically stable, horizontal orientation is achieved by first securing each mirror with a small dab of high vacuum-compatible, thermally matched UV optical adhesive (Dymax OP-67) to a BK7 glass v-block of similar dimensions. The v-blocks rest on a pair of shear mode piezos for cavity length adjustment. In this case we have used a pair of 0.5-mm-thick shear piezos from Ferroperm (Pz27), with a resolution of ≈ 1 nm/V. The first resonance of the "input" and "output" mirror piezos when loaded with the v-block and mirror substrates is 10 and 35 kHz, respectively. To address the need to displace the cavity with respect to the membrane, we have also added a third "common mode" shear piezo below the v-blocks, as shown (unfortunately, this "common" piezo was later found to exhibit ≈ 1 nm/V expansion along the cavity axis in addition to shear displacement, rendering it useless for the prescribed purpose). Where necessary, conductive surfaces and leads were bonded using a UHV compatible silver epoxy (Epotek H21). Mirrors, v-blocks, and piezos were assembled vertically atop a common metal platform. Our platform is made of stainless steel and is secured mechanically to the vibration isolation platform.

5.2.2.1   Cavity Parameters

The cavity length was chosen in order to strike a compromise between cavity spotsize requirements, $w_c << w_m$, and sideband resolution, $\kappa/2\pi = c/4L/\mathcal{F} > \Omega_m/2\pi$ (where w_m is the width of the membrane window (Fig. 4.1) and Ω_m is the mechanical frequency of the membrane). A small spot size is necessary to address a single anti-node of a high-order membrane vibration (otherwise the optomechanical coupling is reduced, as discussed in Section 7.1.3). Our target was the $(6,6)$ mode of a 500 μm membrane, for which we require $2w_c \sim 500/6 \approx 80$ μm. For a symmetric

cavity made of two mirrors of identical radius of curvature R_c, this requires $L \approx 2\pi w_c^4/\lambda^2/R_c \approx 1$ mm$\times(w_c/40~\mu$m$)^4(1~\mu$m$/\lambda)^2(R_c/5$ cm$)$ (see [31]). On the other hand, to achieve sideband resolution, we require $L = c/2/\mathcal{F}/(\Omega_m/2\pi) \approx 0.15$ mm$\times(10^5/\mathcal{F})(\Omega_m/2\pi/5$ MHz$)$. Another practical constraint is the thickness $t_{chip} = 200~\mu$m of the membrane chip, which requires $L > 2t_{chip} > 400~\mu$m in order to place the membrane at cavity center. To meet these three requirements, we chose the smallest radius of curvature mirror we had available ($r_{mirror} = 5$ cm) and constructed a cavity with a nominal length of 750 μm. The actual cavity length was inferred by measuring the ~ 10 GHz frequency difference (transverse mode splitting) between the TEM00 and TEM01 modes of the cavity, given by $f_{00} - f_{01} = \arccos(1 - L/R_c) \times c/L/2\pi$ [31] (the ~ 200 GHz free spectral range for this short cavity is harder to access experimentally). The measurement was made by simultaneously exciting both cavity modes using sidebands generated by a broadband electro-optic modulator. We measure $f_{00} - f_{01} = 11.1$ GHz (error set by the ≈ 10 MHz cavity linewidth), giving $L = 743 \pm 1~\mu$m assuming $R_c = 5$ cm. An operating wavelength of 935.5 nm was used for many of the measurements discussed in this thesis, in which case the cavity waist is 35.7 μm. A more moderate cavity finesse of $\approx 10^4$ is obtained at this wavelength (the precise value of $\mathcal{F}$ varies by $\sim 10\%$ depending on the last digit in λ, ~ 0.1 nm). This results in a linewidth (HWHM) of $\kappa/2\pi = 10.1$ MHz $\times (\mathcal{F}/10^4)$.

5.2.3   Nanopositioning System

There are many ways to conceive of positioning a thin film between two FP mirrors (at least as many late nights for an obsessive fourth-year graduate student, I assure you). To constrain ourselves, and to manage uncertainties about the alignment challenge, we adopted the following pragmatic approach: we would build the nanopositioning system around the traditional cavity with minimal change to its design, and in a manner which would allow us to insert and remove, in situ, the membrane from the cavity, thereby enabling us to perform upgrades to the chip and chip holder in a "plug-and-play" fashion. In return, we were willing to sacrifice some compactness, vibrational stability, vacuum compatibility, and cavity finesse.

The design that we ultimately settled on is pictured in Figure 5.3. It represents a compromise between flexibility, stability, and some insistence on integrating standard, commercially available optomechanics and nanopositioning hardware (as opposed to a custom nanopositioning system). It also represents a natural extension of the standardized setup in our lab for the construction of short, high-finesse cavities, in which one of the mirrors — now replaced by the membrane — is manipulated in the arm of a 5-axis stage designed for fiber alignment. Generally speaking, a commercially available nanopositioning system with our coarse and fine resolution requirements consists of either a piezo/microstepper motor-actuated translation stage or else one of the now standard slip-stick nanopositioning systems pioneered by Attocube [74]. Although less elegant, we chose the former approach because it is considerably less expensive and more extensible. From
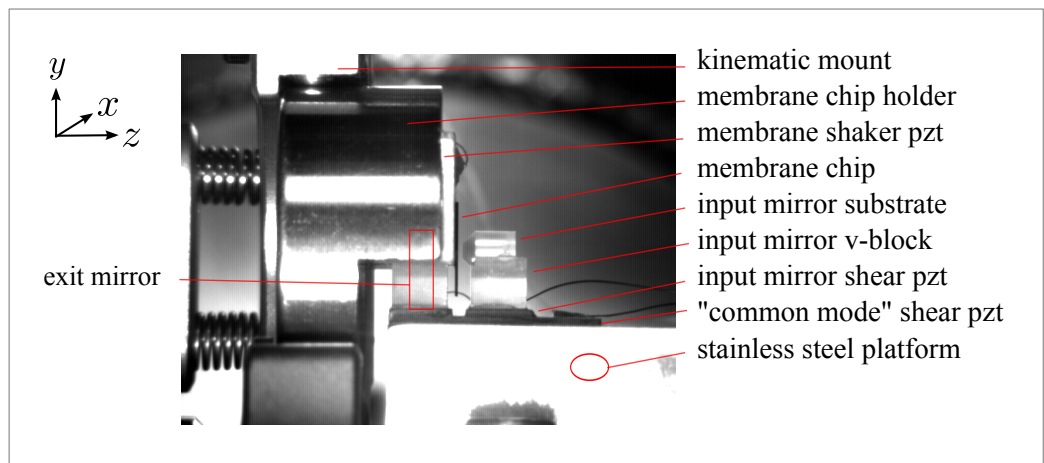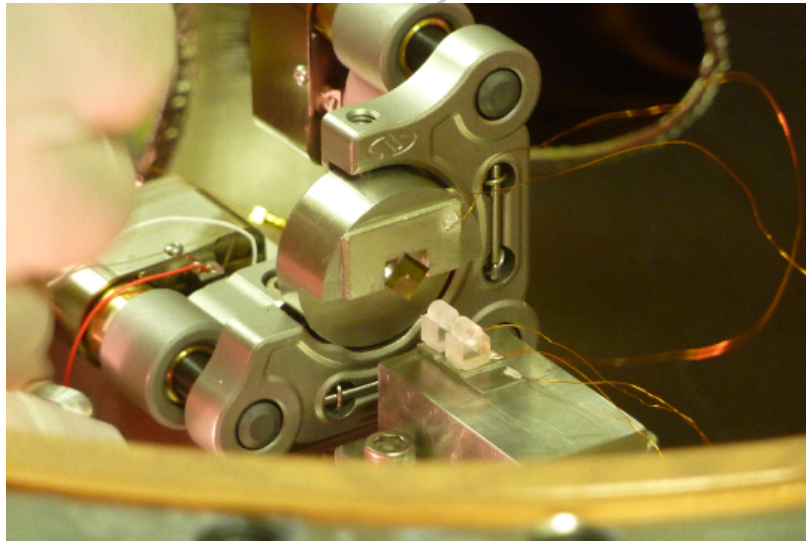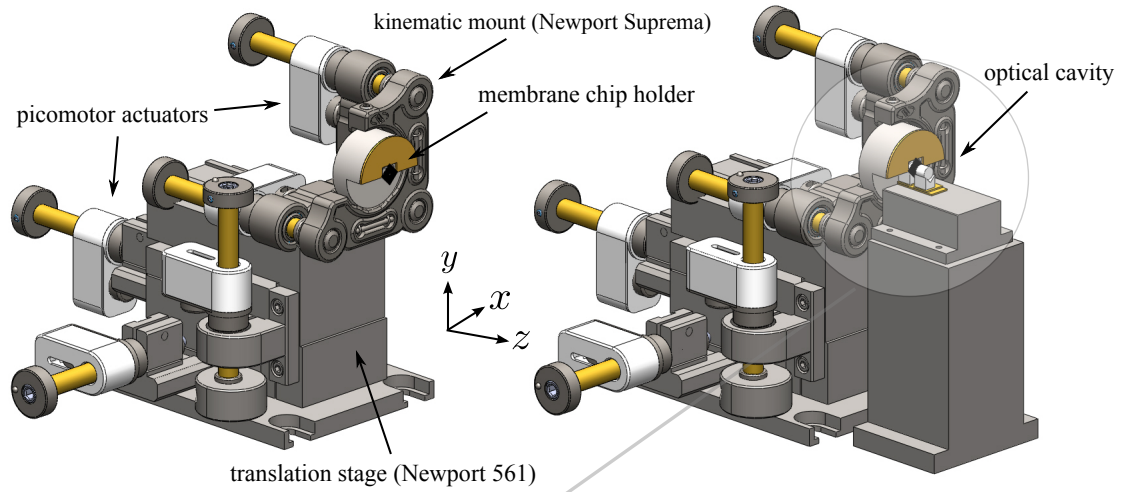
Figure 5.3: Schematic of the MIM apparatus including nanopositioning system.

among the growing family of motorized actuators available, we chose the New Focus Picomotor because of its good reputation with our NIST colleagues. For the translation stage, we chose the 561 fiber positioning stage from Newport, as this stage was both compact and had been used with success for cavity construction and in a project to pull fiber tapers for our group's toriod-based CQED experiment [75]. To incorporate tip/tilt, we fixed the stiffest available kinematic mount from Newport (Suprema SN100) to the top of the translation stage. The resulting fine resolution for each axis is set by the nominal 30 nm stepsize of the Picomotor: $\{x, y, z, \text{tip}, \text{tilt}\} \approx \{30 \text{ nm}, 30 \text{ nm}, 30 \text{ nm}, 0.8\mu \text{ rad}, 0.8\mu \text{ rad}\}$. The coarse range is set by the range of the stage and kinematic mount: $\{12.5 \text{ mm}, 12.5 \text{ nm}, 12.5 \text{ nm}, > 10 \text{ deg}, > 10 \text{ deg}\}$.

The final ingredient that needed to be developed was a jig to adapt the membrane — which must be suspended between the cavity mirrors — to the kinematic mount without sacrificing optical access to the cavity, and without diminishing the mechanical properties of the membrane. This was achieved by judicious lathe-working of a 1" cylindrical steel blank, as shown in Figure 5.4 (a recent upgrade uses Macor and an additional long-range piezo, as shown alongside). A brief digression into details of the Picomotors and the "membrane holder" is provided below.

5.2.3.1   Picomotors

All three axes of the translation stage as well as the tip/tilt axes of the kinematic mount are fitted with standard open-loop, high-vacuum-compatible New Focus Picomotors (model 8302V). The operating principle of the Picomotor is common to all resonant piezo motors — a piezo-electric element at the interface of two frictionally contacted surfaces is vibrated in such as way as to shimmy the two surfaces away from each other. In this case the two surfaces are a screw and its shaft separated by a piezo-electric sleeve, and the action of the piezo vibration is a small advance of the screw inside of its thread. By this "squiggle motor" mechanism, Picomotor actuators are capable of advancing a ball-tip screw over a range of centimeters in microsteps of approximate (but repeatable) magnitude ~ 30 nm. Aside from having a smaller step size, their advantages over standard DC servo motors or stepper motor actuators are true "set it and forget it" operation (de-powering the Picomotor does not result in any micromotion), small backlash (typically 1–2 microsteps), compactness, vacuum compatibility, and economic pricing/availability. Their main disadvantage is a load-dependent step size, which greatly diminishes their utility as bi-directional scanning devices. Closed-loop Picomotors are available which compensate for this deficiency, but are less compact and a great deal more expensive.

Our Picomotors have performed well for us as unidirectional scanners in the axial (z) direction and as coarse positioners in the transverse (x, y) and tip/tilt directions. Indeed, contrary to our original intention, we have relied heavily on the use of a Picomotor to translate the membrane in fine steps along the cavity axis. In doing so, we have become well acquainted with the load hysteresis

of these devices. We have found, in particular, that the step size for our stage varies between 20–26 nm and is typically $\sim 20\%$ different between the backward and forward directions. A HeNe fringe formed between the membrane chip and the back surface of one of the cavity mirrors (see Figure 5.7) has been used to verify the unidirectional step repeatability of the Picomotor over several fringes. For an example of this measurement, see Figure 6.4 in Chapter 5.

5.2.3.2 Membrane Holder

The concept for the membrane holder pictured in Figures 5.3 and 5.4 and derives from considerable trial and error in the process of learning to mount chips containing high-Q suspended films, as discussed in Section 4.7. As discussed in that section, we found that rigidly attaching the chip to a surface tended to reduce (in some cases significantly) the mechanical quality of the membrane, and that this reduction could be minimized by making the attachment points small and as far from membrane as as possible. Aside from minimizing contact area with the chip, the membrane holder needed to provide optical access, convenient integration into the nanopositioning system, and a piezo for fine positioning or resonant driving of the piezo. Two iterations of the design are shown in Figure 5.4. The currently used jig consists of a 1" x 1" stainless steel cylinder machined to slide over the cavity mirrors as pictured. The rear of the 1" cylinder secures into the kinematic mount. The front end is fitted with a 1-mm-thick monolithic piezoelectric plate (Ferroperm Pz27), which has been slotted on a diamond band saw to provide three-point contact with a 5 mm membrane chip. The chip is secured with three small dabs of commercial-grade Krazy Glue (low viscosity cyanoacrylic adhesives allow for rigid bonds with small contact area), which we found to reduce the quality factor of a 50 nm$\times 500\,\mu$m$\times 500\,\mu$m membrane by $\sim$ 30% (see Section 4.7.1). The piezo plate has an unloaded resonance frequency of $\sim$ 1 MHz and a travel range of $\sim$1 nm/(10 V). We unfortunately lost the ground electrical lead on this jig while opening the chamber, rendering it useless for long-range displacement or for applying a calibrated high-frequency dither to the membrane position (in the latter case due to capacitive pickup). However, it is still useful for ring-down excitation. A second-generation design, which has very recently been integrated, replaces the stainless steel with Macor for better electrical isolation and incorporates an additional ultra-compact, long-range piezoelectric ring stack from Noliac (20 nm/V, model CMAR05).

piezo + membrane,
3 pt adhesive contact

kinematic
mount

cavity mirror

upgrade: macor
+ long range pzt
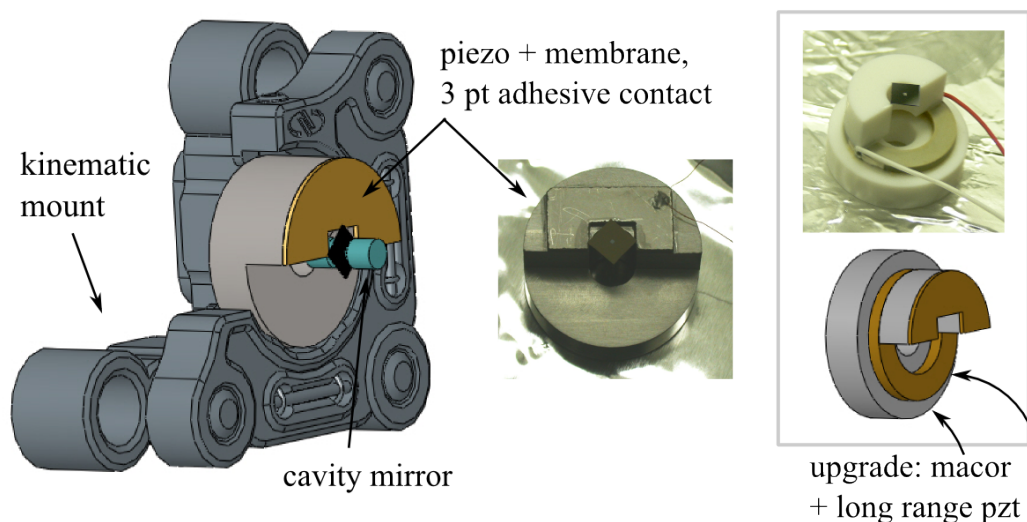
Figure 5.4: Schematic of the membrane chip holder.

5.3 Hardware: Vibration Isolation, Vacuum System, and Optical Layout

5.3.1 Vibration Isolation

The cavity and nanopositioning system sit on top of a dedicated single-stage vibration isolation stack (single rigid platform, single tier of rubber pads) within the vacuum chamber. This is an important component, because the relatively large (compared to the cavity) nanopositioning system results in substantial vibration of the membrane with respect to the end-mirrors. This vibration was as large as ~ 5 nm at seismic frequencies (< 100 Hz) in the first iteration of the experiment, which forced us to operate at a moderate finesse of 10^4 (where we still operate) in order to lock the cavity. The VIS was carefully redesigned and characterized in December of 2008, after an accidental collision between the membrane and one of the end-mirrors (a runaway for-loop in our Picomotor software) led to our re-opening the vacuum chamber. Upon opening the chamber, we verified that low-frequency vibration noise in our cavity lock agreed qualitatively well with the result of a vertical accelerometer measurement on top of the VIS. We then found that, although the entire vacuum chamber sits atop a floating optical table, this vibration was in fact little improved over the seismic acceleration of the laboratory floor. The reasons for this were two-fold: (1) the table felt and sounded like it was floating, but in fact was still picking up seismic noise due to friction between the shaft and housing of one of the pneumatic legs, and that (2) our first VIS, which was designed to eliminate acoustic pickup from the chamber walls, exhibited a broad ~ 100 Hz resonance in the undiminished seismic band. We fixed the first problem by carefully re-balancing the table while monitoring the accelerometer. The second problem was improved upon by increasing the mass of the VIS plate

and by replacing our Viton isolation pads with a combination of soft, under-damped RTV rubber in series with stiff, highly over-damped "NewDamp" elastomer from Newport. The end result was a transfer function with a corner frequency of 20 Hz and a quality factor of ~ 3. We refer the reader to [76] for a useful discussion of the merits of dynamically damped compound springs in the context of vibration isolation. A sketch of our VIS and an illustrative compilation of accelerometer traces is shown in Figure 5.5. Gray, black, pink, red, and green traces correspond to acceleration atop the laboratory floor, optical table before re-balancing, optical table after re-balancing, original VIS (after re-balancing), and new VIS, respectively.
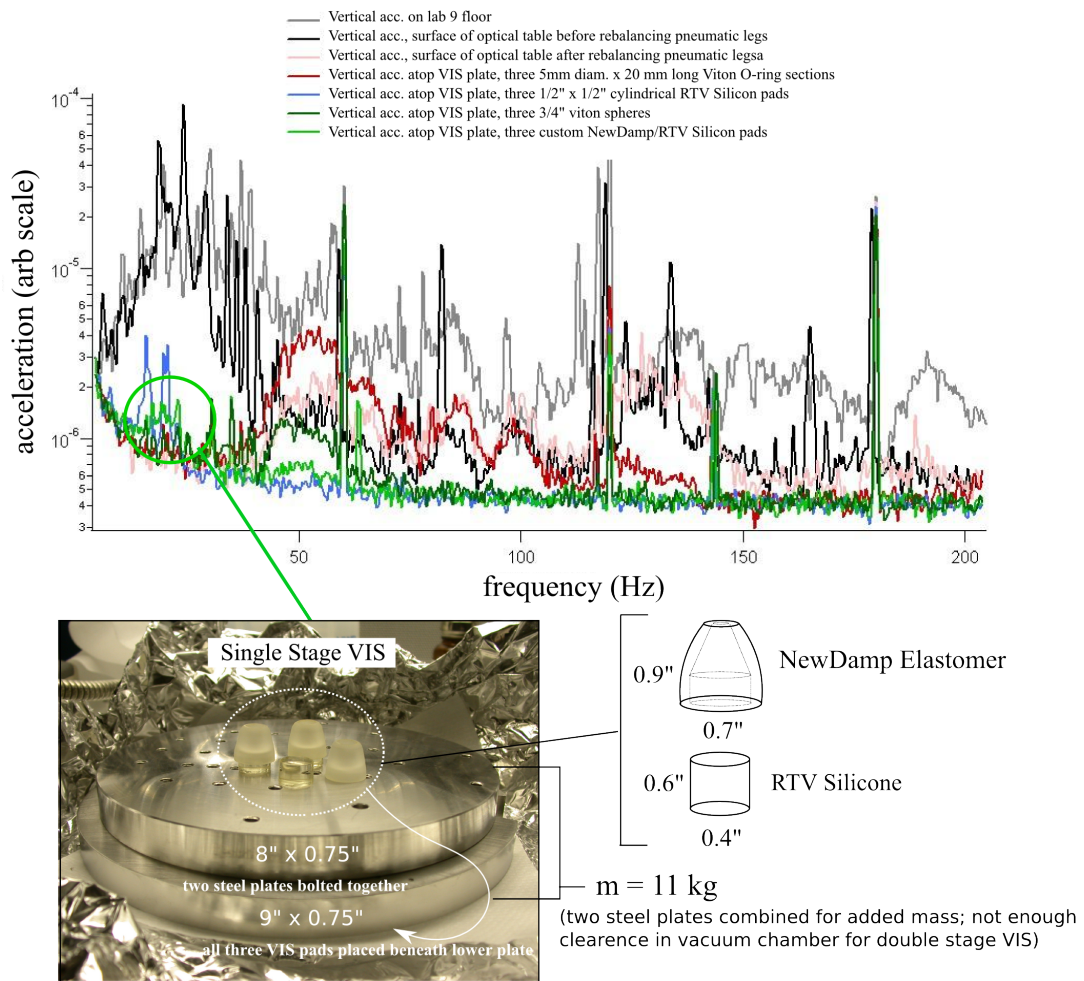
Figure 5.5: VIS and compilation of accelerometer data. Gray, black, pink, red, and green traces correspond to acceleration atop the laboratory floor, optical table before re-balancing, optical table after re-balancing, original VIS (after rebalancing), and new VIS, respectively.

5.3.2 Vacuum System

The primary functions of the vacuum system in this experiment are, in order of importance (1) HV compatibility ($< 10^{-6}$ mbar), (2) large enough size to accommodate our nanopositioning system and VIS, but small enough to permit a vibration-free pump system, and (3) anti-reflective optical access for a NIR laser beam used to interrogate the cavity. To meet these goals, we again borrowed equipment from our atomic physics experiment, which has much more demanding vacuum requirements. While perusing the lab, we discovered lying in the basement a large, cylindrical, stainless steel vacuum chamber with Conflat fittings, formerly built for an atomic beam imaging experiment in the mid 1990s [77]. The chamber, pictured in Figure 5.6, was in pristine condition despite its long hiatus, so we decided to give it a try. We were initially concerned by its size — the 12" (diameter) x 8" (height) inner dimensions are in fact overkill for our requirements — however, the large surface area ($A \approx 0.3$ m^2) is compensated for by the ability to directly mate a $S = 55$ liter/s ion pump (Varian VacIon Plus Starcell) to one of the 6" side flanges, thereby minimizing conduction loss. Using a conservative stainless steel outgassing rate of $q = 10^{-9}$ mbar liters/s/cm^2, we estimate a rough base pressure of $P_f = qA/S \approx 5 \times 10^{-8}$ mbar for the chamber alone [78].

Before assembly, the main body of the chamber was prepped by serially hand wiping with acetone and methanol. The same procedure was followed for the translation stage (which is not rated as HV compatible) and the Picomotors. Cavity, vibration isolation, and flange components, including feedthroughs and viewports, were cleaned according to the thorough description provided in Kevin Birnbaum's thesis [67]. The chamber was first closed in November of 2008. After roughing overnight with a turbopump and approximately one week under the ion-pump, we achieved a pressure of $< 10^{-6}$ mbar in the vicinity of the ion pump as inferred from the pump current. The chamber was re-cycled several times in December 2008 and January 2009, and has been closed until only recently (June 2011). The base pressure that had been achieved over that period was $\sim 8 \times 10^{-7}$ mbar, as inferred from the ion pump current.

Please note that the viewports used on this chamber were also borrowed from our CQED experiment; they have an AR coating from Advanced Thin Films that extends from 800–950 nm ($< 1\%$) and is centered at 850 nm ($\sim 0.1\%$), corresponding to the D2 transition of cesium.

5.3.3 Optical Layout: Locking and Probing the Cavity at Variable Detuning

The optical layout for the experiments described in Chapters 6-9 has evolved substantially over the last two and a half years. Its basic architecture remains unchanged, however, and can be summarized in terms of its primary functions. First, to interrogate the optical cavity, we need to mode-match it with the output of a laser operating at a wavelength near the coating center of the cavity mirrors.
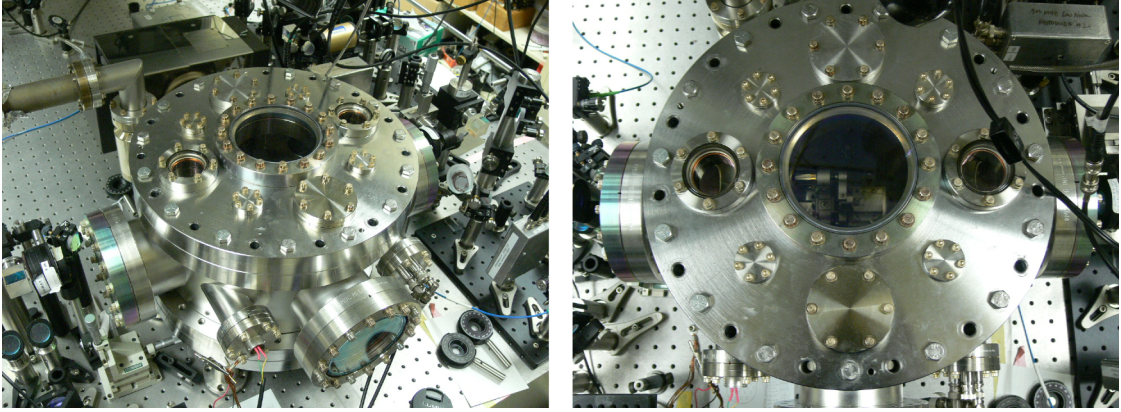
Figure 5.6: Vacuum system for the first-generation optomechanics experiment. A base pressure of $\approx$ 10^{-7} has been achieved using a 55 liter/sec ion pump. The chamber is large enough to accommodate a 11 kg, 9" diameter x 1.5" thickness steel plate for vibration isolation of the nanopositioning system. Cavity, membrane holder, and kinematic mount are dimly visible through the 6" top viewport in the right photo.

The cavity resonance frequency must be then be referenced to the laser (or vice-versa) by a means which allows us to precisely control the detuning and power of the drive field. Finally, in order to generate the lock signal and to make measurements of the membrane's motion, the phase and amplitude of the fields reflected and/or transmitted from the cavity must be monitored using a set of photodetectors. Because the details of the layout have changed, I here focus on the scheme used to obtain the initial cooling results described in Chapter 9. Modifications made for the noise subtraction experiment discussed in Chapter 10 are referred to that chapter.

5.3.3.1   Two-Probe Scheme

A sketch of the basic optical layout is shown in Figure 5.7. For the experiments described in Chapters 6–9, we use a simple two-probe scheme wherein a weak ($<$ 100 nW) "locking" beam is used as a reference to stabilize the cavity length and a second, stronger (1–100 μW) "science" beam is used to drive the cavity at a variable detuning. Both beams are derived a from a single laser using a broadband NIR polarization beamsplitter. For the laser source, we have primarily iterated between a homebrew external cavity diode laser operating at 935 nm (diode from Toptica) and a titanium-sapphire laser operating at 810 nm (kit laser from Schwarz-Electro Optics). After frequency manipulation as described below, both beams are mode-cleaned by passing though a 5 μm PM fiber-based broadband EOM (EOSpace). Each beam then passes through a telescope before being recombined at the input of the optical cavity using a second PBS. A broadband-AR-coated, 300 mm singlet lens is used to focus the beams into the cavity. A mode-matching efficiency as high as $\sim$ 70% has been achieved for the TEM$_{00}$ cavity mode with the membrane in the middle. By rotating the input beam polarizations onto the polarization eigenmodes of the cavity, we can
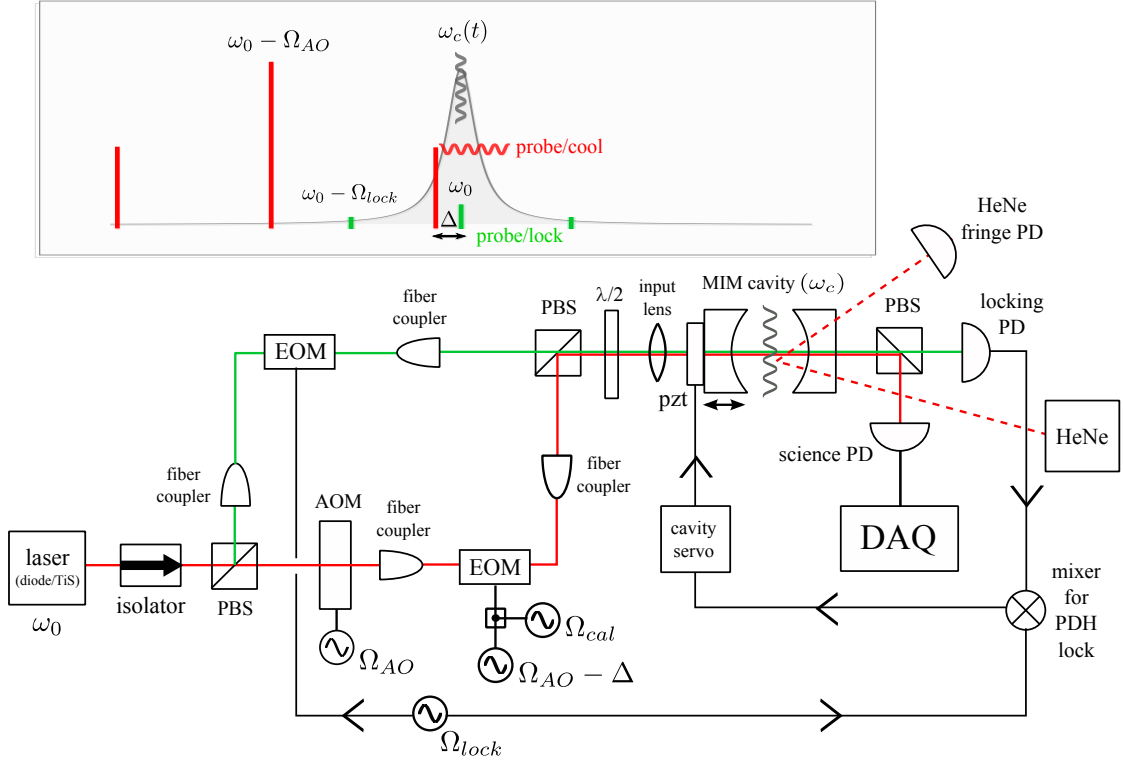
Figure 5.7: Schematic of the optical layout for experiments described in Chapters 6–9. A single laser is split into two beams propagating along separate paths. One of the beams ("locking" beam, green) is modulated using an EOM in order to generate a Pound-Drever-Hall-type error signal in transmission. 10–100 nW of locking light are transmitted from the (symmetric) cavity on resonance, and the error signal is used as a reference to lock the cavity via feedback to one of the end-mirror piezos. The second beam ("science" beam, red) is detuned from the locking beam using an AOM in series with an EOM. This beam enters the cavity at variable detuning and is used as both the cooling beam and the displacement probe, as elaborated in Chapter 8 and Chapter 9. The two beams are isolated by polarization and aligned along orthogonal polarization axes of the cavity.

separate these two beams with an extinction ratio of better than 1% using a PBS at the output of the cavity (in practice, this requires a sequence of $\lambda/2, \lambda/4$ plates before the output PBS). Beyond the output PBS, each beam is directed to a fast, low-noise commercial photodetector (New Focus 1801).

Detuning between the science and locking beam is achieved using a sequence of acousto- and electro-optic modulators, as shown in Figure 5.7. The science beam first receives a nominal red detuning of $\Omega_{AO}/2\pi = 300 - -400$ MHz $gg\kappa/2\pi$ by sending it though a free-space AOM (Isomet) in a double-pass configuration. The beam then passes through a broadband fiber EOM (EOSpace), which generates sidebands with a frequency spacing of $\Omega_{AO} - \Delta$. The first-order blue sideband is detuned by $-\Delta$ from the locking beam, to which the cavity resonance frequency is locked as described below. The rest of the sidebands are far detuned from the cavity by $m\Omega_{AO} \pm \Delta >> \kappa$ (m = 1,2...). We use the near-detuned sideband of the science beam to perform the cooling and

displacement measurement described in Chapter 8. The utility of this technique is that it allows us to independently control the detuning and the input power via the EO modulation frequency and depth, respectively, without adjusting the cavity length. The main disadvantage is that the majority of the input field is directly reflected from the cavity.

5.3.3.2 Lock Error Signal and Displacement Measurement

Generating a cavity lock error signal and monitoring the motion of the membrane are essentially equivalent tasks; both are obtained from a measurement of the fluctuating cavity detuning. In the layout as pictured, we use two techniques to monitor the cavity detuning: (1) we monitor the transmission of the detuned science beam; (2) we monitor the phase of the transmitted locking beam.

Technique (1) is used to measure the displacement of the membrane and the end-mirrors as described in Chapter 8, and consists of directly monitoring the power of the detuned science beam on the science photodetector. To calibrate the resulting photocurrent signal, the science beam is phase modulated with a single tone at a calibrated modulation depth. This is done by adding a second tone (via a power splitter) to the driver of the EO in the science beam path.

Technique (2) is used to generate the lock error signal. This signal is obtained by a self-heterodyne technique: the locking beam is phase modulated with sidebands $\Omega_{lock} \sim 2\kappa$ and the photosignal produced on the locking photodetector is demodulated at the same frequency using an RF mixer (Minicircuits ZSC-2-1). The signal produced at the IF port of the mixer is similar to the PDH error signal [54], and has the advantage over reflection PDH of being free from excess background due to light that is not mode-matched to the cavity. We have used this technique to successfully lock the $\mathcal{F} \sim 4 \times 10^5$ cavity in our CQED experiment with as little as 8 nW of transmitted power [72]. For the MIM cavity operated at $\mathcal{F} \sim 10^4$, we have found it necessary to use larger optical powers to maintain a stable lock. Typical values of power on the locking photodetector and the modulation depth of the locking EO are $\sim$ 50 nW and $\beta_{lock} \sim 1$, respectively. More details on the locking scheme are provided below.

5.3.3.3 Stabilizing the MIM System

For the standard Fabry-Perot cavity, changing the absolute frequency of the input laser ω_0 (used to generate the science and locking beams) by a multiple of the cavity FSR does not affect the optomechanical coupling strength of the end-mirror as long as $\Delta\omega_0/2\pi << FSR$. Rather (because the optomechanical interaction is a Raman process), the dynamics are only sensitive to the relative detuning Δ between science beam and the cavity resonance frequency, $\omega_c/2\pi = m \times FSR$. For a fixed input power, the task of stabilizing the system consists of just adjusting the cavity length or the laser frequency in order to maintain a stable detuning. The MIM system, however, has an extra degree of freedom that must be accounted for, since the optomechanical coupling of the membrane

g varies as a function of its position z_m with respect to one of the end-mirrors (see Figure 3.1). Because of this extra degree of freedom, we ideally must stabilize all three variables $\{\Delta, L, z_m\}$ to maintain a constant value for g. Equivalently, we must stabilize both Δ and the phase of the intracavity standing wave at the position of the membrane: $\theta = 2\omega_0 z_m/c = \omega_0/FSR \times z_m/L$. For a short cavity, it turns out that we can meet these two requirements using a simplified scheme.

First, we lock the cavity length to the laser frequency, ω_0. This is the preferred method for a short cavity, since the cavity FSR = 202 GHz is much larger than the ~ 10 GHz mode-hop free range of the lasers used in the experiment. In the experiments described in Chapters 6-9, we use the error signal derived from the transmitted locking field to apply feedback to the piezo beneath one of the end mirrors. The feedback signal is obtained by passing the raw error signal (mixer IF port) through an inverted pre-amplifier (Stanford Research Systems SR560), a simple op-amp integrator, and a single-pole 3 kHz low-pass filter (to reduce the servo gain at the first piezo resonance, ≈ 10 kHz). The unity gain of the feedback loop is ~ 100 Hz. Stabilizing the laser-cavity detuning of the cavity to within 10% of the linewidth (FWHM) requires that the effective length noise of the cavity be reduced to $\delta L = 10\% \times \lambda/2\mathcal{F} \approx 5$ pm $\times (10^4/\mathcal{F})$, which is within an order of magnitude of the room-temperature Brownian displacement (rms) for the fundamental mode of the 50 nm x 500 μm x 500 μm membrane used in the initial cooling experiment (Chapter 9). This represents an interesting challenge that must be addressed in the future if a higher finesse cavity is used.

The second task is to stabilize θ. Here, we can make use of the fact that because the cavity is short, drift in laser frequency $\delta\omega_0$ (typically $\ll$ GHz) is passively much smaller than the cavity FSR. By locking the cavity resonance to the laser frequency, the change in phase at position z_m then becomes $\delta\theta = \delta\omega_0/FSR \times z_m/L + \omega_0/FSR \times \delta z_m/2L \approx 4\pi\delta z_m/\lambda$. For a thin membrane ($|r_m|^2 \ll 1$), the fractional change in the optomechanical coupling $g_m \approx 2|r_m|g_0\sin(\theta)$ is given by $\delta g_m/g_m \approx \cot(\theta)\delta\theta$, so that at the position of maximal ($g_m = 2|r_m|g_0$) and minimal ($g_m = 0$) coupling the first-order sensitivity is $\delta g_m/g_m = 0$ and $4\pi\delta z_m/\lambda$, respectively. For many applications, particularly where we operate at g_{max}, we have found it sufficient to allow the absolute frequency of the laser to drift while the cavity is locked, and to make measurements on a timescale for which $\delta z_m/\lambda \ll 1$ (~ 10 minutes to an hour when the membrane is at a point of maximal coupling, depending on temperature stability in the lab). This is the approach that has been taken thus far.

We have also set up a HeNe fringe at the exit mirror substrate and the membrane chip in order to calibrate the Picomotors (see Figure 6.4) and to monitor drift of the membrane position. We hoped to use this fringe to perform a slow feedback loop to stabilize the membrane position to within ~ 10 nm. However, currently this application will have to wait until the damaged piezo lead on our membrane chip holder is replaced.

Chapter 6

Linear Optical Properties of the MIM System: Measurements

In this chapter I discuss how steady-state optical properties of our MIM system have been characterized in the lab, drawing heavily from the 1D formalism provided in the Chapter 3. With the exception of the first section (in which real index of the membrane is determined), all of the measurements described below were carried out in the autumn of 2008 through the summer of 2009, in preparation for the optomechanical cooling experiment described in Chapter 9. The ordering of the measurements is altered to follow the structure of chapter 3. In particular, I describe (1) the real index of refraction and thickness of the film, (2) the transmission and absorption losses of the cavity end-mirrors (via the finesse of the bare Fabry-Perot resonator), (3) optomechanical coupling of a membrane placed within the Fabry-Perot, and (4) reflectivity and absorption of the membrane as inferred from the linewidth and transmission of the MIM cavity.

6.1 Membrane Reflectivity and Thickness

Si_3N_4 membranes supplied to us by Norcada (see Chapter 4) are specified according to square dimensions (width $w_m = 0.25$, 0.5, and 1 mm) and thickness ($d_m = 30$, 50, and 100 nm). For some time we have relied on these factory specifications, along with standard ellipsometric measurements of the real index of LPCVD Si_3N_4, to infer their mass and reflectivity [34]. The latter is important for estimating the optomechanical coupling. The former is important for understanding the mechanical properties of the system (e.g., the spectrum of vibrational frequencies). Whereas SEM images have confirmed that w_m is consistent with the factory specification at the $\sim 1\%$ level, a simple reflectivity measurement suggests that the actual thickness of the films can differ from the factory specified value by as much as 30%. This realization, coupled with substantial efforts to process our own films in the clean-room facility at the Caltech KNI and in Oskar Painter's laboratory (efforts led by Painter graduate student Richard Norte and our post-doc Kang-Kuen Ni), have reinforced the need
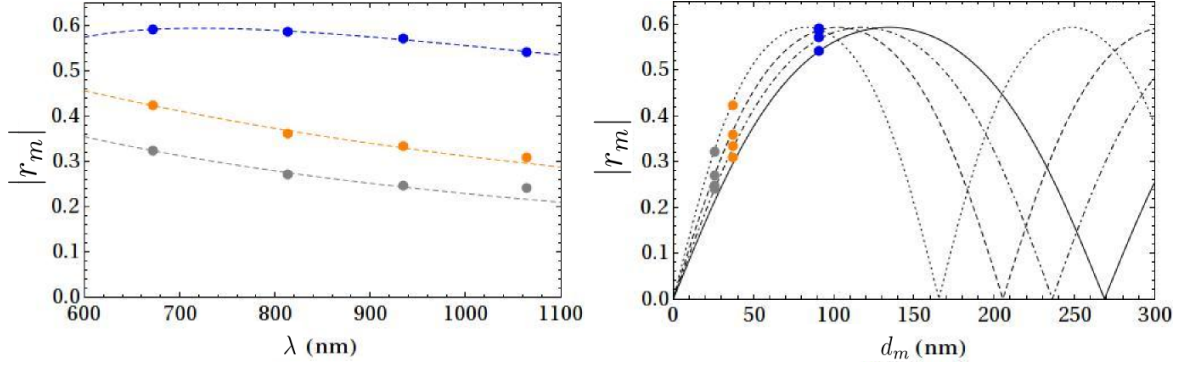
Figure 6.1: Reflectivity of Si_3N_4 membranes from Norcada for three nominal thicknesses (gray = 30 nm, orange = 50 nm, blue = 100 nm). The maximum value, $|r_m|^{max} \approx 0.593$ is consistent with a refractive index of $|n_m| = 1.98$. Assuming a constant index for measurement wavelengths $\lambda = \{672$ nm, 813 nm, 935 nm, 1064 nm$\}$ gives a result consistent with $d_m = \{26$ nm, 37 nm, 91 nm$\}$. The curves at left are a qualitative fit to data for different d_m using $|r_m|$ vs. λ from Eq. 3.4 with fixed $|n_m|$. The curves at right are a qualitative fit to data for different d_m using $|r_m|$ vs. d_m from Eq. 3.4 with constant $|n_m|$ and the four different λ.

to characterize their optical properties from scratch.

Fortunately, there are variety of simple ways to measure the thickness and refractive index of a thin film. If the index of refraction, n_m of the film is known precisely at a specific wavelength, then a direct measurement of reflectivity at this wavelength gives the film thickness, and vice-versa. If neither is known exactly, then one can vary both, and use the fact that at a given wavelength the maximum reflectivity is independent of film thickness for negligible loss. For a low-loss ($Im[n_m] <<$ 1) film embedded in air/vacuum, this value is $|r_m|^{max} = \frac{|n_m|^2 - 1}{|n_m|^2 + 1}$ (see Section 3.1.1). This is the basic principle behind ellipsometry.

We have conducted our own thickness/index measurements by directly measuring power transmission T_m through the film at normal incidence. The measurement is made by focusing a laser beam through a membrane and onto a photodetector (Thorlabs PDA55). The membrane chip is secured to a flipper mirror mount so that measurements of input and transmitted power can be iterated. The laser source is switched between 670 nm (Oz Optics box diode), 813 nm (Schwarz-Optics Ti-Sapph), 935 nm (Toptica diode), and 1064 nm (Innolight YAG). Each measurement is repeated for three membranes with different nominal thicknesses: 30, 50, and 100 nm.

Results for this sequence of measurements are shown in Figure 6.1. Solid circles correspond to measured reflectivity, $|r_m| = \sqrt{1 - T_m}$. Lines correspond to a model which assumes a constant real index from 670 nm –1064 nm (2% variation is expected from standard ellipsometric data [34]). From the reflectivity data for the thickest film, we obtain a maximum value of $|r_m|^{max} \approx 0.593$ near 750 nm. This is consistent a real index of 1.98. We fix this value and the thickness in the formula for $|r_m|$ (Eq. 3.4) to obtain the qualitative fits shown. The model is consistent with membrane thicknesses of 26 nm, 37 nm, and 91 nm, respectively. An independent measurement of the "50 nm" membrane

using the Filmetrix machine at the Caltech KNI obtains a thickness value of 38 nm. The Filmetrix measurement appears to be repeatable to within ± 3 nm for several membranes drawn from the same batch sent from Norcada.

6.2 Characterizing the End-Mirrors: Cavity Linewidth and Finesse

A description of the end-mirror dielectric coating was given in the preceding chapter (Section 3.8). In the group these mirrors are commonly referred to as D1306, in reference to a particular class of "supermirror" coatings that were developed for our CQED project [65] first by Research Electro-Optics, Inc. (REO), and later by Advanced Thin Films, Inc. (ATF). Each D1306 mirror consists of 35 bi-layers of alternating high-index n_H and low-index n_L material deposited on a superpolished Bk7 glass substrate. Each coating layer has a thickness of $\lambda/4n_{H,L}$ for a common "center" wavelength of ≈ 850 nm. Based on a decade-long history of measurements in the Kimble group, we expect these coatings to have maximum reflectivity of $R_{mirror} \approx 99.9985\%$ ($T \approx 15$ ppm) at their center wavelength. As reported in [37], the measured reflectivity is in close agreement with the design value predicted using the transfer matrix approach. Two discrepancies are of importance for our MIM system. First of all, the D1306 center wavelength has been observed to vary by as much as 10 nm between coating runs. This has a large impact on the reflectivity obtained at wavelengths away from the coating center, where we presently operate. Second — as is true for all supermirrors — minute scattering/absorption loss can dominate over mirror transmission unless care is taken while handling the mirrors. Measured loss depends on the details of the reflected laser beam, including its size and location on the mirror. For the D1306 run, the factory target loss was < 3 ppm (associated with coating absorption and imperfections in the supermirror polish). With care and a little luck, this level of absorption has been observed in the lab. However, for most cavities built with D1306 mirrors, including the one in this experiment, the loss is closer to 5 ppm, associated with minor dust particles and scratches on the mirror surface.

We have characterized the mirrors used in our MIM cavity using a standard technique: with the membrane removed, we measure the finesse of the cavity as a function of wavelength. The finesse is inferred from the ratio of the cavity free spectral range $FSR = c/2L$ to the linewidth $\gamma = 2\kappa$ (FWHM) of the cavity transmission function, $|t_{FP}|^2$ (see Eq. 3.14). For our symmetric cavity ($T_1 = T_2 \equiv T_{mirror}$), the finesse is related to the mirror transmission and loss (see Eq. 3.16):

$$\mathcal{F} = \frac{FSR}{\gamma/2\pi} = \frac{2\pi}{T_{mirror} + \delta_1 + \delta_2}. \tag{6.1}$$

The cavity FSR is obtained from the cavity length. We infer a value of $\{L, FSR\} = \{742\ \mu\text{m}, 202\ \text{GHz}\}$
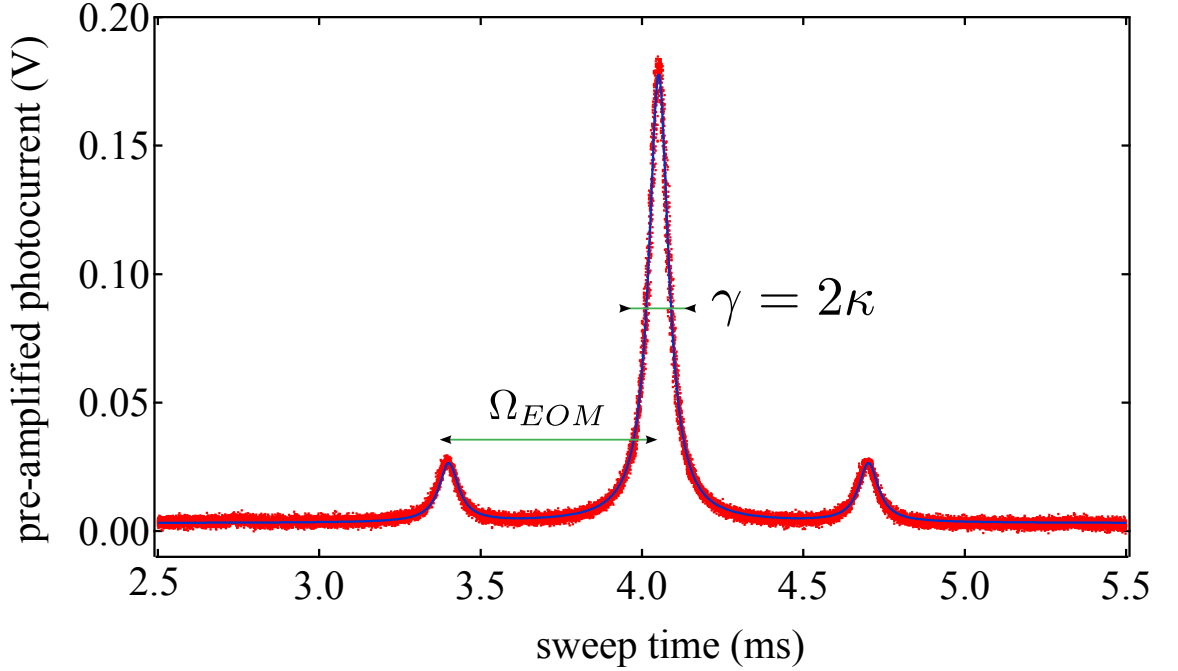
Figure 6.2: Cavity linewidth measurement: the intensity of the transmitted field is measured as a function of time while slowly ($<< 1/\gamma$) translating the end-mirror through resonance. FM sidebands generated by an EOM are used to calibrate the time trace. Data is fit to a triple Lorentzian with $FWHM = \gamma/2\pi \equiv (c/2L)/\mathcal{F}$. Each point in Figure 6.6 corresponds to a the average of a set linewidth measurements made as pictured above. In this figure, $\Omega_{EOM}/2\pi = 150$ MHz and $\gamma/2\pi = 17$ MHz.

from the factory-specified radius of curvature of the mirror substrate, $R_s = 5.0$ cm, the measured 11.0 GHz difference between the resonance frequency of the TEM_{01} and TEM_{00} cavity modes, and the formula for transverse mode splitting provided in [31] (see also Section 5.2.2.1):

$$\omega_c^{00} - \omega_c^{01} = \cos^{-1}\left(1 - \frac{L}{R_s}\right) \times \frac{c}{L}, \tag{6.2}$$

where ω_c^{00} and ω_c^{01} are the resonance frequencies of the TEM_{00} and TEM_{01} cavity modes, respectively.

To measure the cavity linewidth, we monitor the transmitted power of the cavity while sweeping the cavity length across resonance for the TEM_{00} cavity mode. An example of the linewidth measurement is shown in Figure 6.2. Here the cavity was driven with an input power of $\sim 1~\mu$W and the transmission was monitored using a fast photodiode (NF 1801, see layout in Figure 5.7) located after the exit mirror. The probe is slowly swept through resonance (~ 1 ms $\gg 1/\gamma$) by applying a sinusoidal voltage to the shear piezo beneath one of the end-mirrors (Figure 5.2). A broadband fiber EOM (EOSpace) is used to generate frequency sidebands on the probe at ± 150 MHz; this provides a convenient ruler against which the time axis of the photosignal can be calibrated. The calibrated
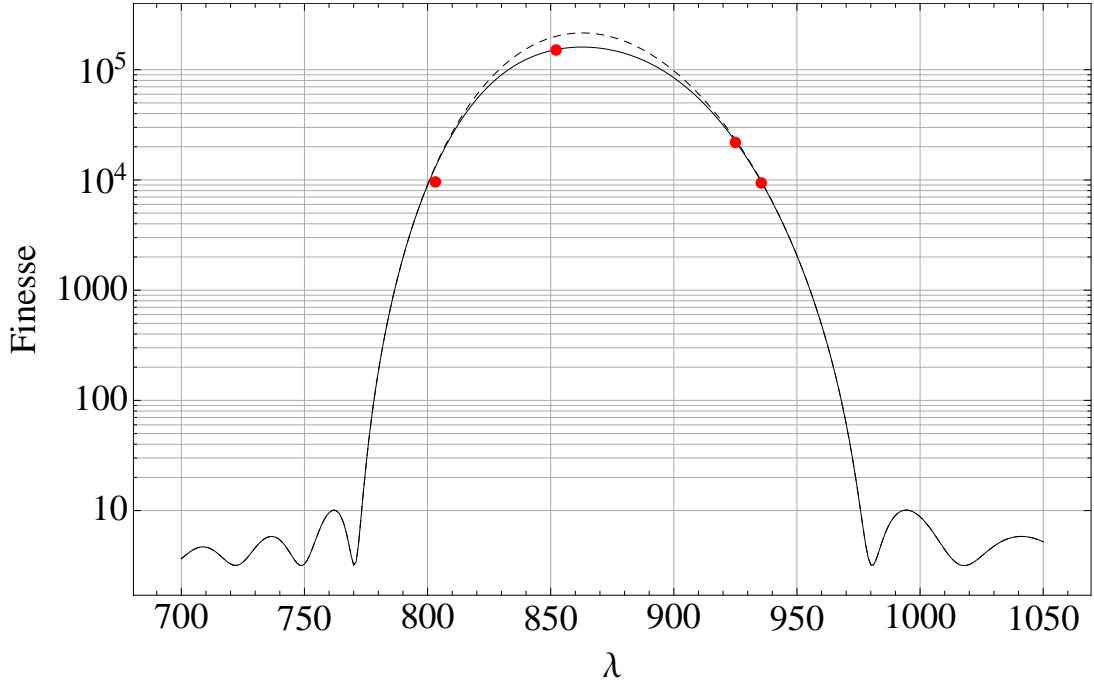
Figure 6.3: D1306 coating curve measurement. Cavity finesse measurements at four wavelengths are here compared to a model in which each mirror has an identical D1306 coating. Coating center wavelength and SA loss are used as free parameters to obtain a qualitative match. Results are consistent with $\lambda = 862.8$ nm and $\delta_1 + \delta_2 = 10$ ppm. Solid and dashed curves correspond to models with and without loss, respectively.

time trace is fit to a symmetric triple Lorentzian in order to extract the linewidth.

By comparing the finesse obtained at various wavelengths, we can generate a model of the coating curve which includes both losses and a shifted coating center. A plot of data and model is shown in Figure 6.3. Here we have measured $\mathcal{F}$ vs. λ for four well-separated wavelengths accessible with a diode laser (910 nm, 935 nm) and a ti-sapphire laser (810 nm, 850 nm). To generate the model, we assume the coating matrix model described in Section 3.8 but allow the coating thickness to deviate from $\lambda/4$ (retaining the full form for M_{plate} in Eq. 3.2). The result is consistent with a coating center of 862.8 nm and an average mirror loss of $(\delta_1 + \delta_2)/2 = 5$ ppm. At 862.8 nm, the calculated D1306 transmission is 14.6 ppm, enabling a loss-limited finesse of $\mathcal{F} \approx 1.6 \times 10^5$. At the wavelengths used in the experiment, 810 nm and 935 nm, the mirror transmission is substantially larger $T_{mirror} \sim 300$ ppm, corresponding to $\mathcal{F} \sim 10^4$. In particular at 935.5 nm, we obtain $\mathcal{F} = 9200$. At this wavelength we usually ignore the mirror losses when characterizing the MIM system.

6.3 Optomechanical Coupling of the Membrane

The procedure for directly measuring $g_m = d\omega_c/dz_m$, the optomechanical coupling of the membrane (see Section 3.3.1), consists of translating the membrane through a distance of $\lambda/2$ while monitoring

the cavity resonance frequency. Our initial efforts at this measurement were frustrated by the realization that (1) a lead on the piezo located behind the membrane chip had been dislodged and that (2) its backup, a single shear piezo placed beneath both the cavity end-mirrors, produced a substantial cavity length change in addition to cavity displacement when driven (there's no such thing as a purely shear-mode piezo!). After some deliberation, we decided to sacrifice continuous membrane position tunability rather than reopen the vacuum chamber. Since then, we have resorted to using a Picomotor on the nano-positioning stage to translate the membrane along the cavity axis. Large Picomotor step size ($\approx$ 30 nm) and small cavity length (large $FSR \approx$ 200 GHz) make a direct measurement of g_m challenging in the current experiment: to wit, for a 50 nm film with $|n_m| = 2.0$ ($|r_m| = 0.42$), one predicts $g_m^{max}/2\pi = 2|r_m|FSR/(\lambda/2) \approx 11$ GHz/(30nm), which is on the order of the mode-hop-free range of our tunable external cavity diode laser (ECDL). The change in resonance frequency when the membrane is placed at an antinode compared to a node is ≈ 56 GHz, which must currently be accessed by a separate laser.

Nevertheless, we have occasionally and laboriously measured g_m by stepping the membrane along the cavity axis and following the cavity resonance by manually tuning the wavelength of the ECDL. A modified procedure is necessary to keep the frequency excursion within the mode-hop free range of the laser. The procedure consists of (1) recording the nominal (cavity resonant) laser frequency, (2) displacing the membrane by a single Picomotor step, Δz_{pm}, (3) manually adjusting the laser frequency in order to bring the cavity back into resonance (via drive current and cavity length of the ECDL), recording the laser frequenct shift, $\Delta \omega_c$, and then returning the laser frequency to its original, now off-resonant value, (4) translating the input mirror to bring the cavity into resonance, (5) repeat. By means of this stroboscopic technique, we can trace $g_m \approx \Delta \omega_c / \Delta z_{pm}$ vs. z_{pm} through its minimum and maximum value, which can be compared to the expected value of $2|r_m|g_0$.

The results of one such measurement are shown in Figure 6.4. The frequency of the laser was monitored using a commercial optical spectrometer with 100 MHz resolution (Burleigh WA-1600). The step size, Δz_{pm}, of the Picomotor is independently calibrated by monitoring a HeNe fringe formed between the exit mirror and the silicon membrane chip (inset). The measured dependence of g_m on z_m can be modeled directly using the matrix methods described in Section 3.3.1. The data is qualitatively consistent with the model shown (dashed red curve). The model assumes that the membrane is at the center of a 742 μm cavity, has a real index value of $|n_m| = 2.0$, and is 50 nm thick ($|r_m| = 0.42$).

6.4   Characterization of Membrane Optical Absorption

Optical absorption in the membrane sets a fundamental limit on the achievable finesse and a practical limit on the intracavity power achievable in the MIM system. Consequently, considerable effort has

Picomotor calibration
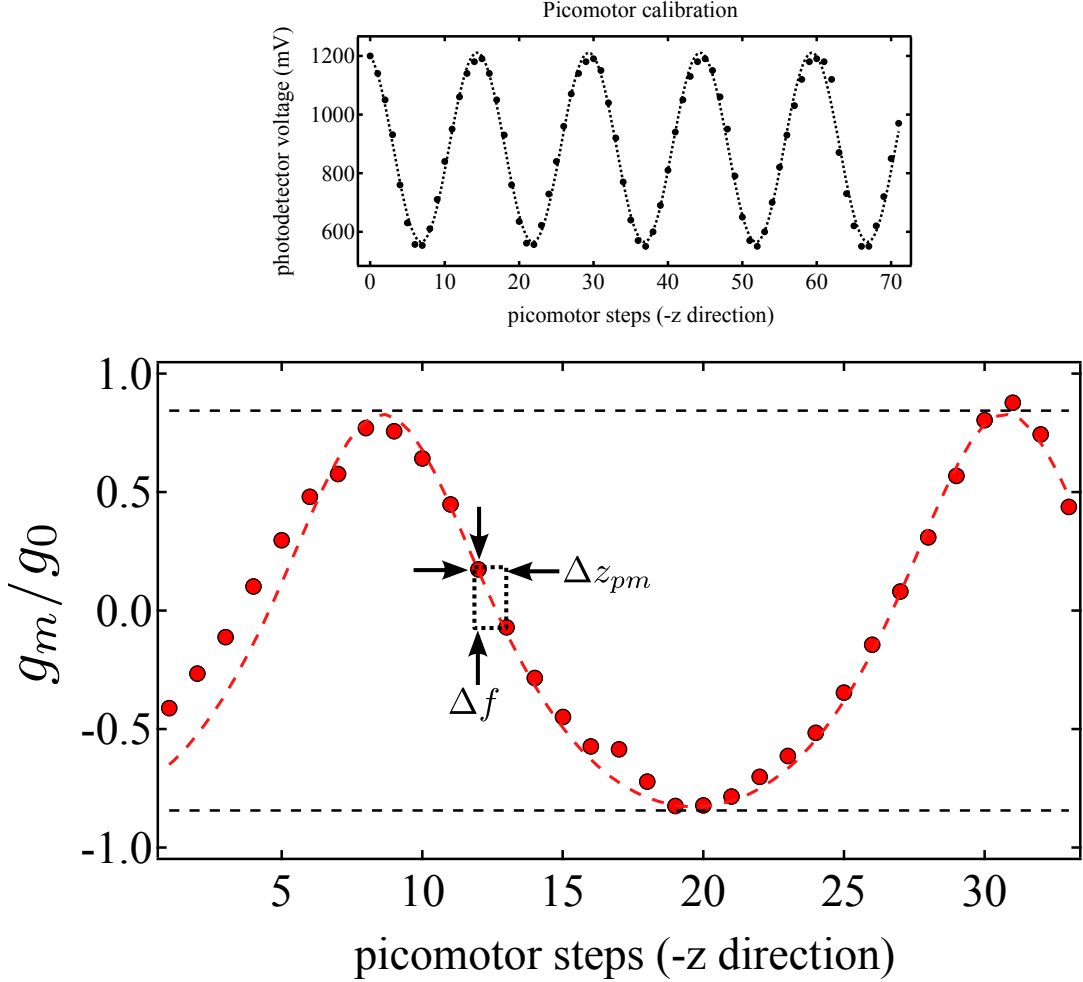
Figure 6.4: Measurement of optomechanical coupling. The membrane is translated along the cavity axis using a piezo motor with a step size of $\Delta z_{pm} \approx 21.1$ nm (calibrated with HeNe as shown in inset). After each step, the frequency of a tunable probe laser is adjusted by Δf in order to keep it in resonance with the cavity. Δf is measured using an optical spectrometer, giving $g_m/2\pi \approx \Delta f/\Delta z_{pm}$. The laser frequency then is returned to its original value, the cavity length is adjusted to return the cavity to resonance, and the procedure is repeated. Results are normalized to the bare cavity coupling, $g_0/2\pi = FSR/(\lambda/2) = 0.432$ GHz/nm. They are consistent with a numerical model for $g_m(z_m)/g_0$ (dotted red line) which assumes a 50-nm-thick film with $|n_m| = 2.0$ has been placed at the center of a 742-μm-long cavity. In this case, $g_m^{max} = 2|r_m|g_0 = 0.843g_0$ (dashed black line).

been made to measure this value in our experiment. The task was anticipated to be difficult at the outset, because stoichiometric silicon nitride (Si_3N_4) is known to possess ultra-low optical absorption at telecom wavelengths. Less is known about the absorptive properties of Si_3N_4 in the near infrared and for micro structures, however, where impurities associated with the fabrication process can play a dominant role and the small volume of material makes loss measurements challenging. In [36], Si_3N_4 microdisk cavities were shown to have losses consistent with $Im[n_m] \sim 10^{-7}$ at 850 nm. Recent measurements in the Harris group [79] have placed a similar bound on Si_3N_4 membranes
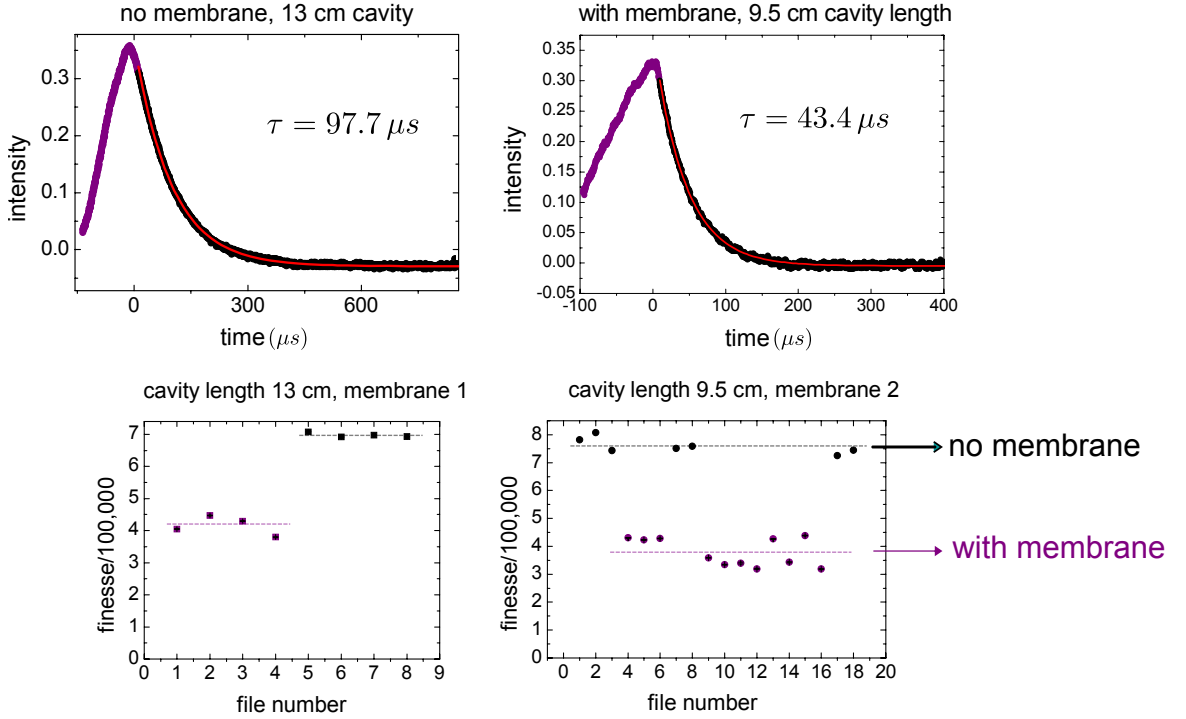
Figure 6.5: Ringdown measurement. A bound on the membrane absorption was first obtained by inserting the film into an ultra-high finesse Fabry-Perot cavity with a long, unstabilized length. Vibration of the membrane/mirrors occasionally pulls the cavity into resonance, whereupon the drive field is quickly shuttered off. The diminished cavity ringdown time is consistent with an added round-trip loss of $\approx 7 \times 10^{-6}$. For a 50 nm membrane positioned at the center of the cavity near a node of the intracavity standing wave, this is consistent with an imaginary index of refraction of $\mathrm{Im}[n_m] \approx 0.8 \times 10^{-4}$ at 850 nm. Lines are a qualitative fit to guide the eye.

purchased from Norcada, by placing the membrane near an antinode of a high-finesse Fabry-Perot cavity operating at 1064 nm. At the time we entered the field, it was known that low-stress Si-doped SiN membranes could exhibit absorption at the level of $\mathrm{Im}[n_m] \sim 10^{-4}$ at 1064 nm. We expected an improvement for our high-stress stoichiometric films, but had to wait until the stabilized cavity apparatus was finalized before making our first serious measurement. Below I describe that measurement as well as a preliminary measurement which informed the current cavity design.

6.4.1 Ringdown Measurement in a Long Cavity with High Finesse

A first estimate of the high-stress film losses was obtained by inserting the film into an open-air, unstabilized, high-finesse Fabry-Perot. This would seem a difficult — if not inevitable — first approach, for in order to measure the predicted round-trip loss introduced by the film, $\delta_m < 10^{-5}$, one would have to use a cavity with a finesse of $\mathcal{F} \sim 10^5$. In length units, the linewidth of this cavity at optical wavelengths is $\lambda/\mathcal{F} \sim 10$ pm, a nontrivial task to align and stabilize even in the absence of a membrane. An attractive feature of ringdown measurements, however, is that they

don't require a cavity that is locked to a stable reference. One simply waits for the cavity to swing — via length vibrations — into resonance with the probe laser. The light is then rapidly shuttered off, in our case with an AOM. The subsequent ringdown decay of the intracavity field is insensitive to length fluctuations. This robust feature makes the ringdown technique rather simple to execute. The rate at which residual circulating power decays through the exit mirror after the input field is turned off is directly related to the cavity finesse (see 2.32b)

$$P_{out}(t) = P_{out}(0)e^{-\gamma t} = P_{out}(0)e^{-\pi ct/2L\mathcal{F}} \tag{6.3}$$

where $\gamma = 2\kappa$ is the FWHM intensity linewidth of the cavity in angular units.

The mirrors for this particular experiment were mounted in standard kinematic mounts (Newport Ultima) on a breadboard located in a clean hood without vibration isolation. The cavity length was chosen to permit a spot size of $< 100~\mu$m and easily accessible ringdown times ($\sim 100~\mu$s) for the predicted loss level. The membrane was fixed to a kinematic mount (Newport Ultima) on an independent 3-axis stage (LineTool). Care was taken to center the window between the mirrors and to roughly align the window normal to the cavity mode by monitoring the retro-reflection of a HeNe laser beam collinear with the an 850 nm probe beam.

For the measurement shown in Figure 6.5, a (fortunate) error in the selection of cavity mirrors resulted in our constructing a cavity with a remarkable finesse of $\mathcal{F} \approx 7 \times 10^5$ at 850 nm, enabling a loss sensitivity of $2\pi/\mathcal{F} \approx 9$ ppm. Ringdown measurements were made with the membrane repeatedly translated into and out of the cavity mode. We observed a marked lack of variation in the reduced ringdown times obtained with the membrane inserted and interpreted these as events for which the membrane was located near a node when the cavity swung through resonance.

Ringdowns were fit with good qualitative agreement to an exponential decay and are consistent with an added round-trip loss of of ≈ 7 ppm. For the case of a 50-nm-thick membrane positioned at the anti-node of the intracavity field, this is consistent with an imaginary index of 0.8×10^{-4} at 850 nm, a number which compares favorably with the low-stress results obtained by the Harris group at the time, but higher than we anticipated for the stoichiometric chemistry. The loss-limited finesse obtainable for a membrane with $\text{Im}[n_m] = 0.8 \times 10^{-4}$ is $\approx 1.4 \times 10^4$ when located at an antinode. With this inference and the expectation that our preliminary results were limited by alignment-related losses, we decided to go ahead and build a stable cavity with coating curves centered at $\lambda = 850$ nm, $\mathcal{F} \approx 2 \times 10^5$. A more careful measurement was eventually made in this cavity, as described in the following section.
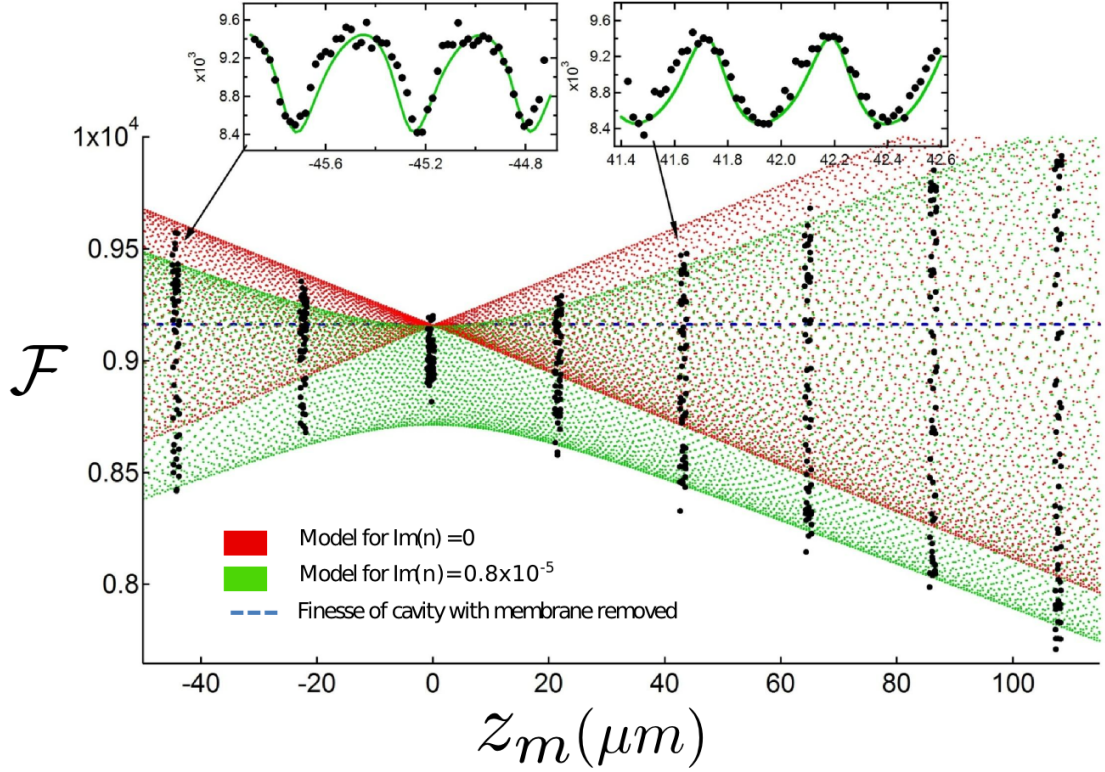
Figure 6.6: Variation of the cavity "finesse" as a function of membrane position. Finesse is defined as the free spectral range of the bare cavity ($c/2L$) divided by the measured linewidth of the MIM cavity, $\gamma = 2\kappa$ (FWHM): $\mathcal{F} = \pi c/L\gamma$ (here γ is in angular units). Variation occurs on two scales. The fine scale (insets) corresponds to translating the membrane between successive nodes of the intracavity field. The coarse scale corresponds to displacement by a significant fraction of the cavity length, L (here in increments of ~ 0.05 L). Modulation at cavity center is attributed to absorption and misalignment-related loss. Away from cavity center, modulation also results from an imbalance in the power residing in the two subcavities, each of different length. The model is generated using the transfer matrix method described in Section 3.3.2. "Droop" of the envelope is consistent with an absorption/alignment loss characterized by $\mathrm{Im}[n_m] = 0.8 \times 10^{-5}$.

6.4.2 Linewidth Measurement in a Short Cavity with Moderate Finesse

A less ambiguous measurement of absorption requires the ability to translate the film in increments $\delta z_m << \lambda$ along the wavefront of the intracavity standing wave while monitoring the linewidth of the MIM cavity, γ. We are capable of doing this with the high-finesse MIM system described in Chapter 5. However, as was detailed in Section 3.3.2, considerable care must be taken in accounting for various parameters in the model of the MIM system which give rise to modulation of γ. These include the real and imaginary index of the membrane, the membrane thickness d_m, position relative to the intracavity field, and coarse position relative to cavity center. The latter effect has been found to dominate in our system because the cavity is short and because for vibrational stability

we currently operate at a moderate bare cavity finesse, $\mathcal{F}_0 = 10^4$; at this finesse we have found that $T_{mirror} = \pi/\mathcal{F}_0 >> \delta_m$, the round-trip loss introduced by the membrane. Moreover, at this moderate finesse, the short length of the cavity makes it difficult to measure finesse via the ringdown method ($2\pi/\gamma \sim 100$ ns). We instead measure the cavity linewidth ($\gamma/2\pi \sim 10$ MHz) using a swept probe, as discussed in Section 6.2.

The procedure we have developed is as follows: (1) the membrane is translated in increments of $\Delta z_{pm} \sim 20 - -30$ nm along the cavity axis using the Picomotor driven translation stage, (2) after each step, the cavity is tuned into resonance with fixed frequency probe laser by translating one of the cavity end-mirrors, (3) the linewidth of the resonance is measured by dithering the cavity length and monitoring the transmission of the cavity, as discussed in Section 6.2, (4) steps 1–3 are repeated until the membrane has been translated through several periods of the intracavity standing wave, (5) steps 1–4 are repeated for several well-separated coarse changes of z_m.

The result of one such set of measurements is shown in Figure 6.6. Here the linewidth has been referred to a finesse value relative to the bare cavity free spectral range: $\mathcal{F} \equiv \pi c/L\gamma$ (note that γ is in angular units). It is worth noting that shortly before this particular measurement was taken, we had not yet developed the model discussed in 3.3.2, and were rather puzzled by the discovery that for some membrane positions, as shown, the MIM cavity linewidth was smaller than the intrinsic cavity linewidth. The membrane was removed and reinserted multiple times to recheck the bare cavity finesse, and each time we had to carefully realign all five degrees of freedom of the membrane — particularly tip/tilt — with respect to the cavity (by minimizing γ). In the meantime, Jeff was independently working on the transfer matrix model and was also puzzled by the same "artifact" in his numerical results. We now understand this to be a real effect by which the etalon formed between the membrane and the end-mirror can alter the photon storage time. After accounting for the fact that we tune the cavity length rather than the laser probe to maintain cavity resonance, we have found that model and data agree well quantitatively. The "envelope" is consistent with a model for a symmetric cavity with $\{\text{Im}[n_m], \text{Re}[n_m], d_m, L, \mathcal{F}_0\} = \{0.8 \times 10^{-5}, 2.0, 50 \text{ nm}, 742\,\mu\text{m}, 9200\}$ where n_m. The variation in cavity finesse near cavity center, however, is more consistent with $\text{Im}[n_m] = 0.6 \times 10^{-6}$. The latter would enable a loss limited cavity finesse of $\approx 2 \times 10^5$ with the membrane positioned at an antinode. We currently believe this result to represent an upper bound on the actual losses, since it remains sensitive to $\sim \mu$rad tip/tilt alignment of the membrane. Moreover, the linewidth inferred losses appear to misrepresent the measured variation in cavity transmission versus membrane position, as discussed in the next section.
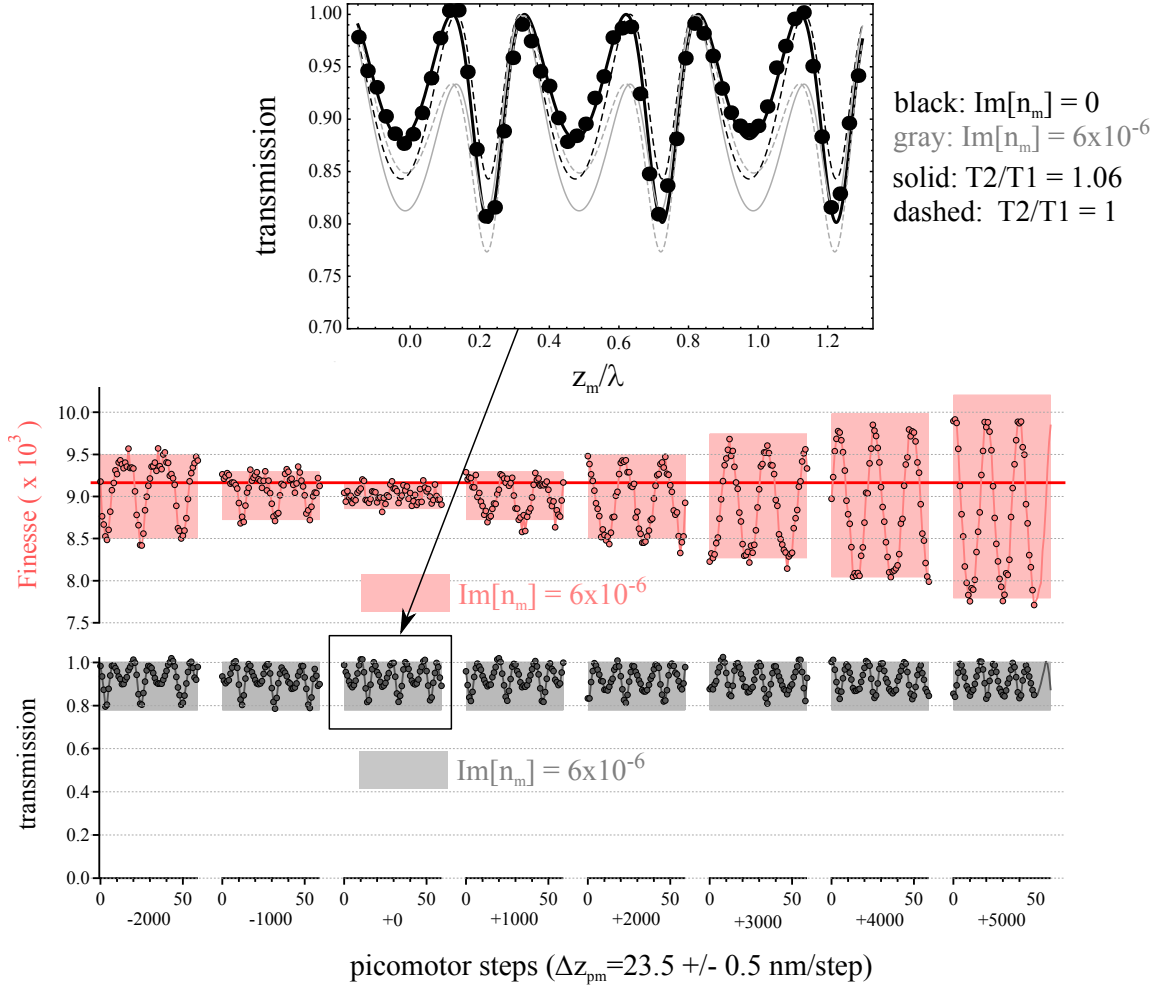
Figure 6.7: Measurement of cavity "finesse" (pink) and peak transmission (gray) as functions of membrane position. Transmission data is normalized to peak transmission when the membrane is at an antinode. Picomotor step size is inferred from the $\lambda/2$ periodicity of the measurement data. Solid pink and gray correspond to the extrema for a model which assumes $\{\text{Im}[n_m], \text{Re}[n_m], d_m, L, \mathcal{F}_0\}$ $= \{0.6 \times 10^{-5}, 2.0, 50\,\text{nm}, 742\,\mu\text{m}, 9200\}$, where n_m is the index of the membrane. In the upper plot, transmission data corresponding to the membrane near cavity center is compared to the model inferred from the finesse data and to the model for a lossless and slightly asymmetric cavity. Black and gray lines correspond to different choices of loss. Dashed and solid black lines correspond to different choice for T_2/T_1. The data is found to agree best with a lossless ($\text{Im}[n_m] = 0$) model for which $T_2/T_1 = 1.06$.

6.5 MIM Cavity Transmission Vs. Membrane Position

The inferred values of $\{\text{Im}[n_m], \text{Re}[n_m], d_m, L, \mathcal{F}_0\}$ can be cross-checked against a measurement of the resonant power transmission of the MIM cavity vs. membrane position. In particular, we have found that this measurement is consistent with a lower absorption loss than the value $\text{Im}[n_m] = 0.8 \times 10^{-5}$ obtained for the membrane in the the previous section.

In Figure 6.7, we record resonant transmitted power and linewidth of the cavity as a function of

the membrane position. Each data point is obtained from a fit to a curve as shown in Figure 6.2. Each pink/gray block corresponds to a sequence of measurements as the membrane is translated in $\sim$ 25 nm steps along the intracavity standing wave. Adjacent blocks are separated by 1000 Picomotor steps $\sim$ 25 nm. The set of data points for each block is normalized to the average of the extrema in that block. The extrema are taken to correspond to when membrane is positioned at a node of the intracavity field. For comparison to the model, we assume a transmission value of unity when the membrane is located at an node.

Results for the linewidth measurement (referred to a finesse value as in the previous section) are consistent with the "envelope" function for a model assuming $\{\mathrm{Im}[n_m], \mathrm{Re}[n_m], d_m, L, \mathcal{F}_0\} = \{0.6 \times 10^{-5}, 2.0, 50\,\mathrm{nm}, 742\,\mu\mathrm{m}, 9200\}$. However, to obtain agreement with the transmission data for $\mathcal{F}_0 = 9200$ and $\mathrm{Re}[n_m] = 2.0$, we have assumed vanishingly small membrane loss ($\mathrm{Im}[n_m] = 0$), a slight asymmetry in the cavity end-mirrors transmission ($T_1/T_2 \approx 1.06$) and a membrane thickness of $d_m \approx 47$ nm. Note that the model assumes, in accordance with the measurement procedure, that after each membrane position the end-mirror is translated to bring the cavity into resonance, while the laser frequency remains fixed.

6.6 Concluding Remarks

We have performed a series of measurements to characterize the linear optical properties of our "membrane-in-the-middle" system, described in Chapter 5. To model these measurements, we've applied the steady-state transfer matrix model described in Chapter 3. We have verified that the optomechanical coupling when the membrane is located near the center of the cavity agrees with the "dispersive coupling" formula (Eq. 3.22,[23]), obtaining a maximum value of $g_m^{max} = 2|r_m|g_0 \approx 0.843g_0 = 2\pi \times 0.432$ GHz/nm at 935 nm for a nominally $d_m =$50-nm-thick film coupled to a cavity of length $L = 742$ μm and finesse $\mathcal{F}_0 = 9200$. We find that the MIM cavity linewidth/finesse varies in a complicated fashion depending on both the reflectivity/loss of the membrane, its position relative to the intracavity standing wave, and its overall distance from the center of the cavity. This variation is consistent with an optical absorption characterized by an imaginary index of $\mathrm{Im}[n_m] = 0.8 \times 10^{-5}$ at 935 nm. Modeling a measurement of the resonant transmitted power vs. membrane position suggests that the absorption may be significantly lower. A value $\mathrm{Im}[n_m] = 0.8 \times 10^{-5}$ and $d_m = 50$ nm would enable a loss-limited cavity finesse of $\mathcal{F} \approx 1.5 \times 10^5$ with the membrane positioned at an antinode. This cavity finesse is within the envelope of the measured mirror coating curve, shown in Figure 6.3. For our cavity length of 742 μm, a finesse of 9200 corresponds to a linewidth of $\kappa/2\pi = 12$ MHz (HWHM), which puts us just inside "bad cavity limit" ($\kappa > \Omega_m$) with respect to a nominal value of $\Omega_m/2\pi = 5$ MHz for the mechanical frequency of the membrane (in particular, the 4.8 MHz (6,6) mode of a $\{d_m, w_m\} = \{50\,\mathrm{nm}, 500\,\mu\mathrm{m}\}$ membrane, around which we built our

apparatus). To achieve sideband resolution, we could operate at a slightly different wavelength on the coating curve. For the optomechanical cooling experiment described in Chapter 9, we operate at a finesse of $\mathcal{F}_0 \approx 10^4$ to mitigate vibration isolation problems. We have has some recent success with a titanium-sapphire laser operating on the opposite side of the coating curve (812–813 nm, where we have not yet carefully measured the membrane absorption coefficient) with a finesse of $\mathcal{F}_0 \approx 3 \times 10^4$.

Chapter 7

Thermal Noise in a Multimode MIM Sytem

In the next two chapters we elaborate on the task of characterizing displacement noise in the "membrane-in-the-middle" system. The tools we have found necessary to develop are: (1) a way to understand optomechanical coupling between higher-dimensional spatial modes of the membrane and the optical cavity, (2) a model for how multimode Brownian vibration of the membrane is written onto the intensity of the intracavity field, (3) methods to measure and calibrate these fluctuations, and (4) an accounting of competing sources of noise in the measurement, especially mirror substrate thermal noise. The first two subjects are treated in this chapter. It is hoped that, in addition to clarifying subsequent results, the discussion herein provides insight into ways in which the simplicity of the MIM system can be further enhanced.

7.1 Optomechanical Coupling Between Transverse Optical and Mechanical Modes

Until now our treatment of optomechanical coupling has been one-dimensional. In the transfer matrix model developed in Chapter 3, we assumed that the cavity mode was a plane wave and that the membrane was a rigid plate (Figure 7.1). We then studied the effect of translating the equilibrium position z_m of membrane along the cavity axis, obtaining a maximum linear optomechanical coupling of $g_m^{max} = 2|r_m|\omega_c/L$ when the membrane is located halfway between a node and an antinode of the intracavity field near the midpoint of the cavity (see Section 3.3.1). Here $|r_m|$ is the reflectivity of the membrane, L is the length of the cavity, and $g_m(z_m) \equiv \delta\omega_c/\delta z_m$ gives the cavity resonance frequency shift $\delta\omega_c$ resulting from a small displacement δz_m of the membrane's equilibrium position. To model vibration of the membrane, we can attach the plate to a pendulum spring that produces small amplitude fluctuations $\delta z_m(t) << \lambda$ along the cavity axis.

As illustrated in Figure 7.1, the 1D spring model is only an approximation when applied to
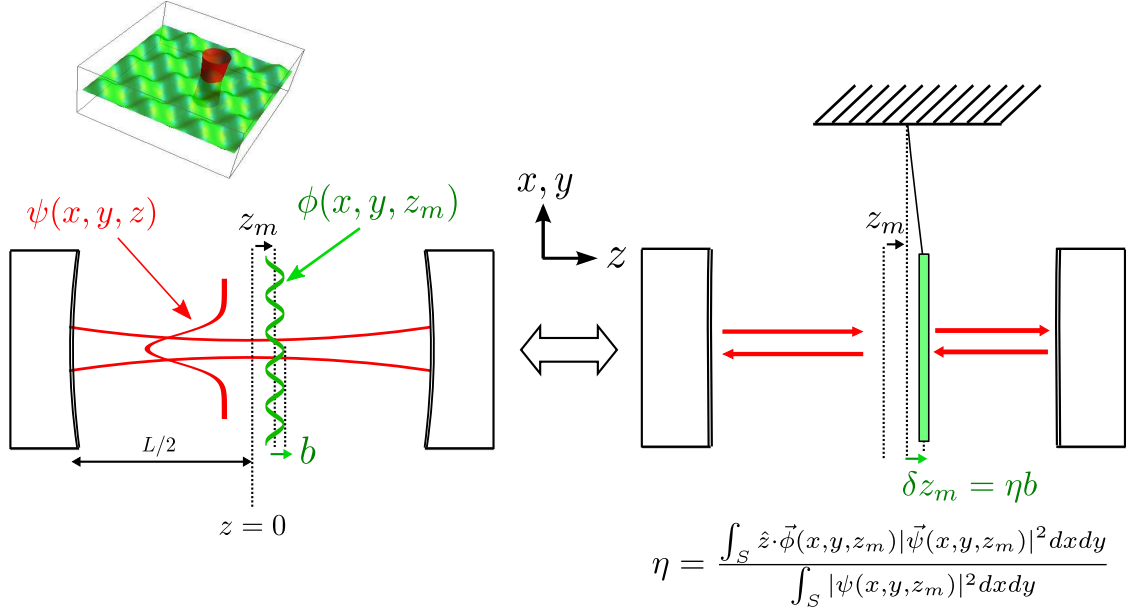
Figure 7.1: Sketch of the problem: the amplitude of the intracavity field and the displacement of the membrane surface both exhibit spatial variation perpendicular to the cavity axis. The intracavity field is described by a Hermite-Gauss mode, $\vec{\psi}(x,y,z)$. Displacement of the membrane surface is described by a vibrational mode $b(t)\vec{\phi}(x,y,z)$. Vibration of the membrane surface produces a cavity resonance frequency shift $\delta\omega_c = g_m(z_m)\eta b \equiv g_m(z_m)\delta z_m$. The "effective" equilibrium displacement of the membrane, δz_m, is equal to the weighted average of the displaced membrane surface over the normalized intensity profile of the intracavity field.

an internal vibrational mode of the membrane, characterized by mode shape function $\vec{\phi}(x,y,z)$ (Section 7.1.1), which does not produce a uniform translation of the membrane, but rather a local displacement that varies sinusoidally across its surface. Nor is the intracavity field a plane wave. In a Fabry-Perot resonator with spherically curved mirrors, the intracavity field amplitude takes the form of a Hermite-Gauss mode, characterized by mode shape function $\vec{\psi}(x,y,z)$ [31] (Section 7.1.2). The lowest order ("TEM$_{00}$") mode is characterized by an intensity profile that decays like a Gaussian in the radial direction. In our cavity with length $L = 742$ μm and mirror radius of curvature $R_c = 5$ cm, the diameter of this Gaussian is $2w_c = 71.4$ μm (Section 5.2.2.1). By design, this dimension is comparable to the spacing between adjacent nodes for the (6,6) vibrational mode of the $\{d_m, w_m\} = \{50$ nm$, 0.5$ mm$\}$ membrane coupled to the cavity (i.e., 500 μm/6 = 83.3 μm).

In this more complicated setting, we can express the cavity resonance frequency shift produced by vibration of the membrane surface (in a single mode) as $\delta\omega_c = g_m(z_m)\eta b \equiv g_m(z_m)\delta z_m$; here b denotes the amplitude of the vibrational mode, δz_m the "effective" equilibrium displacement of the membrane and η a "spatial overlap" factor proportional to the weighted average of the vibrating membrane surface over the intensity profile of the intracavity field. In the following sections we will substantiate this claim. Although for simplicity we will focus on internal vibrations of membranes,
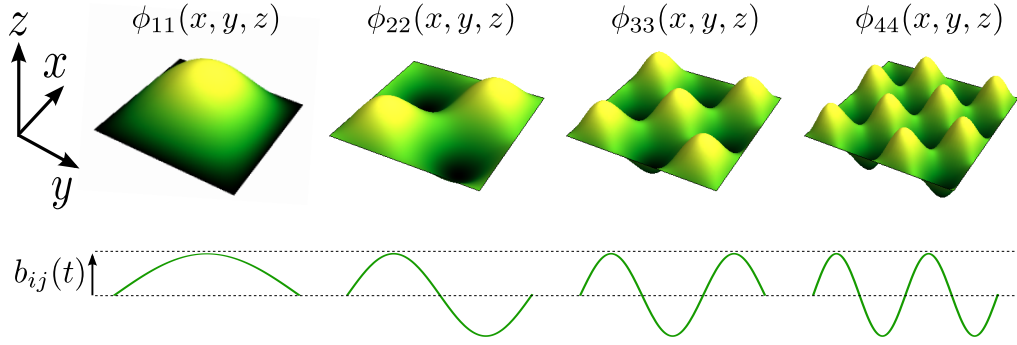
Figure 7.2: Vibrational modes $\vec{u}_{ij}(x, y, z, t) = b_{ij}(t)\phi_{ij}(x, y, z)\hat{z}$ of a square membrane. Mode-shape functions $\phi_{ij}(x, y, z)$ are normalized to $\phi_{ij} = 1$ at an antinode. $b_{ij}(t)$, the generalized amplitude of mode (i, j), represents the amplitude at an antinode. The effective mass of b_{ij} is $m_{ij} = \langle E_{ij} \rangle / \langle b_{ij}^2 \rangle \Omega_{ij}^2 = m_{phys}/4$, where $\langle E_{ij} \rangle$ is the average energy of the oscillator.

the treatment used applies equally well to internal vibrations of the end-mirror substrates. Substrate thermal noise will play an important role in Chapter 10; the concept is introduced here as a case study in Section 7.3.2.

7.1.1 Internal Modes of an Elastic Body: Displacement and Effective Mass

The internal modes of a three-dimensional elastic body are obtained by solving the elastic wave-equation (for example, see Section 4.2.1). Eigensolutions to the wave equation ("modes") are vector fields, $\vec{u}_k(x, y, z, t)$ which describe the displacement of each point in the body from its equilibrium position (x, y, z) at time t. We will use index k to denote a mode of a generic 3-dimensional body (like the membrane or mirror substrates) and indices (i, j) when referring specifically to a square membrane vibrational mode. We assume solutions of the form:

$$\vec{u}_k(x, y, z, t) = b_k(t)\vec{\phi}_k(x, y, z). \tag{7.1}$$

Here $\vec{\phi}_k(x, y, z)$ is a real-valued, unitless mode-shape function and $b_k(t)$ is a function of time with units of length, representing the generalized amplitude of ϕ_k. Hereafter will refer to the b_k as the amplitude of "mode ϕ_k", to emphasize that the magnitude of b_k depends on the normalization of the mode-shape function. $b_k(t)$ is assumed to obey the equation of motion for an internally damped harmonic oscillator (see Section 2.2). In the Fourier domain $(b_k(\Omega) = \int_{-\infty}^{\infty} b_k(t)e^{-i\Omega t}dt)$:

$$(-\Omega^2 + i\Gamma_k(\Omega)\Omega + \Omega_k^2)b_k(\Omega) = F_k(\Omega)/m_k \tag{7.2}$$

where F_k is a generalized external force and m_k is the "effective mass" of coordinate b_k, to be defined below.

We will also assume that the eigenmodes comprise a complete, orthogonal set, so that any vibration of the elastic body can be written in the form $\vec{u}(x, y, z, t) = \sum_k b_k(t)\vec{\phi}_k(x, y, z)$ and

$$\int_V \vec{\phi}_k(x, y, z) \cdot \vec{\phi}_{k'}(x, y, z)dxdydz = N\delta_{k,k'}, \tag{7.3}$$

where $\delta_{k,k'}$ is the Kronecker-delta function, N is a normalization factor, and V is the volume of the body.

In the absence of dissipation ($\Gamma_k = 0$) each infinitesimal mass element in the body, $\rho(x, y, z)dV$, describes 1D harmonic motion around its equilibrium position with amplitude $b_k(t)\vec{\phi}_k(x, y, z)$, frequency Ω_k, and potential energy $\frac{1}{2}\rho(x, y, z)dVb_k^2(t)|\vec{\phi}_k(x, y, z)|^2\Omega_k^2$. The total energy E_k of the mode is given by summing the energy of each mass element. For a thermally excited damped harmonic oscillator, the average energy of mode ϕ_k is given by equipartition:

$$\langle E_k \rangle = \langle b_k^2 \rangle \Omega_k^2 \int_V \rho(x, y, z)|\vec{\phi}_k(x, y, z)|^2 dV = k_B T, \tag{7.4}$$

where $\langle\ \rangle$ signifies the time average and $|\vec{\phi}|^2 \equiv \vec{\phi}^* \cdot \vec{\phi}$ for vector quantities (for scalar quantities it means the square modulus).

The integral in Eq. 7.4 has units of mass and can be identified as the effective mass m_k of the generalized amplitude b_k relative to the energy normalization condition $\langle E_k \rangle = m_k\Omega_k^2\langle b_k^2 \rangle$. The effective mass is related to the physical mass $m_{phys} \equiv \int_V \rho(x, y, z)dxdydz$ by a purely geometric "effective mass coefficient", $\alpha_k \equiv m_k/m_{phys}$. In the simple case of uniform density, $\rho(x, y, z) = \rho$, we find

$$\alpha_k \equiv \frac{m_k}{m_{phys}} = \frac{1}{V}\int_V |\vec{\phi}_k(x, y, z)|^2 dV = \frac{N}{V} \tag{7.5a}$$

$$\langle b_k^2 \rangle = \frac{\langle E_k \rangle}{\alpha_k m_{phys}\Omega_k^2}. \tag{7.5b}$$

Note that there remains an essential ambiguity in the definition of b_k and m_k until a normalization N for $\vec{\phi}_k(x, y, z)$ is chosen. This choice is completely arbitrary, and the game is to make a convenient choice depending on the physical process being modeled. We will ultimately be interested in the displacement of a small patch of the membrane surface, defined by the size and location of the cavity mode piercing the membrane. Towards this end, it is convenient to normalize the mode-shape function by setting its maximum value to unity, i.e., $\max\left(|\vec{\phi}_k|\right) = 1$. b_k then describes the amplitude of the point of maximum displacement in mode ϕ_k.

For a square membrane with mode indices (i, j), this normalization gives $|\vec{\phi}_{ij}| = 1$ at each antinode. b_{ij} then represents the displacement of an antinode from the equilibrium position of the membrane. The vibrational mode shapes and eigenfrequencies of a square membrane with width w_m are given by (see Section 4.2.1):

$$\vec{\phi}_{ij}(x, y, z) = \sin\left(\frac{i\,\pi x}{w_m}\right) \sin\left(\frac{j\,\pi y}{w_m}\right) \hat{z}; \ \{i, j\} \in \{1, 2, 3...\} \tag{7.6a}$$

$$\Omega_{ij} = \frac{1}{w_m}\sqrt{\frac{T}{2\rho}}\sqrt{\frac{i^2 + j^2}{2}}. \tag{7.6b}$$

The effective mass of b_{ij} turns out to be the same for all modes of a square membrane:

$$m_{ij} = \rho\, t \int_0^{w_m} \int_0^{w_m} \sin^2\left(\frac{i\,\pi x}{w_m}\right) \sin^2\left(\frac{j\,\pi y}{w_m}\right) dx dy \tag{7.7a}$$

$$= \frac{1}{4}\rho\, t w_m^2 = \frac{1}{4} m_{phys}. \tag{7.7b}$$

It's interesting to contrast this against the case of a circular drum of diameter w_m, whose modes are described by Bessel functions $J_m(r)$ [49]. Using the same normalization convention:

$$\vec{\phi}_{ij}(r, \theta, z) = \frac{J_j(2x_{ij}r/w_m)\cos(j\theta)}{\max\left(|J_j(2x_{ij}r/w_m)|\right)}\hat{z} \tag{7.8a}$$

$$i \in \{1, 2, 3...\}, j \in \{0, 1, 2, ...\}; x_{ij} \equiv i^{th}\ zero\ of\ J_j(r) \tag{7.8b}$$

$$\Omega_{ij}/2\pi = \frac{1}{w_m}\sqrt{\frac{T}{2\rho}}\frac{2x_{ij}}{\pi}. \tag{7.8c}$$

In contrast to square membrane modes, the effective mass of circular membrane modes varies widely with mode order. Of particular interest are the mode-shape functions of axisymmetric ($j = 0, \max\left(|J_0(2x_{i0}r/w_m)|\right) = 1$) modes. This subset of "confined" modes can have significantly reduced effective masses because most of their displacement is localized to a reduced diameter $\sim w_m/x_{i0}$:

$$m_{i0} = \rho\, t \int_0^{2\pi} \int_0^{w_m/2} J_0^2(2x_{i0}\,r/w_m)r dr d\theta = m_{phys}J_1^2(x_{i0}). \tag{7.9}$$

In Figure 7.20, the inverse effective mass coefficient (m_{phys}/m_{ij}) of square and circular drum modes is compared. In particular, we compare the subset of odd-ordered square modes ($\phi_{i,j}$; $i = 1, 3, 5...$; $j = 1, 3, 5...$) and axisymmetric circular (ϕ_{i0}; $i = 1, 2, 3...$) modes. These are modes that have an antinode at the geometric center of the membrane. Their significance is as follows: if the cavity waist were infinitesimally small and located at the center of the membrane, then $\delta\omega_c = \omega_c - \langle\omega_c\rangle = g_m b_{ij}$ would be the cavity resonance frequency shift induced by vibrational amplitude b_{ij}. Circular membranes may indeed be an attractive alternative in the future, owing to their small effective mass and the reduced density of modes which have non-zero amplitude at
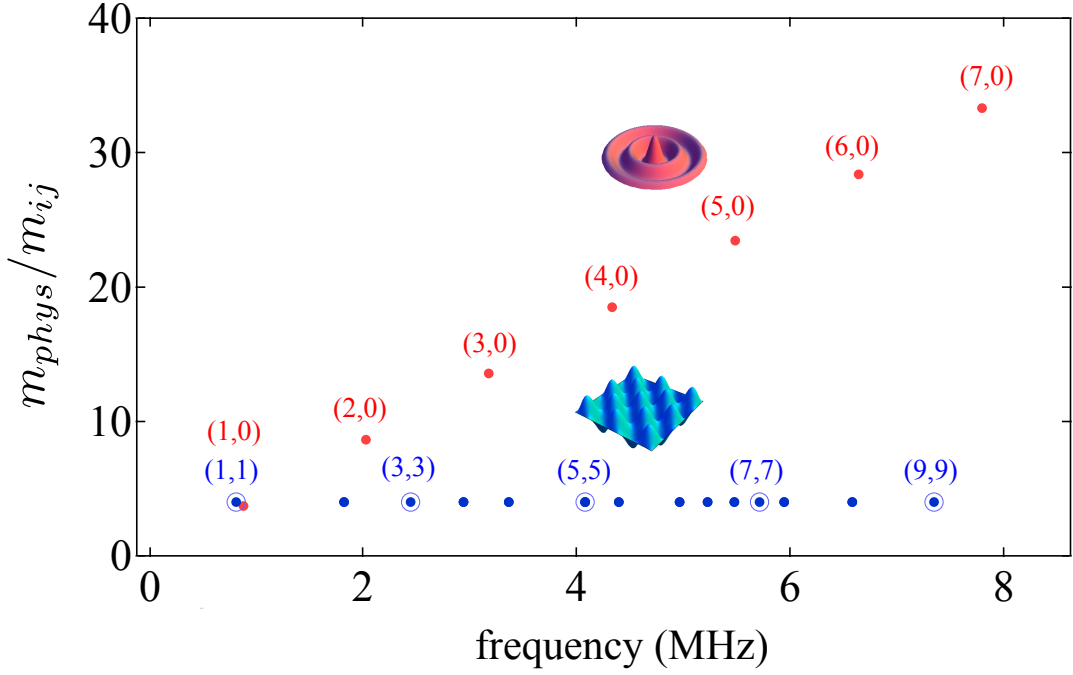
Figure 7.3: Inverse effective mass coefficient of odd-ordered square membrane modes ($\phi_{i,j}$; $i = 1, 3, 5...$; $j = 1, 3, 5...$) and axisymmetric circular membrane modes ($\phi_{i0}, i = 1, 2, 3...$) as a function of frequency for membrane diameter $w_m = 500\,\mu$m and tension $\mathcal{T} = 900$ MPa. The choice of modes is relevant to the situation where the membrane is probed at its center by a TEM$_{00}$ cavity mode. In this case — as explained in Section 7.1.3 — all square and non-axisymmetric circular membrane modes have vanishing optomechanical coupling.

cavity center. At the time of this writing, collaboration with Richard Norte in the Painter group has produced some high quality preliminary devices ($w_m = 200 - -300\,\mu$m, $Q_{10} \sim 10^6$).

In the next two subsections we derive the effective optomechanical coupling for a cavity spatial mode with finite size and arbitrary location with respect to cavity center.

7.1.2 Internal Modes of a Fabry-Perot Cavity: Hermite-Gaussian Modes

In Chapters 2 and 3 we modeled the intracavity field as a superposition of plane waves traveling normal to the cavity axis. Here we consider a more realistic model of our Fabry-Perot cavity, in which the circulating field is allowed to diffract. Our cavity is composed of two highly reflective end-mirrors each having the same radius of curvature $R_c = 5$ cm and separated by a distance $L = 0.743$ mm. The electric field in this cavity can be written as a superposition of spatial modes $\vec{\psi}_n$ with generic index n:

$$\vec{E}(x, y, z, t) = \sum_k E_n(t)\vec{\psi}_n(x, y, z), \tag{7.10}$$

which are a solution to the Helmholtz equation

$$(\vec{\nabla}^2 + k_n^2)\vec{\psi}_n(x,y,z) = 0 \tag{7.11}$$

subject to the boundary condition $\vec{\psi}_n(x,y,z) \approx 0$ at the (high reflective) mirror surface.

When $L < 2R_c$ (as in our case), the mirror surfaces coincide with the wavefront of a Hermite-Gaussian beam[31]. This reflects the fact that solutions to (7.11) in the paraxial approximation — "Hermite-Gauss Modes" — can be written as the superposition of forward and backward propagating Hermite-Gaussian beams, $\psi^\pm$ [31]. Hereafter we will approximate the Gaussian beam as planar, so that the polarization vector is perpendicular to the cavity axes. We will use indices (m,n) to represent Hermite-Gaussian mode "TEM$_{mn}$", which has mode shape function:

$$\psi_{mn}(x,y,z) = \psi_{mn}^+(x,y,z) - \psi_{mn}^-(x,y,z) \tag{7.12a}$$

$$\psi_{mn}^\pm(x,y,z) = i|N_{mn}|e^{-\frac{x^2+y^2}{w(z)^2}} H_m\left[\frac{\sqrt{2}x}{w(z)}\right] H_n\left[\frac{\sqrt{2}}{w(z)}\right] e^{\mp i(k_{mnq}z+\phi(x,y,x))} \tag{7.12b}$$

$$\phi(x,y,z) = \phi_G(z) + \frac{\pi(x^2+y^2)}{\lambda R(z)^2}. \tag{7.12c}$$

Here z is the position along the cavity axis with $z = 0$ at cavity center (assuming that the two mirrors have the same radius of curvature), H_m is the mth Hermite polynomial, $w(z)$ is the $1/e^2$ radius of the transverse intensity profile, $R(z)$ is the radius of curvature of the diffracting wave-front, ϕ_G is the "Guoy" phase, k_{mnq} is the cavity resonance frequency in wavenumber units, and $|N_{mn}|$ is a normalization factor. For our cavity length ($L = 0.742$ μm) and mirror radius ($R_c = 5$ cm), these various components take on the values:

$$z_R = \frac{\pi w_c^2}{\lambda} = \frac{L}{2}\sqrt{\frac{2R_c}{L} - 1} \approx 5.8L \tag{7.13a}$$

$$w(z) = w_c\sqrt{1 + \left(\frac{z}{z_R}\right)^2} \approx w_c = 35.8 \ \mu\text{m @ 935 nm} \tag{7.13b}$$

$$R(z) = z + z_R^2/z \approx 33.5L/z \tag{7.13c}$$

$$\phi_G(z) = \tan^{-1}(z/z_R) \approx z/z_R \tag{7.13d}$$

$$f_{mnq} = \frac{\omega_{nmq}}{2\pi} = \frac{k_{nmq}c}{2\pi} = \frac{c}{2L}\left(q + (n+m+1)\frac{\cos^{-1}(1-L/R_c)}{\pi}\right) \tag{7.13e}$$

$$\approx q \times 202 \text{ GHz} + (n+m+1) \times 11 \text{ GHz}, \tag{7.13f}$$

where z_R is the "Rayleigh length" of the cavity, and f_{mnq} the cavity resonance frequency. Our cavity has a nominal free spectral range of ≈ 202 GHz and "transverse mode splitting" ≈ 11 GHz.

For most of the experiments we have performed in the lab we use lowest order cavity mode,

TEM_{00}, which has a Gaussian transverse profile:

$$\psi_{00}(x,y,z) = |N_{00}|e^{-\frac{x^2+y^2}{w(z)^2}}\sin(k_{00q}z + \theta(x,y,z)). \tag{7.14}$$

Also note that by construction the Hermite-Gauss beams obey the orthogonality relations:

$$\int_{-\infty}^{\infty}\psi_{nm}^{\pm *}(x,y,z)\psi_{n'm'}^{\pm}(x,y,z)dx \propto \delta_{n,n'} \tag{7.15a}$$

$$\int_{-\infty}^{\infty}\psi_{nm}^{\pm *}(x,y,z)\psi_{n'm'}^{\pm}(x,y,z)dy \propto \delta_{m,m'} \tag{7.15b}$$

$$\int_{V_c}\psi_{nm}^{*}(x,y,z)\psi_{n'm'}(x,y,z)dxdydz \propto \delta_{m,m'}\delta_{n,n'}, \tag{7.15c}$$

where the last integral is over the cavity volume, V_c .

7.1.3 Optomechanical Coupling, "Effective Displacement", and "Spatial Overlap"

We now consider the situation illustrated at the top of Figure 7.4: a compliant end-mirror vibrating in mode $\phi_k(x,y,z)$ with amplitude b_k is coupled to a Hermite-Gauss mode, $\psi_{mn}(x,y,z)$, of a Fabry-Perot cavity.

Note: for notational simplicity we hereafter drop the longitudinal and transverse indices, qmn, in the parameterization of the optomechanical system. This is justified by the fact that in practice usually only one cavity mode is excited.

When $b_k = 0$, the resonance frequency of the cavity is $\langle\omega_c\rangle$. When $b_k > 0$, then the cavity resonance frequency is displaced by an amount

$$\delta\omega_c = \omega_c - \langle\omega_c\rangle = g_0\eta_k b_k \equiv g_0\delta z_0^k. \tag{7.16}$$

Factor $g_0 = \langle\omega_c\rangle/L$ here corresponds to the optomechanical coupling for a rigid mirror in a two-mirror cavity, factor η_k depends on the spatial overlap between of the mechanical and optical spatial modes and will be referred to as the *"spatial overlap factor"*, and $\delta z_0^k \equiv \eta_c b_k$ is referred to as the *"effective displacement"* of mode ϕ_k.

We ask: how is η_k related to the spatial profile of the mechanical mode and the cavity mode? To get a handle on the situation, we can compute the phase shift experienced by the circulating Hermite-Gaussian beam upon reflection from the vibrating mirror (relative to the mirror in its equilibrium position $b_k = 0$). To simplify the problem, we assume that the intracavity wavefront is nearly planar ($\hat{k} \approx \hat{z}$) at the mirror surface. We then follow closely the arguments of Gillespie and

Raab [52], who express the phase shift upon reflection as:

$$\psi_{mn}^+(x,y,z) \rightarrow \psi_{mn}^-(x,y,z)e^{2ik_{mn}b_k\vec{\phi}_k(x,y,z)\cdot\hat{z}} \tag{7.17a}$$

$$\approx \psi_{mn}^-(x,y,z)(1 + 2ik_{mn}b_k\vec{\phi}_k(x,y,z)\cdot\hat{z}) \tag{7.17b}$$

$$= \sum_{m'n'} c_{m'n'}\psi_{m'n'}^-(x,y,z) \tag{7.17c}$$

$$\approx \psi_{mn}^-(x,y,z)\left(1 + 2ik_{mn}b_k \cdot \frac{\int_S |\psi_{mn}^-(x,y,z)|^2\vec{\phi}_k(x,y,z)\cdot\hat{z}d\sigma}{\int_S |\psi_{mn}^-(x,y,z)|^2 d\sigma}\right) \tag{7.17d}$$

$$= \psi_{mn}^-(x,y,z)\left(1 + 2ik_{mn}b_k \cdot \frac{\int_S |\psi_{mn}(x,y,z)|^2\vec{\phi}_k(x,y,z)\cdot\hat{z}d\sigma}{\int_S |\psi_{mn}(x,y,z)|^2 d\sigma}\right). \tag{7.17e}$$

Here $|\psi|^2$ here indicates $\psi^*\psi$ for scalar quantities and S denotes the integral over the surface of the miror. The assumptions behind each step are: (7.17b) b_k is much smaller than λ_{mnq}, (7.17d) the Hermite-Gauss modes form a complete set, (7.17d) the Hermite-Gauss modes are orthogonal according to (7.15) and only the original unperturbed mode of the cavity is resonant with the incoming laser. Eq. 7.17d is obtained by applying Eq. 7.15 to both sides of Eq. 7.17c. Eq. 7.17e follows from the relationship between Hermite-Gaussian beams and modes given in Eqs. 7.12a and 7.12b.

Eq. 7.17e suggests that displacing vibrational mode ϕ_k from equilibrium by an amount b_k is equivalent to displacing the entire mirror by an *"effective displacement"* magnitude:

$$\delta z_0^k = \frac{\int_S |\psi_{mn}(x,y,z)|^2\vec{\phi}_k(x,y,z)\cdot\hat{z}d\sigma}{\int_S |\psi_{mn}(x,y,z)|^2 d\sigma} \cdot b_k \equiv \eta_k b_k \tag{7.18}$$

such that the cavity resonance frequency shift is given by $\delta\omega_c = g_0\delta z_0^k$. The spatial overlap factor, η_k, is the weighted averaged of spatial mode function $\phi_k(x,y,z)$ over the normalized intensity profile of the cavity mode, $|\psi_{mn}(x,y,z)|^2/\int_S |\psi_{mn}(x,y,z)|^2 d\sigma$, where S indicates evaluation at the surface of the mirror.

By direct analogy, we infer that a membrane in the "membrane-in-the-middle" system, vibrating in a single mode ϕ_{ij} with amplitude b_{ij}, will produce a cavity resonance frequency shift given by $\delta\omega_c = g_m(z_m)\eta_{ij}b_{ij}$ where

$$\eta_{ij} = \frac{\int_S |\psi_{mn}(x,y,z)|^2\vec{\phi}_{ij}(x,y,z)\cdot\hat{z}d\sigma}{\int_S |\psi_{mn}(x,y,z)|^2 d\sigma}. \tag{7.19}$$

Mode ϕ_{ij} is then described by an effective displacement $\delta z_m^{ij} \equiv \eta_{ij}b_{ij}$; δz_m^{ij} corresponds to the displacement of the membrane's equilibrum position required to shift the cavity resonance frequency by $g_m(z_m)\eta_{ij}b_{ij}$. η_{ij} is referred to as the spatial overlap factor for membrane mode ϕ_{ij}. The main assumption made in drawing the above analogy is that, to first order, the phase of the field
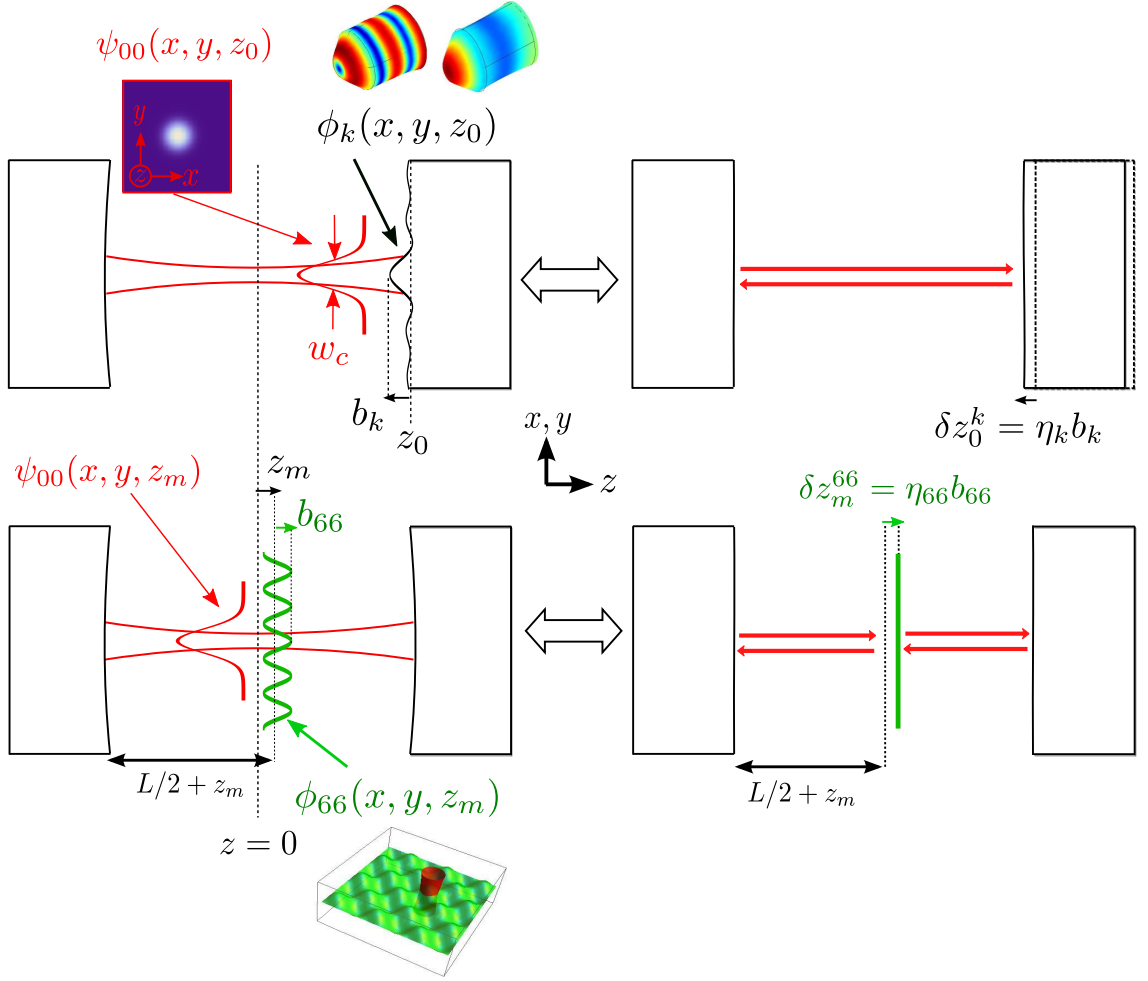
Figure 7.4: Reducing the optomechanical system to one dimension. Upper plot: in a typical situation, Hermite-Gaussian mode $\psi_{00}(x, y, z)$ (TEM$_{00}$) is coupled to a vibrational mode of one of the end-mirror substrates, characterized by the product of mode-shape function $\phi_k(x, y, z)$ and generalized amplitude $b_k \ll \lambda$. Amplitude b_k gives rise to a shift in the cavity resonance frequency $\delta\omega_c = g_0 \eta_k b_k$, where $g_0 = \omega_{c,mn}/L$ is the canonical end-mirror optomechanical coupling and η_k is the weighted average of $\phi_k(x, y, z_0)$ over the normalized intensity profile $|\psi_{00}(x, y, z_0)|^2 / \int_S |\psi_{00}(x, y, z_0)|^2 d\sigma$, evaluated at the position of the mirror surface, z_0. This is equivalent to displacing the entire mirror by "effective" magnitude $\delta z_0^k = \eta_k \delta b_k$. Lower plot: the same set of reasoning applies to the "membrane-in-the-middle". Here we have represented the (6,6) mechanical mode of a square membrane as the product of mode shape function $\phi_{66}(x, y, z)$ and generalized amplitude b_{66}. Vibration amplitude b_{66} gives rise to a resonance frequency shift $\delta\omega_c = g_m \eta_{66} b_{66}$, where g_m is the 1D dispersive optomechanical coupling for the MIM system derived in Section 3.3.1 and η_{66} is defined as above. This is equivalent to a displacement of the equilibrium position of the membrane by an amount $\delta z_m^{66} = \eta_{66} b_{66}$.

transmitted through the membrane is $Arg[t_m]$ for all modes ϕ_{ij} (doesn't depend on the vibrational mode-shape).

Note that we can also define an effective mass of the effective displacement — a useful expression for more complicated structures like the end-mirrors, discussed in Section 7.3.2. For generic vibrational modes with index k (representing either the mirror or the membrane), this quantity is defined:

$$m_{eff}^k \equiv \frac{m_k}{\eta_k^2} = \frac{\langle E_k \rangle}{\Omega_k^2 \langle \delta z_m^{k\,2} \rangle} \tag{7.20a}$$

$$= \frac{\frac{1}{V} \int_V |\vec{\phi}_k(x,y,z)|^2 dxdydz \times \int_S |\psi_{mn}(x,y,z)|^2 dxdydz}{\int_S \hat{z} \cdot \vec{\phi}_k(x,y,z) |\psi(x,y,z)|^2 dxdydz} \cdot m_{phys}, \tag{7.20b}$$

where recall $|\vec{\phi}|^2 = \vec{\phi}^* \cdot \vec{\phi}$ for vectors and $|\psi|^2 = \psi^* \psi$ for scalars. The expression for m_{eff}^k is useful because it does not depend on the choice of normalization for either ψ_{mn} or ϕ_k.

The common thread between all of these expressions is the spatial overlap factor, η_k. We now consider a relevant example of its computation.

7.1.3.1 Example: TEM$_{00}$ and Square Membrane

We will usually be concerned with the spatial overlap between a square membrane (width w_m) and a TEM$_{00}$ cavity mode (waist w_c). Assume that the membrane is located near the geometric center of the cavity ($z_m << L/2$) and displaced by (x_0, y_0) from the cavity axis. In this case the expression for the spatial overlap at the equilibrium position of the membrane ($z = z_m$) simplifies to:

$$\vec{\phi}_{ij}(x,y,z_m) = \sin\left(\frac{i\pi(x + \frac{w_m}{2})}{w_m}\right) \sin\left(\frac{j\pi(y + \frac{w_m}{2})}{w_m}\right) \hat{z} \tag{7.21a}$$

$$\psi_{mn}^+(x,y,z_m) \approx i|N_{00}|e^{\frac{-(x-x_0)^2-(y-y_0)^2}{w_c^2}} e^{ik_{mn}z_m} \tag{7.21b}$$

$$\eta_{ij} \approx \frac{2}{\pi w_m^2} \int_{-\frac{w_m}{2}}^{\frac{w_m}{2}} \int_{-\frac{w_m}{2}}^{\frac{w_m}{2}} \sin\left(\frac{i\pi(x + \frac{w_m}{2})}{w_m}\right) \sin\left(\frac{j\pi(y + \frac{w_m}{2})}{w_m}\right) e^{\frac{-2(x-x_0)^2-2(y-y_0)^2}{w_c^2}} dxdy. \tag{7.21c}$$

In Figure 7.5 we compute the spatial overlap between a square membrane mode and a TEM$_{00}$ optical mode for two sets of parameters, $\{w_c, w_m, x_0, y_0\} = \{35.7\ \mu m, 500\ \mu m, 0\ \mu m, 0\ \mu m\}$ and $\{35.7\mu\ m, 500\ \mu\ m, 45\ \mu m, 120\ \mu m\}$, the latter corresponding to the position used in the optomechanical cooling experiment in Chapter 9. Note that in the first case, only odd-ordered modes are coupled to the cavity. In the latter case, the (6,6) mode that we would like to address has reduced optomechanical coupling characterized by a spatial overlap factor of $\eta_{66} = 0.64$.
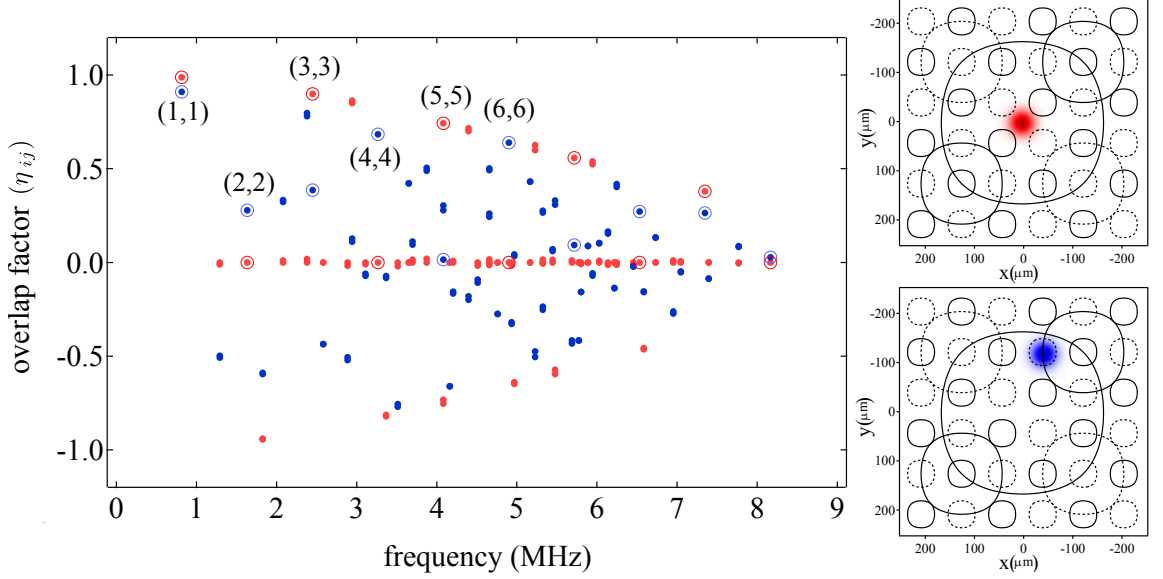
Figure 7.5: Spatial overlap factor between the TEM$_{00}$ cavity mode ($w_c = 35.7\,\mu$m) and the first 100 modes of a square membrane with dimensions $\{d_m, w_m\} = \{50\text{ nm}, 0.5\text{ mm}\}$. Red points correspond to the membrane centered on the optical mode, $\{x_0, y_0\} = \{0\,\mu\text{m}, 0\,\mu\text{m}\}$. Blue points correspond to an offset of $\{x_0, y_0\} = \{45\,\mu\text{m}, 120\,\mu\text{m}\}$. Circles indicate "diagonal" modes ϕ_{ii}. Contours for $\phi_{11,33,66}(x, y, z_m) = \pm 1/2$ are shown in the upper- and lower-right plots, with a density plot of the optical mode $\psi_{00}(x - x_0, y - y_0, z_m)$ overlaid. z_m is the the equilibrium position of the membrane.

7.2 Multimode Vibration of the MIM Cavity and "Effective Displacement"

In general, cavity resonance frequency fluctuations will arise due to multi-mode vibration of both the mirrors and the membrane. We can express the sum effect in terms of the vibrational modes of mirror 1 (index k_1), mirror 2 (index k_2), and the membrane (index (i, j)), respectively, as

$$\delta\omega_c = g_1 \sum_{k_1} \eta_{k_1} b_{k_1} + g_m \sum_{ij} \eta_{ij} b_{ij} + g_2 \sum_{k_2} \eta_{k_2} b_{k_2} \tag{7.22a}$$

$$= g_1 \sum_{k_1} \delta z_1^{k_1} + g_m \sum_{ij} \delta z_m^{ij} + g_2 \sum_{k_2} \delta z_2^{k_2} \tag{7.22b}$$

where $g_{1,2,m}$ denote the frequency shift per unit rigid axial displacement of mirror 1, mirror 2, and the membrane, respectively, η represents the spatial overlap factors defined by Eq. 7.18, and $\delta z \equiv \eta b$ is the effective displacement associated with η (Eq. 7.18). All three of $g_{1,2,m}$ will depend on the membrane's position, as discussed in Section 7.3.2.3.

We can express multimode displacement of mirror 1, mirror 2, and the membrane in the shorthand notation

$$\delta\omega_c = g_1 \delta z_1 + g_m \delta z_m + g_2 \delta z_2, \tag{7.23}$$

$\delta z_{m,1,2}$ are obtained by summing over the corresponding set of vibrational for the membrane, mirror 1, and mirror 2 in Eq. 7.22. We refer to $\delta z_{m,1,2}$ as the (total) effective displacement of the membrane, mirror 1, and mirror 2, respectively.

Finally, we can associate with $\delta\omega_c$ an *effective cavity length change*

$$\delta L \equiv \delta\omega_c/g_0 \tag{7.24}$$

defined as the cavity length change necessary to produce $\delta\omega_c$ in a standard two-mirror resonator (with no membrane).

For stochastic changes, the power spectral density of each of these variables are related accordingly:

$$S_{\omega_c}(\Omega) = S_L(\Omega)/g_0^2 \tag{7.25a}$$

$$= g_1^2 S_{z_1} + g_m^2 S_{z_m} + g_2^2 S_{z_2} \tag{7.25b}$$

$$= g_1^2 \sum_{k_1} S_{z_1^{k_1}} + g_m^2 \sum_{ij} S_{z_m^{ij}} + g_2^2 \sum_{k_2} S_{z_2^{k_2}} \tag{7.25c}$$

$$= g_1^2 \sum_{k_1} \eta_{k_1}^2 S_{b_{k_1}} + g_m^2 \sum_{ij} \eta_{ij}^2 S_{b_{ij}} + g_2^2 \sum_{k_2} \eta_{k_2}^2 S_{b_{k_2}}. \tag{7.25d}$$

We now consider multimode thermal motion as an example.

7.3 Multimode Thermal Noise Spectrum

We are now in a position to describe multimode vibration of the "membrane-in-the-middle" (as well as the multimode vibration of our end-mirror substrates). We first consider only membrane motion. A single internal mode of the membrane is described by generalized amplitude b_{ij} and obeys the equation of motion for a damped harmonic oscillator given in Eq. 7.2. This equation is characterized by effective mass m_{ij}, undamped resonance frequency Ω_{ij}, and damping coefficient $\Gamma_{ij}(\Omega)$. Applying the Fluctuation Dissipation Theorem as described in Section 2.2, the power spectral density of thermal fluctuations of b_{ij}, $S_{b_{ij}}(\Omega)$, is given by (Eq. 2.17):

$$S_{b_{ij}}(\Omega) = |\chi_{ij}(\Omega)|^2 4k_B T_b \Gamma_{ij}(\Omega) \tag{7.26a}$$

$$= \frac{4k_B T_{bath}\Gamma_{ij}(\Omega)}{m_{ij}} \frac{1}{(\Omega_{ij}^2 - \Omega^2)^2 + \Omega^2\Gamma_{ij}^2(\Omega)} \frac{m^2}{Hz}, \tag{7.26b}$$

where $\chi_{ij}(\Omega) = F_{ij}(\Omega)/b_{ij}(\Omega)$ is the mechanical susceptibility as determined from Eq. 7.2 and $4k_B T_{bath}\Gamma_{ij}(\Omega)$ is the spectral density of thermal force fluctuations experienced by b_{ij}. Note that the generic frequency-dependent damping term reduces to a constant $\Gamma_{ij}(\Omega) \to \Gamma_{ij}$ for velocity

damping and $\Gamma_{ij}(\Omega) \to \Gamma_{ij}(\Omega_{ij}) \cdot \Omega_{ij}/\Omega$ for structural damping, as discussed in Section 2.2.

In the limit that all of the modes are decoupled, the total thermal noise spectrum is given by an incoherent sum according to Eq. 7.25. Expressed as effective length fluctuations, the total spectrum of cavity resonance frequency fluctuations produced by thermal motion of the membrane is thus given by:

$$S_L(\Omega)|_{mem} = g_0^{-2} S_{\omega_c}(\Omega)|_{mem} = \sum_{ij} \frac{g_m^2}{g_0^2} \eta_{ij}^2 \frac{4 k_B T_{bath} \Gamma_{ij}(\Omega)}{m_{ij}} \frac{1}{(\Omega_{ij}^2 - \Omega^2)^2 + \Omega^2 \Gamma_{ij}(\Omega)^2}. \qquad (7.27)$$

With optical spring/damping forces included (Section 2.4, Eqs. 2.52), we can model the multi-mode thermal noise spectrum as:

$$S_L(\Omega)|_{mem} \approx \sum_{ij} \frac{g_m^2}{g_0^2} \eta_{ij}^2 \frac{4 k_B T_{bath} \Gamma_{ij}}{m_{ij}} \frac{1}{((\Omega_{ij} + \Delta\Omega_{opt}^{ij}(\Omega))^2 - \Omega^2)^2 + \Omega^2(\Gamma_{ij}(\Omega) + \Gamma_{opt}^{ij}(\Omega))^2}. \qquad (7.28)$$

Expressions for optical spring shift Ω_{opt}^{ij} and damping rate Γ_{opt}^{ij} will depend on $\{m_{ij}, \Omega_{ij}, \eta_{ij}\}$. We review these expressions in detail in Section 9.1.

For weak intrinsic and optical damping (Eq. 2.52), we can approximate the noise spectrum as a a superposition of velocity damped oscillators (this is a good approximation near each thermal noise peak)

$$S_L(\Omega)|_{mem} \approx \sum_{ij} \frac{g_m^2}{g_0^2} \eta_{ij}^2 \frac{4 k_B T_{bath} \Gamma_{ij}}{m_{ij}} \frac{1}{((\Omega_{ij} + \Delta\Omega_{opt}^{ij})^2 - \Omega^2)^2 + \Omega^2(\Gamma_{ij} + \Gamma_{opt}^{ij})^2}, \qquad (7.29)$$

where $\Gamma_{ij}(\Omega_{ij}) \equiv \Gamma_{ij}$, $\Delta\Omega^{ij}(\Omega_{ij}) \equiv \Delta\Omega_{opt}^{ij}$, and $\Gamma_{opt}^{ij}(\Omega_{ij}) \equiv \Gamma_{opt}^{ij}$.

When the noise peaks are well resolved, the effective temperature of each mode, $T_{eff}^{ij} \equiv m_{ij} \langle b_{ij}^2 \rangle / k_B$, is obtained by integrating the total noise spectrum over the noise peak centered at Ω_{ij}.

$$T_{eff}^{ij} \approx \frac{g_0^2}{g_m^2} \frac{1}{\eta_{ij}^2} \frac{m_{ij} \Omega_{ij}^2}{k_B} \int_{\Omega_{ij}} S_L(\Omega) d\Omega / 2\pi \approx \frac{\Gamma_{ij}}{\Gamma_{ij} + \Gamma_{opt}^{ij}} T_{bath}, \qquad (7.30)$$

where $\int_{\Omega_{ij}}$ denotes an integral over the noise peak centered at Ω_{ij}.

7.3.1 Membrane Thermal Noise: Examples

7.3.1.1 Role of Spatial Overlap and Mechanical Quality.

An example of broadband thermal noise for a $\{d_m, w_m\} = \{50 \text{ nm}, 0.5 \text{ mm}\}$ square membrane is shown in Figure 7.6. Here we use a physical mass of $m_{phys} = 33.75$ ng, a tension of $\mathcal{T} = 900$ MPa, and a uniform mechanical quality factor of $Q_{ij} = 1 \times 10^6$ for all modes, consistent with structural damping of the form $\Gamma_{ij}(\Omega) = \Omega_{ij}^2/(\Omega Q_{ij})$ (Section 7.3.1.2). The point we'd like to illustrate with this plot is the role that optomechanical overlap plays in determining the effective displacement noise
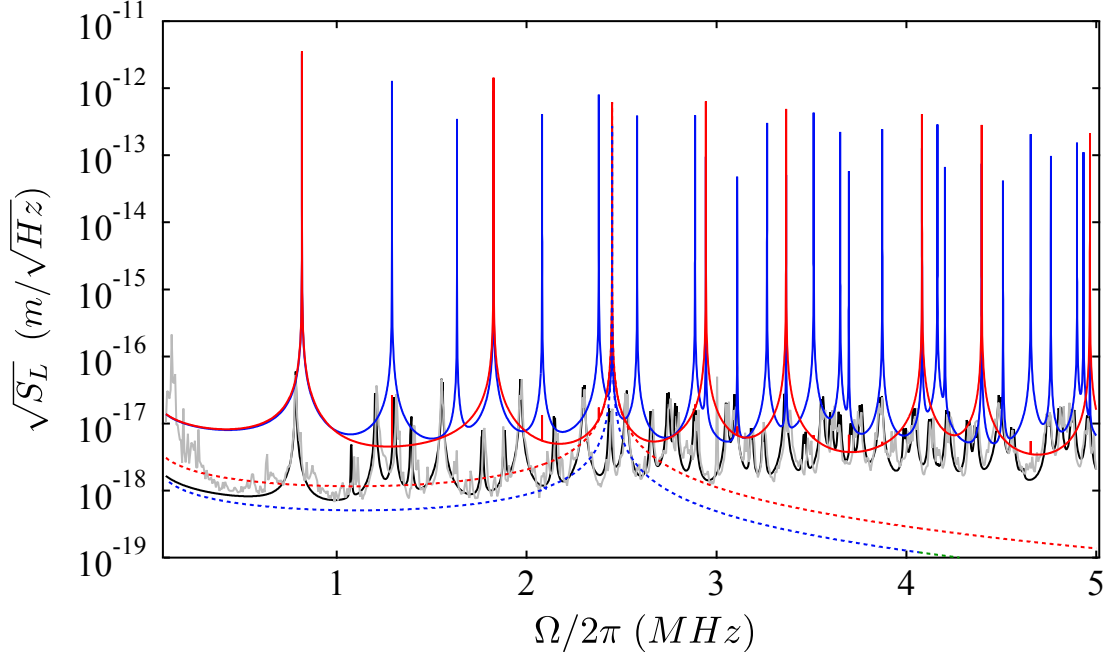
Figure 7.6: Illustration of the role of spatial mode overlap. Here we model the effective cavity length noise produced by Brownian vibration of a square membrane with dimensions $\{d_m, w_m\, m_{phys}, \mathcal{T}, Q_{ij}\}$ = $\{50\text{ nm}, 0.5\text{ mm}, 33.75\text{ ng}, 900\text{ MPa}, 10^6\}$ coupled to a TEM$_{00}$ cavity mode with $w_c = 35.7\ \mu$m. The cavity mode pierces the membrane at two different positions corresponding to Figure 7.5: $(x_0, y_0) = (0\,\mu\text{m}, 0\,\mu\text{m})$ (red) and $(45\,\mu\text{m}, 120\,\mu\text{m})$ (blue). These two positions give rise to different spatial overlap factors η_{ij}, hence the difference between the noise spectra. Dashed lines corresponds to an individual (3,3) vibrational mode. Gray and black lines correspond to measured and modeled internal vibrations of the cavity end-mirror substrates, described in Section 7.3.2. Note that the origin of the frequency axis is 10 kHz.

spectrum. We plot $S_L(\Omega)$ (Eq. 7.27) for the two locations of the TEM$_{00}$ mode as shown in Figure 7.5. Significantly, we observe that the noise floor is dominated by the off-resonant contribution from neighboring peaks, and that this structure, which is is due to the effective motion of multiple internal modes, depends on the spectrum of overlap coefficients. Thermal noise of the mirror substrates can be treated in a similar way, and we show for comparison the modeled and measured thermal noise of the cavity mirrors, discussed below (Section 7.3.2).

7.3.1.2 Structural Vs. Velocity Damping

As discussed in [29], velocity damping does not accurately describe the internal dynamics of most elastic bodies far from resonance. A more accurate description is obtained by allowing the phase lag φ of the elastic restoring force (modeled by a complex spring constant) to depend on the oscillation frequency in a generic fashion, $k_{ij}b_{ij}(\Omega) \to k_{ij}(1 + i\varphi_{ij}(\Omega))b_{ij}(\Omega)$. The result is a frequency-dependent damping term, $\Gamma_{ij}(\omega) = \Omega_{ij}^2 \varphi_{ij}(\Omega)/\Omega$. Two forms of damping are common. "Velocity" damping corresponds to the canonical dashpot system, for which the time lag of the restoring force is linearly pro-
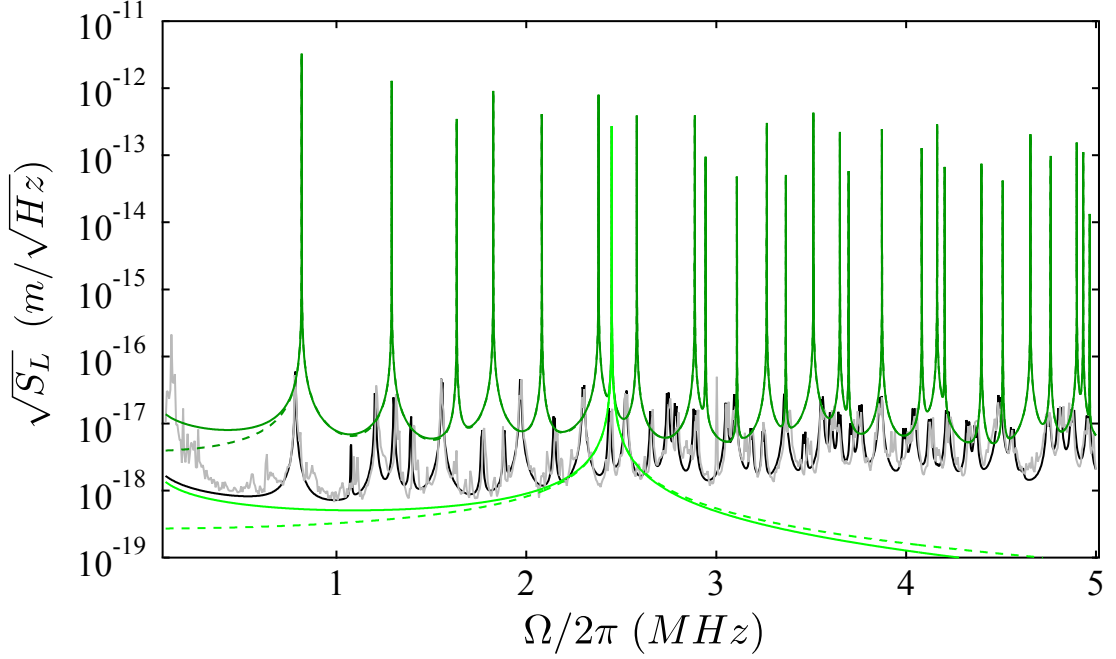
Figure 7.7: Comparison of structural and velocity damping. Here we re-calculate the effective cavity length noise spectrum shown in blue in figure 7.6 ($g_m = g_0$ and $\{d_m, w_m\, m_{phys}, \mathcal{T}, Q_{ij}\, w_c, x_0, y_0\} = \{50\text{ nm}, 0.5\text{ mm}, 33.75\text{ ng}, 900\text{ MPa}, 10^6, 35.7\,\mu\text{m}, 45\,\mu\text{m}, 120\,\mu\text{m}\}$) using two different mechanical damping models. Solid dark blue corresponds to structural damping, $\Gamma_{ij}(\Omega) = \Omega_{ij}^2/Q_{ij}\Omega$ with $Q_{ij} = 10^6$. Dashed dark green corresponds to velocity damping, $\Gamma_{ij}(\Omega) = \Gamma_{ij} = \Omega_{ij}/Q_{ij}$, with $Q_{ij} = 10^6$. Solid and dashed light green lines correspond to an individual (3,3) membrane peak for structural and velocity damping, respectively. Gray and black lines correspond to measured and modeled internal vibrations of the cavity end-mirror substrates, described in Section 7.3.2. Note that the origin of the frequency axis is 10 kHz.

portional to the oscillation frequency, $\varphi_{ij}(\Omega) = \Omega/Q_{ij}\Omega_{ij}$. This gives rise a frequency-independent damping $\Gamma_{ij}(\Omega) = \Gamma_{ij} = \Omega_{ij}/Q_{ij}$. "Structural" damping is common to many vibrating elastic solids and corresponds to the case for which the time lag is frequency independent, $\varphi_{ij}(\Omega) = 1/Q_{ij}$. The resulting damping rate depends linearly on frequency $\Gamma_{ij}(\Omega) = \Gamma_{ij}\Omega_{ij}/\Omega$, and manifests itself as a frequency-independent quality factor — roughly consistent, for example, with the membrane quality factor measurements made in Chapter 4.

For our current system, $\{d_m, w_m\, m_{phys}, \mathcal{T}, Q_{ij}\, w_c\} = \{50\text{ nm}, 0.5\text{ mm}, 33.75\text{ ng}, 900\text{ MPa}, \sim 10^6, 35.7\,\mu\text{m}\}$ the effect of internal damping is only significant at frequencies below. This point is illustrated in Figure 7.7.

7.3.2 Mirror Substrate Thermal Noise

The mirror substrates forming our MIM cavity were described in detail in Chapter 3. Their dimensions are recapped in Figure 7.8. The internal vibration of these substrates was once the subject of
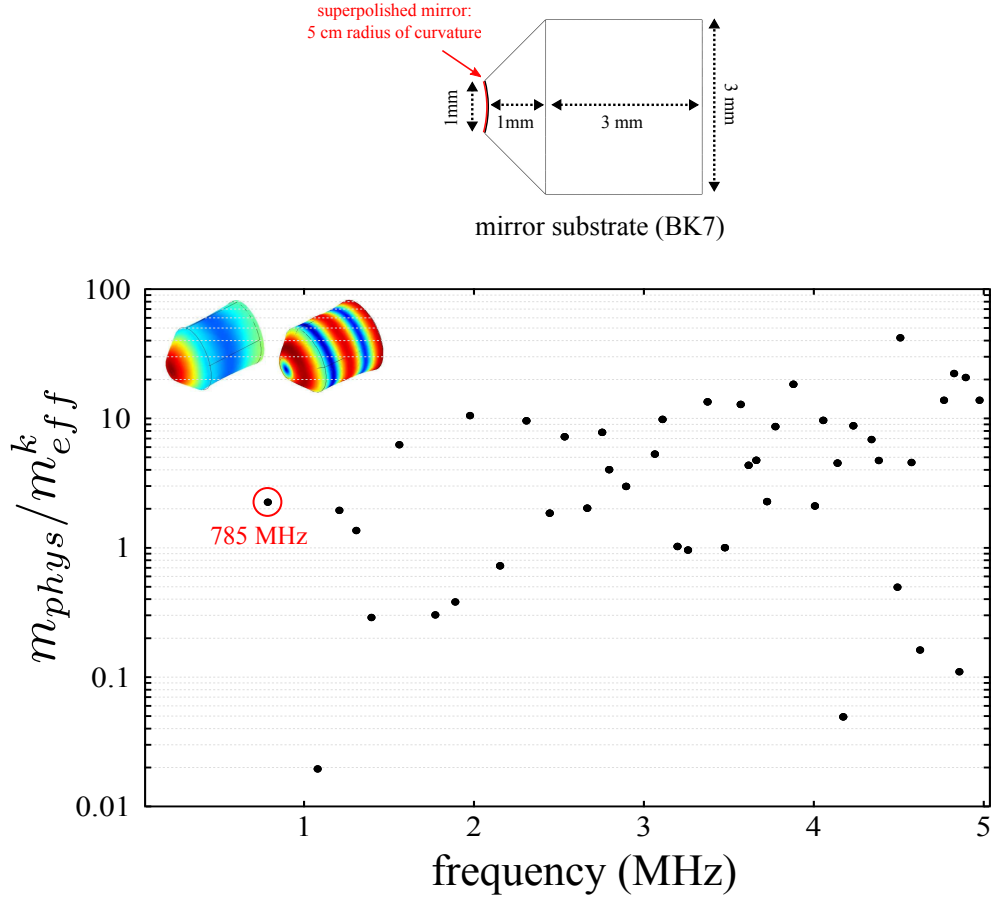
Figure 7.8: Effective mass of our mirror vibrational modes: here we plot the inverse effective mass coefficient of the *effective displacement* for each mirror mode, m_{phys}/m_{eff}^k, as defined by Eq. 7.20b and Eq. 7.31. To compute these values, we assume a TEM_{00} cavity mode with waist of 35.7 μm that is centered on the axis of the cylindrical mirror substrate. Only axisymmetric modes have finite effective mass.

vigorous investigation in our lab. Originally designed for short, $L \sim 10\,\mu$m, cavities for our CQED project, it was thought that their displacement might produce enough intensity noise to limit the lifetime of an atom trapped by the cavity field (for details, we refer the reader to Joe Buck's thesis [69]). An analogous set of concerns is addressed in Chapter 10, as we anticipate the same intensity noise to limit the base temperature of a laser-cooled membrane mode. In light of this concern and because a body of historical data was available [69], we have found it important to sanity check our thermal noise model against the more complicated internal vibration of the mirror substrates.

7.3.2.1 Effective Mass Coefficients

The spatial overlap factors and effective masses of the mirror substrates are difficult to obtain analytically. Our post-doc, Kang-Kuen Ni, was able to solve for the vibrational mode shape functions numerically using the finite element software available from COMSOL[80]. A description of the

"Structural Mechanics" module she used is provided in [81]. In the model, we have made the following assumptions: (a) we assume that the substrate is a homogeneous block of Bk7 glass, (b) we assume that the mirror is "free", i.e., we ignore the fact that a fraction of its surface is bound with adhesive to a Bk7 glass v-block (see Figure 5.2), (c) we ignore the $\approx 10 - \mu$m-thick dielectric coating deposited on the polished mirror face, and (d) we ignore the 5 cm radius of curvature of the mirror face. We also assume the following density, Young's modulus, and Poisson's ratio associated with Bk7 glass: $\{\rho, E, \nu\} = \{2.51 \text{ g/cm}^3, 81 \text{ GPa}, 0.208\}$. With these assumptions and the dimensions given in Figure 7.8, COMSOL is used to find solutions to the 3D elastic wave equation. This produces a set of eigenmodes and their eigenfrequencies $\{\vec{\phi}_k(x, y, z), \Omega_k\}$. From among these modes, we restrict our attention to those which are axisymmetric. We do this under the assumption that the cavity mode is centered on the mirror, in which case the non-axisymmetric modes are expected to have small optomechanical overlap. The remaining modes correspond roughly to longitudinal cylinder modes ($m_{eff}^k \approx m_{phys}/2$) mixed with thick circular plate modes. The mass of the cylinder is ≈ 61 mg and the length is $L_s = 4$ mm; the latter predicts a fundamental frequency of roughly $\sqrt{E/\rho}/2L_s \sim 710$ kHz. Comsol predicts 785 kHz, which is coincidentally near the ~ 800 kHz fundamental of our $\{d_m, w_m, \mathcal{T}\} = \{50 \text{ nm}, 0.5 \text{ mm}, 900 \text{ MPa}\}$ square membranes.

In Figure 7.8, we plot the effective mass coefficients of the *effective* mirror displacement, m_{eff}^k, as defined in Eq. 7.20. We assume a TEM$_{00}$ mode with waist $w_c = 35.7 \, \mu$m that is centered on the axis of the cylindrical mirror substrate, and which therefore is only coupled to axially symmetric vibration modes of the substrate. As noted earlier, the definition of m_{eff}^k does not depend on the overall normalization of ϕ_k or ψ_{mn}. The algorithm we use is

$$\frac{m_{eff}^k}{m_{phys}} = \frac{\frac{1}{V} \int_V ||\vec{\phi}_k(r, \theta, z)||^2 r dr d\theta dz}{\left(\frac{2}{\pi w_m^2} \int_0^{2\pi} \int_0^{0.5 \text{ mm}} \phi_k(r, \theta, z_0) e^{\frac{-2r^2}{w_c^2}} r dr d\theta\right)^2}, \tag{7.31}$$

where V is the volume of the mirror substrate and z_0 is the position of the mirror face.

7.3.2.2 Mirror Substrate Noise

The spectrum of eigenfrequencies and effective masses can be used to predict the effective cavity length noise produced by thermal motion of the mirror substrates. With no membrane in the middle, the effective cavity length noise is given by the incoherent sum of the effective displacement of each mirror:

$$S_L(\Omega)|_{sub} = S_{z_1}(\Omega) + S_{z_2}(\Omega) \tag{7.32a}$$

$$S_{z_{(1,2)}}(\Omega) = \sum_k \frac{4k_B T_{bath} \Gamma_{k,(1,2)}(\Omega)}{m_{eff}^{k,(1,2)}} \frac{1}{(\Omega_{k,(1,2)}^2 - \Omega^2)^2 + \Omega^2 \Gamma_{k,(1,2)}^2(\Omega)}; \tag{7.32b}$$
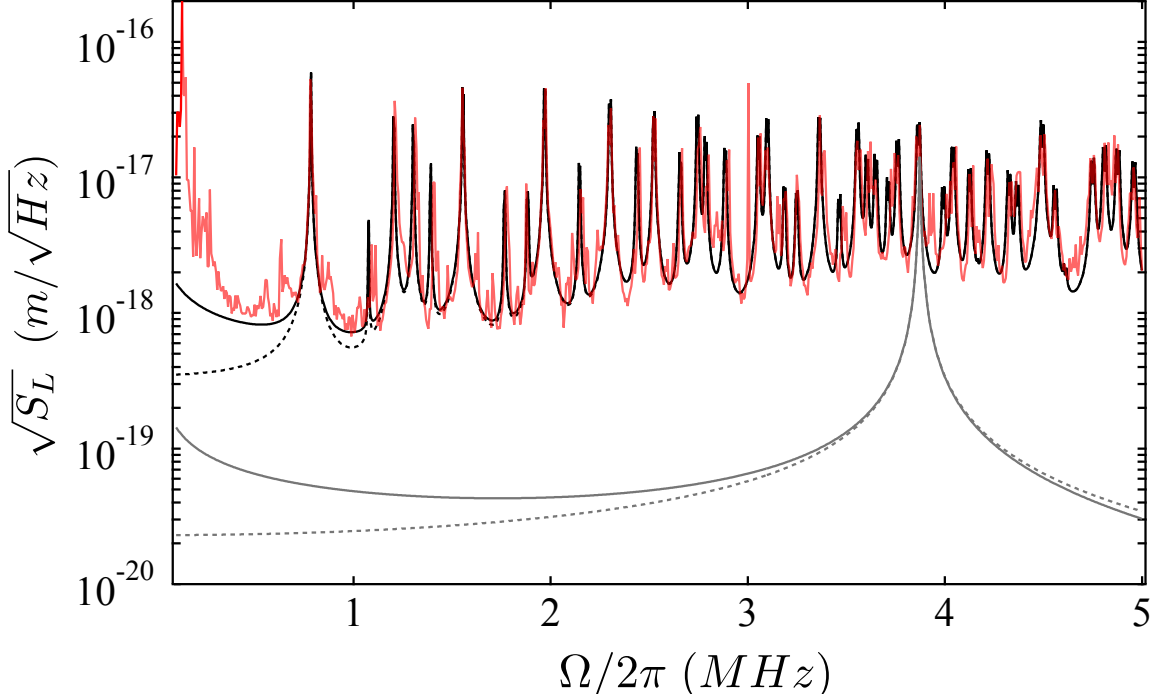
Figure 7.9: Model and measurement of the effective cavity length noise due to thermal excitation of *both* end-mirror substrates (Eq. 7.32). Solid and dashed correspond to internal and velocity damping models, respectively. Black and gray correspond to the full multimode spectrum noise spectrum and the thermal noise spectrum of a single peak, respectively. Pink corresponds to a measurement made using a detuned probe, as discussed in the following section. A qualitative match was achieved by assuming a uniform quality factor of 650 for the mirror modes and by an ad hoc adjustment of the eigenfrequencies of mirrors 1 and 2 by a factor of 0.995 and 0.998, respectively.

where "1" and "2" indicate the input and output mirrors, respectively. Note we have used the fact that the optomechanical coupling of each mirror position is g_0 in a normal FP cavity.

This model is as shown in Figure 7.9 alongside a measurement performed with the membrane removed, as explained in the next chapter. In the figure we compare the prediction for velocity and internal damping models. The discrepancy is small, and both models are found to be in good qualitative agreement with the measurement. To achieve this qualitative match, we assume that all of the mirror modes have a quality factor of $Q_k = 650$, consistent with the internal damping model. We also make an ad hoc adjustment of the eigenfrequencies by a factor of 0.995 and 0.998 from the model prediction, respectively, to match the splitting of each peak in the measured noise spectra – believed to correspond to small dimensional differences in the two mirrors.

7.3.2.3 End-Mirror Coupling in a MIM Cavity

It's important to mention that taking an incoherent sum of the effective displacement noise of each end-mirror substrate *does not* describe the effective cavity length noise due to the substrates when
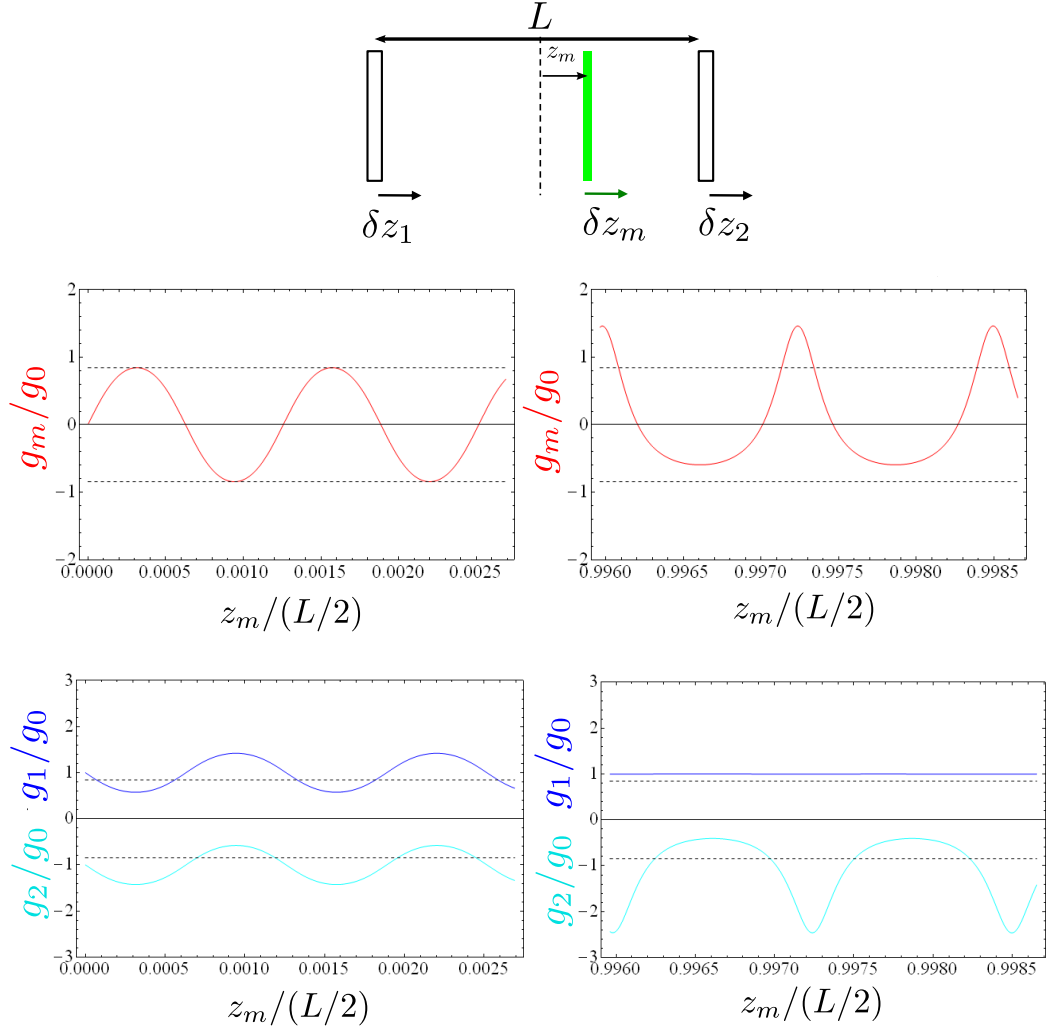
Figure 7.10: Plots of membrane and single end-mirror coupling in the MIM cavity as a function of position of the membrane. Red, purple, and cyan curves correspond to the optomechanical coupling of the membrane, mirror 1, and mirror 2, respectively, for the 1-dimensional system sketched at the top. The left column and the right column correspond to the equilibrium membrane position, z_m located near cavity center and near mirror 2, respectively.

the membrane is present. This is because unlike a normal Fabry-Perot cavity, the MIM cavity is sensitive to common-mode translation of the two mirrors (indeed, translating the two mirrors in tandem is *indistinguishable* from translating the the membrane). To include this effect, we first numerically compute the optomechanical coupling of the entry (mirror 1) and exit (mirror 2) end mirrors in the MIM cavity as a function of membrane position, using the plane-wave model discussed in Section 3.3.1. The results are shown in Figure 7.10, with g_m/g_0, g_1/g_0, and g_2/g_0 representing the optomechanical coupling of the membrane (effective displacement δz_m), mirror 1 (effective displacement δz_1), and mirror 2 (effective displacement δz_2) relative to the canonical end-

mirror coupling, $g_0 = \omega_c/L$. All three couplings are functions of the membrane's equilibrum position, z_m. By numerically adding and subtracting the curves shown in Figure 7.10, it can be shown that:

$$\delta\omega_c = g_1\delta z_1 + g_2\delta z_2 + g_m\delta z_m \tag{7.33a}$$

$$2g_0 = g_1\left(1 + \frac{2z_m}{L}\right) - g_2\left(1 - \frac{2z_m}{L}\right) \tag{7.33b}$$

$$-g_m = g_1 + g_2. \tag{7.33c}$$

There are at least two interesting ways to write (7.33a): in terms of end mirror displacements $\delta z_{1,2}$, and in terms of symmetric/antisymmetric displacement: $\delta z_\pm = (\delta z_1 \pm \delta z_2)/2$. Combining (7.33b) and (7.33c), we find:

$$\delta\omega_c = g_1\delta z_1 + g_2\delta z_2 + g_m\delta z_m = g_+\delta z_+ + g_-\delta z_- + g_m\delta z_m \tag{7.34a}$$

$$g_1 = g_0 - \frac{g_m}{2}\left(1 - \frac{2z_m}{L}\right) \tag{7.34b}$$

$$g_2 = -g_0 - \frac{g_m}{2}\left(1 + \frac{2z_m}{L}\right) \tag{7.34c}$$

$$g_+ = g_1 + g_2 = -g_m \tag{7.34d}$$

$$g_- = g_1 - g_2 = 2\left(g_0 + g_m\frac{z_m}{L}\right). \tag{7.34e}$$

Evidently the optomechanical coupling of δz_1 and δz_2 are both functions of the membrane position z_m. As expected, the optomechanical coupling (g_+) to symmetric displacement (δz_+) is equivalent to the optomechanical coupling of the membrane (g_m) and vanishes when the membrane is at a node or an antinode of the intracavity field. The optomechanical coupling (g_-) to antisymmetric (cavity-length-changing) displacement of the mirrors (δz_-) is a complicated function of membrane position, but reduces to twice the canonical coupling ($2g_0$) when the membrane is located at the midpoint of the cavity.

Finally, using expressions for g_1 and g_2 and assuming $z_m = 0$, we can write down the total effective displacement noise of MIM cavity as:

$$S_L(\Omega) = \left(1 - \frac{g_m}{2g_0}\right)^2 S_{z_1}(\Omega) + \left(1 + \frac{g_m}{2g_0}\right)^2 S_{z_2}(\Omega) + \left(\frac{g_m}{g_0}\right)^2 S_{z_m}(\Omega), \tag{7.35a}$$

where superscripts $\{1, 2, m\}$ indicate displacement noise of mirror 1, mirror 2, and the membrane, respectively.

Chapter 8

Cavity-Based Thermal Noise Measurement

In the previous chapter we described the optomechanical coupling of an internally vibrating mirror or membrane in the MIM system. We then developed a model for the multimode thermal noise of the composite system. In this chapter we discuss the task of measuring thermal noise in lab, developing in detail several subjects that have been points of concern. In overview: (1) we describe an input-output model for the MIM cavity based on the canonical two-mirror optomechanical system. (2) We derive transfer function characterizing two techniques used to map membrane/mirror fluctuations into photocurrent fluctuations. The first technique consists of driving the cavity with a detuned input field and monitoring the transmitted power. The second technique consists of driving the cavity with a resonant input field and monitoring the phase of the reflected field, using the "Pound-Drever-Hall" method. (3) We predict the shot noise limited sensitivity of these measurements and compare to the predicted thermal noise of the membrane. (4) We detail a technique for calibration of the displacement measurement by phase modulating of the input field. (5) We walk through three important examples: (a) measurement of the temperature of a single membrane mode, (b) calibration of the spectrum of "spatial overlap" factors, $\{\eta_{ij}\}$ (Section 7.1.3) using a multimode thermal noise measurement, and (c) characterization of the broadband displacement noise background due to laser frequency noise and thermal motion of the end-mirror substrates.

8.1   Basic Approach: Measurement Response Function

To treat mirror and membrane motion on equal footing, we will use the fact that in any optomechanical system, displacement of the mechanical element manifests itself as a displacement of the cavity resonance frequency, $\delta\omega_c(t) = g\delta z(t)$, where the definition of displacement coordinate $\delta z(t)$ and optomechanical coupling g depends on the geometry of the system (see, e.g., Section 7.1.3). In the lab, with help of the cavity transfer function, we transform cavity frequency fluctuations into

photocurrent fluctuations, $\delta i(t) = i(t) - \langle i \rangle$, by directing the field leaking out of the cavity onto a photodiode. The transformation constitutes a "measurement", and we will assume that it is linear and described by a response function $G_{i,\omega_c}(\Omega)$ (Section 2.1):

$$G_{i,\omega_c}(\Omega) = \frac{\delta i(\Omega)}{\delta \omega_c(\Omega)} \; A/Hz; \;\; \{\delta i(\Omega), \delta \omega_c(\Omega)\} = \int_{-\infty}^{\infty} \{\delta i(t), \delta \omega_c(t)\} e^{-i\Omega t} dt. \qquad (8.1)$$

In the framework of linear response theory, measurement of noisy signals can be described using the transfer function $|G_{i,\omega_c}(\Omega)|^2$ (Eq. 2.12). By noise, we will mean a random signal, e.g., a noisy photocurrent $i(t)$, described by a single-sided power spectral density, $S_i(\Omega)$ (Eq. 2.9), with units of A^2/Hz, normalized such that $\int S_i(\Omega) d\Omega / 2\pi = \langle i^2(t) \rangle$. The mapping of cavity resonance frequency noise into photocurrent noise is characterized by:

$$S_i(\Omega) = |G_{i,\omega_c}(\Omega)|^2 S_{\omega_c}(\Omega). \qquad (8.2)$$

Using the nomenclature from Section 7.1.3, the generic relationship between photocurrent noise, cavity resonance frequency noise, and effective/actual displacement noise for multimode vibration of the membrane can be summarized as follows:

$$S_i(\Omega) = |G_{i,\omega_c}(\Omega)|^2 S_{\omega_c}(\Omega) = |G_{i,\omega_c}(\Omega)|^2 g_m^2 S_{z_m}(\Omega) = |G_{i,\omega_c}(\Omega)|^2 g_m^2 \sum_{ij} \eta_{ij}^2 S_{b_{ij}}(\Omega). \qquad (8.3a)$$

Here $S_{z_m}(\Omega)$ is the spectral density of effective membrane displacement, and $S_{b_{ij}}(\Omega)$ is spectral density of fluctuations in physical vibrational mode amplitude b_{ij}.

8.2 Input-Output Model of the MIM Cavity

8.2.1 Two-Mirror Model

Our treatment of the MIM system will be based on the input-output formalism of a canonical two-mirror optomechanical system, borrowing heavily from the description given in Sections 2.3–2.4. In that setting, the "equation of motion" for a single mode of the intracavity field is given by (Eq.

2.33):

$$\dot{a}(t) = -\left(\kappa + i(\Delta - \delta\omega_c(t))\right)a(t) + \sqrt{2\kappa_1}E_{in}(t) \tag{8.4a}$$

$$\delta\omega_c(t) = g_0\delta z_1(t) + g_0\delta z_2(t) \tag{8.4b}$$

$$E_{out}(t) = \sqrt{2\kappa_2}a(t) \tag{8.4c}$$

$$E_{ref}(t) = \sqrt{2\kappa_1}a(t) - E_{in}(t) \tag{8.4d}$$

$$\{P_{in}(t), P_{out}(t), P_{ref}(t)\} \equiv \{|E_{in}(t)|^2, |E_{out}(t)|^2, |E_{ref}(t)|^2\}. \tag{8.4e}$$

The variables in this formula are as follows:

- $\Delta \equiv \omega_0 - \langle\omega_c\rangle$ is the mean detuning between the monochromatic input field (frequency ω_0) and the cavity (resonance frequency $\omega_c(t) = \langle\omega_c\rangle + \delta\omega_c(t)$).

- $\{E_{in}(t), E_{out}(t), E_{ref}(t)\}$ are the complex amplitudes of the fields incident, transmitted, and reflected from the cavity, respectively, in the frame rotating at the frequency of the input laser, ω_0, normalized so that their square modulus gives optical power in the beam $\{P_{in}(t), P_{out}(t), P_{ref}(t)\}$. The incident field is assumed to be perfectly mode-matched to the cavity.

- $a(t)$ is the complex amplitude of the intracavity mode $\psi(x, y, z)$ in the frame rotating at ω_0, normalized so that $|a(t)|^2$ is the intracavity energy.

- κ is the total amplitude decay rate of the cavity. $\{\kappa_1, \kappa_2\}$ are the amplitude decay rates through the input mirror (mirror 1) and output mirror (mirror 2). For a lossless, high-finesse cavity, $\kappa = \kappa_1 + \kappa_2$.

- $\{\delta z_1(t), \delta z_2(t)\}$ are the effective displacements of mirrors 1 and 2 (see Section 7.3).

- $g_0 \equiv \omega_c/L$ is the "canonical" optomechanical coupling for an end-mirror in an idealized planar two-mirror resonator.

For a stationary cavity ($\delta\omega_c = 0$) and a monochromatic input field, $E_{in}(t) = \langle E_{in}\rangle$, detuned from resonance by $\Delta \equiv \omega_0 - \langle\omega_c\rangle$, the amplitude reflection and transmission coefficients of the cavity are given by:

$$F_R(\Delta) \equiv \frac{\langle E_{ref}\rangle}{\langle E_{in}\rangle} = \frac{2\kappa_1}{\kappa + i\Delta} - 1 \tag{8.5a}$$

$$F_T(\Delta) \equiv \frac{\langle E_{out}\rangle}{\langle E_{in}\rangle} = \frac{2\sqrt{\kappa_1\kappa_2}}{\kappa + i\Delta} \tag{8.5b}$$

$$|F_R(\Delta)|^2 + |F_T(\Delta)|^2 = 1 \text{ for no internal losses.} \tag{8.5c}$$

8.2.2 Extension of Two-Mirror Model to MIM System

We will use the canonical system as a model for the MIM system with a weakly reflective membrane. Several modifications are necessary. The first is the replacement of end-mirror coupling g_0 with functions $\{g_1(z_m), g_2(z_m), g_m(z_m)\}$ describing the z_m-dependent optomechanical coupling of mirror 1, mirror 2, and in the MIM system, as described in Section 7.3.2.3:

$$\delta\omega_c(t) = g_1(z_m)\delta z_1(t) + g_2(z_m)\delta z_2(t) + g_m(z_m)\delta z_m(t). \tag{8.6}$$

Two other differences are important to note: the interpretation of $\psi(x, y, z)$ and $\{\gamma_1, \gamma_2\}$ for the MIM system. For a regular Fabry-Perot cavity, $\psi(x, y, z)$ is a TEM_{mn} mode. For the MIM system, $\psi(x, y, z)$ approximates a TEM_{nm} mode in the transverse direction but has a different amplitude on the left- and right-hand side of the membrane. We will assume, moreover, that membrane reflectivity is weak enough that ratio of the field amplitude on the left and right side of the membrane reaches steady state much faster than the cavity decay time, so that $\psi(x, y, z)$ can be treated as a time-independent mode shape with amplitude $a(t)$ normalized so that $|a(t)|^2$ is the sum of the energies on the left- and right-hand sides of the cavity.

As a result of the power mismatch on the left and right hand sides of the cavity, we must be careful interpreting $\{\kappa_1, \kappa_2\}$, which are in general functions of the membrane's position. When losses from the mirrors and the membrane are negligible, it's still the case that $\kappa_1 + \kappa_2 = \kappa$ and that κ is the HWHM linewidth of the cavity power transmission function. One more equation relating the three rates can be obtained by considering the steady-state cavity transmission on resonance. Using Eq. 8.4 and assuming that the input field is monochromatic, we find:

$$F_T(\Delta = 0) = \sqrt{\frac{4\kappa_1\kappa_2}{\kappa^2}} \equiv F_{T,max}(z_m) \tag{8.7a}$$

$$F_R(\Delta = 0) = \frac{2\kappa_1 - \kappa}{\kappa} \equiv F_{R,min}(z_m). \tag{8.7b}$$

The resonant transmission $F_{T,max}(z_m)$ and reflection $F_{R,min}(z_m)$ are both functions of membrane position z_m as well as membrane/mirror reflectivities $\{r_m, r_1, r_2\}$. They can be obtained numerically by the method discussed in Section 3.4. Our symmetric MIM cavity ($r_1 \approx r_2$) behaves approximately like a regular symmetric cavity with $0.8 \lesssim F_{T,max}(z_m) \lesssim 1$; this is shown numerically in Figure 8.6 and by a measurement in Figure 6.7.
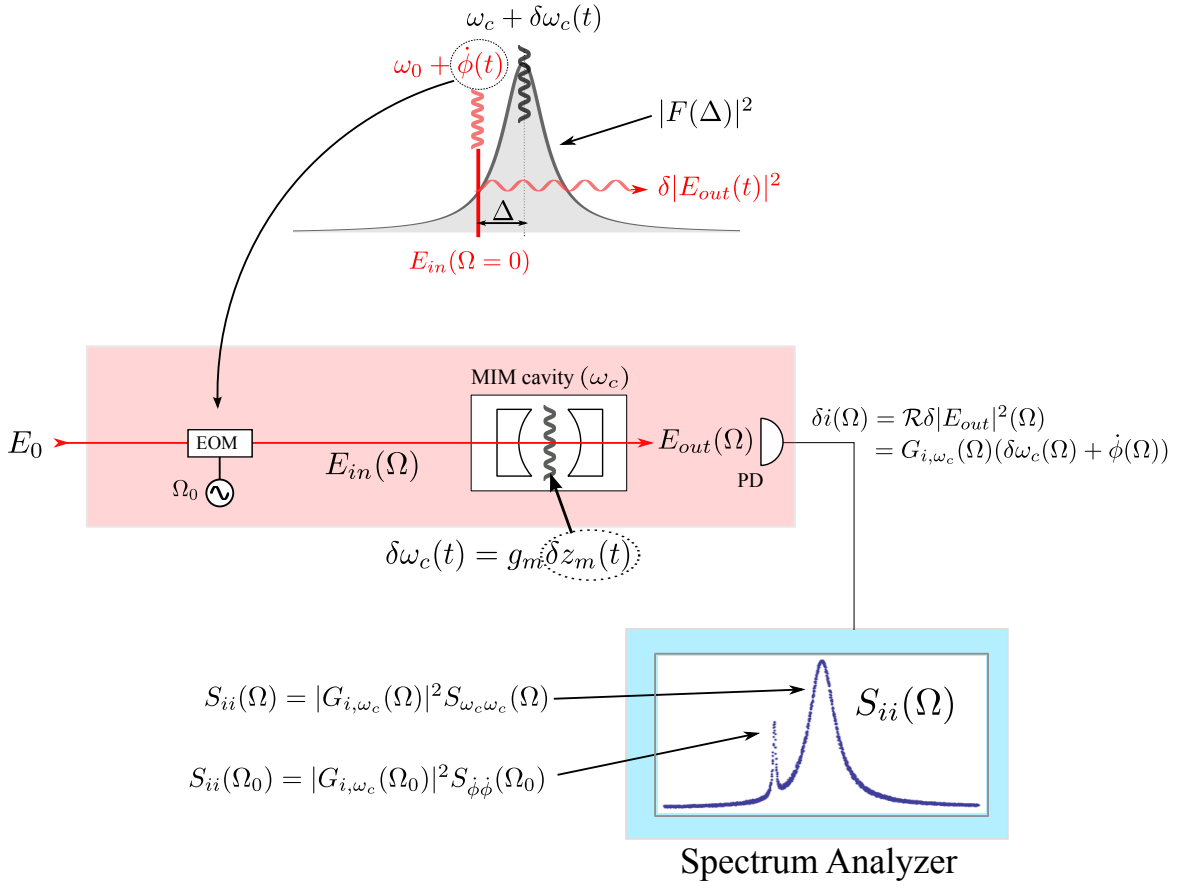
Figure 8.1: Block diagram of the detuned probe measurement

8.3 Response Function of the Detuned Probe (DP) Transmission Measurement

8.3.1 Slow Modulation: Steady-State Treatment

As illustrated in Figure 8.1, for this method we drive the cavity with a monochromatic input field, $E_{in}(t) = E_0$, and monitor the transmitted power. The steady-state cavity transmission as a function of detuning $\Delta \equiv \omega_0 - \langle \omega_c \rangle$ is obtained by solving (8.4) with $\dot{a} = 0$ and $\delta\omega_c = 0$:

$$|F_T(\Delta)|^2 = \frac{1}{1 + \Delta^2/\kappa^2} |F_{T,max}|^2. \tag{8.8}$$

Directing the output field to a photodetector produces a photocurrent proportional to its responsivity $\mathcal{R}$ (A/W):

$$i(t) = \mathcal{R}|E_{out}(t)|^2 = \mathcal{R}|F_T(\Delta)|^2|E_0|^2. \tag{8.9}$$

When ω_c is modulated slowly compared to the cavity linewidth κ, the resulting photocurrent modulation is approximated by differentiating the steady-state expression (Eq. 8.8), which gives

$$G_{i,\omega_c}(\Omega << \kappa) \approx \frac{d\,i}{d\,\omega_c} = \mathcal{R}|E_0|^2 \frac{d|F_T(\Delta)|^2}{d\omega_c} = \langle i \rangle \left(\frac{2\Delta}{\kappa^2} \right) \left(\frac{1}{1 + \Delta^2/\kappa^2} \right), \qquad (8.10)$$

where $\langle i \rangle = \mathcal{R}\langle |E_{out}(t)|^2 \rangle$ denotes the time-averaged (DC) value of the photocurrent. The response function in this case is independent of Ω, since the intracavity cavity field was assumed to instantaneously respond to cavity resonance frequency change. Note that this equation is true for both the standard Fabry-Perot cavity and the MIM cavity in the "slow modulation" limit.

8.3.2   Fast Modulation: Perturbative Treatment

To determine the measurement transfer function at frequencies comparable to the cavity decay time, one must conduct a more careful analysis based on the equation of motion of the cavity field (8.4). In this equation we allow the resonance frequency of the cavity to undergo a small fluctuations $\delta\omega_c(t) << \kappa$. We can simplify Eq. 8.4a by expressing variables as small fluctuations about their mean value, i.e.,

$$\{\delta a(t), \delta a^*(t), \delta E_{in}(t), \delta E_{ref}(t), \delta E_{out}(t)\} = \{\langle a \rangle, \langle a^* \rangle, \langle E_{in} \rangle, \langle E_{ref} \rangle, \langle E_{out} \rangle\} \qquad (8.11a)$$

$$- \{a(t), a^*(t), E_{in}(t), E_{ref}(t), E_{out}(t)\}. \qquad (8.11b)$$

If the input field is static ($\delta E_{in}(t) = 0$), the fluctuating part of the intracavity field obeys

$$\delta\dot{a}(t) \approx -(\kappa + i\Delta)\,\delta a(t) + i\delta\omega_c(t)\langle a \rangle, \qquad (8.12)$$

where $\langle a \rangle = \sqrt{2\kappa_1}\langle E_{in} \rangle/(\kappa + i\Delta)$.

The photocurrent derived from the output field is given by:

$$i(t) = \mathcal{R}|E_{out}(t)|^2 = 2\kappa_2 \mathcal{R}(|\langle a \rangle|^2 + \langle a \rangle \delta a^*(t) + \langle a \rangle^* \delta a(t)). \qquad (8.13)$$

Formally applying the Fourier transform (Eq. 2.1) to both sides of Eqs. 8.12–8.13 gives:

$$\delta a(\Omega) = \frac{i\delta\omega_c(\Omega)}{\kappa + i(\Delta + \Omega)}\langle a \rangle \qquad (8.14a)$$

$$[\delta a^*](\Omega) = \frac{-i\delta\omega_c(\Omega)}{\kappa - i(\Delta - \Omega)}\langle a \rangle^* \qquad (8.14b)$$

$$\delta i(\Omega) = 2\kappa_2 \mathcal{R}\left(\langle a \rangle [\delta a^*](\Omega) + \langle a \rangle^* \delta a(\Omega)\right) \qquad (8.14c)$$

$$= \langle i \rangle \delta\omega_c(\Omega)\left(\frac{i}{\kappa + i(\Delta + \Omega)} - \frac{i}{\kappa - i(\Delta - \Omega)} \right) \qquad (8.14d)$$

where $[\delta a^*](\Omega)$ is the Fourier transform of $\delta a^*(t)$.

The response function $G_{i,\omega_c}(\Omega) \equiv \delta i(\Omega)/\delta\omega_c(\Omega)$ inferred from Eq. 8.14 can be expanded as the product of the slow modulation solution (8.10) and a correction factor due to the finite response time of the cavity:

$$G_{i,\omega_c}(\Omega) \equiv \frac{\delta i(\Omega)}{\delta\omega_c(\Omega)} = \langle i \rangle \left(\frac{i}{\kappa + i(\Delta + \Omega)} - \frac{i}{\kappa - i(\Delta - \Omega)} \right) \tag{8.15a}$$

$$|G_{i,\omega_c}(\Omega)| = \langle i \rangle \left(\frac{2\Delta}{\kappa^2} \right) \left(\frac{1}{1 + \Delta^2/\kappa^2} \right) \sqrt{\frac{(\kappa^2 + \Delta^2)^2}{(\kappa^2 + \Delta^2)^2 + 2(\kappa - \Delta)(\kappa + \Delta)\Omega^2 + \Omega^4}} \tag{8.15b}$$

$$\text{Arg}[G_{i,\omega_c}(\Omega)] = -\tan^{-1}\left[\frac{\Delta^2 + \kappa^2 - \Omega^2}{2\Omega\kappa} \right]. \tag{8.15c}$$

For a typical setting of $\Delta = -\kappa$ used to implement optical damping in later chapters, the transfer function for the detuned probe measurement is given by:

$$|G_{i,\omega_c}(\Omega)|^2(\Delta = -\kappa) = \frac{\langle i \rangle^2}{\kappa^2} \times \frac{1}{1 + \Omega^4/4\kappa^4}. \tag{8.16}$$

8.4   Response Function of the Pound-Drever-Hall (PDH) Measurement

The Pound-Drever-Hall (PDH) method is a "self-heterodyne" technique used to measure the phase of the field reflected from the cavity [82, 54]. In PDH, a local oscillator (LO) is generated by phase modulating the input field at a frequency Ω_0 much larger than the cavity linewidth; the resulting "PDH" sidebands are directly reflected from the cavity. The remaining carrier portion of the input field is tuned into resonance with the cavity ($\Delta = 0$). A fraction gets into the cavity and leaks back out with a phase shift that is proportional to $\delta\omega_c(t)$. When combined on a photodetector, the beat between the reflection of far-detuned sidebands and the near-resonant carrier produces a rapidly fluctuating photocurrent fluctuation $\delta i(t) = \epsilon(t)\sin(\Omega_0 t + \phi)$ whose slowly varying envelope $\epsilon(t)$ is proportional to $\delta\omega_c(t)$. The PDH "error signal", $\epsilon(t)$, is extracted using a mixer. Important advantages of the PDH technique are (1) Ω_0 is typically an RF frequency, near which technical noise (e.g., noise produced by photodetector electronics) can be significantly reduced, and (2) the photosignal is produced without modulating — to first order — the intensity of the intracavity field, hence significantly reducing radiation pressure effects.

8.4.1   Fast Modulation

We here carry out a derivation of the response function for the PDH method that is appropriate for modulation frequencies much smaller than the PDH sideband frequency, Ω_0 which is much larger
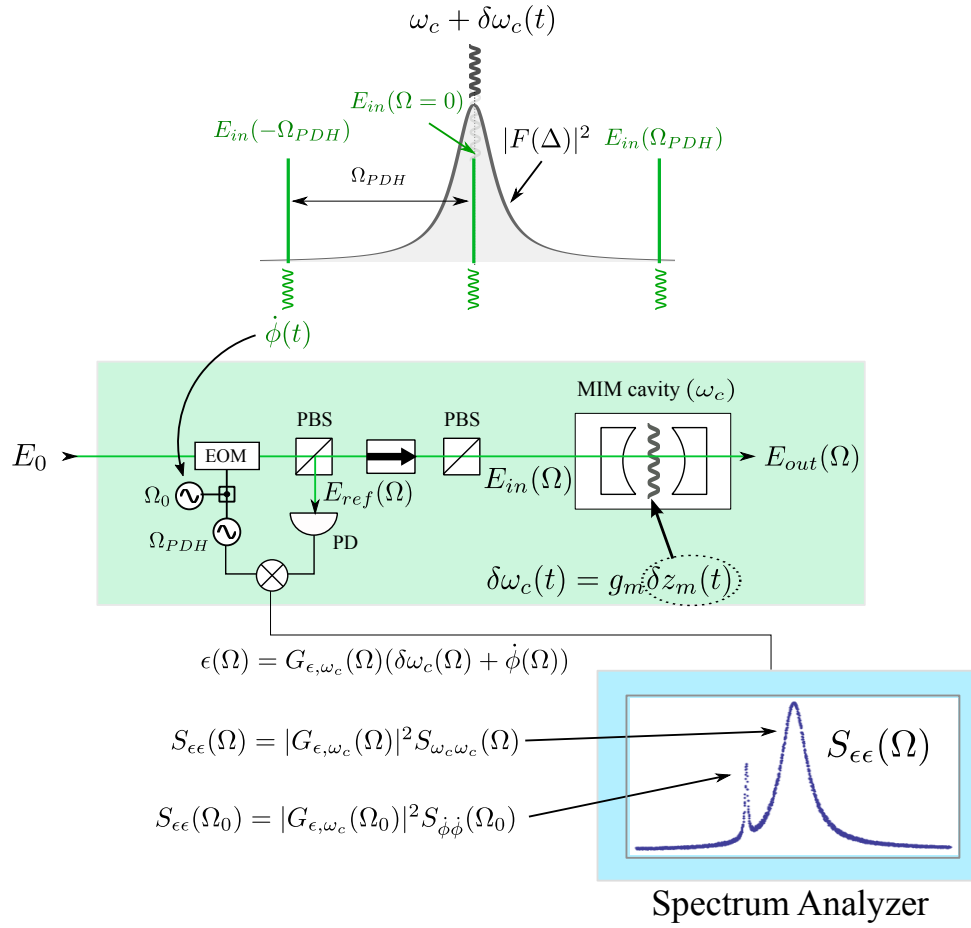
Figure 8.2: Block diagram of the Pound-Drever-Hall measurement

than the cavity linewidth $\Omega_0 >> \kappa$. We first expand the slowly varying envelope of the phase modulated input field using the Jacobi-Anger Expansion:

$$E_{in}(t) = E_0 e^{i\alpha \sin(\Omega_0 t)} = E_0 \sum_n J_n(\alpha) e^{in\Omega_0 t}, \tag{8.17}$$

where α is the phase modulation depth, J_n is the nth-order Bessel function of the first kind, and the sum is understood to extend over all integers from $-\infty$ to ∞.

Letting $a(t) = \langle a \rangle + \delta a(t)$, we can express the equation of motion for the field to first order in

$\delta a / \langle a \rangle$ as:

$$\dot{a}(t) = -(\kappa + i\Delta)a(t) + i\delta\omega_c(t)\langle a \rangle + \sqrt{2\kappa_1}E_{in}(t) \tag{8.18a}$$

$$E_{in}(t) = E_0 \sum_n J_n(\alpha)e^{in\Omega_0 t} \tag{8.18b}$$

$$E_{out}(t) = \sqrt{2\kappa_2}a(t) \tag{8.18c}$$

$$E_{ref}(t) = -E_{in}(t) + \sqrt{2\kappa_1}a(t), \tag{8.18d}$$

where $\langle a \rangle = \sqrt{2\kappa_1}E_0 J_0(\alpha)/(\kappa + i\Delta)$.

Inserting the expression for $\langle a \rangle$ into (8.18) and applying the Fourier transform to both sides gives

$$a(\Omega) = \frac{\sqrt{2\kappa_1}}{\kappa + i(\Delta + \Omega)} \left(\sum_n J_n(\alpha)\delta(\Omega - n\Omega_0) - \frac{i\delta\omega_c(\Omega)}{\kappa + i\Delta} \right) E_0 \tag{8.19a}$$

$$E_{ref}(\Omega) = \sqrt{2\kappa_1}a(\Omega) - E_{in}(\Omega). \tag{8.19b}$$

For PDH, the input field carrier frequency is usually on resonance ($\Delta = 0$) and the phase modulation frequency is large $\Omega_0 >> \kappa$. In this case we can simplify (8.19c) to include only the directly reflected field and the sidebands generated on the carrier inside the cavity:

$$E_{ref}(\Omega) \approx \left(\frac{2\kappa_1}{\kappa + i\Omega} - 1 \right) E_0 \sum_n J_n(\alpha)\delta(\Omega - n\Omega_0) - \frac{i}{\kappa + i\Omega}\frac{2\kappa_1}{\kappa}\delta\omega_c(\Omega)J_0(\alpha)E_0. \tag{8.20}$$

It's instructive at this point to move back into the time domain and consider a sinusoidal frequency modulation, $\delta\omega_c(t) = \delta\omega_{c,0}\cos(\Omega_m t) << \kappa$. In this case:

$$E_{ref}(t) = \sum_n \left(\frac{2\kappa_1}{\kappa + in\Omega_0} - 1 \right) E_0 J_n(\alpha)e^{in\Omega_0 t} - i\frac{2\kappa_1}{\kappa}\delta\omega_{c,0}J_0(\alpha)\frac{1}{2}\left(\frac{e^{i\Omega_m t}}{\kappa + i\Omega_m} + c.c. \right) E_0. \tag{8.21}$$

The average power in the reflected beam is approximately

$$\langle |E_{ref}(t)|^2 \rangle \approx |E_0|^2 \left(1 - (4\kappa_1\kappa_2/\kappa^2)J_0^2(\alpha) \right). \tag{8.22}$$

The relevant fluctuating part of the reflected power is contributed by terms which are oscillating at frequencies $\pm\Omega_0 \pm \Omega_m$. Using $\Omega_0 >> \kappa$, $J_1(\alpha) = -J_{-1}(\alpha)$, keeping only terms linear in $\delta\omega_c/\kappa <<$

1, and ignoring terms oscillating at $2\Omega_0$, we obtain

$$\delta|E_{ref}(t)|^2 \equiv |E_{ref}(t)|^2 - \langle|E_{ref}(t)|^2\rangle \tag{8.23a}$$

$$= \left|-J_1(\alpha)e^{i\Omega_0 t} - J_{-1}(\alpha)e^{-i\Omega_0 t} - i\delta\omega_{c,0}J_0(\alpha)\frac{2\kappa_1}{\kappa}\frac{1}{2}\left(\frac{e^{i\Omega_m t}}{\kappa + i\Omega_m} + c.c.\right)\right|^2 |E_0|^2 \tag{8.23b}$$

$$= \left(2J_1(\alpha)\sin(\Omega t) + \delta\omega_{c,0}J_0(\alpha)\frac{2\kappa_1}{\kappa}\,\mathrm{Re}\left[\frac{e^{i\Omega_m t}}{\kappa + i\Omega_m}\right]\right)^2 |E_0|^2 \tag{8.23c}$$

$$\approx 4J_0(\alpha)J_1(\alpha)|E_0|^2\frac{\delta\omega_{c,0}}{\kappa}\frac{2\kappa_1}{\kappa}\sqrt{\frac{1}{1 + (\Omega_m/\kappa)^2}}\cos\left(\Omega_m t - \tan^{-1}\left(\frac{\Omega_m}{\kappa}\right)\right)\sin(\Omega_0 t). \tag{8.23d}$$

The PDH error signal is obtained by passing $i(t) = \mathcal{R}|E_{ref}(t)|^2$ through a mixer to extract the slowly varying envelope of the $\sin(\Omega_0 t)$ quadrature. For an ideal mixer with no conversion loss, the resulting photocurrent is:

$$\epsilon(t) = 4J_0(\alpha)J_1(\alpha)\mathcal{R}|E_0|^2\frac{\delta\omega_{c,0}}{\kappa}\frac{2\kappa_1}{\kappa}\sqrt{\frac{1}{1 + (\Omega_m/\kappa)^2}}\cos\left(\Omega_m t - \tan^{-1}(\Omega_m/\kappa)\right) \tag{8.24a}$$

$$= 4J_0(\alpha)J_1(\alpha)\frac{\langle i\rangle}{1 - (4\kappa_1\kappa_2/\kappa^2)J_0^2(\alpha)}\frac{\delta\omega_{c,0}}{\kappa}\frac{2\kappa_1}{\kappa}\sqrt{\frac{1}{1 + (\Omega_m/\kappa)^2}}\cos\left(\Omega_m t - \tan^{-1}\left(\frac{\Omega_m}{\kappa}\right)\right). \tag{8.24b}$$

The relationship between the error signal and the cavity resonance frequency fluctuations is given by the response function $G_{\epsilon,\omega_c}(\Omega)$:

$$G_{\epsilon,\omega_c}(\Omega) \equiv \frac{\epsilon(\Omega)}{\delta\omega_c(\Omega)} = \frac{8(\kappa_1/\kappa)J_0(\alpha)J_1(\alpha)}{1 - (4\kappa_1\kappa_2/\kappa^2)J_0(\alpha)^2}\langle i\rangle\frac{1}{\kappa}\sqrt{\frac{1}{1 + (\Omega/\kappa)^2}}e^{-i\tan^{-1}(\Omega/\kappa)}. \tag{8.25}$$

In the limit that the reflectivity of the membrane is small, our symmetric $(r_1 = r_2)$ MIM cavity is described by $\kappa_1 \approx \kappa_2 \approx \kappa/2$ and $\alpha \approx 1$, which gives the transfer function:

$$|G_{\epsilon,\omega_c}(\Omega)|^2 \approx 10 \times \frac{1}{\kappa^2}\left(\frac{1}{1 - \Omega^2/\kappa^2}\right)\langle i\rangle^2. \tag{8.26}$$

8.4.2 The Effect of Mode-Mismatch

In general the input field is not perfectly mode-matched to the cavity, and we must account for this effect on the measurement response function. Mode-mismatch may be due to the polarization or spatial profile of the input beam. To obtain a simple model, we ignore the former by assuming that the input field is linearly polarized along one of the birefringent axes of the cavity. We then divide the input beam into two non-interfering spatial modes, one which interacts with the cavity, $\vec{E}_{in}^a$, and

one which is directly reflected, $\vec{E}_{in}^b$:

$$\vec{E}_{in}(t) = \vec{E}_{in}^a(t) + \vec{E}_{in}^b(t). \tag{8.27}$$

Vector notation is here used to represent the fact that modes a and b are spatially orthogonal over the transverse plane, and as such do not interfere. The orthogonality rule is $\vec{E}_{in}^a(t) \cdot \vec{E}_{in}^{a*}(t) = |E_{in}^a(t)|^2$, $\vec{E}_{in}^a(t) \cdot \vec{E}_{in}^{b*}(t) = 0$. The power in the beam is then expressed as:

$$P_{in}(t) = \vec{E}_{in}(t) \cdot \vec{E}_{in}^*(t) = |E_{in}^a(t)|^2 + |E_{in}^b(t)|^2. \tag{8.28}$$

Field $\vec{E}_{in}^a$ couples to the cavity according to Eq. 8.4, but field $\vec{E}_{in}^b$ is directly reflected. The reflected and transmitted fields can be written

$$\vec{E}_{ref}(t) = \vec{E}_{ref}^a(t) + \vec{E}_{ref}^b(t) \tag{8.29a}$$

$$= \vec{E}_{ref}^a(t) - \vec{E}_{in}^b(t) \tag{8.29b}$$

$$\vec{E}_{out}(t) = \vec{E}_{out}^a(t). \tag{8.29c}$$

Since the two spatial modes don't interfere, the total transmitted and reflected power is

$$P_{ref}(t) = |E_{ref}^a(t)|^2 + |E_{in}^b(t)|^2 \tag{8.30a}$$

$$P_{out}(t) = |E_{out}^a(t)|^2. \tag{8.30b}$$

We now define the mode-matching efficiency ξ^2 as the ratio of the average power in field "a" to the total average power in the field:

$$\xi^2 \equiv \frac{\langle |E_{in}^a(t)|^2 \rangle}{\langle |E_{in}^a(t)|^2 \rangle + \langle |E_{in}^b(t)|^2 \rangle} = \frac{\langle P_{in}^a \rangle}{\langle P_{in} \rangle}. \tag{8.31}$$

For the detuned probe measurement, only light that is coupled to the cavity passes through to the transmission photodetector. Importantly, this means that the transfer function $|G_{i,\omega_c}(\Omega)|^2$ does not depend on the mode matching efficiency.

More care must be taken with the PDH measurement (in reflection). In this case the input field can be modeled

$$\vec{E}_{in}(t) = \vec{E}_0^a e^{i\alpha_a \sin(\Omega_0 t)} + \vec{E}_0^b e^{i\alpha_b \sin(\Omega_0 t)} \tag{8.32}$$

where the subscripts on the modulation depth indicate a possibly different phase-modulation depth for the two spatial modes.

The mean photocurrent and the error signal for the PDH measurement become:

$$\langle i \rangle = \mathcal{R}|E_0^a|^2 \left(1 - (4\kappa_1\kappa_2/\kappa^2)J_0(\alpha)^2\right) + \mathcal{R}|E_0^b|^2 \tag{8.33a}$$

$$\epsilon(t) \approx 4J_0(\alpha)J_1(\alpha)\mathcal{R}|E_0^a|^2\frac{\delta\omega_{c,0}}{\kappa}\frac{2\kappa_1}{\kappa}\sqrt{\frac{1}{1 + (\Omega_m/\kappa)^2}}\cos\left(\Omega_m t - \tan^{-1}\left(\frac{\Omega_m}{\kappa}\right)\right) \tag{8.33b}$$

which gives the following modified PDH response function:

$$G_{\epsilon,\omega_c}(\Omega) = \frac{8(\kappa_1/\kappa)J_0(\alpha)J_1(\alpha)}{1 - (4\kappa_1\kappa_2/\kappa^2)J_0(\alpha)^2 + (1 - \xi^2)/\xi^2}\langle i \rangle\frac{1}{\kappa}\sqrt{\frac{1}{1 + (\Omega/\kappa)^2}}e^{-i\tan^{-1}(\Omega/\kappa)}. \tag{8.34}$$

8.5 Shot Noise Sensitivity: What to Expect

The sensitivity of the detuned probe and PDH measurements are ultimately limited by shot noise on the photocurrent. To quantify this sensitivity, we can compare the power spectral density of shot noise to the power spectral density of the fluctuations generated by the cavity displacement noise.

To derive the photocurrent shot noise, recall that the power spectral density of $i(t)$ can be written as the Fourier transform of the autocorrelation of $i(t)$ (the Wiener-Khintchine Theorem, Eq. 2.7). Here we use the convention for a single-sided power spectral density (Eq. 2.9):

$$S_i(\Omega) \equiv 2\int_{-\infty}^{\infty}\langle i(\tau)i(t + \tau)\rangle e^{-i\Omega t}dt \tag{8.35a}$$

$$\langle i(\tau)i(t + \tau)\rangle \equiv \lim_{T\to\infty}\frac{1}{T}\int_{-T/2}^{T/2}i(\tau)i(t + \tau)d\tau, \tag{8.35b}$$

with the normalization $\int_0^{\infty}S_i(\Omega)d\Omega/2\pi = \langle i^2 \rangle$.

Shot noise is a consequence of the corpuscular nature of photoelectrons. For an infinitely fast photodetector, the underlying random arrival of photons gives rise to a rapidly pulsed photocurrent of the form $i(t) = \sum_k e\delta(t - t_k)$. The autocorrelation of $i(t)$ is also described by a delta function $\langle i(\tau)i(t + \tau)\rangle = e\langle i \rangle\delta(t)$, which gives rise to a white-noise power spectral density:

$$S_i^{shot}(\Omega) = 2e\langle i \rangle \ A^2/Hz. \tag{8.36}$$

The white shot noise approximation is valid for frequencies much smaller than the detector bandwidth, B_{det}. Beyond this frequency the actual shot noise spectrum is diminished.

For the detuned probe measurement with power mode-matching efficiency of ξ^2, the shot noise on the transmission photodetector is:

$$S_i^{shot}(\Omega) = 2e\langle i \rangle = 2e\mathcal{R}\langle P_{out}\rangle = 2e\mathcal{R}|F_T(\Delta)|^2\xi^2\langle P_{in}\rangle. \tag{8.37}$$

For the Pound-Drever-Hall (PDH) measurement with a power mode-matching efficiency of ξ^2, the shot noise on the PDH error signal can be modeled as:

$$S_\epsilon^{shot}(\Omega) = 2e\langle i \rangle = 2e\mathcal{R}\langle P_{ref} \rangle = 2e\mathcal{R}\xi^2\langle P_{in}\rangle \left(\left(1 - J_0(\alpha)^2(4\kappa_1\kappa_2/\kappa^2)\right) + (1 - \xi^2)/\xi^2 \right). \quad (8.38)$$

We can use Eqs. 8.37–8.38 to compute the expected shot-noise-limited sensitivity of the detuned probe and PDH measurements to thermal motion. We express this sensitivity in terms of the "shot noise equivalent" cavity resonance frequency noise, $S_{\omega_c}^{shot}(\Omega)$, and the "shot noise equivalent" cavity length noise, $S_L^{shot}(\Omega) = S_{\omega_c}^{shot}(\Omega)/g_0^2$. $S_{\omega_c}^{shot}(\Omega)$ is the cavity resonance frequency noise necessary to achieve a signal-to-shot noise of one at Fourier frequency $f = \Omega/2\pi$, and $S_L^{shot}(\Omega)$ is the length noise necessary to achieve a signal to noise of one in a standard Fabry-Perot.

For the detuned probe (DP) measurement:

$$\sqrt{S_L^{shot,DP}(\Omega)} = \frac{1}{g_0}\sqrt{S_{\omega_c}^{shot,DP}(\Omega)} = \frac{1}{g_0}\frac{\sqrt{S_i^{shot}(\Omega)}}{|G_{i,\omega_c}(\Omega)|} \quad (8.39a)$$

$$= \left(\frac{\kappa^2 + \Delta^2}{2\Delta}\right)\sqrt{\frac{2e}{\mathcal{R}\langle P_{out}\rangle}}\sqrt{\frac{(\kappa^2 + \Delta^2)^2 + 2(\kappa - \Delta)(\kappa + \Delta)\Omega^2 + \Omega^4}{(\kappa^2 + \Delta^2)^2}}. \quad (8.39b)$$

For the PDH measurement with a mode-matching efficiency of ξ:

$$\sqrt{S_L^{shot,PDH}(\Omega)} = \frac{1}{g_0}\sqrt{S_{\omega_c}^{shot,PDH}(\Omega)} = \frac{1}{g_0}\frac{\sqrt{S_\epsilon^{shot}(\Omega)}}{|G_{\epsilon,\omega_c}(\Omega)|} \quad (8.40a)$$

$$= \frac{\kappa}{4}\sqrt{\frac{2e}{\mathcal{R}\langle P_{ref}\rangle}}\sqrt{1 + \Omega^2/\kappa^2}\left(\frac{1 - J_0(\alpha)^2(4\kappa_1\kappa_2/\kappa^2) + (1 - \xi^2)/\xi^2}{(2\kappa_1/\kappa)J_0(\alpha)J_1(\alpha)}\right). \quad (8.40b)$$

Now consider the "science" cavity and the science membrane with nominal parameters:

$$\{L, FSR, \mathcal{F}, \kappa\} = \{0.742 \text{ mm}, 202 \text{ GHz}, 10^4, 10 \text{ MHz}\} \quad (8.41a)$$

$$\{\Omega_m, d_m, w_m, m, Q_m\} = \{2\pi \times 1\text{MHz}, 50\,\text{nm}, 500\,\mu\text{m}, 10\,\text{ng}, 10^6\}. \quad (8.41b)$$

The shot noise sensitivity of the DP measurement to cavity resonance frequency and effective

cavity length noise are:

$$\sqrt{S_{\omega_c}^{DP,shot}(\Omega)} = 2\pi \times 0.76 \, \frac{\text{Hz}}{\sqrt{\text{Hz}}} \times \frac{\kappa/2\pi}{10 \text{ MHz}} \times \sqrt{\frac{100 \, \mu\text{W}}{\langle P_{out} \rangle}} \tag{8.42a}$$

$$\times \sqrt{\frac{0.55 \text{ A/W}}{\mathcal{R}}} \times \left(\frac{\kappa^2 + \Delta^2}{2\Delta\kappa} \right) \sqrt{\frac{(\kappa^2 + \Delta^2)^2 + 2(\kappa - \Delta)(\kappa + \Delta)\Omega^2 + \Omega^4}{(\kappa^2 + \Delta^2)^2}} \tag{8.42b}$$

$$\sqrt{S_L^{DP,shot}(\Omega)} = 1.8 \times 10^{-18} \, \frac{\text{m}}{\sqrt{\text{Hz}}} \times \frac{L}{0.742 \text{ mm}} \times \frac{935 \text{ nm}}{\lambda} \times \frac{\kappa/2\pi}{10 \text{ MHz}} \times \sqrt{\frac{100 \, \mu\text{W}}{\langle P_{out} \rangle}} \tag{8.42c}$$

$$\times \sqrt{\frac{0.55 \text{ A/W}}{\mathcal{R}}} \times \left(\frac{\kappa^2 + \Delta^2}{2\Delta} \right) \sqrt{\frac{(\kappa^2 + \Delta^2)^2 + 2(\kappa - \Delta)(\kappa + \Delta)\Omega^2 + \Omega^4}{(\kappa^2 + \Delta^2)^2}}. \tag{8.42d}$$

And for PDH:

$$\sqrt{S_{\omega_c}^{PDH,shot}(\Omega)} = 2\pi \times 0.19 \, \frac{\text{Hz}}{\sqrt{\text{Hz}}} \times \frac{\kappa/2\pi}{10 \text{ MHz}} \times \sqrt{\frac{100 \, \mu\text{W}}{\langle P_{ref} \rangle}} \tag{8.43a}$$

$$\times \sqrt{\frac{0.55 \text{ A/W}}{\mathcal{R}}} \times \sqrt{1 + \left(\frac{\Omega}{\kappa} \right)^2} \left(\frac{1 - J_0(\alpha)^2 (4\kappa_1\kappa_2/\kappa^2) + (1 - \xi^2)/\xi^2}{(2\kappa_1/\kappa)J_0(\alpha)J_1(\alpha)} \right) \tag{8.43b}$$

$$\sqrt{S_L^{PDH,shot}(\Omega)} = 4.4 \times 10^{-19} \, \frac{\text{m}}{\sqrt{\text{Hz}}} \times \frac{L}{0.742 \text{ mm}} \times \frac{935 \text{ nm}}{\lambda} \times \frac{\kappa/2\pi}{10 \text{ MHz}} \times \sqrt{\frac{100 \, \mu\text{W}}{\langle P_{ref} \rangle}} \tag{8.43c}$$

$$\times \sqrt{\frac{0.55 \text{ A/W}}{\mathcal{R}}} \times \sqrt{1 + \left(\frac{\Omega}{\kappa} \right)^2} \left(\frac{1 - J_0(\alpha)^2 (4\kappa_1\kappa_2/\kappa^2) + (1 - \xi^2)/\xi^2}{(2\kappa_1/\kappa)J_0(\alpha)J_1(\alpha)} \right). \tag{8.43d}$$

The last factor on the RHS of Eq. 8.43d is ≈ 1.2 for perfect mode matching ($\xi^2 = 1$), a symmetric, lossless cavity ($\kappa_1 = \kappa_2 = \kappa/2$), and a typical PDH modulation depth of $\alpha = 1$.

We can compare the shot noise equivalent cavity length noise to the predicted effective cavity length noise arising from thermal motion of the of the membrane, using the expression for weak optical damping given in Eq. 7.29:

$$\sqrt{S_L(\Omega_{eff}^{ij})} = \eta_{ij} \frac{g_m}{g_0} \sqrt{S_{b_{ij}}(\Omega_{eff}^{ij})} = \eta_{ij} \frac{g_m}{g_0} \sqrt{\frac{4k_B T_{bath} Q_{ij}}{m_{ij} \Omega_{ij}^3}} \frac{\Omega_{ij}}{\Omega_{eff}^{ij}} \frac{\bar{n}_{ij}^{eff}}{\bar{n}_{ij}^{bath}} \tag{8.44a}$$

$$= 2.3 \times 10^{-13} \, \frac{\text{m}}{\sqrt{\text{Hz}}} \times \eta_{ij} \times \frac{g_m}{g_0} \times \sqrt{\frac{T_{bath}}{298\text{K}}} \times \sqrt{\frac{10 \text{ ng}}{m_{ij}}} \times \sqrt{\frac{Q_{ij}}{10^6}} \times \left(\frac{5 \text{ MHz}}{\Omega_{ij}/2\pi} \right)^{3/2} \times \frac{\Omega_{ij}}{\Omega_{eff}^{ij}} \times \frac{\bar{n}_{ij}}{\bar{n}_{ij}^{bath}}. \tag{8.44b}$$

Here $\Omega_{eff}^{ij} = \Omega_{ij} + \Delta\Omega_{opt}^{ij}$ ($\approx \Omega_{ij}$ for weak optical spring/damping) is the mechanical frequency shifted by the optical spring, and $\bar{n}_{ij} \approx k_B T_{eff}^{ij} / \hbar\Omega_{eff}^{ij}$ is the thermal occupation number after optomechanical cooling (see Section 2.4).

Expressed in terms of cavity resonance frequency noise:

$$\sqrt{S_{\omega_c}(\Omega_{eff}^{ij})} = g_0 \sqrt{S_L(\Omega_{eff}^{ij})} \tag{8.45a}$$

$$= 2\pi \times 0.98 \times 10^6 \frac{\text{Hz}}{\sqrt{\text{Hz}}} \times \eta_{ij} \times \frac{g_m}{g_0} \times \frac{0.742 \text{ mm}}{L} \times \frac{\lambda}{935 \text{ nm}} \times \sqrt{\frac{T_{bath}}{298\text{K}}} \times \sqrt{\frac{10 \text{ ng}}{m_{ij}}} \tag{8.45b}$$

$$\times \sqrt{\frac{Q_{ij}}{10^6}} \times \left(\frac{5 \text{ MHz}}{\Omega_{ij}/2\pi}\right)^{3/2} \times \frac{\Omega_{ij}}{\Omega_{eff}^{ij}} \times \frac{\bar{n}_{ij}}{\bar{n}_{ij}^{bath}}. \tag{8.45c}$$

For $\Omega_{66}/2\pi = 4.8$ MHz (the (6,6) mode or our "science" membrane), the room-temperature thermal occupation number is $\bar{n}_{66}^{bath} = 1.3 \times 10^6$, the spatial overlap factor for the TEM$_{00}$ mode is $\eta_{66} \lesssim 0.64$, and $g_m^{max}/g_0 \approx 0.84$ at 935 nm. For an initial value of $Q_{66} = 4 \times 10^6$, the peak thermal noise at $\bar{n}_{66} = 1$ would be $\{ \sqrt{S_L(\Omega_{eff}^{66})}, \sqrt{S_{\omega_c}(\Omega_{eff}^{66})} \} \approx \{2 \times 10^{-19} \text{ m}/\sqrt{Hz}, 0.09 \text{ Hz}/\sqrt{Hz}\}$. Eq. 8.43 implies that a PDH measurement should be able to sense this noise with ~ 1 mW of power incident on the detector (assuming good mode-matching efficiency).

8.6 Calibration of the Measurement Response Function by Phase Modulating the Input Field

From the standpoint of the detuned probe and PDH measurements, a small sinusoidal modulation of the cavity resonance frequency by an amount $\delta\omega_c(t) = \alpha \cos(\Omega_0 t)$ is equivalent to a small sinusoidal modulation of the instantaneous frequency of the input field by an amount $\dot{\phi}(t) = -\alpha \cos(\Omega_0 t)$. (Here we express the instantaneous frequency as the derivative of the instantaneous phase, ϕ.) Using this property, we can determine the measurement response functions $G_{i,\omega_c}(\Omega_0)$ and $G_{\epsilon,\omega_c}(\Omega_0)$ by applying a calibrated sinusoidal phase modulation to the input field. This is an important result that will be used extensively in the rest of this chapter and also in Chapter 10. Its proof is given below.

8.6.1 Detuned Probe Measurement: Response to PM of the Input Field

Phase modulation of the input field can be introduced as $E_{in}(t) \rightarrow E_{in}(t)e^{i\phi(t)}$. We here assume that the field before phase modulation is monochromatic, $E_{in}(t) = E_0$, and that the phase modulation is small, $e^{i\phi(t)} \approx 1 + i\phi(t)$. The fields transmitted and circulating in a stationary cavity ($\delta\omega_c(t) = 0$) driven by a phase-modulated input field are then given by (linearizing about small displacements

$\delta a(t) = a(t) - \langle a \rangle$ as in Section 8.3.2):

$$\langle a \rangle = \frac{\sqrt{2\kappa_1}}{\kappa + i(\Delta + \Omega)} E_0 \qquad (8.46a)$$

$$\delta \dot{a}(t) = -\left(\kappa + i\Delta\right) \delta a(t) + \sqrt{2\kappa_1} E_0 i\phi(t) \qquad (8.46b)$$

$$i(t) = \mathcal{R}|E_{out}(t)|^2 = 2\kappa_2 \mathcal{R}(|\langle a \rangle|^2 + \langle a \rangle \delta^* a(t) + \langle a \rangle^* \delta a(t)). \qquad (8.46c)$$

Applying the Fourier transform to both sides of Eq. 8.46 and doing some algebraic manipulation, we obtain the following solution to first order in the small parameter ϕ:

$$\delta a(\Omega) = \frac{\sqrt{2\kappa_1}}{\kappa + i(\Delta + \Omega)} E_0 i\phi(\Omega) \qquad (8.47a)$$

$$[\delta a^*](\Omega) = \frac{\sqrt{-2\kappa_1}}{\kappa - i(\Delta - \Omega)} E_0 i\phi(\Omega) \qquad (8.47b)$$

$$\delta i(\Omega) = 2\kappa_2 \mathcal{R}(\langle a \rangle [\delta^* a](\Omega) + \langle a \rangle^* \delta a(\Omega)) \qquad (8.47c)$$

$$= \langle i \rangle \left(\frac{(\kappa + i\Delta)}{\kappa + i(\Delta + \Omega)} - \frac{(\kappa - i\Delta)}{\kappa - i(\Delta - \Omega)} \right) i\phi(\Omega), \qquad (8.47d)$$

where $[\delta a^*](\Omega)$ is the Fourier transform of $\delta a^*(t)$ and $\delta i(\Omega)$ is the Fourier transform $\delta i(t) = i(t) - \langle i \rangle$.

The detuned probe response function for phase modulation is remarkably similar to that for cavity resonance frequency modulation:

$$G_{i,\phi}(\Omega) \equiv \frac{\delta i(\Omega)}{\phi(\Omega)} = i \left(\frac{(\kappa + i\Delta)}{\kappa + i(\Delta + \Omega)} - \frac{(\kappa - i\Delta)}{\kappa - i(\Delta - \Omega)} \right) \langle i \rangle \qquad (8.48a)$$

$$= \Omega G_{i,\omega_c}(\Omega) e^{i\pi/2}. \qquad (8.48b)$$

Indeed, the DP response function for intantanteous frequency modulation and cavity resonance frequency modulation are equivalent in the small modulation limit:

$$G_{i,\dot{\phi}}(\Omega) \equiv \frac{\delta i(\Omega)}{\dot{\phi}(\Omega)} = G_{i,\omega_c}(\Omega). \qquad (8.49)$$

Thus to determine $G_{i,\omega_c}(\Omega_0)$, we can apply a calibrated phase modulation $\phi(t) = \beta_0 \sin(\Omega_0 t)$ and measure $i(t) = i_0 \cos(\Omega_0 t + \theta) = \beta_0 \Omega_0 |G_{i,\omega_c}(\Omega)| \cos(\Omega_0 t + \text{Arg}[G_{i,\omega_c}(\Omega_0)])$.

8.6.2 PDH Measurement: Response to PM of the Input Field

We now consider the effect of adding a small phase modulation ϕ to the input field in addition to the high-frequency sidebands used to generate a PDH error signal (Eq. 8.17). Here we consider a sinusoidal modulation of the form $\phi(t) = \beta \sin(\Omega_m t) \ll 2\pi$. The equation of motion for the

circulating and reflected field for a stationary cavity ($\delta\omega_c(t) = 0$) is given by:

$$\dot{a}(t) = -(\kappa + i\Delta)a(t) + \sqrt{2\kappa_1}E_{in}(t) \tag{8.50a}$$

$$E_{in}(t) = E_0 \left(1 + \frac{\beta}{2}\left(e^{i\Omega_m t} - e^{-i\Omega_m t}\right)\right) \sum_n J_n(\alpha)e^{in\Omega_0 t} \tag{8.50b}$$

$$E_{ref}(t) = -E_{in}(t) + \sqrt{2\kappa_1}a(t), \tag{8.50c}$$

where α and Ω_0 are the PDH phase modulation depth and sideband frequency; the latter is assumed to be much larger than frequencies of interest in ϕ.

On resonance ($\Delta = 0$), the field reflected from the cavity is given by:

$$\frac{E_{ref}(t)}{E_0} = \sum_n \left(F_R(n\Omega_0) + \frac{\beta}{2}F_R(n\Omega_0 + \Omega_m)e^{i\Omega_m t} - \frac{\beta}{2}F_R(n\Omega_0 - \Omega_m)e^{-i\Omega_m t}\right) J_n(\alpha)e^{in\Omega_0 t}. \tag{8.51}$$

As in the case for which ω_c is modulated, the average reflected power is approximated by

$$\langle|E_{ref}(t)|^2\rangle \approx |E_0|^2 \left(1 - (4\kappa_1\kappa_2/\kappa^2)J_0(\alpha)^2\right). \tag{8.52}$$

The relevant fluctuating part of the reflected power is contributed by terms which are oscillating at frequencies $\pm\Omega_0 \pm \Omega_m$. Using $\Omega_0 >> \kappa$, $J_1(\alpha) = -J_{-1}(\alpha)$, $F_R(\Omega_0 \pm \Omega_m) \approx F_R(\Omega_0) \approx -1$, and ignoring terms oscillating at $2\Omega_0$, we find

$$\delta|E_{ref}(t)|^2 = |E_{ref}(t)|^2 - \langle|E_{ref}(t)|^2\rangle \tag{8.53a}$$

$$\approx -\frac{\beta}{2}J_0(\alpha)J_1(\alpha)|E_0|^2(F_R(\Omega_m)e^{i(\Omega_0+\Omega_m)t} - F_R(\Omega_m)e^{i(-\Omega_0+\Omega_m)t} \tag{8.53b}$$

$$- F_R(-\Omega_m)e^{i(\Omega_0-\Omega_m)t} + F_R(-\Omega_m)e^{i(-\Omega_0-\Omega_m)t} + F_R(0)e^{i(\Omega_0+\Omega_m)t} \tag{8.53c}$$

$$- F_R(0)e^{i(\Omega_0-\Omega_m)t} + F_R(0)e^{i(-\Omega_0-\Omega_m)t} - F_R(0)e^{i(-\Omega_0+\Omega_m)t} + c.c.). \tag{8.53d}$$

Collecting terms and using $F_R(-\Omega_m)^* = F_R(\Omega_m)^*$ gives

$$\frac{\delta|E_{ref}(t)|^2}{|E_0|^2} \approx 4\beta J_0(\alpha)J_1(\alpha)\left(\text{Im}\left[F_R(\Omega_m)\right]\cos(\Omega_m t) + \left(\text{Re}\left[F_R(\Omega_m)\right] + \frac{2\kappa_1 - \kappa}{\kappa}\right)\sin(\Omega_m t)\right)\sin(\Omega_0 t). \tag{8.54}$$

Though not obvious, the slowly varying envelope and resulting PDH error signal reduce to the

same functional form as Eqs. 8.23–8.24:

$$\frac{\delta|E_{ref}(t)|^2}{|E_0|^2} = 4J_0(\alpha)J_1(\alpha)\frac{\beta\Omega_m}{\kappa}\frac{2\kappa_1}{\kappa}\sqrt{\frac{1}{1+\Omega_m^2/\kappa^2}}\cos\left(\Omega_m t - \tan^{-1}(\Omega_m/\kappa)\right)\sin(\Omega_0 t) \quad (8.55a)$$

$$\epsilon(t) = 4J_0(\alpha)J_1(\alpha)\frac{\langle i\rangle}{1-J_0^2(\alpha)(4\kappa_1\kappa_2/\kappa^2)}\frac{\beta\Omega_m}{\kappa}\frac{2\kappa_1}{\kappa}\sqrt{\frac{1}{1+\Omega_m^2/\kappa^2}}\cos\left(\Omega_m t - \tan^{-1}(\Omega_m/\kappa)\right),$$
$$(8.55b)$$

which gives the following PDH response function to phase modulation and instantaneous frequency modulation (in the small modulation limit):

$$G_{\epsilon,\phi}(\Omega) = \Omega G_{\epsilon,\omega_c}(\Omega)e^{-i\pi/2} \quad (8.56a)$$

$$G_{\epsilon,\dot\phi}(\Omega) = G_{\epsilon,\omega_c}(\Omega). \quad (8.56b)$$

Thus to determine $G_{\epsilon,\omega_c}(\Omega_0)$, we can apply a calibrated phase modulation $\phi(t) = \beta_0\sin(\Omega_0 t)$ and measure $\epsilon(t) = \epsilon_0\cos(\Omega_0 t + \theta) = \beta_0\Omega_0|G_{i,\omega_c}(\Omega)|\cos(\Omega_0 t + \text{Arg}[G_{i,\omega_c}(\Omega_0)])$.

8.7 Experimental Walk-Through: Temperature Measurement Using the Detuned Probe Method

In this section we walk through a "bread-and-butter" displacement noise measurement using the detuned probe method. The goal is determine the effective temperature, T_{eff}^{ij}, of a specific membrane vibrational mode, (i,j), using the relations:

$$T_{eff}^{ij} = \frac{m_{ij}\langle b_{ij}^2\rangle}{k_B} = \frac{m_{ij}}{k_B}\int_{\Omega_{ij}} S_{b_{ij}b_{ij}}(\Omega)d\Omega/2\pi = \frac{m_{ij}}{k_B}\frac{1}{g_m^2\eta_{ij}^2}\int_{\Omega_{ij}} S_{\omega_c}(\Omega)d\Omega/2\pi \quad (8.57a)$$

$$S_i(\Omega) = |G_{i,\omega_c}(\Omega)|^2 S_{\omega_c}(\Omega) \quad (8.57b)$$

where the $\int_{\Omega_{ij}}$ indicates an integral over the noise peak centered at Ω_{ij}. In this example we consider the $(i,j) = (6,6)$ mode of the $\{d_m, w_m\} = \{50\text{ nm}, 500\,\mu\text{m}\}$ "science" membrane coupled to the TEM$_{00}$ mode of the "science" MIM cavity described in Chapters 5 and 6, having properties $\{L, FSR, \mathcal{F}, \kappa/(2\pi)\} = \{0.742\text{ mm}, 202\text{ GHz}, \approx 10^4, \approx 10\text{ MHz}\}$. We carry out the measurement in the limit of negligible optical damping ($T_{eff}^{66} \approx T_{bath} \approx 298$ K), but the method also applies in the case of weak damping (Section 2.4).

Specifics of the DP procedure are as follows: we drive the cavity with a input field at a red detuning $\Delta/(2\pi) \approx 100$ MHz and with $\approx 1\,\mu$W optical power using light from a $\lambda = 935$ nm diode laser (Eagleyard). Light exiting the transmission port of the cavity is collected on a fast

photodiode (New Focus 1801). The resulting photocurrent is processed by a sequence of electronics before software-based spectral analysis. The sequence consists of: (1) transforming the current into a voltage using a transimpedance amplifier (gain $G_T \approx 20$ V/mA, internal to the photodetector), (2) mixing the voltage signal down to ~ 10 kHz (Minicircuits ZAD-6), (3) pre-amplifying/filtering the mixed-down signal (SR560 pre-amp, gain $= \times 1000$, filter $= 30$ kHz LP with 6 dB/decade rolloff), and then (4) digitizing the pre-amplified voltage (National Instruments PCI-6259, sample rate $= 500$ kHz). The power spectral density of the digitized voltage signal is obtained using Labview software [83]. It is related to the photocurrent by the transfer function $|G_{i,V}(\Omega)|^2$ of the electronic processing chain:

$$S_V(\Omega) = |G_{i,V}(\Omega)|^2 (S_i(\Omega_{LO} + \Omega) + S_i(\Omega_{LO} - \Omega)) \tag{8.58}$$

where Ω_{LO} is the local oscillator of the mixer. We choose Ω_{LO} so that the signal of interest is near $\Omega_{LO} + \Omega$, at the cost of introducing some extra noise (e.g., off-resonant thermal noise, shot noise) due to the $\Omega_{LO} - \Omega$ signal component.

To trace $S_V(\Omega)$ back to $S_i(\Omega)$ back to $S_{b_{ij}}(\Omega)$, we use both the phase modulation technique described in Section 8.6, as well as a "direct" calibration based on individually determining the free parameters entering Eqs. 8.57–8.58. We elaborate below on several important experimental details.

8.7.1 Spectrum Analyzer: Effective Noise Bandwidth

In the preceding discussion we envision an ideal spectrum analyzer for computing $S_V(\Omega_0)$. This can be achieved by passing the voltage through a Delta function notch filter centered at Ω_0 followed by an rms voltmeter. Normalizing the measred rms^2 power by the bandwidth of the filter would give $S_V(\Omega_0) = \int_0^\infty S_V(\Omega)\delta(\Omega - \Omega_0)d\Omega/2\pi / \int_0^\infty \delta(\Omega - \Omega_0)d\Omega/2\pi \ A^2/Hz$. A laboratory spectrum analyzer has a finite filter bandwidth, however, and since we're dealing with narrow spectral features ($\Gamma_m/2\pi \sim 1$ Hz for $\{\Omega_m/(2\pi), Q_m\} \sim \{10^6, 10^6\}$) we must be careful in our interpretation of the measured $S_V(\Omega)$. When the appropriate settings are chosen, most spectrum analyzers display noise power units by computing a weighted average over an effective filter function, i.e., $S_V(\Omega_0) = \int_0^\infty S_V(\Omega)W(\Omega - \Omega_0)d\Omega/2\pi / \int_0^\infty W(\Omega - \Omega_0)d\Omega/2\pi$, where for instance $W(\Omega)$ may be a 1-Hz-FWHM Gaussian centered at 0 Hz [56, 84]. If the signal is a coherent sinusoidal tone with frequency Ω_0 and amplitude A, i.e., $S_V(\Omega) = A^2/2\delta(\Omega - \Omega_0)$, then the inferred spectral density is $S_V(\Omega_0) = (A^2/2) \cdot (W(0)/\int_0^\infty W(\Omega - \Omega_0)d\Omega/2\pi)$. Factor $ENBW \equiv (\int_0^\infty W(\Omega - \Omega_0)d\Omega/2\pi)/W(0)$ is referred to as the "effective noise bandwidth" of the filter. For a digital spectrum analyzer, $W(\Omega)$ describes the effect of windowing the finite time trace [83]. We customarily use a Hanning window, in which case the theoretical effective noise bandwidth for a 1-Hz-wide filter is 1.33 Hz. We have checked that this is the case for our FFT software by analyzing a tone generated by a calibrated RF synthesizer. We have also checked that when the filter is wider than the spectral feature, the PSD is normalized
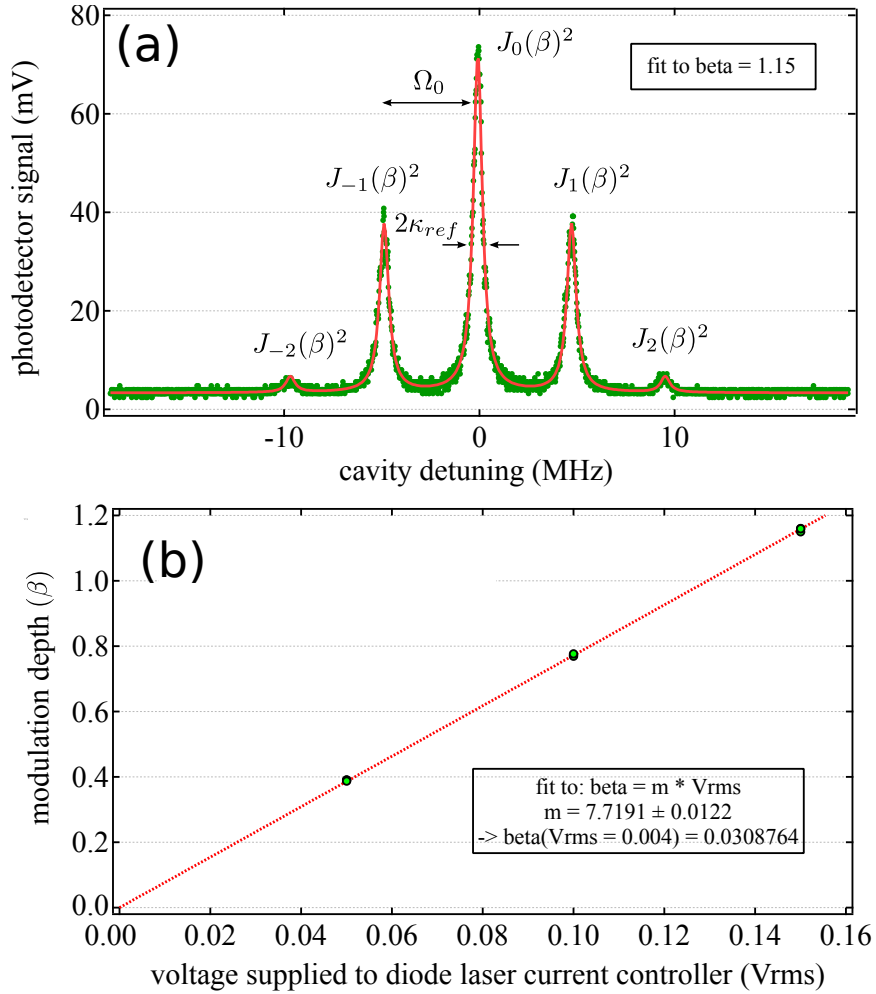
Figure 8.3: Calibration of PM modulation: the phase-modulated field is coupled to an optical cavity with a linewidth smaller than the modulation frequency, $\kappa_{ref} << \Omega_0$. Power transmitted through the cavity is monitored as a function of detuning, which is varied by sweeping the length of the cavity. The resulting transmission curve (Eq. 8.59) is fit to a multiple-Lorentzian weighted by Bessel functions, which reveals the modulation depth. For data shown in (a) the fit values are $\Omega_0/(2\pi) = 4.83$ MHz, $\beta = 1.15$, $\kappa_{ref}/(2\pi) = 280$ kHz. In (b) the response of the phase modulator — in this case the diode laser current — is measured as a function of drive amplitude (voltage applied to the current controller). A linear fit is used to estimate β for small drive.

so that the integral gives the mean-squared amplitude. To do this, we send the signal from a filtered white-noise source into the digitizer and check that the integral over the PSD gives the same result as power displayed by an RMS voltmeter. Whenever a fit to a spectral feature is made (e.g., a Lorentzian thermal noise peak), one must ensure that the effective noise bandwidth is much narrower than the linewidth of that feature.

8.7.2   Calibrating the Phase Modulation Depth

The input field is phase modulated in order to calibrate the photocurrent signal. Rather than use an EOM, for the measurement described here we modulate the diode laser drive current, $i_d(t) = \langle i_d \rangle + \delta i_{d,0} \cos(\Omega_0 t)$, where $\Omega_0 \approx \Omega_{66}$. This results in direct FM modulation of the the laser field (and some residual AM, which we found to be negligible for the results below), characterized by an instantaneous frequency: $\dot{\phi}(t) = \beta_{fm} \cos(\Omega_0 t + \theta_0)$. For single-frequency modulation this is equivalent to phase modulation by an amount $\phi(t) = \beta \sin(\Omega_0 t + \theta_0) = (\beta_{fm}/\Omega_0) \sin(\Omega_0 t + \theta_0)$.

To calibrate the modulation depth, we couple a fraction of the input field into an independent reference cavity with a linewidth $\kappa_{ref} \ll \Omega_0$. This cavity has the following optical properties at $\lambda = 935$ nm: $\{L, FSR, \mathcal{F}, \kappa/(2\pi)\} \approx \{10 \text{ cm}, 3 \text{ GHz}, \approx 10^4, \approx 300 \text{ kHz}\}$. Transmission of frequency modulated light through this "resolved" cavity assumes the simplified form:

$$|E_{out}(\Delta)|^2 = |E_{in}|^2 \sum_{n=-\infty}^{\infty} |F_T(\Delta + n\Omega_0)|^2 J_n^2(\beta), \tag{8.59}$$

a multiple-Lorentzian vs. Δ with peak heights $J_n^2(\beta)$ at frequencies $\pm n\Omega_0$.

Phase modulation depth β is determined by comparing the relative heights of peak values $|E_{out}(n\Omega_0)|^2$. $|E_{out}(\Delta)|^2$ is measured by sweeping the cavity length across resonance with a triangle wave and monitoring the voltage produced by a photodetector monitoring the power transmitted from the cavity. An oscilloscope trace for one half-period is shown in Figure 8.3a, where the time scale has been normalized to the linewidth obtained by fitting to Eq. 8.59. A multiple-Lorentzian fit to the curve shown in Figure 8.3a gives $\beta = 1.16$. To extrapolate the modulator's response to lower β, we measure β vs. $i_{d,0}$ for different $i_{d,0}$, and verify that the trend is linear. For large values of β, this is done using the reference cavity measurement. For small β, we send the laser through the science cavity at a fixed detuning and monitor $\sqrt{S_i(\Omega_0)} = |G_{i,\omega_c}(\Omega_0)|\Omega_0\beta/\sqrt{2}$ vs. $i_{d,0}$. An example response curve is shown in Figure 8.3b (only large β measurements are shown).

For the thermal noise measurement, we use a modulation depth of $\beta = 0.03$ at $\Omega_0/(2\pi) = 4.83$ MHz, corresponding to an rms FM deviation of $\sqrt{S_{\dot{\phi}}(\Omega_0)} = \beta\Omega_0/\sqrt{2} = 2\pi \times 102$ kHz. The equivalent cavity length noise for the science cavity at $\lambda = 935$ nm is given by $\sqrt{S_{\dot{\phi}}(\Omega_0)}/g_0 \approx 0.23$ pm/$\sqrt{Hz}$. This small level is chosen to be on the order of the peak effective cavity length noise (Eq. 7.24) associated with the (6,6) membrane mode with $\Omega_{66}/(2\pi) = 4.8$ MHz and $Q_{66} \sim 1.5 \times 10^6$: $\sqrt{S_L(\Omega_{66})} = (g_m/g_0)\eta_{66}\sqrt{k_B T/m_{66}\Omega_{66}^2}\sqrt{2\pi Q_{66}/\Omega_{66}} \approx (g_m/g_0)\eta_{66} \times 0.21$ pm/$\sqrt{Hz}$, where $\eta_{66} \lesssim 0.65$ is the "spatial overlap" factor described in Section 7.3.1.1 and g_m is the optomechanical coupling of the membrane (Section 3.3.1).

$$S_V(\Omega_0) = \frac{\beta^2 \Omega_0^2}{2} |G_T(\Omega_0)|^2 |G_{i,\omega_c}(\Omega_0)|^2$$

maximum sensitivity at $\Delta \approx \kappa/\sqrt{3}$

Δ_{brf}

detuning between probe and lock beams (MHz)
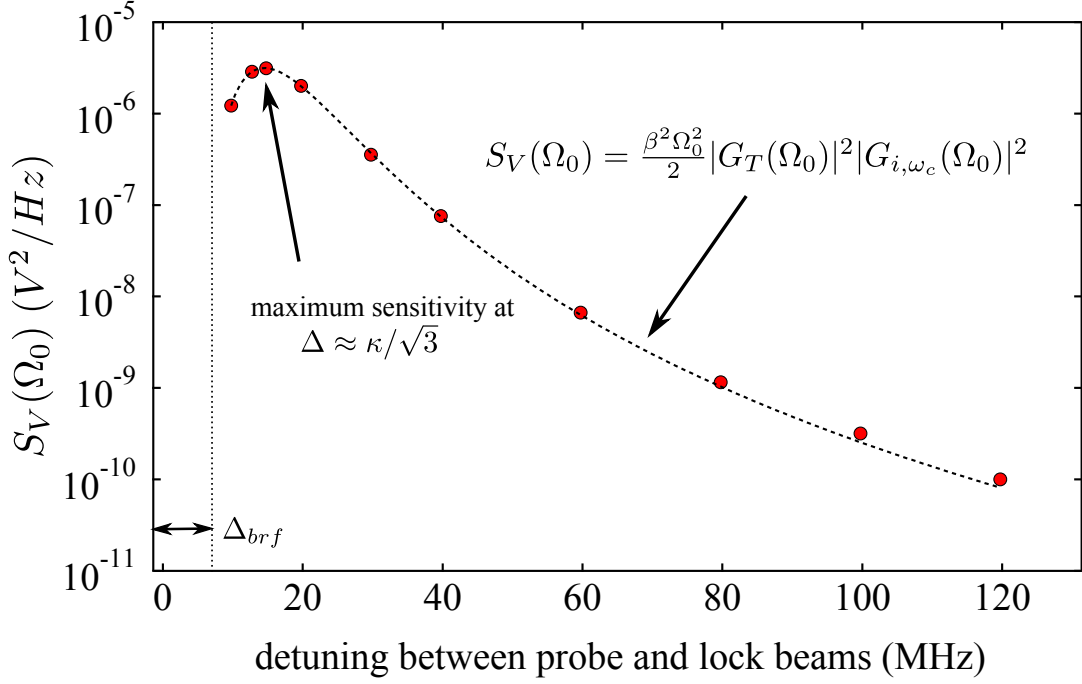
Figure 8.4: Characterization of transduction factor $G_{i,\omega_c}(\Omega_{66})$. The point here is to verify the functional form given in Eq. 8.60c and to determine $\{\Delta, \kappa\}$ from the fit. Toward this end, phase modulation with small modulation depth $\beta << 2\pi$ at frequency $\Omega_0 \approx \Omega_{66} \approx 2\pi \cdot 4.84$ MHz is applied to of the cavity input field ("probe" field). Fluctuations on the transmitted power are monitored via the power spectral density of the transimpedance-amplified photocurrent produced by the cavity transmission photodetector, $S_V(\Omega_0)$. This value is monitored as a function of the detuning between the probe and a secondary field to which the cavity is locked on resonance (this field is polarized along the opposite birefringent axis of the cavity). Fitting to a scaled Eq. 8.60 gives the detuning of the probe field from cavity resonance, the cavity birefringent splitting, and the cavity linewidth. It also verifies the functional form of the detuned probe transfer function.

8.7.3 Characterizing the Transfer Function

We can verify the functional dependence of $|G_{i,\omega_c}(\Omega_{66})|^2$ on Δ and κ by applying a small phase modulation to the input ("probe") field at $\Omega_0 \approx \Omega_{66} = 4.84$ MHz and monitoring the transimpedance-amplified photocurrent of the transmission photodetector $S_V(\Omega_0)$ vs. detuning, which should obey the relations:

$$S_V(\Omega_0) = |G_T(\Omega_0)|^2 S_i(\Omega_0) \tag{8.60a}$$

$$S_i(\Omega_0) = \frac{\Omega_0^2 \beta^2}{2} |G_{i,\omega_c}(\Omega_0)|^2 \tag{8.60b}$$

$$|G_{i,\omega_c}(\Omega_0)|^2 = \langle i \rangle^2 \left(\frac{2\Delta}{\kappa^2}\right)^2 \left(\frac{1}{1 + \Delta^2/\kappa^2}\right)^2 \frac{\left(\kappa^2 + \Delta^2\right)^2}{(\kappa^2 + \Delta^2)^2 + 2(\kappa - \Delta)(\kappa + \Delta)\Omega_0^2 + \Omega_0^4} \tag{8.60c}$$

$$\langle i(\Delta) \rangle = \frac{\langle i(\Delta = 0) \rangle}{1 + \Delta^2/\kappa^2} \tag{8.60d}$$

where $G_T(\Omega_0)$ V/A is the photodetector transimpedance gain.

The method for adjusting the cavity detuning is described in Section 5.3.3.1; it consists of locking the cavity to a second beam with a tunable frequency difference from the probe beam. Though the frequency difference is precisely controlled by an EOM driven by an RF synthesizer, the absolute detuning of the probe from the cavity is obscured by the fact that the locking and probing beams enter the cavity along orthogonal polarization eigenmodes, which exhibit a birefringent splitting Δ_{brf}. The resonance frequency splitting between these eigenmodes depends on the membrane position.

A plot of $S_V(\Omega_0)$ vs. $\Delta + \Delta_{brf}$ is shown in Figure 8.4. $|G_T(\Omega_0 < 2\pi \times 100 \text{ MHz})| = 2 \times 10^4$ V/A is the factory-specified transimpedance gain of the New Focus 1801 photodetector used. We use the full expression in Eq. 8.60 for the fit. The fit gives a cavity linewidth $\kappa/(2\pi) = 12.9$ MHz (HWHM), which depends weakly on membrane position as discussed in Section 6.4. The fit also reveals that the birefringent spitting in this case is $\Delta_{brf}/(2\pi) = 6.9$ MHz (also a function of membrane position). The factial difference between the full expression for $|G_{i,\omega_c}(\Omega_0)|^2$ and approximate expression obtained by setting $\Omega_0 = 0$ in (8.60c) is $\approx \Omega_0^4/4\kappa^4 << 1\%$ at $\Delta = -\kappa$. We believe that the discrepancy between data and fit at large detuning is due to residual amplitude modulation due to current modulation of the diode laser (for the results here we operate the diode current near saturation to reduce residual AM).

8.7.4   Uncertainties

To obtain the temperature of the membrane from $S_i(\Omega)$ and $G_{i,\omega_c}(\Omega)$, we must assign values to membrane optomechanical coupling g_m, "spatial overlap factor" η_{66}^{00}, and effective mass m_{66}. Uncertainties are described below.

Optomechanical Coupling, g_m: To obtain g_m, we have measured the shift in ω_c resulting from a calibrated displacement of the equilibrium membrane position, z_m, using the definition $g_m \equiv d\omega_c/dz_m$. An example of this measurement is shown in Section 6.3. The measurement agrees with the model for a $d_m = 50$-nm-thick membrane with n = 2.0 (Section 3.3.1), which gives a maximum value of $g_m = 2|r_m|g_0 = 2\pi \cdot 2 \cdot 0.42 \cdot 202$ GHz$/(935$ nm$/2) = 0.36$ MHz/pm when the membrane is located halfway between a node and the antinode of the intracavity field. This result does not agree with the values of $n_m = 1.98$ and $d_m = 37$ nm inferred from a Filmetrics thin-film measurement and a direct measurement of the membrane reflectivity (Section 6.1), which suggest that $|r_m| = 0.36$ and $g_m^{max} = 2\pi \cdot 0.31$ MHz/pm. For the temperature measurement, we position the membrane at a location z_m where $g_m = g_m^{max}$ by maximizing the photocurrent response. At this location, g_m is insensitive to first order in small drifts of the membrane position. We therefore estimate that g_m lies somewhere between $2\pi \cdot 0.31$ MHz/pm and $2\pi \cdot 0.36$ MHz/pm.

Spatial Overlap Factor, η_{66}: To determine the "spatial overlap factor", η_{66}, between the (6,6) membrane vibrational mode and the TEM$_{00}$ mode of the cavity (Section 7.1.3), we measure the "apparent" temperatures of various modes of the membrane $\eta_{ij}^2 T_{eff}^{ij}$ in order to constrain the transverse (x_0, y_0) position of the membrane with respect to the cavity axis. This method is described in Section 8.7.7 of this chapter. Uncertainty in the determination of η_{66} depends on the uncertainty in the inferred position (x_0, y_0) and in the value used for the waist size w_c of the cavity mode. The position uncertainty alone gives a range of values for η_{66} between 0.57 and 0.64, and is believed to dominate over the uncertainty due to the value of w_c.

Effective Mass, m_{66}: The effective mass for all vibrational modes of a high-stress square membrane is $m_{phys}/4$, as discussed in Section 7.1.1. m_{phys} depends on the dimensions and density of the membrane. Literature values for the density ρ of stoichiometric Si$_3$N$_3$ density vary between 2.7 g/cm^3 and 3.1 g/cm^3, with the higher density corresponding to bulk material and lower density corresponding to high-stress LPCVD (Table 4.1). Eigenfrequencies of the drum modes are consistent with the value of 2.7 g/cm^3 if the transverse dimensions and tension are assumed to agree with the values specified by Norcada ($w_m = 500 \, \mu$m and $\mathcal{T} = 900$ MPa, respectively). We nevertheless assume a possible range of values between 2.7 and 3.1 g/cm^3 for the measurement. The transverse dimensions of the membrane, $\{w_{m,x}, w_{m,y}\}$, have been shown to be precise to $< 1\%$ from the design value of $\{500 \, \mu\text{m}, 500 \, \mu\text{m}\}$ by SEM imaging. The thickness, d_m, based on a reflectivity measurement lies between 37 nm and the factory design value of 50 nm. The combined uncertainty gives a range of effective mass values $m_{66} = \rho w_{m,x} w_{m,y} d_m / 4$ between 6.1 and 9.7 ng.

8.7.5   Calibrating the Electronics Downstream of the Photodetector

To "directly" calibrate the displacement noise spectrum according to Eqs. 8.57–8.58, we must determine the transfer function $|G_{V,i}(\Omega)|^2$ which maps $S_i(\Omega)$ to $S_V(\Omega)$. This depends on the details of the transimpedance amplifier, mixer, pre-amplifer, and digitizer. To determine this transfer function we replace the output of the photodetector with a calibrated voltage source $V(t) = V_0 \cos(\Omega_0 t)$, making sure to match the 50 Ohm output impedance of the photodetector. Using a 1 Hz BW Hanning window (ENBW = 1.33 Hz) we obtain $|G_{V,i}(\Omega_0)|^2 = G_T(\Omega_0)^2 * 1.33 * S_V(\Omega_0)/(V_0^2/2) = (R(\Omega_0) * 0.0045)^2$, where $G_T(\Omega_0) \approx 2 \times 10^4$ V/A is the factory-specified transimpedance gain of the photodetector. This correction factor is already included in the upper plot in Figure 8.5, so that $S_V(\Omega)$ refers to the noise at the output of the transimpedance amplifier. $G_T(\Omega)$ is approximately constant for frequencies much less than the 100 MHz bandwidth of the photodetector (including DC for this model, New Focus 1801), so we assume that $S_V(\Omega)/\langle V \rangle^2 = S_i(\Omega)/\langle i \rangle^2$. We complete the measurement by simultaneously recording the small value $\langle V \rangle$, carefully subtracting any DC voltage offsets at the output of the transimpedance amplifier.

8.7.6   Measurement Result

Results of a single thermal noise measurement are summarized in Figure 8.5. The upper plot displays the raw power spectral density of the digitized voltage signal after the pre-amp, $S_V(\Omega)$, averaging in V^2/Hz units over ~ 10 trials. The ENBW of the FFT is 1.33 Hz and the Fourier frequency scale has been shifted by the 4.82 MHz mixer LO frequency to represent the physical photocurrent noise frequency. The span shown contains two significant contributions. The Lorentzian feature at $\Omega_{66}/(2\pi) \approx 4.828$ MHz is proportional to the actual displacement noise spectrum $S_{b_{66}}(\Omega)$ (Eq. 2.17) of the (6,6) membrane mode and gives a fitted linewidth of $\Gamma_{66}/(2\pi) = 3.0$ Hz (FWHM), which is consistent with a quality factor of $Q_{66} = 1.6 \times 10^6$. The narrow feature corresponds to the calibrated phase modulation.

Using the methods described in Sections 8.7.1–8.7.5, we can directly trace $S_V(\Omega)$ back to $S_{b_{66}}(\Omega)$ and compare this to the PM calibration technique (Section 8.6). To simplify notation, we here introduce the useful "normalized" response function coefficient, $H_{i,\omega_c}(\Omega)$:

$$H_{i,\omega_c}(\Omega) \equiv \frac{G_{i,\omega_c}(\Omega)}{\langle i \rangle^2} \approx \frac{1}{\kappa^2} \left(\frac{2\Delta\kappa}{\Delta^2 + \kappa^2} \right)^2. \tag{8.61}$$

The following three equations relate the raw data and the desired noise spectrum (the last equation is not independent from the first two):

$$S_{b_{66}}(\Omega)_{Direct} = \frac{1}{g_m^2 \eta_{66}^2} \frac{1}{|H_{i,\omega_c}(\Omega)|^2} \frac{S_i(\Omega)}{\langle i \rangle^2} \approx \frac{1}{g_m^2 \eta_{66}^2} \frac{1}{|H_{i,\omega_c}(\Omega)|^2} \frac{S_V(\Omega)}{\langle V \rangle^2} \tag{8.62a}$$

$$S_{b_{66}}(\Omega)_{PM} = \frac{S_V(\Omega)}{1.33 \times S_V(\Omega_0)} \frac{\Omega_0^2 S_\phi(\Omega_0)}{g_m^2 \eta_{66}^2} \tag{8.62b}$$

$$S_\phi(\Omega_0) = \frac{\beta^2}{2} = \frac{1.33 \times S_V(\Omega_0)}{\Omega_0^2 |H_{i,\omega_c}(\Omega_0)|^2}. \tag{8.62c}$$

The first two equations correspond to the "direct" and PM-calibrated thermal noise spectra, respectively. The third relation allows us to compare the two calibrations by computing β in two ways. The resolved cavity technique gives $\beta = 0.03$, as discussed above. Using experimental values of

$$\{\eta_{66}, g_m/(2\pi), m_{66}, \kappa/(2\pi), \Omega_{66}/(2\pi), \Delta/(2\pi)\}$$
$$\approx \{0.64, 0.35\,\text{MHz/pm}, 8.44\ \text{ng}, 14\,\text{MHz}, 4.82\,\text{MHz}, 97\,\text{MHz}\} \tag{8.63}$$

with Eq. 8.62c gives $\beta = 0.026$.

We use $\beta = 0.03$ and the PM calibration technique to obtain the lower plot in Figure 8.5.
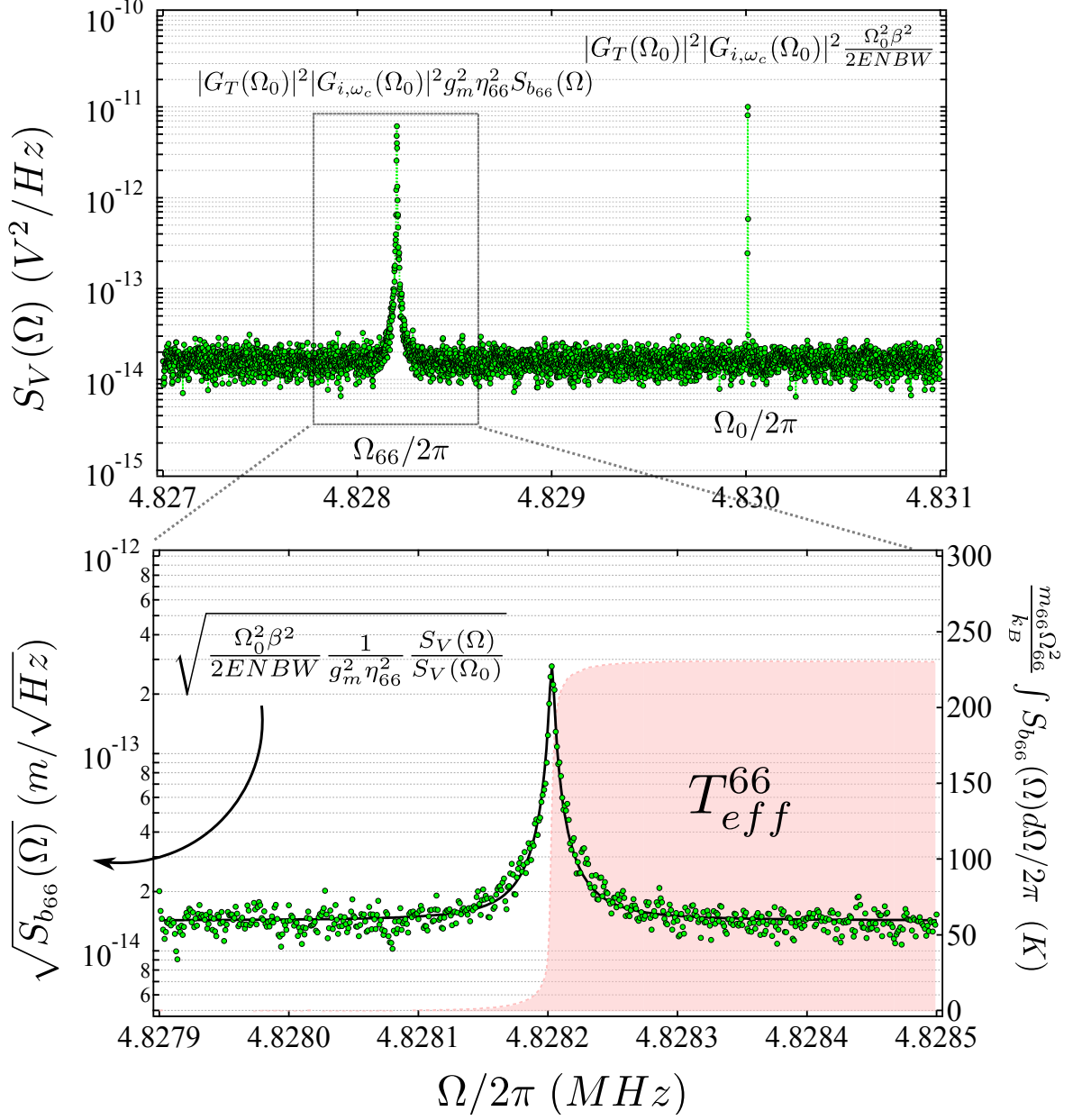
Figure 8.5: Calibration of the photocurrent noise spectrum to obtain the effective temperature of the (6,6) mode of the "science" membrane: T_{eff}^{66}. Raw data (upper plot) corresponds to the power spectral density of voltage fluctuations at the output of the photocurrent transimpedance amplifier with gain $G_T(\Omega)$ V/A. The span shown contains a Lorentzian feature proportional to the power spectrum of displacement of a single membrane vibrational mode $S_V(\Omega) = |G_T(\Omega_{66})|^2 g_m^2 \eta_{66}^2 |G_{i,\omega_c}(\Omega_{66})|^6 S_{b_{66}}(\Omega)$ and a narrow feature (delta-function convoluted with a Hanning windowing function) corresponding to phase modulation of the laser $S_V(\Omega_0) = |G_T(\Omega_{66})|^2 |G_{i,\omega_c}(\Omega_0)|^2 \beta^2 \Omega_0^2 / 2ENBW$. Normalizing by $S_V(\Omega_0)$ enables mapping from $S_V(\Omega)$ to $S_{b_{66}}(\Omega)$, as shown in the lower plot. Integrating over the processed spectrum determines the effective temperature of the mode (Eq. 8.57).

Subtracting the background and integrating over the resulting noise spectrum gives:

$$T_{eff}^{66}|_{PM} = \frac{m_{66}\Omega_{66}^2}{k_B} \int_{\Omega_{ij}} S_{b_{66}}(\Omega)d\Omega/2\pi = \frac{(8.44\text{ng}) \times (2\pi \times 4.82 \text{ MHz})^2}{1.38 \times 10^{-23} \text{ J/K}} \times (0.64 \text{ pm})^2 \quad (8.64\text{a})$$

$$= 232 \text{ K} + \{0, 60\}_{\eta_{66}} + \{-64, 37\}_{m_{66}} + \{-13, 64\}_{g_m} = 232 \text{ K} + \{-74, 196\} \quad (8.64\text{b})$$

$$T_{eff}^{66}|_{\text{"direct"}} = 232 \text{ K} \times (0.026/0.03)^2 = 174\text{K} + \{-55, 147\} \quad (8.64\text{c})$$

where the error bars are due to the uncertainties described in Section 8.7.4: $\{g_m/(2\pi), m_{66}, \eta_{66}\} = \{0.31 - -0.36 \text{ MHz/pm}, 6.1 - -9.7 \text{ ng}, 0.57 - -0.64\}$

For the ~ 1 μW power and $\Delta/(2\pi) = 100$ MHz detuning used, we expect negligible reduction in effective temperature due to radiation pressure back-action (we elaborate on this in Chapter 9). Hence the above result is consistent with an expected value of $T_{eff}^{ij} \approx T_{room} \approx 298$ K.

8.7.7 Thermal Noise "Spectroscopy" to Determine the Spatial Overlap Coefficients

An important free variable in the thermal noise calibration is the spatial overlap between the membrane and cavity mode, η_{ij} (Section 7.1.3). To compute the spectrum of spatial overlap factors, we need to know the shape of the membrane vibrational mode, the shape of the TEM_{mn} cavity mode, and the position (x_0, y_0) of the cavity mode relative to the center of the membrane. The first two can be determined a priori from the membrane and cavity dimensions. We can determine (x_0, y_0) experimentally by using the multimode effective length noise spectrum, $S_{LL}(\Omega)$, as a spectroscopic tool. To do this, we note that the ratio of the areas beneath different noise peaks is proportional to the ratio of spatial overlap factors:

$$\frac{\int_{\Omega_{ij}} S_L(\Omega)d\Omega/2\pi}{\int_{\Omega_{i'j'}} S_L(\Omega)d\Omega/2\pi} = \frac{\eta_{ij}^2 \int_{\Omega_{ij}} S_{b_{ij}}(\Omega)d\Omega/2\pi}{\eta_{i'j'}^2 \int_{\Omega_{i'j'}} S_{b_{i'j'}}(\Omega)d\Omega/2\pi} = \frac{\eta_{ij}^2 T_{eff}^{ij}/m_{ij}\Omega_{ij}^2}{\eta_{i'j'}^2 T_{eff}^{i'j'}/m_{i'j'}\Omega_{i'j'}^2} \xrightarrow{\Gamma_{opt}=0} \frac{\eta_{ij}^2}{\eta_{i'j'}^2}\frac{\Omega_{i'j'}^2}{\Omega_{ij}^2}. \quad (8.65)$$

Here the effective mass $m_{ij} = m_{phys}/4$ has dropped out because of how we've defined it for a square membrane vibration (relative to the displacement at an antinode, see Section 7.1.1). The effective temperatures cancel in the absence of optical damping, $T_{eff}^{ij} = T_{bath}$ (Section 7.3).

Importantly, it is not necessary to absolutely calibrate the effective length noise spectrum in order to measure these ratios. It is however necessary to account for the detector and cavity response functions at different frequencies. In the example below we make a PDH measurement. Integrating the the raw transimpedance amplified error signal gives:

$$\frac{\int_{\Omega_{ij}} S_V(\Omega)d\Omega/2\pi}{\int_{\Omega_{i'j'}} S_V(\Omega)d\Omega/2\pi} \xrightarrow{\Gamma_{opt}=0} \frac{|G_T(\Omega_{ij})|^2}{|G_T(\Omega_{i'j'})|^2}\frac{|G_{\epsilon,\omega_c}(\Omega_{ij})|^2}{|G_{\epsilon,\omega_c}(\Omega_{i'j'})|^2}\frac{\eta_{ij}^2}{\eta_{i'j'}^2}\frac{\Omega_{i'j'}^2}{\Omega_{ij}^2} \approx \frac{\eta_{ij}^2}{\eta_{i'j'}^2}\frac{\Omega_{i'j'}^2}{\Omega_{ij}^2}. \quad (8.66)$$

The final approximation is appropriate when (1) the transimpedance gain is nearly flat, as in the example below (we use a DC coupled detector with bandwith 150 MHz $\gg \Omega_{ij}/2\pi$), and (2) for $\Omega_{ij} \lesssim \kappa$, in which case the cavity response $|G_{\epsilon,\omega_c}(\Omega)|$ is also nearly flat.

To determine the "likelihood" that the optical mode is at position (x_0, y_0), we perform a linear chi-square analysis [85]. The chi variable $\chi_{ij,i'j'}(x_0, y_0)$ is the difference between the measured ratio and the predicted ratio based on the mode shape of the membrane and the cavity, as described in Section 7.1.3.1. The chi-square probability (likelihood) distribution is defined:

$$\chi_{ij,i'j'}(x_0, y_0) = \sqrt{\frac{\int_{\Omega_{ij}} S_V(\Omega) d\Omega/2\pi}{\int_{\Omega_{i'j'}} S_V(\Omega) d\Omega/2\pi}} - \frac{\Omega_{i'j'}|G_{\epsilon,\omega_c}(\Omega_{ij})||\eta_{ij}|(x_0, y_0)}{\Omega_{ij}|G_{\epsilon,\omega_c}(\Omega_{i'j'})||\eta_{i'j'}|(x_0, y_0)} \tag{8.67a}$$

$$P(x_0, y_0) = \frac{e^{-(\chi_{66,11}^2 + \chi_{33,11}^2 + \chi_{22,11}^2 + \cdots)/N}}{\int_S e^{-(\chi_{66,11}^2 + \chi_{33,11}^2 + \chi_{22,11}^2 + \cdots)/N} dx dy}, \tag{8.67b}$$

where the integral $\int_S$ is over the surface of the membrane and N is the number of independent ratios measured.

The spectrum of overlap coefficients $\{\eta_{ij}\}$ is determined from $P(x_0, y_0)$ by either evaluating at the position of highest likelihood (maximum P) or by computing moments of the distribution:

$$\langle \eta_{ij} \rangle = \int \eta_{ij}(x_0, y_0) P(x_0, y_0) dx dy \tag{8.68a}$$

$$SD(\eta_{ij}) = \int (\eta_{ij,00}(x_0, y_0)^2 - \langle \eta_{ij} \rangle^2) P(x_0, y_0) dx dy. \tag{8.68b}$$

An example of "thermal noise spectroscopy" is outlined in Figure 8.6. Here we have probed the TEM$_{00}$ mode of the cavity using the PDH method (the details are not crucial for this ratiometric measurement). A small optical power is used ($\langle P_{out} \rangle < 1~\mu$W) in order to minimize optical heating/damping (we find that this is still an important consideration for the resonant PDH probe). The power spectral density of the transimpedance amplified error signal is processed with a commercial spectrum analyzer (HP 4395A). In power spectrum mode, the analyzer records values $\langle V^2(\Omega) \rangle \equiv \int_{\Omega-(2\pi)B/2}^{\Omega+(2\pi)B/2} S_V(\Omega') d\Omega'/2\pi$, where B is the effective noise bandwidth (ENBW, Section 8.7.1) in non-angular units. We use ENBW = 100 Hz, much larger than the mechanical linewidth $\Gamma_{ij}/2\pi$, so that $\langle V^2(\Omega_{ij}) \rangle \propto \eta_{ij}^2 \int_{\Omega_{ij}} S_{b_{ij}}(\Omega) d\Omega/2\pi$ as in Eq. 8.65. In order to avoid systematic error due to creep of the membrane position z_m and other parameters, we perform a nonlinear sweep which quickly scans the analyzer center frequency over the range of interest: in this case a set of 10 kHz windows centered on frequencies $\{\Omega_{11}, \Omega_{22}, \Omega_{33}, \Omega_{44}, \Omega_{26}, \Omega_{62}, \Omega_{66}\}$.

Figure 8.6 corresponds to an effort to center the optical beam at one of the (6,6) antinodes. We are typically able to constrain the position to within several microns based on the standard deviation (SD) of the chi-square value. Near an antinode of the (6,6) mode, we have been able to constrain
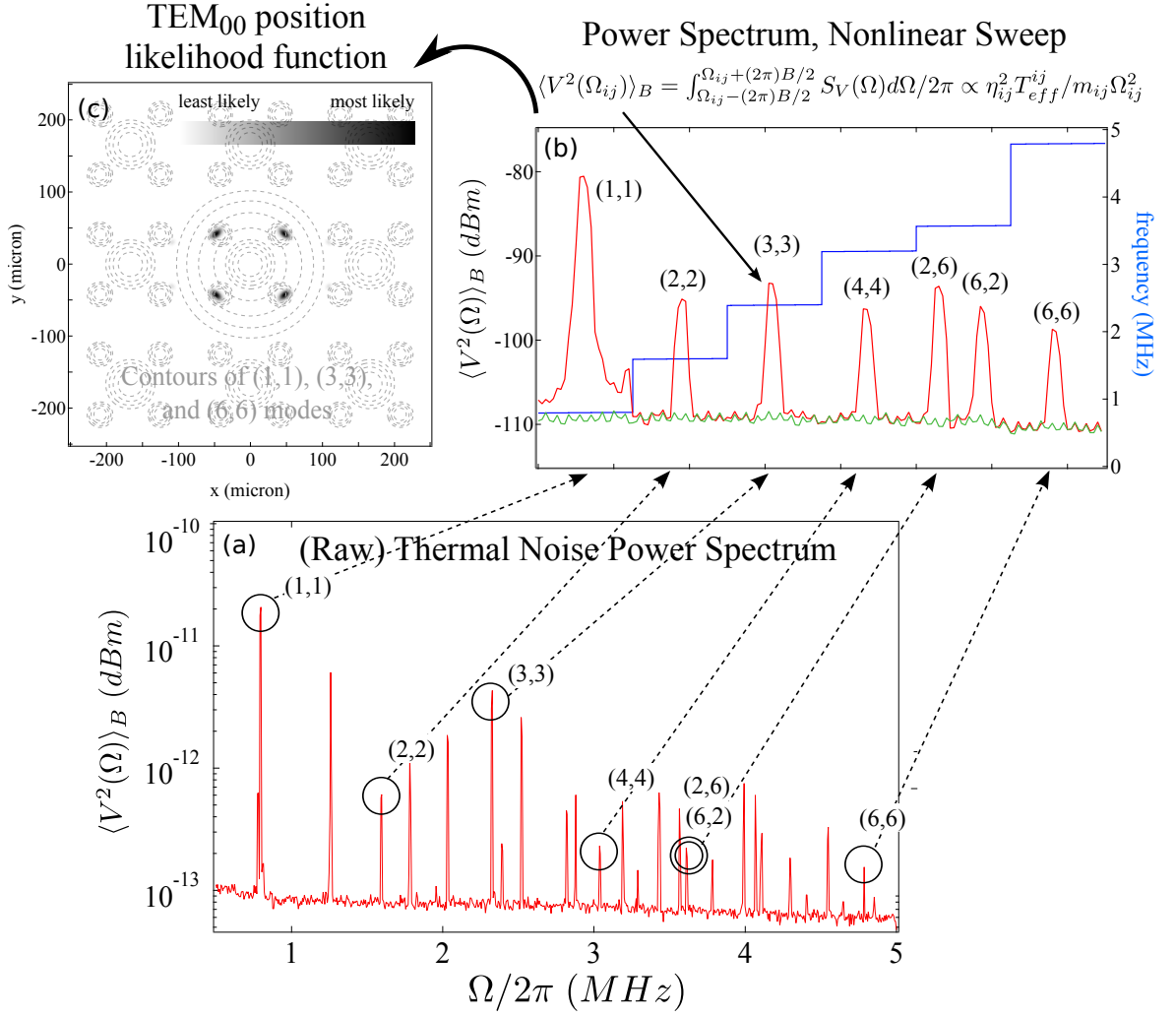
Figure 8.6: Schematic of the "thermal noise spectroscopy" technique for determining the membrane position. Plot (a) is a typical power spectrum of the transimpedance-amplified PDH error signal, proportional to the cavity length noise spectrum. To avoid systematics, the spectrum analyzer is rapidly swept in "list frequency" mode across a subset of noise peaks, using a bandwidth B $\gg \Gamma_{ij}$. The result is shown in plot (b). Each peak is proportional to the total effective displacement $\eta_{ij}^2 T_{eff}^{ij}/m_{ij}\Omega_{ij}^2$. Ratios of the peaks determine the position-dependent quantity $\eta_{ij}^2\Omega_{i'j'}^2/\eta_{i'j'}^2\Omega_{ij}^2$, provided that the probe is weak enough that $T_{eff}^{ij} \approx T_{bath}$ for each mode. For each possible location of the optical mode, the measured ratios are compared to the predicted ratios based on independent knowledge of the membrane size and cavity waist (Section 7.1.3.1). A linear chi-square analysis gives the position probability ("chi-square likelihood") distribution shown in plot (c), which in turn predicts the set of spatial overlap factors $\{\eta_{ij}\}$
.

the overlap coefficient to within 10% of its maximum theoretical value, $\eta_{66} = 0.64$ for the science cavity (Section 7.1.3).

8.8 Substrate and Laser Noise Measurements

Laser phase/frequency noise and thermal vibration of the end-mirror substrates — "substrate noise" in Section 7.3.2 — both limit sensitivity to membrane thermal motion in the MIM system. The effective cavity length noise due to substrate motion is given by Eq. 7.25:

$$S_L(\Omega)|_{sub} = g_0^{-2} S_{\omega_c}(\Omega)|_{sub} = \left(\frac{g_1}{g_0}\right)^2 S_{z_1}(\Omega) + \left(\frac{g_1}{g_0}\right)^2 S_{z_2}(\Omega). \tag{8.69}$$

Here $\{S_{z_1}(\Omega), S_{z_2}(\Omega)\}$ are the spectral density of effective displacement for mirrors $\{1, 2\}$ (Eq. 7.32) and $\{g_1, g_2\}$ are the optomechanical coupling of mirrors $\{1, 2\}$. Recall that $g_{1,2} \neq g_0$ when the membrane is placed between the mirrors, as described in Section 7.3.2.3.

Small fluctuations of the instantaneous frequency of the incident laser field produce a similar effect on the intracavity field as cavity resonance frequency fluctuations. This was shown in Section 8.6, and is discussed in greater rigor in a later chapter (Section 10.8). The effective cavity length noise associated with fluctuations of the instantaneous laser frequency ω_0 will be defined:

$$S_L^0(\Omega) \equiv g_0^{-2} S_{\omega_0}(\Omega). \tag{8.70}$$

In overview, the frequency noise on our home-brew external-cavity diode laser (Eagleyard) operating at 935 nm is roughly $\sqrt{S_{\omega_0}(\Omega)} \sim 2\pi \times 10$ Hz/$\sqrt{\text{Hz}}$ at $\Omega/2\pi \sim 1$ MHz, corresponding to an effective length noise of $\sqrt{S_L^0(\Omega)} \sim 2\pi \times 10/g_0 \sim 10^{-17}$ m/$\sqrt{\text{Hz}}$. We have since moved to a titanium-sapphire laser (Schwarz Electro-Optics) operating at ~ 810 nm. We have found the frequency noise on this laser to be $< 2\pi \times 1$ Hz/$\sqrt{\text{Hz}}$ at $\Omega/2\pi \sim 1$ MHz, corresponding to an effective length noise of $\lesssim 10^{-18}$ m/$\sqrt{\text{Hz}}$. By contrast, the effective length noise produced by the end-mirror substrates has been found to vary between $S_L(\Omega) \sim 5 \times 10^{-18}$ and 5×10^{-17} m/$\sqrt{\text{Hz}}$. This noise is commensurate with Brownian vibration of our "science" membrane when optically damped to ~ 10 phonons, as expressed in Eqs. 8.44–8.45 and further elaborated in Chapter 10.

To measure this extraneous noise, we remove the membrane from the cavity. In this case $g_{1,2} = g_0$. We then perform the detuned probe measurement as described in Section 8.3 using the TEM$_{00}$ mode of the cavity. The power spectral density of cavity resonance frequency fluctuations, $S_{\omega_c}(\Omega)$, laser frequency fluctuations, $S_{\omega_0}(\Omega)$, and transimpedance amplified photocurrent fluctuations, $S_V(\Omega)$, are related by:

$$S_V(\Omega) = |G_T(\Omega)|^2 |G_{i,\omega_c}(\Omega)|^2 (S_{\omega_c}(\Omega)|_{sub} + S_{\omega_0}(\Omega)) \tag{8.71}$$

where $G_T(\Omega)$ is the transimpedance gain of the photodetector.

We calibrate this noise spectrum as discussed in Section 8.6: by phase modulating the input field

at frequency Ω_0 with a modulation depth β. This results in a reference peak:

$$S_V(\Omega_0) = |G_T(\Omega_0)|^2 |G_{i,\omega_c}(\Omega_0)|^2 \frac{\Omega_0^2 \beta^2}{2} \frac{1}{ENBW}. \tag{8.72}$$

Assuming that the transimpedance gain is flat over the frequency range of interest gives

$$S_{\omega_c}(\Omega)|_{sub} + S_{\omega_0}(\Omega) = S_V(\Omega) \cdot \frac{1}{S_V(\Omega_0)} \frac{\Omega_0^2 \beta^2}{2} \frac{1}{ENBW} \frac{|G_{i,\omega_c}(\Omega_0)|^2}{|G_{i,\omega_c}(\Omega)|^2}. \tag{8.73}$$

This expression includes measured variables $\{S_V(\Omega), S_V(\Omega_0), \Omega_0, \beta, \Delta, \kappa, g_0\}$, and a complicated "filter" function $|G_{i,\omega_c}(\Omega_0)|^2/|G_{i,\omega_c}(\Omega)|^2 \xrightarrow{\{\Omega,\Omega_0\}\ll\kappa} 1$, which is due to the finite response time of the cavity.

The measurements described below were made with an Agilent 4395A spectrum analyzer in "noise" mode (for further description, see Section 4.5.4 and [56]). The photodetector used was a New Focus 1801 with a transimpedance gain of $|G_T(\Omega < 2\pi \cdot 100 \text{ MHz})| \approx 2 \times 10^4$ V/A.

8.8.1   Laser Frequency Noise

8.8.1.1   Diode Laser

Diode laser frequency noise dominates over substrate noise in our science cavity, i.e., $S_{\omega_0}(\Omega)|_{diode} \gg S_{\omega_c}(\Omega)|_{sub}$. We have measured $S_{\omega_0}(\Omega)|_{diode}$ directly from the transmission of a detuned probe as described above, using Eq. 8.73. For the measurement shown in Figure 8.7, the operating wavelength is $\lambda \approx 935$ nm, the power on the transmission photodetector is $\langle P_{out} \rangle \approx 90\,\mu$W, and the cavity linewidth was measured to be $\kappa \approx 10.8$ MHz. A spectrum analyzer bandwidth of ENBW ≈ 100 Hz was used.

Figure 8.7 shows three contributions to the measured noise: detector noise (black), shot noise (green), and laser FM noise (red). Detector noise is obtained with the laser blocked. Shot noise plus detector noise is obtained by directly coupling $\approx 90\,\mu$W from the diode laser onto the detector without passing through the cavity. Subtracting the detector noise gives the shot noise spectrum shown in green (we have determined that this is not laser intensity noise by verifying a $\sqrt{\langle P \rangle}$ scaling with power incident on the detector). Laser FM noise is obtained by coupling $\approx 90\,\mu$W through the cavity and onto the photodetector at a detuning $\Delta \approx -\kappa$. Subtracting laser + shot noise gives the red curve shown. All curves are multiplied by the PM calibration factor given on the RHS of Eq. 8.73 (calibration peak not shown in figure).

The measured diode laser FM noise in the range $\Omega/(2\pi) = 500$ kHz to 5 MHz appears to be structureless and has a magnitude of $S_{\omega_0}(\Omega) = 30--40$ Hz/$\sqrt{\text{Hz}}$ ($S_L^0(\Omega) = 6--8 \times 10^{-17}$ m/$\sqrt{\text{Hz}}$). The peak near 800 kHz is the fundamental vibration of the mirror substrates, as discussed in the next subsection. Note that the inferred shot-noise sensitivity of 1–2 Hz/$\sqrt{\text{Hz}}$ (green curve) is consistent
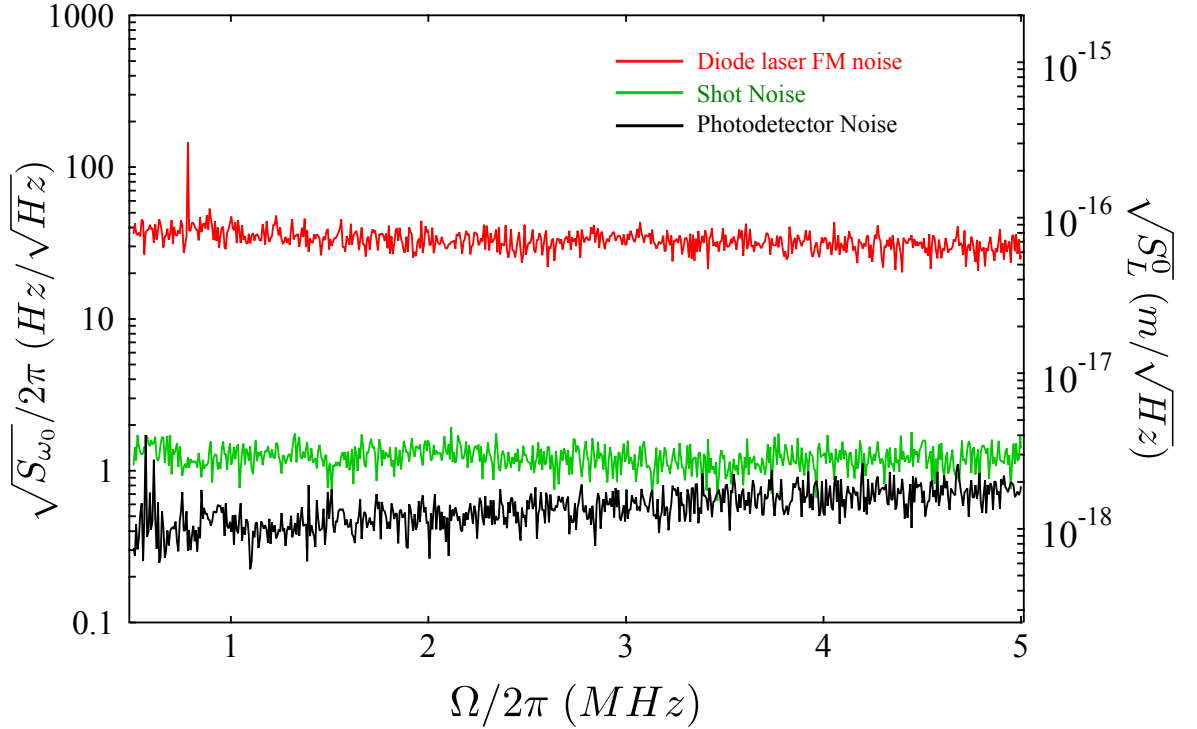
Figure 8.7: Measurement of frequency noise on our $\lambda = 935$ nm external-cavity diode laser. The measurement was made by passing $\approx 90\,\mu$W through the science cavity at a detuning $\Delta = \kappa \approx 2\pi \cdot 10.8$ MHz and monitoring the transmitted intensity fluctuations. Detector noise and shot noise are shown in black and green for comparison. These contributions are independently measured and subtracted from the raw signal in order to obtain the red curve shown. All three curves are multiplied by a calibration factor obtained from a known phase modulation of the input beam (not shown). The right-hand scale expresses the noise as an effective cavity length displacement.

with the value of 0.9 Hz/$\sqrt{\text{Hz}}$ predicted by incorporating the above measurement parameters into Eq. 8.42.

8.8.1.2 Titanium-Sapphire Laser

The frequency noise exhibited by our titanium-sapphire (ti-sapph) laser is small compared to the substrate noise in our science cavity, i.e., $S_{\omega_0}(\Omega)|_{TiS} << S_{\omega_c}(\Omega)|_{sub}$. It was therefore not practical to use the science cavity for its measurement. We have instead used a fiber-based interferometer as described in [86]. The basic idea is to send the light through a long-baseline, imbalanced Mach-Zender (MZ) interferometer. The effective path length of the long arm is sensitive to small fluctuations in the instantaneous frequency of the laser. Consequently, laser phase noise produces intensity noise on the output of the MZ. This noise can be calibrated by applying a known phase modulation to the input field. In Figure 8.8 we show the result of one such measurement without giving experimental details. This measurement was performed with great care by our post-doc, Yi Zhao. The broad peak at ~ 600 kHz is believed to correspond to relaxation-oscillation of the ti-sapph crystal. The
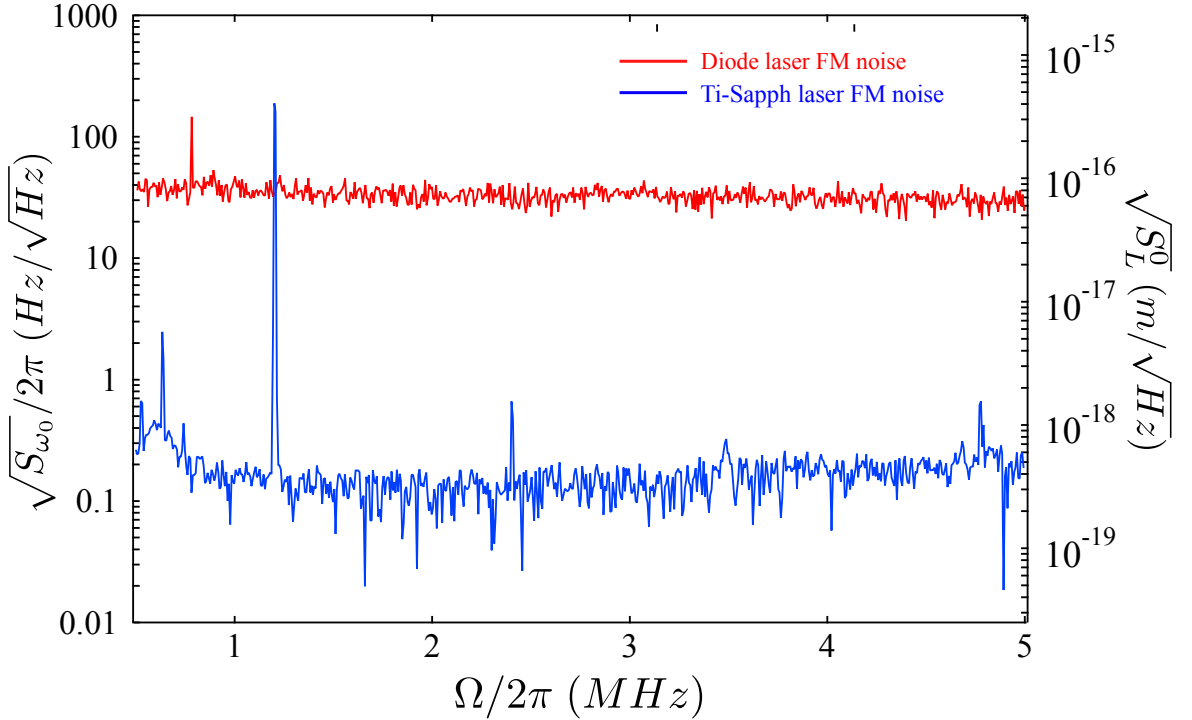
Figure 8.8: Comparison of diode laser frequency noise (red) and ti-sapph laser frequency noise (blue). The right-hand scale expresses the noise in units of effective cavity length displacement. Diode laser noise was measured by coupling radiation through the science cavity at a detuning $\Delta = -\kappa$ and monitoring the transmitted intensity fluctuations. Ti-Sapph noise was measured using an imbalanced fiber-based Mach-Zender interferemoter, using the method described in [86].

narrow peak at 1.2 MHz is a calibration peak. The FM noise spectrum from 1 MHz to 5 MHz is at the level of 0.1–0.2 Hz/$\sqrt{\text{Hz}}$, or effectively 3–6×10^{-19} m/$\sqrt{\text{Hz}}$ in cavity length units. This low noise is at the level of the zero-point displacement of our science membrane were it to be optically damped to the ground state, as expressed in Eq. 8.42. The ti-sapph laser's low noise also enables the substrate noise measurement discussed in the following subsection.

8.8.2 Substrate Noise

To measure the substrate noise, we remove the membrane from the cavity and perform the detuned probe measurement using the low noise ti-sapph laser (in this case $S_L(\Omega)|_{sub} >> S_L^0(\Omega)|_{TiS}$). For this measurement, the operating wavelength was $\lambda \approx 805$ nm, the power on the transmission photodetector was $\langle P_{out} \rangle \approx 100\,\mu$W, and the cavity linewidth was measured to be $\kappa \approx 9$ MHz. A spectrum analyzer bandwidth of $ENBW \approx 30$ kHz was used. The inferred substrate noise is shown in Figure 8.9. Three major contributions to the measurement noise spectrum are shown: detector noise, shot noise, and the desired substrate thermal noise. Detector noise is recorded with the laser field blocked and shot noise is estimated by directly coupling 100 μW into the photodetector (by-
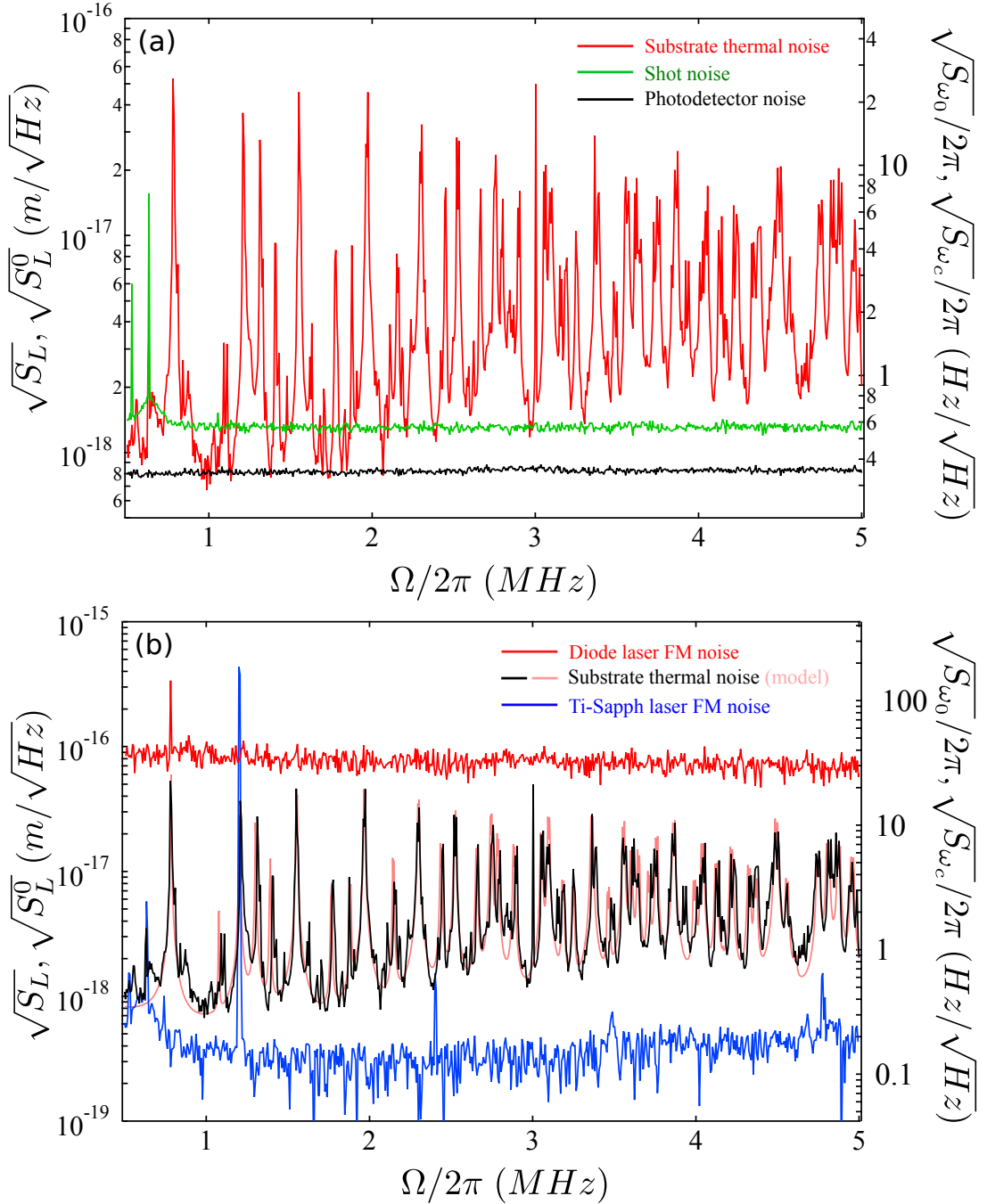
Figure 8.9: Measurement of substrate thermal noise and comparison to laser frequency noise. Substrate noise was measured by coupling $\approx 100\,\mu$W of radiation from the low noise Ti-Sapph laser through the science cavity (TEM$_{00}$ mode) at detuning $\Delta = -\kappa \approx 2\pi \cdot 9$ MHz and monitoring the transmitted intensity fluctuations. In the upper plot we compare the relative contributions of detector noise (black) and shot noise (green), which have been subtracted from the raw signal to obtain the red curve shown. In the lower plot we compare the measured substrate noise to the measured frequency noise of our diode (red) and ti-sapph (blue) laser. We also compare the substrate noise to a numerical finite element model, shown in pink.

passing the cavity). The shot noise curve shown in green has been corrected by subtracting the measured detector noise (black). For the detuned probe measurement we coupled $\langle P_{out} \rangle = 100 \ \mu$W through the science cavity at a detuning of $\Delta \approx -\kappa$. The resulting spectrum shown in red is corrected by subtracting both the black and green curves. All shown curves are calibrated using the phase modulation method summarized in Eq. 8.73.

The substrate noise measurement reveals a dense spectrum of vibrational peaks with the lowest order peak occuring at 785 kHz. The vibrational peaks between 785 kHz and 5 MHz are spaced by $\sim$ 10–100 kHz and appear to have a common quality factor of roughly $Q_m = 650$. The off-resonant noise is at a level of 1–2$\times 10^{-18}$ m/$\sqrt{\text{Hz}}$. The noise peaks reach a level of 1–4$\times 10^{-17}$ m/$\sqrt{\text{Hz}}$. The peaks shown here are slightly smoothed by the large bandwidth of 30 kHz used. In Figure 8.9 we compare the substrate noise to the diode laser and ti-sapph laser noise as well as a numerical finite element model developed by our post-doc Kang-Kuen Ni. This model — which is in remarkable agreement — is discussed in detail in Section 7.3.2. Also note that the inferred shot noise sensitivity of 1–1.5 m/$\sqrt{\text{Hz}}$ is a factor of two larger than the predicted sensitivity of 0.7 m/$\sqrt{\text{Hz}}$ based on incorporating the above parameters into Eq. 8.42 (using a photodetector responsivity of $\mathcal{R} \approx 0.5$ at 805 nm).

Chapter 9

Optomechanical Cooling

In Chapter 2 we derived the optical spring and damping rates experienced by a compliant end-mirror in a Fabry-Perot cavity. In this chapter we apply that model to our "membrane-in-the-middle" apparatus (Figure 9.1), consisting of a short, high-finesse ($\mathcal{F} \approx 10^4$) Fabry-Perot cavity coupled to a stiff, high mechanical quality ($\Omega_m/2\pi > 10^6$, $Q_m > 10^6$) Si_3N_4 membrane. We anticipate that our system can be used to realize significant optomechanical cooling rates, possibly even to access the quantum regime from *room temperature* [14]. In the lab, however, we are presently limited to $\bar{n} > 100$, owing to various technical challenges described below. Significantly, we note that as of the time of this writing several groups have managed to prepare the quantum mechanical ground state of a NEMS-scale mechanical oscillator using a combination of cryogenic and optomechanical cooling [15, 6, 10], while the Yale group's efforts with SiN membranes in a cryogenic version of [23] is currently limited by laser phase noise [61].

To help summarize the reasoning leading up to this experiment, this chapter begins with a review of optical spring and damping forces, with an emphasis on extending the canonical two-mirror system described in Section 2.4 to the MIM system. We carefully step through the application of a simple "weak damping" model to our system, showing that significant optomechanical cooling can be observed for only microwatts of input optical power. We then present measurements we have performed to validate the weak damping model. Operationally, the experiment consists of measuring the membrane's displacement using a strong red-detuned probe (Section 8.3). In our main example we demonstrate that with ~ 1 W of power circulating in the cavity, the mean-squared Brownian vibration amplitude of a higher-order membrane mode (the (6,6) mode, with frequency $\Omega_{66}/2\pi = 4.83$ MHz and mechanical quality $Q_{66} = 1.5 \times 10^6$) can be suppressed by a factor $\approx 3 \times 10^3$. This corresponds to a reduction in temperature from $T_{room} \approx 300$ K to an effective value of $T_{eff}^{66} \approx 100$ mK, or equivalently, a reduction in mean thermal occupation from $\bar{n}_{66}^{room} = k_B T_{room}/\hbar\Omega_{66} \approx 1.3 \times 10^6$ to $\bar{n}_{66} \approx 500$ phonons. The amount of "refrigeration" we have achieved is limited by the amount of power we can couple into the cavity for technical reasons and — we anticipate — the background intracavity intensity fluctuations associated with thermal motion
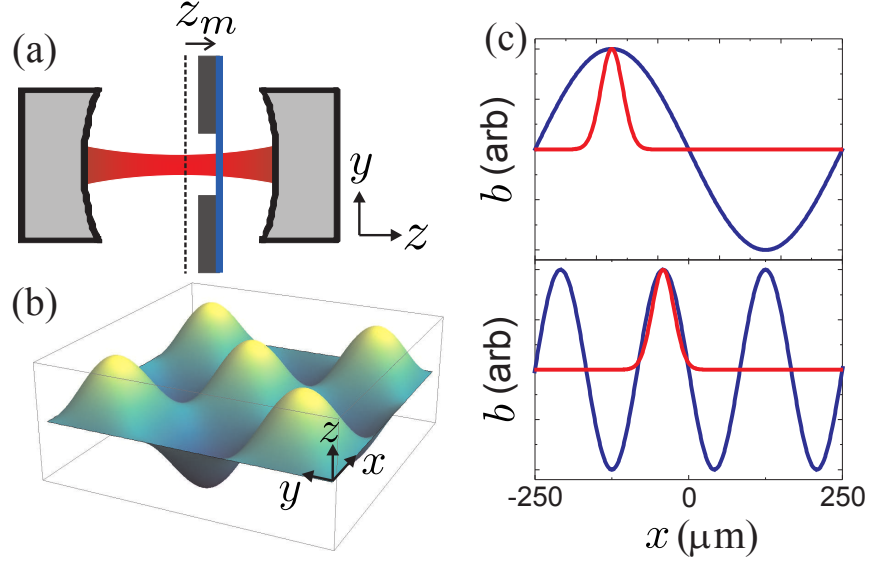
Figure 9.1: (a) Experimental overview: membrane window (thickness $d_m = 50$ nm, square dimension $w_m = 500$ μm) in a short cavity (lenth $L = 742$ μm, finesse $(F) \approx 10^4$). (b) Illustration of (3,3) membrane mode amplitude with $b_{33}\phi_{33}(x, y)$. (c) Intensity profile of TEM$_{00}$ optical mode $|\psi_{00}|^2$ (red solid line) compared to amplitude of membrane modes (2,2) (top) and (6,6) (bottom) with a cavity spot size of $w_c = 35.6$ μm.

of the end-mirror substrates, which we address in the next chapter.

9.1 Radiation Pressure Back-Action: Compressed Review and Extension to MIM System

9.1.1 Compressed Review

In Chapter 2 we described the effect of radiation pressure on a compliant end-mirror in a Fabry-Perot cavity. The end-mirror in this — the "canonical" — optomechanical system (Figure 2.1) is envisioned as a rigid plate with effective (= physical) mass m attached to a massless pendulum spring. The mass-spring system is modeled as a driven, damped harmonic oscillator with displacement amplitude b (coinciding with the position of the mirror surface), resonance frequency Ω_m, and energy damping rate, Γ_m. The driving force has two contributions: a Langevin force F_L, which describes Brownian motion of b, and a radiation pressure $F_{rad} = 2P_{circ}/c$, where P_{circ} is the optical power circulating between the cavity end-mirrors. Crucially, optomechanical coupling between the position of the mirror and the resonance frequency of the cavity implies that the circulating power is a function of

mirror position $b(t)$:

$$m\ddot{b}(t) + \Gamma_m m\dot{b}(t) + m\Omega_m^2 b(t) = F_L(t) + F_{rad}(b(t), t). \tag{9.1}$$

For sufficiently weak optomechanical coupling, the position-dependent radiation pressure force can be described as the sum of a force proportional to the position and the velocity of the mirror; these correspond to the the "optical spring" and "optical damping" forces, respectively:

$$F_{rad}(b(t), t) \approx -k_{opt} b(t) - m\Gamma_{opt}\dot{b}(t). \tag{9.2}$$

From the standpoint of linear response theory (Section 2.1), the optical spring and damping forces manifest themselves as a modification to the mechanical susceptibility, $\chi(\Omega)$, defined as follows:

$$\chi(\Omega) \equiv \frac{b(\Omega)}{F(\Omega)}; \quad \{b(\Omega), F(\Omega)\} = \int_{-\infty}^{\infty} \{b(t), F(t)\} e^{-i\Omega t} dt. \tag{9.3}$$

In the presence of the position-dependent radiation pressure force,

$$F_{rad}(\Omega) = -k_{opt}(\Omega) b(\Omega) - im\Gamma_{opt}(\Omega) b(\Omega), \tag{9.4}$$

the susceptibility of the mirror to the Langevin force becomes:

$$\chi_{eff}(\Omega) = \frac{b(\Omega)}{F_L(\Omega)} = \frac{1/m}{\Omega_m^2 - \Omega^2 + k_{opt}(\Omega)/m - i(\Gamma_m(\Omega) + \Gamma_{opt}(\Omega))\Omega}. \tag{9.5a}$$

The frequency dependence of $\{\Gamma_m(\Omega), \Gamma_{opt}(\Omega), k_{opt}(\Omega)\}$ is a consequence of the fact that a lossy mechanical resonator does not have a well-defined frequency. When both the intrinsic and optical spring are underdamped, then this frequency dependence can be approximately neglected. We will refer to this as the "weak damping" approximation

$$\{\Gamma_m(\Omega), \Gamma_{opt}(\Omega), k_{opt}(\Omega)\} \approx \{\Gamma_m(\Omega_m), \Gamma_{opt}(\Omega_m), k_{opt}(\Omega_m)\} \equiv \{\Gamma_m, \Gamma_{opt}, k_{opt}\}, \tag{9.6}$$

and we will approximate the optical spring as a small frequency shift:

$$\chi_{eff}(\Omega) \approx \frac{1/m}{(\Omega_m + \Delta\Omega_{opt})^2 - \Omega^2 - i(\Gamma_m + \Gamma_{opt})\Omega} \tag{9.7a}$$

$$\Delta\Omega_{opt} \equiv k_{opt}(\Omega_m)/(2m). \tag{9.7b}$$

Thermal flucutuations of b are described by the mechanical transfer function $|\chi_{eff}(\Omega)|^2$ acting

on the power spectral density of Langevin force fluctuations, $S_{F_L}(\Omega)$.

$$S_b(\Omega) = |\chi_{eff}(\Omega)|^2 S_{F_L}(\Omega) \tag{9.8a}$$

$$S_{F_L}(\Omega) = \frac{4k_B T_{bath}}{\Omega} \, \text{Im} \left[\chi_0(\Omega)^{-1} \right] = 4k_B T_{bath} \Gamma_m(\Omega), \tag{9.8b}$$

where $\chi_0(\Omega)$ is the natural susceptibility of the system ($F_{rad} = 0$). The latter expression is a consequence of the Fluctuation-Dissipation Theorem, as described in Section 2.2.

In the weak damping limit, the thermal fluctuations are described by a Lorentzian with a shifted frequency (due to the optical spring) and linewidth (due to the optical damping):

$$S_b(\Omega) = |\chi_{eff}(\Omega)|^2 \times 4k_B T_{bath} \Gamma_m m \approx \frac{4k_B T_{bath} \Gamma_m/m}{((\Omega_m + \Delta\Omega_{opt})^2 - \Omega^2)^2 + (\Gamma_m + \Gamma_{opt})^2 \Omega^2}. \tag{9.9}$$

An important consequence of the modified mechanical response is the phenomenon of optical cooling/heating, which corresponds to a reduction/enhancement of the effective temperature of b. For weak damping:

$$T_{eff} = \frac{m}{k_B} \int_0^\infty \Omega^2 S_{bb}(\Omega) \frac{d\Omega}{2\pi} \approx T_{bath} \frac{\Gamma_m}{\Gamma_m + \Gamma_{opt}}, \tag{9.10}$$

or in terms of thermal occupation number:

$$\bar{n} \equiv \frac{k_B T_{eff}}{\hbar(\Omega_m + \Delta\Omega_{opt})} \approx \frac{k_B T_{eff}}{\hbar\Omega_m} = \bar{n}_{bath} \frac{\Gamma_m}{\Gamma_m + \Gamma_{opt}}. \tag{9.11}$$

The sign of Γ_{opt} depends on the sign of the correlations between the mirror position and the radiation pressure force. For positive optical damping $\Gamma_{opt} > 0$, the effective temperature of the oscillator is reduced. This is analagous to the suppression of noise in an electronic circuit using negative feedback.

9.1.2 Model for Radiation Pressure Damping

9.1.2.1 Two-Mirror Resonator

In the canonical system, the parametric coupling between displacement amplitude b and the amplitude a of the intracavity standing wave is described by the following pair of differential equations (Section 2.3–2.4),

$$m\ddot{b}(t) + m\Gamma_m \dot{b}(t) + m\Omega_m^2 b(t) = F_L(t) + F_{rad}(t) \tag{9.12a}$$

$$\dot{a}(t) = -\left(\kappa + i(\omega_0 - \omega_c - g_0 b(t)) \right) a(t) + \sqrt{2\kappa_1} E_{in}(t) \tag{9.12b}$$

$$E_{out}(t) = \sqrt{\kappa_2} a(t) \tag{9.12c}$$

$$E_{ref}(t) = \sqrt{\kappa_1} a(t) - E_{in}(t). \tag{9.12d}$$

Variables $\{g_0, a(t), E_{in}(t), E_{out}(t), E_{ref}(t), \kappa, \kappa_1, \kappa_2, \omega_c, \omega_0\}$ correspond to the end-mirror optomechanical coupling, the amplitude of the intracavity standing wave, the amplitude of the input/output/reflected electric field, the total amplitude decay rate of the intracavity field, the amplitude decay rate of the intracavity field through the input (mirror 1) and output (mirror 2) mirror, the resonance frequency of the cavity, and the frequency of the input field, respectively. $a(t)$ and $E_{in}(t)$ are complex amplitudes expressed in the frame rotating at ω_0 and normalized so that $|a(t)|^2 = U_c(t)$ is the slowly varying envelope of the intracavity energy and $|E_{in}(t)|^2$ is the slowly varying envelope of the power coupled to the cavity.

The radiation pressure force $F_{rad}(t)$ can be computed from the gradient of the intracavity energy, with respect to the mirror position. For a low-loss cavity: $F_{rad} = dU_c/db \approx -(d\omega_c/db) \cdot U_c/\omega_c$ (Eq. 2.39). In the canonical two-mirror system, this reduces to the familar expression in terms of the circulating power (Eq. 2.37):

$$F_{rad}(t) = -g_0 U_c(t)/\omega_c = 2P_{circ}(t)/c. \tag{9.13}$$

(Sign convention discussed in Section 2.4.)

Solving Eq. 9.12 to first order in the small parameter $g_0 b/\kappa$ gives the following expressions for the optical spring shift and damping rates in the "weak damping" approximation (see derivation in Section 2.4, Eq. 2.51):

$$\Gamma_{opt} = 2\langle n_c \rangle \frac{g_0^2 b_{zp}^2}{\kappa} \left(\frac{1}{1 + (\Delta + \Omega_m)^2/\kappa^2} - \frac{1}{1 + (\Delta - \Omega_m)^2/\kappa^2} \right) \tag{9.14a}$$

$$\Delta\Omega_{opt} = \langle n_c \rangle \frac{g_0^2 b_{zp}^2}{\kappa} \left(\frac{(\Delta + \Omega_m)/\kappa}{1 + (\Delta + \Omega_m)^2/\kappa^2} + \frac{(\Delta - \Omega_m)/\kappa}{1 + (\Delta - \Omega_m)^2/\kappa^2} \right), \tag{9.14b}$$

where $\Delta = \omega_0 - \omega_c$ is the detuning of the input field, $\langle n_c \rangle \equiv \langle |a|^2 \rangle / \hbar\omega_c$ is the intracavity photon number and $x_{zp} = \sqrt{\hbar/2m\Omega_m}$ is the zero-point displacement.

The optical damping rate is proportional to the difference in the strength of the red and blue sidebands generated by modulation of the cavity resonance frequency. When the input field is red-detuned ($\Delta < 0$), the damping rate is positive, $\Gamma_{opt} > 0$. Microscopically, this corresponds to a situation in which photons scattered from the mirror surface preferentially receive a blue shift before exiting the cavity.

9.1.2.2 Extension to the MIM System

The optomechanical interaction between the amplitude b_{ij} of a membrane vibrational mode and the amplitude a of a single mode of the intracavity field is described by the following pair of coupled

differential equations in the limit that the membrane reflection coefficient is "small" (Section 8.2):

$$m_{ij}\ddot{b}_{ij}(t) + m_{ij}\Gamma_{ij}\dot{b}_{ij}(t) + m_{ij}\Omega_{ij}^2 b_{ij}(t) = F_L^{ij}(t) + F_{rad}^{ij}(t) \tag{9.15a}$$

$$\dot{a}(t) = -\left(\kappa + i(\omega_0 - \omega_c - \sum_{ij} g_{ij}b_{ij}(t))\right)a(t) + \sqrt{2\kappa_1}E_{in}(t); \; g_{ij} \equiv g_m\eta_{ij} \tag{9.15b}$$

$$E_{out}(t) = \sqrt{2\kappa_2}a(t) \tag{9.15c}$$

$$E_{ref}(t) = \sqrt{2\kappa_1}a(t) - E_{in}(t). \tag{9.15d}$$

These formulas are a formally equivalent to the coupled equations of motion for the canonical two-mirror optomechanical system, Eq. 9.12. The generalizations that have been made are as follows:

- Generalized displacement amplitude $b_{ij}(t)$ is the amplitude of the displacement vector field $\vec{\phi}_{ij}(x, y, z_m) = \hat{z}\sin(i\pi x/w_m)\sin(j\pi x/w_m)$ describing drum vibrations of the $w_m \times w_m$ square membrane surface (Section 7.1.1).

- For vibrational modes of the membrane, effective mass m_{ij} is defined relative to the energy normalization condition $m_{ij} = \langle U_{ij}\rangle/\Omega_{ij}^2\langle b_{ij}^2\rangle = \int_V \rho\vec{\phi}_{ij} \cdot \vec{\phi}_{ij}dV = m_{phys}/4$ (Section 7.1.1).

- For the membrane resonator, Ω_{ij} is the eigenfrequency of the (i, j) vibrational mode and $\Gamma_{ij} = \Omega_{ij}/Q_{ij}$ is the energy damping rate of the of the (i, j) vibrational mode, characterized by mechanical quality Q_{ij} – Γ_{ij} and Q_{ij} may in general depend on the vibrational frequency (Section 7.3.1.2).

- Brownian motion of generalized amplitude $b_{ij}(t)$ is described by a thermal force with spectral density $S_{F_L^{ij}}(\Omega) = 4k_B T_{bath}m_{ij}\Gamma_{ij}(\Omega)$. The frequency dependence of the damping term accounts for the "structural" damping behavior in bulk elastic resonators (Section 7.3.1.2).

- In the MIM cavity, $\{a, E_{in}, E_{out}, E_{ref}, \kappa, \kappa_1, \kappa_2, \omega_c, \omega_0\}$ have the same interpretation as in Eq. 9.12 with two important subtleties: (a) the intracavity mode is a more complicated mode-shape that has different amplitudes on the left and right of the membrane (the sum of the energy on both sides is $|a|^2$); (b) the total amplitude decay rate, κ, and the amplitude decay rate through the input mirror κ_1 and output mirror κ_2 are all functions of the equilibrium membrane position, z_m (See discussion in Section 8.2).

- In the MIM system, the optomechanical coupling for a single mode (i, j) is described by $\delta\omega_c = g_{ij}b_{ij} = \eta_{ij}g_m(z_m)b_{ij}$. $g_m(z_m)$ gives the resonance frequency shift resulting from a small displacement of the membrane equilibrium position δz_m, and in general depends on the absolute membrane position relative to the intracavity standing wave (Section 3.3.1). Factor η_{ij} accounts for the spatial overlap between the TEM_{mn} cavity mode and membrane

vibrational mode, and is given by the ratio of the antinode displacement and the displacement of the membrane surface S averaged over the intensity profile of the cavity mode: $\eta_{ij} \equiv \int_S |\psi_{mn}(x,y,z)|^2 \vec{\phi}(x,y,z) \cdot \hat{z} d\sigma / \int_S |\psi_{mn}(x,y,z)|^2 d\sigma$ (see Section 7.1.3).

In the MIM system, the generalized radiation force experienced by coordinate b_{ij} is given by:

$$F_{rad}^{ij}(t) = -g_{ij} U_c(t)/\omega_c = \eta_{ij} g_m(z_m) U_c(t)/\omega_c. \tag{9.16}$$

By direct analogy to the two mirror system, the thermal noise spectrum for a single, underdamped vibration of the membrane in the presence of a weak optical spring is given by (assuming the membrane mode in question is well isolated in frequency from other modes):

$$S_{b_{ij}}(\Omega) \approx \frac{4 k_B T_b \Gamma_{ij}(\Omega)}{m_{ij}} \frac{1}{((\Omega_{ij} + \Delta\Omega_{opt}^{ij})^2 - \Omega^2)^2 + \Omega^2 (\Gamma_{ij}(\Omega) + \Gamma_{opt}^{ij})^2} \tag{9.17a}$$

$$\Gamma_{opt}^{ij} = 2\langle n_c \rangle \frac{(g_{ij} b_{zp}^{ij})^2}{\kappa} \left(\frac{1}{1 + (\Delta + \Omega_{ij})^2/\kappa^2} - \frac{1}{1 + (\Delta - \Omega_{ij})^2/\kappa^2} \right) \tag{9.17b}$$

$$\Delta\Omega_{opt}^{ij} \equiv = \langle n_c \rangle \frac{(g_{ij} b_{zp}^{ij})^2}{\kappa} \left(\frac{(\Delta + \Omega_{ij})/\kappa}{1 + (\Delta + \Omega_{ij})^2/\kappa^2} + \frac{(\Delta - \Omega_{ij})/\kappa}{1 + (\Delta - \Omega_{ij})^2/\kappa^2} \right) \tag{9.17c}$$

$$T_{eff}^{ij} \approx \frac{m_{ij}}{k_B} \int_0^\infty \Omega^2 S_{b_{ij}b_{ij}}(\Omega) d\Omega/2\pi \approx \frac{\Gamma_{ij}}{\Gamma_{ij} + \Gamma_{opt}^{ij}} T_{bath}, \tag{9.17d}$$

where $\langle n_c \rangle \equiv \langle |a|^2 \rangle / \hbar\omega_c$ is the generalized intracavity photon number and $b_{zp}^{ij} = \sqrt{\hbar/2 m_{ij} \Omega_{ij}}$ is the zero-point displacement. To deal with multimode thermal noise, we here retain the frequency dependence of the $\Gamma_{ij}(\Omega)$ associated with structural damping: $\Gamma_{ij}(\Omega) = \Gamma_{ij}(\Omega_{ij})\Omega_{ij}/\Omega = \Omega_{ij}^2/Q_{ij}\Omega$ (Section 7.3.1.2). The integration $\int_{\Omega_{ij}}$ is here understood to exclude off-resonant displacement of other vibrational modes for the multimode resonator.

9.1.3 Experimental Parameters: What to Expect

We now compute the optical spring shift and damping force (Eq. 9.17) for experimental parameters relevant to our membrane-in-the-middle apparatus (Chapters 5 and 6):

$$\{L, FSR, \lambda, \mathcal{F}, \kappa, \kappa_1, \kappa_2\} = \{0.742 \text{ mm}, 202 \text{ GHz}, 935 \text{ nm}, 10^4, 2\pi \cdot 20 \text{ MHz}, 2\pi \cdot 10 \text{ MHz}, 2\pi \cdot 10 \text{ MHz}\} \tag{9.18a}$$

$$\{\Omega_m, Q_m, d_m, w_m, \mathcal{T}\rho\} = \{2\pi \cdot 5 \text{ MHz}, 10^6, 50 \text{ nm}, 500 \, \mu\text{m}, 900 \text{ MPa}, 2.7 \text{ g/cm}^3\}. \tag{9.18b}$$

Variables $\{L, FSR, \lambda\}$ are the actual length and free spectral range of the optical cavity in the absence of the membrane at an operating wavelength of λ. $\{\mathcal{F}, \kappa, \kappa_1, \kappa_2\}$ are the approximate finesse, total amplitude decay rate (HWHM linewidth), input mirror amplitude decay rate, and output mirror amplitude decay rate for the optical cavity in the absence of the membrane (these

values very with the exact position of λ on the mirror coating curve). Variables $\{\Omega_m, Q_m\}$ are the typical frequency and mechanical quality of a higher-order mode of the membrane, which has material properties $\{d_m, w_m, \mathcal{T}, \rho\}$, corresponding to thickness, square width, tension, and density.

9.1.3.1 Intracavity Photon Number

We first compute the intracavity photon number, which depends on the steady-state input and output power, $\{\langle P_{in}\rangle, \langle P_{out}\rangle = \{\langle |E_{in}|^2\rangle, \langle |E_{out}|^2\rangle\}$ (we here assume that the input field is monochromatic), and the magnitude of cavity decay rates $\{\kappa, \kappa_1, \kappa_2\}$. With the membrane removed, our Fabry-Perot cavity is nearly symmetric and lossless: $\kappa_1 \approx \kappa_2 \approx \kappa/2$ (Section 6.2). However, with the membrane in the cavity, decay rates $\{\kappa, \kappa_1, \kappa_2\}$ are all functions of the membrane position. The steady-state intracavity photon number in this more generic case is given by solving Eq. 9.15 with $\dot{a} = 0$ and $b_{ij} = 0$ (Eq. 8.5):

$$\langle n_c\rangle = \frac{\langle |a|^2\rangle}{\hbar\omega_c} = \frac{\langle P_{out}\rangle}{\hbar\omega_c\kappa}\frac{\kappa}{2\kappa_2} = \frac{\langle P_{in}\rangle}{\hbar\omega_c\kappa}\frac{2\kappa_1}{\kappa}\frac{1}{1+\Delta^2/\kappa^2} \tag{9.19a}$$

$$\langle P_{out}\rangle = \frac{\langle P_{out}(\Delta = 0)\rangle}{1+\Delta^2/\kappa^2}. \tag{9.19b}$$

The ratio $2\kappa_1/\kappa$ can be determined from the resonant transmission/reflection of the MIM cavity (Eq. 8.5). Assuming negligible internal loss, so that $\kappa_1 + \kappa_2 = \kappa$:

$$\frac{\langle P_{ref}(\Delta = 0)\rangle}{\langle P_{in}\rangle} = \frac{\langle P_{in}\rangle - \langle P_{out}(\Delta = 0)\rangle}{\langle P_{in}\rangle} = \left(\frac{2\kappa_1}{\kappa} - 1\right)^2 \tag{9.20a}$$

$$\rightarrow \frac{2\kappa_1}{\kappa} = 2 - \frac{2\kappa_2}{\kappa} = \sqrt{1 - \frac{\langle P_{out}(\Delta = 0)\rangle}{\langle P_{in}\rangle}} + 1. \tag{9.20b}$$

The magnitude of $\langle P_{out}(\Delta = 0)\rangle/\langle P_{in}\rangle$ depends on the position of the membrane in the cavity. It can be computed numerically by the method discussed in Section 3.4, and has been measured for our "science" cavity as discussed in Section 6.5. For our low-loss, 50-nm-thick membrane with reflectivity $r_m = 0.42$ at 935 nm, the magnitude of $\langle P_{out}(\Delta = 0)\rangle/\langle P_{in}\rangle$ varies between 0.8 and 1.0 and has a magnitude of ≈ 0.9 when the membrane is positioned halfway between a node and an antinode of the intracavity field. At this position, for which $g_m = 2r_m g_0$, we find $2\kappa_1/\kappa \approx (g_m/g_0)^2 \approx 0.7$ and $2\kappa_2/\kappa \approx 2 - (g_m/g_0)^2 \approx 1.3$.

For relevant cavity parameters, we have:

$$\langle n_c\rangle = 0.750 \times 10^6 \times \left(\frac{\langle P_{in}\rangle}{10\,\mu\text{W}}\right)\left(\frac{\lambda}{935\,\text{nm}}\right)\left(\frac{10\,\text{MHz}}{\kappa/2\pi}\right)\left(\frac{2\kappa_1}{\kappa}\right)\left(\frac{1}{1+\Delta^2/\kappa^2}\right) \tag{9.21a}$$

$$= 0.750 \times 10^6 \times \left(\frac{\langle P_{out}(\Delta = 0)\rangle}{10\,\mu\text{W}}\right)\left(\frac{\lambda}{935\,\text{nm}}\right)\left(\frac{10\,\text{MHz}}{\kappa/2\pi}\right)\left(\frac{\kappa}{2\kappa_2}\right)\left(\frac{1}{1+\Delta^2/\kappa^2}\right). \tag{9.21b}$$

It's useful to use the quantity $\langle P_{out}(\Delta = 0)\rangle$ because in the lab we can measure this number

without worrying about input mode-matching. Also, for a perfectly mode-matched, symmetric cavity, $\langle P_{out}(\Delta = 0)\rangle = \langle P_{in}\rangle$.

9.1.3.2 Effective Mass and Zero-Point Amplitude

The vibrational modes of the membrane were discussed in detail in Sections 4.2 and 7.1.1. The effective mass of generalized displacement amplitude b_{ij} coinciding with the displacement of an antinode on the membrane surface is given by $m_{ij} = m_{phys}/4$. Thus we have, for the effective mass and the zero-point amplitude:

$$m_{ij} = 8.44 \text{ ng} \times \left(\frac{\rho}{2.7 \text{ g/cm}^2}\right)\left(\frac{d_m}{50 \text{ nm}}\right)\left(\frac{w_m}{500\,\mu\text{m}}\right)^2 \tag{9.22a}$$

$$b_{zp}^{ij} = \sqrt{\frac{\hbar}{2m_{ij}\Omega_{ij}}} = 4.45 \times 10^{-16} \text{ m} \times \left(\frac{8.44 \text{ ng}}{m_{ij}}\right)^{1/2}\left(\frac{5 \text{ MHz}}{\Omega_{ij}/2\pi}\right)^{1/2}. \tag{9.22b}$$

9.1.3.3 Optomechanical Coupling and Spatial Overlap

For a nearly lossless 50-nm-thick film at 935 nm, the reflection coefficient is $r_m = 0.42$. Using Eq. 3.22 derived for $g_m(z_m)$ and defining the vibrational amplitude b as the amplitude of an antinode, we have for a single membrane mode (dropping the indices i and j):

$$g_m^{ij} \equiv \frac{\delta\omega_c}{b_{ij}} = \eta_{ij}g_m(z_m) = \eta_{ij} \times \frac{-2|r_m|\sin(2kz)}{\sqrt{1 - |r_m|^2\cos^2(2kz)}} \times g_0 \leq \eta_{ij} \times 2r_m \times \frac{\omega_c}{L} \tag{9.23a}$$

$$= 2\pi \times 0.363 \frac{\text{MHz}}{\text{pm}} \times \left(\frac{\eta_{ij}}{1}\right)\left(\frac{r_m}{0.42}\right)\left(\frac{743\,\mu\text{m}}{L}\right)\left(\frac{935 \text{ nm}}{\lambda}\right). \tag{9.23b}$$

9.1.3.4 Optical Damping and Spring Shift

The full expressions for "weak" optical damping and spring rates given in 9.17 can be expressed:

$$\Gamma_{opt}^{ij} = 2\pi \times 3.92 \text{ kHz} \times \left(\frac{\langle P_{out}(\Delta = 0)\rangle}{10\,\mu\text{W}}\right)\left(\frac{10 \text{ MHz}}{\kappa/2\pi}\right)^2\left(\frac{743\,\mu\text{m}}{L}\right)^2\left(\frac{r_m}{0.42}\right)^2\left(\frac{\eta_{ij}}{1}\right)^2 \tag{9.24a}$$

$$\times \left(\frac{935 \text{ nm}}{\lambda}\right)\left(\frac{5 \text{ MHz}}{\Omega_{ij}/2\pi}\right)\left(\frac{8.44 \text{ ng}}{m_{ij}}\right)\left(\frac{\kappa}{2\kappa_2}\right)\left(\frac{1}{1 + \Delta^2/\kappa^2}\right)\left(\frac{\kappa^2}{(\Omega_{ij} + \Delta)^2 + \kappa^2} - \frac{\kappa^2}{(\Omega_{ij} - \Delta)^2 + \kappa^2}\right) \tag{9.24b}$$

and

$$\Delta\Omega_{opt}^{ij} = 2\pi \times 1.96 \text{ kHz} \times \left(\frac{\langle P_{out}(\Delta = 0)\rangle}{10\,\mu\text{W}}\right)\left(\frac{10 \text{ MHz}}{\kappa/2\pi}\right)^2\left(\frac{743\,\mu\text{m}}{L}\right)^2\left(\frac{r_m}{0.42}\right)^2\left(\frac{\eta_{ij}}{1}\right)^2 \tag{9.25a}$$

$$\times \left(\frac{935 \text{ nm}}{\lambda}\right)\left(\frac{5 \text{ MHz}}{\Omega_{ij}/2\pi}\right)\left(\frac{8.44 \text{ ng}}{m_{ij}}\right)\left(\frac{\kappa}{2\kappa_2}\right)\left(\frac{1}{1 + \Delta^2/\kappa^2}\right)\left(\frac{\kappa(\Omega_{ij} + \Delta)}{(\Omega_{ij} + \Delta)^2 + \kappa^2} - \frac{\kappa(\Omega_{ij} - \Delta)}{(\Omega_{ij} - \Delta)^2 + (\kappa)^2}\right). \tag{9.25b}$$

Two important limits exist for the unitless terms at the far right, corresponding to the difference of the strength of the blue sideband and the red sideband generated on the intracavity field by the vibrating membrane. In the sideband unresolved or "bad" cavity limit ($\Omega_{ij} << \kappa$), they reduce to

$$\frac{\kappa^2}{(\Omega_{ij}+\Delta)^2+\kappa^2} - \frac{\kappa^2}{(\Omega_{ij}-\Delta)^2+\kappa^2} \xrightarrow{\Omega_{ij}<<\kappa} \frac{4\Omega_{ij}}{\kappa}\frac{\Delta/\kappa}{(1+(\Delta/\kappa)^2)^2} = \frac{\pm\Omega_{ij}}{\kappa} \text{ for } \Delta = \pm\kappa \quad (9.26a)$$

$$\frac{\kappa(\Omega_{ij}+\Delta)}{(\Omega_{ij}+\Delta)^2+\kappa^2} - \frac{\kappa(\Omega_{ij}-\Delta)}{(\Omega_{ij}-\Delta)^2+(\kappa)^2} \xrightarrow{\Omega_{ij}<<\kappa} \frac{2\Delta/\kappa}{1+(\Delta/\kappa)^2} \leq \pm 1 \text{ for } \Delta = \pm\kappa. \quad (9.26b)$$

In the sideband resolved or "good cavity" limit, $\Omega_{ij} >> \kappa$, with $\Delta = \pm\Omega_{ij}$ (in which case only one sideband is resonant), the prefactors reduce to

$$\frac{\kappa^2}{(\Omega_{ij}+\Delta)^2+\kappa^2} - \frac{\kappa^2}{(\Omega_{ij}-\Delta)^2+\kappa^2} \xrightarrow{\Omega_{ij}>>\kappa} \pm 1 \text{ for } \Delta = \pm\Omega_{ij} \quad (9.27a)$$

$$\frac{\kappa(\Omega_{ij}+\Delta)}{(\Omega_{ij}+\Delta)^2+\kappa^2} - \frac{\kappa(\Omega_{ij}-\Delta)}{(\Omega_{ij}-\Delta)^2+\kappa^2} \xrightarrow{\Omega_{ij}>>\kappa} \pm\frac{\kappa}{2\Omega_{ij}} \text{ for } \Delta = \pm\Omega_{ij}. \quad (9.27b)$$

In practice, we currently operate the cavity in between the "good" and "bad" cavity limit, using the (6,6) mode with $\Omega_{66}/2\pi \approx 5$ MHz and the cavity at a wavelength for which $\kappa/2\pi \approx 10$ MHz. In this case the unitless factors (Eqs. 9.27a and 9.27b) are roughly 0.5 for both the spring and damping rates.

9.1.3.5 Effective Temperature and Thermal Occupation Number

For parameters used in the previous section, we expect substantial radiation pressure damping rate for ~ 10 microwatts of power coupled into the cavity. For damping rates much smaller than the mechanical frequency or the cavity linewidth, we can naively apply $T_{eff}^{ij} = T_{bath} \times \Gamma_{ij}/(\Gamma_{ij} + \Gamma_{opt}^{ij})$ (Eq. 9.17d) to predict the effective temperature and occupation number $\bar{n}_{ij} = k_B T_{eff}^{ij}/\hbar\Omega_{ij}$ of the damped mode. In the limit $\Gamma_{opt}^{ij} >> \Gamma_{ij}$:

$$T_{eff}^{ij} = 0.38 \text{ K} \cdot \left(\frac{10\,\mu\text{W}}{\langle P_{out}(\Delta=0)\rangle}\right)\left(\frac{\kappa/2\pi}{10\text{MHz}}\right)^2\left(\frac{L}{743\,\mu\text{m}}\right)^2\left(\frac{0.42}{r_m}\right)^2\left(\frac{1}{\eta_{ij}}\right)^2\left(\frac{\lambda}{935\text{ nm}}\right) \quad (9.28a)$$

$$\cdot\left(\frac{10^6}{Q_{ij}}\right)\left(\frac{\Omega_{ij}/2\pi}{5\text{ MHz}}\right)^2\left(\frac{m_{ij}}{8.44\text{ ng}}\right)\left(\frac{2\kappa_2}{\kappa}\right)\left(\frac{1}{1+\Delta^2/\kappa^2}\right)^{-1}\left(\frac{\kappa^2}{(\Omega_{ij}+\Delta)^2+\kappa^2} - \frac{\kappa^2}{(\Omega_{ij}-\Delta)^2+\kappa^2}\right)^{-1}$$

$$(9.28b)$$

$$\bar{n}_{ij} = 1590 \cdot \left(\frac{10\,\mu\text{W}}{\langle P_{out}(\Delta=0)\rangle}\right)\left(\frac{\kappa/2\pi}{10\text{MHz}}\right)^2\left(\frac{L}{743\,\mu\text{m}}\right)^2\left(\frac{0.42}{r_m}\right)^2\left(\frac{1}{\eta_{ij}}\right)^2\left(\frac{\lambda}{935\text{ nm}}\right)\left(\frac{10^6}{Q_{ij}}\right)$$

$$(9.28c)$$

$$\cdot\left(\frac{\Omega_{ij}/2\pi}{5\text{ MHz}}\right)\left(\frac{T_{bath}}{300\text{ K}}\right)\left(\frac{m_{ij}}{8.44\text{ ng}}\right)\left(\frac{2\kappa_2}{\kappa}\right)\left(\frac{1}{1+\Delta^2/\kappa^2}\right)^{-1}\left(\frac{\kappa^2}{(\Omega_{ij}+\Delta)^2+\kappa^2} - \frac{\kappa^2}{(\Omega_{ij}-\Delta)^2+\kappa^2}\right)^{-1}.$$

$$(9.28d)$$

For cavity and membrane parameters used in the measurements below, $\{\kappa/2\pi, L, \Delta, \lambda, \Omega_{66}/2\pi,$ $Q_{66}, m_{66}, r_m, \eta\} \approx \{10 \text{ MHz}, 742 \,\mu\text{m}, 5 \text{ MHz}, 935 \text{ nm}, 5 \text{ MHz}, 1.5 \times 10^6, 8.44 \text{ ng}, 0.42, 0.64\}$, the full expression for weak optical damping (Eq. 9.24) gives $\Gamma_{opt}^{66}/2\pi \approx 4.0(\kappa/2\kappa_2)$ kHz for $\langle P_{out} \rangle = 100 \,\mu W$. The resulting effective temperature is and $T_{eff}^{66} \approx 0.25(2\kappa_2/\kappa)$ K, corresponding to a thermal occupation number $\bar{n}_{66} \approx 1.0 \times 10^3 (2\kappa_2/\kappa)$, which represents significant optomechanical cooling for moderate circulating powers of ~ 1 W. We now test these predictions.

9.2 Measurements of Optomechanical Cooling

We have carried out a sequence of measurements to confirm the simple model for weak optomechanical cooling (Eq. 9.17), using the apparatus described in Chapter 5 and 6. For these experiments, we focus on the TEM$_{00}$ mode of the cavity and the (6,6) vibrational mode of a $\{d_m, w_m\} = \{50 \text{ nm}, 500 \,\mu\text{m}\}$ membrane with intrinsic mechanical frequency $\Omega_{66} = 4.82$ MHz. Below we list how parameters $\{m_{66}, \kappa, \Gamma_{66}, g_m, \eta_{66}\}$ entering the formula for the spring and damping forces (9.17) were determined prior to this optomechanical cooling experiment. The uncertainties of the measurements are listed in Section (8.7.4).

- We assume $m_{ij} = m_{phys}/4 = 8.44$ ng, based on the factory-specified dimensions and a density of 2700 kg/m^3 [39].

- A value of $r_m = 0.42$ at $\lambda = 935$ nm is inferred from an estimated real index value of 2.0 (see section 6.1).

- The intrinsic mechanical damping rate $\Gamma_{66} = \Omega_{66}/Q_{66} \approx 4.83 \text{ MHz}/1.5 \times 10^6 \approx 3.2$ Hz is determined from a ringdown measurement (section 4.6.2) using a HeNe in place of the probing beam and exciting the membrane using a piezo shaker located behind the membrane (Section 5.2.3.2).

- The cavity linewidth κ varies with membrane position and is determined by sweeping the cavity with an FM modulated probe (Section 6.2). A value of $\kappa \approx 13.5$ MHz is obtained when the membrane is positioned for maximal coupling and $\lambda = 935$ nm.

- Optomechanical coupling rate $g_m(z_m)$ is fixed to its maximum value $2r_m g_0 = 0.84 g_0$ at $\lambda = 935$ nm by maneuvering the membrane axially until the optical spring frequency shift at a fixed input power is maximized (see Sections 6.3 and 5.3.3.3 for further discussion).

- To determine is the spatial overlap η_{ij} (Section 7.1.3.1), we use the known membrane dimensions, the cavity spot size, and the location of the cavity mode on the membrane surface as inferred from the "thermal noise spectroscopy" technique described in Section 8.7.7. For the (6,6) vibrational mode coupled to the TEM$_{00}$ mode of the cavity, we estimate $\eta_{66} = 0.64$; this

is based on spot-size estimate of $w_c = 35.6\,\mu$m ($1/e^2$ intensity waist) and an estimate that the optical mode has been displaced by $\{x_0, y_0\} = \{45\,\mu\text{m}, 120\,\mu\text{m}\}$ from cavity center.

In the experiment we vary the power and detuning of the input ("cooling") field while monitoring the transmitted intensity fluctuations. From these fluctuations we infer the apparent cavity length noise (ignoring mirror substrate noise): $S_L(\Omega)|_{mem} = \sum_{ij}(g_{ij}^2/g_0^2)S_{b_{ij}}(\Omega)$ (see Eq. 7.28). Details of the method for cavity stabilization and control over detuning for this experiment are described in Section 5.3.3. A description of the "detuned probe" measurement is given in Section 8.3. Data acquisition details are described in Section 8.7. We here use the "direct" temperature calibration procedure described in that section, wherein the detuning, transmitted power, and cavity linewidth are used to infer the transfer function between membrane vibration and transimpedance-amplified photocurrent $V(t)$ on the transmission photodetector (responsivity $\mathcal{R}$, transimpedance gain $G_T(\Omega)$). In summary:

$$\frac{S_V(\Omega)}{S_L(\Omega)} = \mathcal{R}^2 G_T(\Omega)^2 \langle P_{out} \rangle^2 \left(\frac{g_0}{\kappa}\right)^2 \left(\frac{2\Delta/\kappa}{1 + \Delta^2/\kappa^2}\right)^2 \frac{\left(\kappa^2 + \Delta^2\right)^2}{(\kappa^2 + \Delta^2)^2 + 2(\kappa - \Delta)(\kappa + \Delta)\Omega^2 + \Omega^4} \quad \text{(9.29a)}$$

$$\langle P_{out} \rangle = \langle P_{out}(\Delta = 0) \rangle \frac{1}{1 + \Delta^2/\kappa^2} \quad \text{(9.29b)}$$

$$S_L(\Omega \approx \Omega_{66}) \approx \left(\frac{g_0}{g_{66}}\right)^2 \frac{4k_B T_{bath}\Gamma_{66}}{m_{66}} \frac{1}{((\Omega_{66} + \Delta\Omega_{opt}^{66})^2 - \Omega^2)^2 + \Omega^2(\Gamma_{66} + \Gamma_{opt}^{66})^2}, \quad \text{(9.29c)}$$

where $g_{66} = \eta_{66} \cdot g_m(z_m)$.

9.2.1 Optomechanical Cooling with a Diode Laser

A measurement of the thermal noise of the (6,6) mode with a "strong" red-detuned input field provided by a 935 nm diode laser is shown in Figure 9.2. The input power has been set so that $\langle P_{out} \rangle \approx 23\,\mu$W at $\Delta = 0$. The detuning is then progressively changed from $\Delta/2\pi = $ -93 MHz to $\Delta/2\pi = -6$ MHz. All other parameters are fixed.

At $\Delta/2\pi = $ -93 MHz, the back-action from the cavity field is weak, and the effective damping rate inferred from the linewidth of a Lorentzian fit is $\Gamma_{66} + \Gamma_{opt}^{66} \approx 2\pi \times 4.3$ Hz. This is comparable to the intrinsic mechanical linewidth $\Gamma_{66} \approx 2\pi \times 3.4$ Hz and suggests an effective temperature (Eq. 9.17d) of $T_{eff}^{66} = 298$ K $\times 3.2$ Hz$/4.3$ Hz $= 249$ K. By contrast, the value for Γ_{opt}^{66} estimated from Eq. (9.17b) is $\Gamma_{opt}^{66} \approx 2\pi \times 0.1$ Hz. Persistently larger-than-expected Γ_{opt}^{66} at large detuning appears to be due to the fact that the peak frequency drifts during the time period for measurement (~ 1 minute in this case for 40 averages of an FFT with 1 Hz resolution bandwidth). On the other hand, the area underneath the Lorentzian fit suggests an effective temperature of $T_{eff}^{66} \approx k_B^{-1} m_{66}(g_0/g_m)^2\Omega_{66}^2 \int_{\Omega_{66}} S_L(\Omega)d\Omega/2\pi$ $= 176$ K. The discrepancy of this value from room temperature is believed to reflect the $\sim 2\times$ uncertainty in the values entering the measurement transfer function (9.29), as detailed in Section
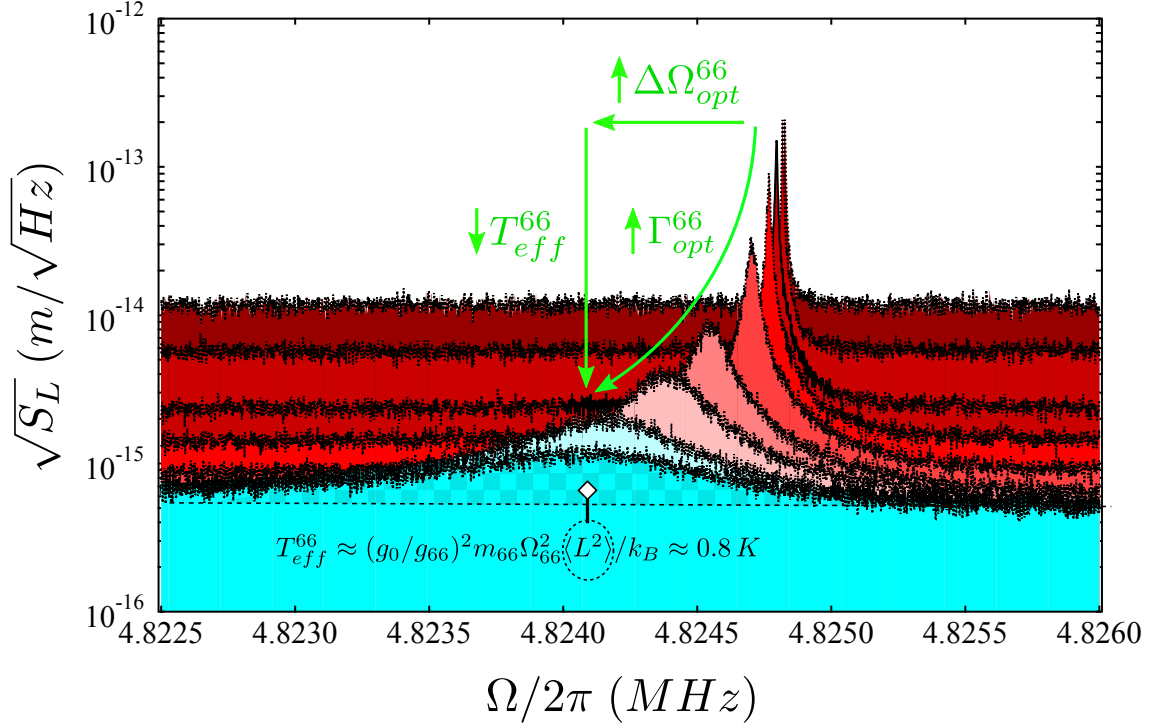
Figure 9.2: Brownian motion of the (6,6) drum mode in the presence of a strong detuned probe. Here we plot the apparent cavity length noise $S_L(\Omega)$ (Eq. 9.29) of the MIM cavity near Ω_{66}. The input power is fixed so that $\langle P_{out}(\Delta = 0)\rangle \approx 23~\mu W$ and the detuning is varied from $\Delta/2\pi =$ -93 MHz to -6 MHz. As the detuning is decreased, a modified mechanical susceptibility to the thermal force is observed, manifesting as a lowered frequency (optical anti-spring, $\delta\Omega_{opt}^{66} < 0$), an increased damping rate (optical damping, $\Gamma_{opt}^{66} > 0$), and a lowering of the mean-squared vibration amplitude, $\langle b_{66}^2\rangle$, corresponding to optomechanical cooling ($T_{eff}^{66} < T_{bath}$). At a detuning of -6 MHz, optomechanical cooling from room temperature to ≈ 1 K is observed, coinciding with an increased damping rate and negative frequency shift both of ≈ 1 kHz. Temperature is inferred from the mean-squared effective cavity length noise $\langle L^2\rangle = \int_{\Omega_{66}} S_L(\Omega)d\Omega/2\pi$ using the formula shown in the figure. Comparison to the model (Eq. 9.17) for a similar measurement is shown in the next figure.

8.7.4.

Optomechanical cooling is observed by changing the detuning from $-\Delta = 2\pi \times 96$ MHz $>> \kappa$ to $-\Delta = 2\pi \times 6$ MHz $\sim \Omega_{66}$. This increases both the circulating power and the ratio of blue and red sidebands in the cavity. For $\Delta < 0$, and the modified mechanical susceptibility is manifest as a simultaneous lowering of the peak response frequency, $\delta\Omega_{opt}^{66}(\Delta = -2\pi \times 6$ MHz$) \approx 2\pi \times -650$ Hz < 0, increasing of the mechanical damping rate, $\Gamma_{opt}^{66}(\Delta = -2\pi \times 6$ MHz$) \approx 2\pi \times 940$ Hz $>> \Gamma_{66}$, and lowering of the mean-squared displacement (area beneath the Lorentzian), characterized by $T_{eff}^{66}(\Delta = -2\pi \times 6$ MHz$) \approx 0.76$ K $<< 298$ K. The area and linewidth inferred occupation number are $\bar{n}_{66} \approx$ 3300 and 4400, respectively. The values estimated from Eq. 9.28 are $\{\Gamma_{opt}^{66}/(2\pi), \Delta\Gamma_{opt}^{66}/(2\pi), \bar{n}_{66}\} \approx$ $\{670(\kappa/2\kappa_2)$ Hz$, -255(\kappa/2\kappa_2)$ Hz$, 6100(2\kappa_2/\kappa)\}$. For $\kappa/2\kappa_2 \approx 1.3$ (Eq. 9.20) the damping rate and

temperature compare favorably with the measured values. A factor of two discrepancy is apparent for the frequency shift, which we do not yet understand.

Also note the apparent reduction in the thermal displacement background. This is due to the increased magnitude of the measurement transfer function (9.29a) for smaller Δ. The detector used for this measurement is shot noise limited at an incident power of $\approx 100\,\mu$W. For the measurements shown, $\langle P_{out} \rangle \lesssim 23\,\mu$W, so rather than shot noise, the progressively lowering noise floor here reflects the apparent displacement of the constant output noise of the photodetector transimpedance amplifier. Using Eq. 8.42, the estimated shot noise sensitivity of $\Delta = -2\pi \times 6$ MHz measurement is $\approx 1.2 \times 10^{-17}\,\mathrm{m}/\sqrt{\mathrm{Hz}}$; here we are far from this sensitivity. This may in part be due to laser noise. Indeed, as shown in Figure 8.9, our 935 nm diode laser exhibits an effective cavity length noise of $\approx 7 \times 10^{-16}\,\mathrm{m}/\sqrt{\mathrm{Hz}}$ at 5 MHz. This background suggests a practical limit to cooling with the diode laser using current parameters at the level of $\bar{n}_{66} \sim 1000$.

9.2.2 Multimode Cooling: Comparison to Model

In Figure 9.3 we compare the theoretical model (Eq. 9.17) to a measurement of $\{\Gamma_{opt}, T_{eff}\}$ vs. Δ for both the (6,6) mode ($\Omega_{66} = 4.83$ MHz) and the (1,1) mode ($\Omega_{11} = 4.83$ MHz) of the membrane. The input power is set so that $\langle P_{out}(\Delta = 0) \rangle \approx 10\,\mu$W, and the membrane is positioned axially so that $g_m \approx 2r_m g_0$. At the measured position (Section 8.7.7), $(x_0, y_0) \approx (45\,\mu\mathrm{m}, 120\,\mu\mathrm{m})$, we estimate that the spatial overlap factors for these two modes are $\{\eta_{11}, \eta_{66}\} \simeq \{0.69, 0.64\}$ with an uncertainty of 10%. The quality factors for these two modes are also different. Independent ringdown measureements give $\{Q_{11}, Q_{66}\} = \{5.8 \times 10^4, 1.5 \times 10^6\}$. Representative error bars are applied to the large detuning measurement of $\{T_{eff}^{11}, T_{eff}^{66}\}$, which are expected to coincide with $T_{bath} \approx 298$ K. The discrepancy is believed to reflect the net $\sim 2\times$ uncertainty in the measurement transfer function (Eq. 9.29) based on uncertainties in $\{g_m, \eta_{ij}, m_{ij}\}$, as detailed in Section 8.7.4.

9.2.3 Cooling to ~ 100 mK with a Low-Noise Titanium-Sapphire Laser

The preceding measurements were performed using $\lambda = 935$ nm radiation from a low power diode laser. After propagating through the optical beam path (Section 5.3.3), we were restricted in the power available from this laser to moderate input powers of several tens of microwatts. We also observed that cooling to an occupation number of $\bar{n}_{66} < 10^4$ with this laser resulted in a distorted thermal noise peak, as evidenced in the blue peak in figure 9.2. As discussed above, we suspect that this behavior is due to the relatively high frequency noise spectral density of the diode laser at 5 MHz ($\sim 10^{-16}\,\mathrm{m}/\sqrt{\mathrm{Hz}}$ when expressed as apparent cavity length noise; Section 8.8.1.1).

As soon as the preliminary results in [14] were finalized, we switched to a high-power, low-noise titanium-sapphire laser (ti-sapph). The measured frequency noise on this laser at 5 MHz is
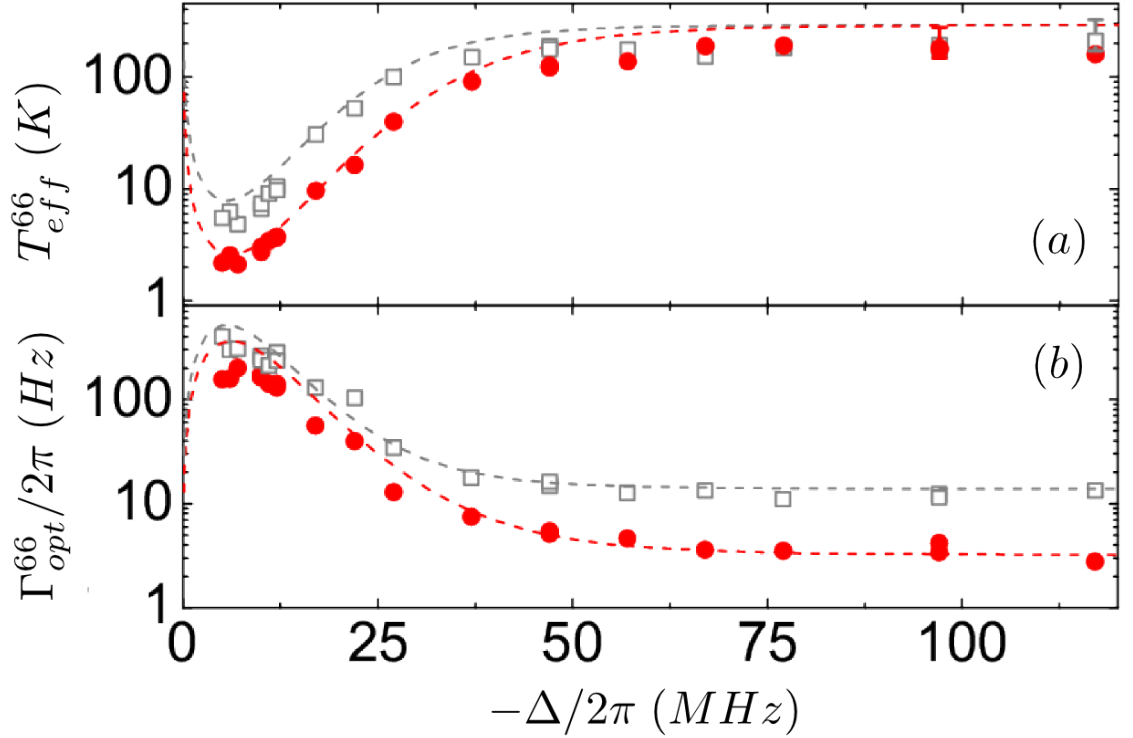
Figure 9.3: Demonstration of cavity cooling [14] of the $(6, 6)$ (red circles) and $(1, 1)$ (grey squares) modes with frequencies $\{\Omega_{11}/2\pi, \Omega_{66}/2\pi\} = \{0.80 \text{ MHz}, 4.83 \text{ MHz}\}$ and initial quality factors $\{Q_{11}, Q_{66}\} = \{5.8 \times 10^4, 1.5 \times 10^6\}$, where Q_{ij} is measured via ringdown. For these data the cavity input power is fixed so that $\langle P_{out}(\Delta = 0) \rangle \approx 10 \ \mu\text{W}$. The representative error bars show the uncertainty due to our knowledge of $\{g_m, \eta_{ij}, m_{ij}\}$ (Section 8.7.4). Panel (a): measured mode temperature (points) and theoretically expected cooling (lines) as a function of detuning Δ from the cavity resonance. Panel (b): Corresponding measured effective mechanical linewidth and theoretical expectation. In both models, we assume $\kappa/2\kappa_2 = 1$ when computing the intracavity photon number (Eq. 9.19b).

$\sim 10^{-19} \text{ m}/\sqrt{\text{Hz}}$ (expressed as an apparent cavity length noise) (Section 8.8.1.2). We maneuvered the wavelength of this laser to the opposite side of the mirror coating curve (Figure 6.3), $\lambda \approx 810$ nm, to maintain a moderate finesse of $\mathcal{F} \approx 10^4$ at which the cavity length could be stabilized. For the following measurements, the cavity linewidth was measured to be $\kappa \approx 8.5$ MHz (HWHM) when the membrane was positioned to maximize g_m. The absolute value of g_m also changes at this wavelength for two reasons: because of the tighter intracavity standing wave spacing ($g_0 \propto \lambda^{-1}$) and because of the increased reflectivity of the film. (According to Eq. 3.3 the reflectivity of a 50 nm film changes from 0.423 to 0.465 for an index of 2.0.) The net increase in the optomechanical coupling over the $\lambda = 935$ nm field is $(935/810) \times (0.465/0.423) = 1.27$. The intracavity photon number for a given input power also decreases by a factor of λ (Eq. 9.19b). The optical damping rate for a given input power (Eq. 9.24) then changes fractionally by a factor $\sim \lambda^{-1} g_m^2 \kappa^{-1}$ of
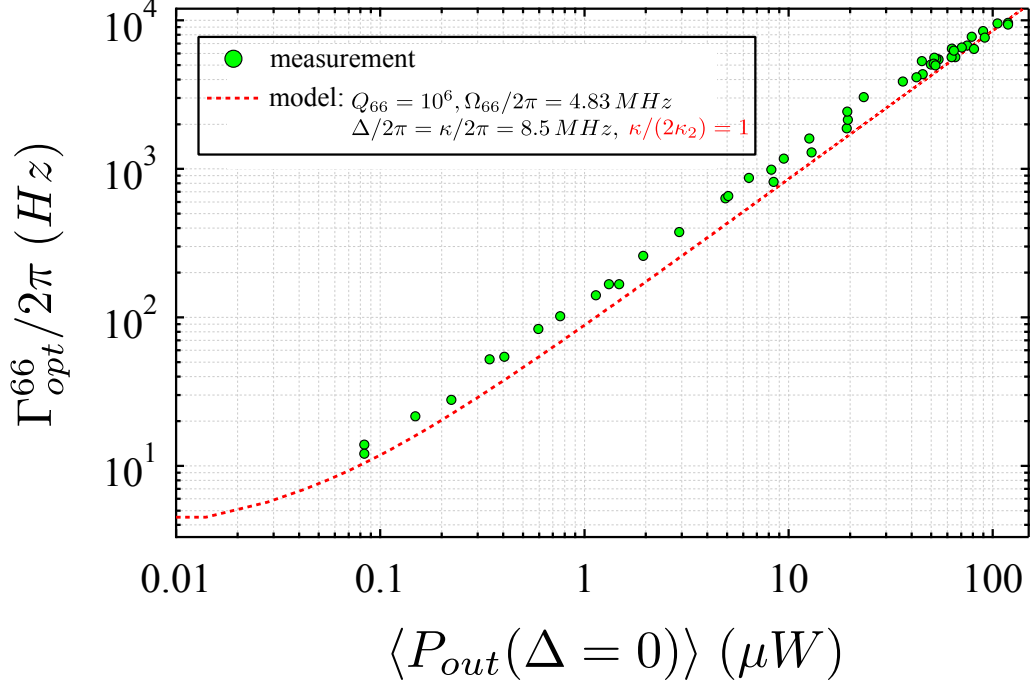
Figure 9.4: Stronger damping of the (6,6) mode with a low noise Ti-Sapph laser operating at 810 nm. Here the detuning has been fixed at $\Delta/(2\pi) = -\kappa/(2\pi) = -8.5$ MHz. The effective damping rate is obtained from a Lorentzian fit to the apparent cavity length noise spectrum S_L (Eq. 9.29). The points at higher power have been obtained from a fit to multiple Lorentzian, including the off-resonant displacement of nearby vibrational modes, as shown in Figure 9.6. Note that the model assumes $\kappa/(2\kappa_2) = 1$.

$(935/810) \times (0.465/0.423)^2 \times (13.75/8.5) \approx 2.2$.

In Figure 9.4, we fix the input field detuning at $\Delta = -\kappa$ and change the optical power from $\langle P_{out}(\Delta = -\kappa)\rangle = 0.1\,\mu$W to 100 μW, beyond which the cavity length servo is unstable (a problem that we have yet to solve). We then compare the measured damping rate of the (6,6) mode to the weak cooling model (Eq. 9.4), using $\kappa/2\kappa_2 = 1$. We observe a systematic discrepancy of $\approx 50\%$ consistent with our uncertainties in $\{g_m, \eta_{66}, m_6\}$ and the predicted value of $\kappa/2\kappa_2 = 1.3$ (Eq. 9.20). At large optical powers the off-resonant displacement noise of the (6,6) mode begins to overlap significantly with neighboring vibrational modes. We then had to fit to multiple Lorentzians to estimate the linewidth, an example of which is shown in Figure 9.6. At the highest power, the observed optical damping rate is $\Gamma_{opt}^{66} \approx 10$ kHz, which suggests a final occupation number of $\bar{n}_{66} \approx 1.3 \times 10^6 * 3.2/10^4 \approx 410$ phonons.

In Figure 9.5, we vary both the the detuning and power in order to minimize and maximize damping of the (6,6) mode. As a consistency check on the calibration of $S_{b_{66}b_{66}}(\Omega)$, we plot both the damping rate inferred from the width of a Lorentzian fit against the effective temperature inferred the area beneath the Lorentzian fit. We also compare these measurements to the weak cooling
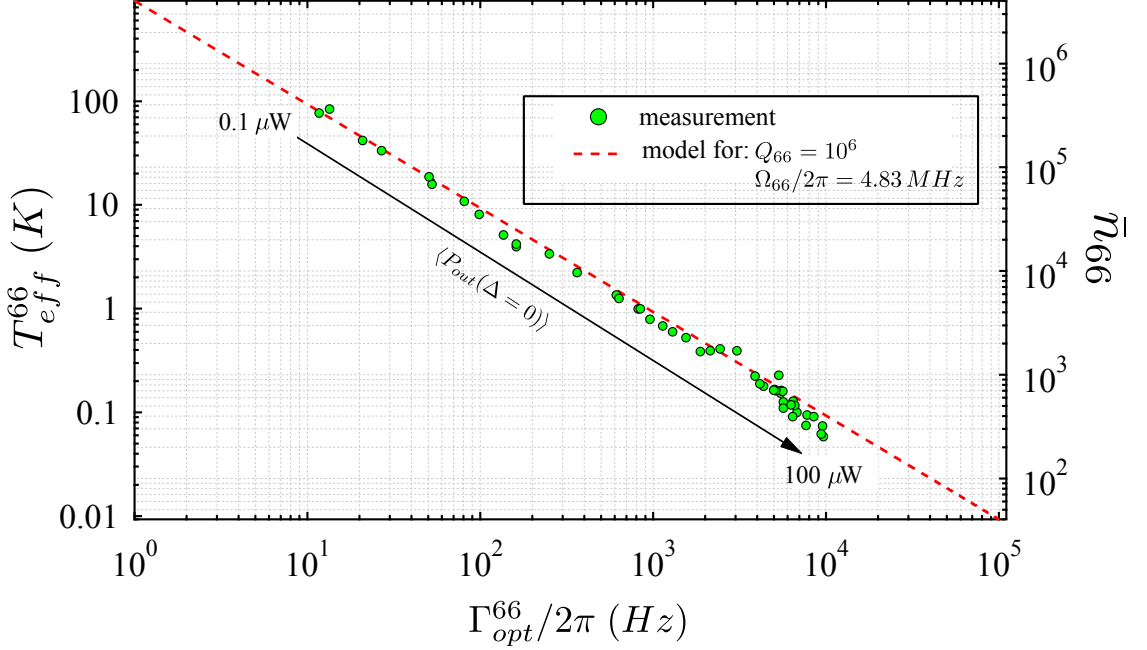
Figure 9.5: Demonstration of optomechanical cooling of the (6,6) vibrational membrane mode ($\Omega_m/2\pi$ = 4.83 MHz) from room temperature to approximately 100 mK, corresponding to a reduction in occupation number from 1.3×10^6 to ≈ 500. Input power has been varied so that the transmitted power on resonance, $\langle P_{out}(\Delta = 0) \rangle$, ranges from 0.1 μW to 100 μW. Detuning is also varied from $\Delta > 100$ MHz to $\Delta \approx \Omega_{66}$ in order to minimize and maximize the damping rate. We plot the measure damping rate vs. the measured effective temperature (green points) and compare to the model (red curve) T_{eff}^{66} = 298 K $\times \Gamma_{66}/(\Gamma_{66} + \Gamma_{opt}^{66})$, using $\Gamma_{66}/2\pi$ = 3.2 Hz. Data points at low temperature were fit to multiple Lorentzians to include off-resonant displacement of nearby vibrational modes, as shown in Figure 9.6.

model (red line) for which T_{eff}^{66} = $298K \times \Gamma_{66}/(\Gamma_{66} + \Gamma_{opt}^{66})$, with Γ_{66} = 3.2 Hz. High-temperature measurements are omitted because of the difficulty in obtaining the narrow natural linewidth of the oscillator — this appears to be due to thermal drift of the peak frequency. For temperatures $T_{eff}^{66} \lesssim 100$ K, the discrepancy between the linewidth- and area-inferred temperature is $< 50\%$, with the lowest measured temperatures coinciding with $\bar{n}_{66} \approx 400 - -500$. The growing discrepancy at occupation numbers $\bar{n}_{66} < 1000$ is believed to be due to the encroachment of off-resonant vibration from neighboring thermal noise peaks, as discussed in the next paragraph.

When optically damping the (6,6) mode to $\Gamma_{opt}^{66} \sim 10$ kHz, we begin to observe an elevated displacement noise background due to the off-resonant vibration of neighboring modes. For the low temperature point in Figure 9.5, the optical damping rate and effective temperature were obtained from a multiple-Lorentzian fit including vibrational modes (6,6), (3,8):(8,3), and (5,7):(7,5). An example is shown in Figure 9.6. Here we plot the multimode spectrum in terms the apparent
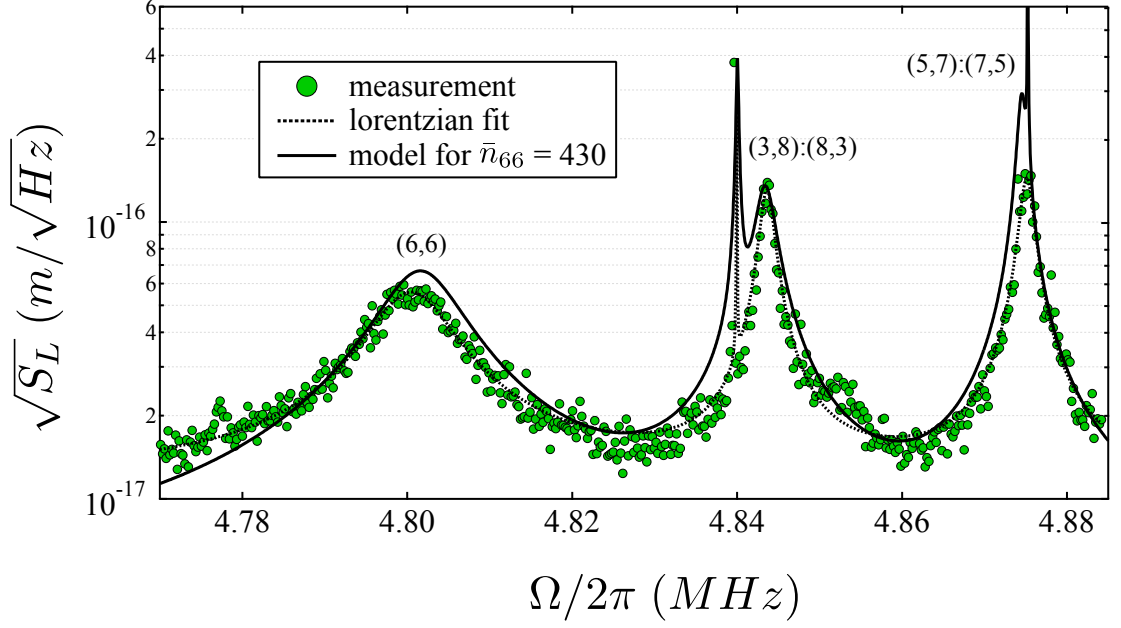
Figure 9.6: Multimode cooling: neighboring thermal noise peaks begin to overlap when Γ_{opt} is on the order of the mode frequency splitting. Here we show the thermal noise in the vicinity of the $(6,6)$ mode when an optical damping rate of $\Gamma_{opt}^{66} \approx 10$ kHz has been applied. We express the noise in terms of apparent cavity length displacement, $S_L(\Omega)$ (Eq. 9.29). The dotted line is a multiple-Lorentzian fit to modes $\{(6,6), (3,8), (8,3), (5,7), (7,5)\}$ which assumes that their noise adds incoherently. This fit is used to obtain the the value of Γ_{opt}^{66} and T_{eff}^{66} for one of the bottom-right points in Figure 9.4. As a consistency check, we use the weak cooling model (9.17) with input power as a free parameter to generate the solid black curve. The model is constrained to give an occupation number of of $\bar{n}_{66} = 430$ for the $(6,6)$ mode, corresponding to the temperature inferred from the measured values of Γ_{opt}^{66} and Γ_{66}. Quality factors and overlap factors for each mode have been independently determined for the model.

cavity length displacement $S_L(\Omega) = \sum_{ij} \eta_{ij}^2 (g_m^2/g_0^2) S_{b_{ij}}(\Omega)$ (see Eq. 7.28). In the figure, the dotted line corresponds to a five-Lorentzian fit with the linewidth and area left as free variables for each peak. This line is used to estimate the linewidth and temperature of a point in Figures 9.4 and 9.5. Also shown is a model for multimode cooling based on an incoherent sum of five noise peaks, all damped according to Eq. 9.17. To generate this model, we separately measure the intrinsic mechanical quality factor of each mode using a HeNe and a piezo shaker (Section 5.2.3.2); this gives $\{Q_{66}, Q_{38}, Q_{83}, Q_{57}, Q_{75}\} = \{1.5, 1.5, 1.4, 0.84, 0.71\} \times 10^6$. From the transverse position of the optical beam, which was remeasured at a position $(x_0, y_0) = (40.5\,\mu\text{m}, 120\,\mu\text{m})$ we determine the different overlap factors for each mode as $\{\eta_{66}, \eta_{38}, \eta_{83}, \eta_{57}, \eta_{75}\} = \{0.63, 0.11, 0.36, 0.10, 0.11\}$. In the model we also assume that each mode is decoupled, so the displacement noise peaks add incoherently. The model is constrained so that $\bar{n}_{66} = 430$, corresponding to the upper bound for the temperature estimate obtained from the linewidth measurement in Figure 9.6.

Finally, in Figure 9.7 we provide a global perspective by plotting the measured cavity length
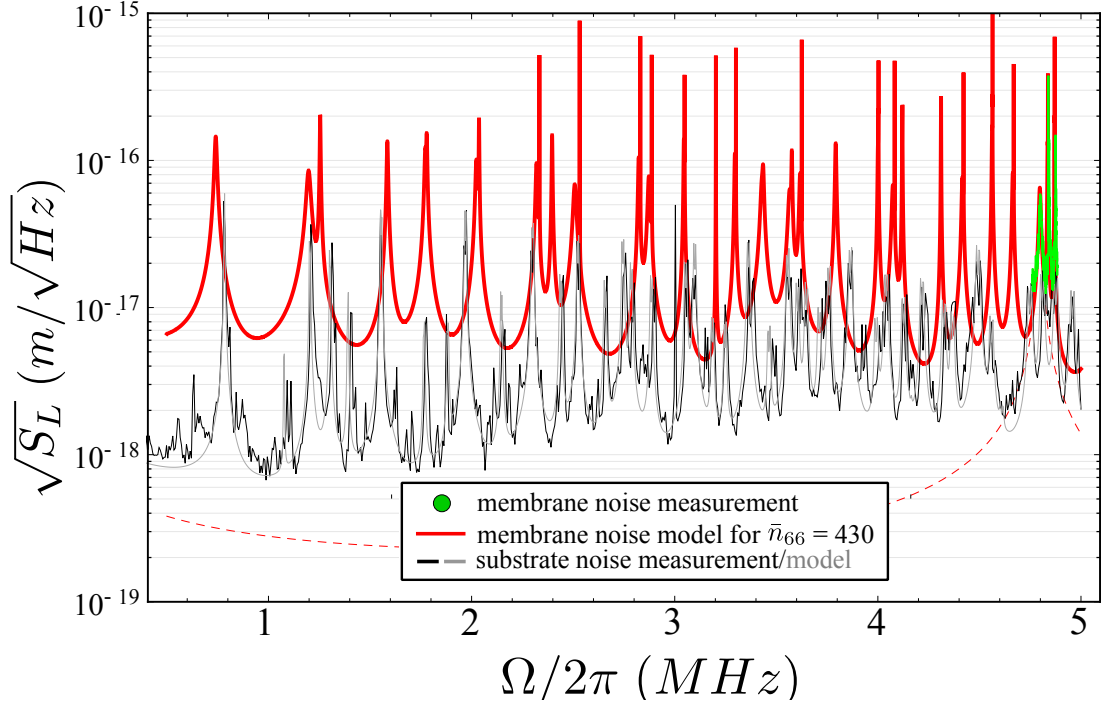
Figure 9.7: Measurement (green) and model (red) of multimode cooling of the membrane compared to measurement (black) and model (gray) of end-mirror substrate noise. Noise is expressed as apparent cavity length displacement, $S_L(\Omega)$ (Eq. 9.29). Measured cooling data corresponds to the data in Figure 9.6. Modeled cooling data represents an extension of the model in Figure 9.6, which is bootstrapped to $\bar{n}_{66} \approx 430$ based on the linewidth inferred from a experimental fit to the measurement. Substrate noise curves correspond to measurement and model with the membrane removed, as discussed in Section 8.8.2. Note that substrate noise and off-resonant vibration of the membrane both provide a broadband displacement noise background of $\sim 10^{-17} - -10^{-18}$ m/$\sqrt{\text{Hz}}$. This is significantly higher than the off-resonant background of just the (6,6) mode, shown in dashed red. The broadband noise background is expected to match the thermal noise of (6,6) mode if cooled to $\bar{n}_{66} < 100$ using current parameters.

displacement noise (green) against the same multimode model (red) extending to a span from 100 kHz to 5 MHz. For the extended model we assume that $Q_{ij} = 1.5 \times 10^6$ for all modes other than those characterized specifically, $\{(6,6), (3,8), (8,3), (5,7), (7,5)\}$. Natural frequencies are extrapolated from $\Omega_{66}/2\pi = 4.83$ MHz and overlap factors are inferred from $(x_0, y_0) = (40.5\,\mu\text{m}, 120\,\mu\text{m})$. The dashed red line shows the contribution from only the (6,6) mode to highlight the fact that the background is dominated by the off-resonant contribution from other membrane modes. In the next chapter, we argue that placing the optical mode near the center of the membrane can significantly reduce this "off-resonant" background because in this case η_{ij} vanishes for all even-ordered modes (e.g., (2,2) and (2,3)). The remaining displacement noise background is anticipated to be the thermal noise of the end-mirror substrates, as discussed in Section 8.8.2. To illustrate this point, in Figure 9.7 we have added the measurement (black) and model (gray) of the end-mirror substrate noise for the bare cavity, as discussed in Section 8.8.2. We note that this background is significant
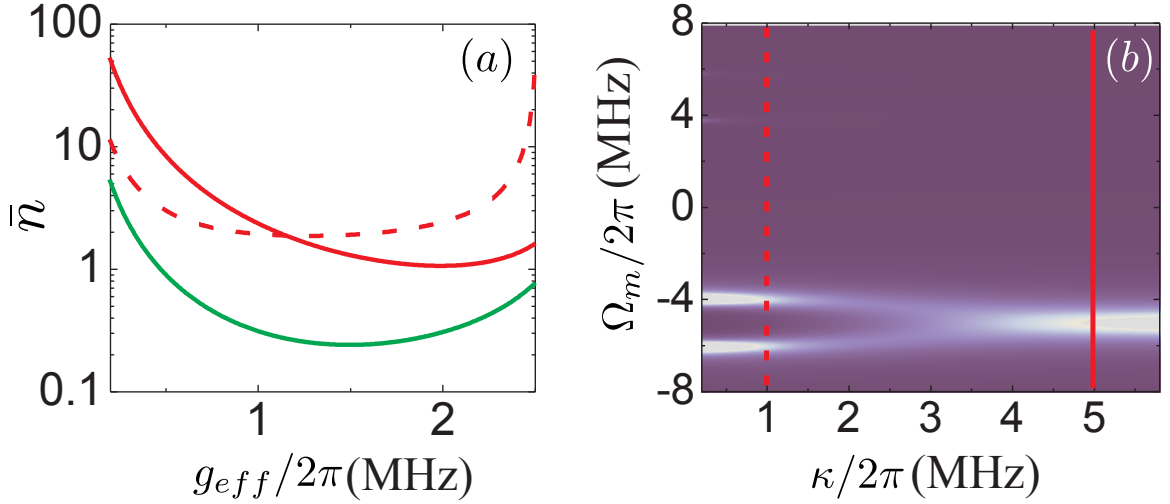
Figure 9.8: (a) Calculated achievable phonon number as a function of coupling strength g_{eff} for parameters described in the text. The solid line is for a cavity with $\kappa = 2\pi \times 5$ MHz and the dashed line for $\kappa = 2\pi \times 1$ MHz. The green line would result for $\kappa = 2\pi \times 5$ MHz upon increasing Q_m to 4×10^7, which may be possible for a thinner SiN film. (b) Emergence of normal-mode splitting as the cavity linewidth is varied for fixed mechanical frequency $\omega_m = 2\pi \times 5$ MHz and coupling $g_{\text{eff}} = 2\pi \times 1$ MHz. The exact spectrum $S_b(\omega)$ is displayed in this density plot where zero weight corresponds to the blue shading and white to maximum mechanical response. The lines mark the position of the parameters used in (a).

for occupation numbers of < 100 for the (6,6) mode. Ways around this problem include using a smaller or higher mechanical quality membrane, cryogenic pre-cooling of the apparatus, or active feedback. We address this subject in detail in the next chapter.

9.3 Limits to Optomechanical Cooling in our System

At the time it was being designed, our post-doc Cindy Regal put serious thought into what the fundamental limits of optomechanical cooling would be in our system. Importantly, optical damping can no longer be treated as "weak" for the rates $\Gamma_{opt}/(2\pi) > 100$ kHz necessary to cool a $\Omega_m/(2\pi) \sim 1$ MHz oscillator with mechanical quality $Q_m \sim 10^6$ to an occupation of less than 10 from room temperature. In this case the optical damping rate becomes comparable to the mechanical frequency and/or the cavity linewidth. There are a number of tradeoffs that must be considered in this situation. Strictly, full ground-state cooling requires $\bar{n}\Gamma_m \ll 2\kappa \ll \Omega_m$, i.e., fully resolved sidebands and an oscillator with a large enough Q_m to allow the required damping. For our results it is most relevant to consider instead the case $\bar{n}\Gamma_m \lesssim 2\kappa \sim \Omega_m$ and track the results into a regime of strong cooling, characterized by $g_{\text{eff}} = \eta_{ij} g_m b_{zp}^{ij} \langle n_c \rangle > 2\kappa$ [5, 87, 16]. For completeness, I here present Cindy's calculation of the expected final phonon occupation number $\bar{n}$ based on an exact solution to the coupled equations of motion discussed in [87].

Figure 9.8a shows the calculated phonon number as a function of the cooling strength for the realistic parameters: $Q_m = 4 \times 10^6$, $\Omega_m/2\pi = 5$ MHz, $\Delta = -\omega_m$, $\bar{n}_{room} = k_b T_{room}/\hbar \Omega_m = 1.2 \times 10^6$, and $\kappa = 2\pi \times 2.5$ and 0.5 MHz (see caption). Note $\kappa = 2\pi \times 2.5$ MHz corresponds to $\mathcal{F} = 40,000$ for a $L = 0.74$ mm cavity, and smaller values of κ can be achieved either by increasing the finesse or using a longer cavity. Figure 9.8a shows that reaching $\bar{n} \sim 1$ from room temperature is theoretically achievable for demonstrated parameters before reaching the static bistability point ($g_{\text{eff}} = \Omega_m/2$ for $2\kappa << \Omega_m$) [88]. Another outstanding goal is achieving strong coupling between a ground-state mechanical resonator and the cavity field [5, 87, 16]. Figure 9.8b illustrates the spectral function $S_b(\Omega)$ as a function of the cavity linewidth for $g_{\text{eff}} = 2\pi \times 1$ MHz. The normal-mode splitting indicative of strong coupling appears for phonon occupancies near unity.

9.4 Concluding Remarks

Observing quantum effects of a mesoscopic oscillator coupled to an ambient thermal bath would be a significant advance. Future work should address experimental challenges to achieving the occupations shown in Figure 9.8, such as reducing laser phase noise and mitigating the thermal noise of the Fabry-Perot cavity substrates (see Chapter 10). However, to implement a full range of quantum protocols with these oscillators one must achieve occupations $\bar{n} \ll 1$. This will require higher Q-frequency products or lower initial thermal occupation, as illustrated by the green line in Figure 9.8a. Realizing even higher room temperature Q-frequency products than those shown in Figure 4.11 is a subject of ongoing investigation in our lab. Further, while our work here focuses on room temperature, we note that recent results in [41] indicate that, unlike amorphous SiO_2, the dissipation in silicon nitride films decreases monotonically from room temperature down to ~ 100 K. This makes operating at liquid nitrogen temperature a viable option for decreasing the initial occupation number and increasing the mechanical quality factor (enabling lower optical cooling base temperatures), while maintaining a simple cryogenic system more compatible with atom experiments than helium refrigeration.

Chapter 10

Suppression of Extraneous Thermal Noise in a Cavity-Optomechanical System

This chapter describes work performed by Post-doc Yi Zhao and me to understand and address the end-mirror thermal noise shown in black in Figure 9.7. It was realized that this extraneous thermal noise — an issue exacerbated by the fact that our experiment takes place at room temperature — would limit sensitivity to membrane displacement and thereby the efficacy of attempts to optically damp its motion. Inspired by a discussion with visiting Professors Jun Ye and Peter Zoller in the autumn of 2010, we developed a technique to independently sense the extraneous thermal motion by simultaneously monitoring the resonance frequency of two distinct spatial modes of the cavity. We then devised an open-loop feedback technique to suppress its effect on the intracavity field. This technique involved electro-optically mapping the extraneous noise onto the frequency of the incident field, with gain chosen in order to cancel the associated fluctuations on the laser-cavity detuning (in effect this is the same as "locking" the cavity length to a precision finer than the thermal displacement amplitude of the mirrors). Our approach reduces the intracavity radiation pressure fluctuations associated with extraneous thermal motion, which otherwise may lead to noise heating of the membrane. Importantly, our approach also has the capacity to modify those radiation pressure force fluctuations which are produced by the membrane itself, if the feedback signal is correlated with the membrane's motion. The effect of this electro-optic "back-action" is analogous to "colding-damping" [89], and can either suppress or enhance "intrinsic" cavity back-action forces [24] used to damp the membrane (Chapter 9). We had to contend with this effect because the extraneous noise measurement contained some residual sensitivity to the membrane's motion. As a consequence, we found that extraneous noise suppression came at the cost of moderately diminished optical cooling rates. This sacrifice is not required, however. Remarkably, it should be possible to simultaneously suppress extraneous thermal noise and *enhance* optical damping with small modifications to the

membrane or cavity geometry. I elaborate on all of these points below. The chapter is adapted from a manuscript written for a more general optomechanics audience, and contains some rehashing of details explained in earlier chapters.

10.1 Introduction

The field of cavity opto-mechanics [90] has experienced remarkable progress in recent years [1, 91, 3, 18], owing much to the integration of micro- and nano-resonator technology. Using a combination of cryogenic pre-cooling [8, 9, 10] and improved fabrication techniques [11, 12, 13, 92], it is now possible to realize systems wherein the mechanical frequency of the resonator is larger than both the cavity decay rate and the mechanical re-thermalization rate [4, 14, 15, 6, 61]. These represent two basic requirements for ground-state cooling using cavity back-action [17, 16, 24], a milestone which has recently been realized in several systems [10, 15, 6], signaling the emergence of a new field of cavity "quantum" opto-mechanics [18].

Reasons why only a few systems have successfully reached the quantum regime [10, 15, 6] relate to additional fundamental as well as technical sources of noise. Optical absorption, for example, can lead to thermal path length changes giving rise to mechanical instabilities [9, 93]. In cryogenically pre-cooled systems, absorption can also introduce mechanical dissipation by the excitation of two-level fluctuators [9, 4]. Both effects depend on the material properties of the resonator. Another common issue is laser frequency noise, which can produce random intra-cavity intensity fluctuations. The radiation pressure associated with these intensity fluctuations can lead to mechanical heating sufficient to prevent ground-state cooling [29, 94, 95]. A fully quantum treatment of laser frequency noise heating in this context was recently given in [96].

In this chapter we address an additional, ubiquitous source of extraneous noise — thermal motion of the cavity apparatus (including substrate and supports) — which can dominate in systems operating at room temperature. Thermal noise is well understood to pose a fundamental limit on mechanics-based measurements [29] spanning a broad spectrum of applications, including gravitational interferometry [52, 97], atomic force microscopy [98], ultra-stable laser reference cavities [99], and NEMS/MEMS-based sensing [100, 101]. Conventional approaches to its reduction involve the use of low-loss construction materials [102, 103] and cryogenic operation temperatures [10, 15, 6], as well as various forms of feedback [104, 89, 105, 106, 107]. Indeed, schemes for optomechanical cooling [3, 108] were developed to address this very problem, with the focus on suppression of thermal noise associated with a single oscillatory mode of the system.

Here we are concerned specifically with *extraneous* thermal motion of the apparatus. In a cavity optomechanical system, this corresponds to structural vibrations *other than* the mode under study, which lead to extraneous fluctuations of the cavity resonance frequency. Like laser frequency noise
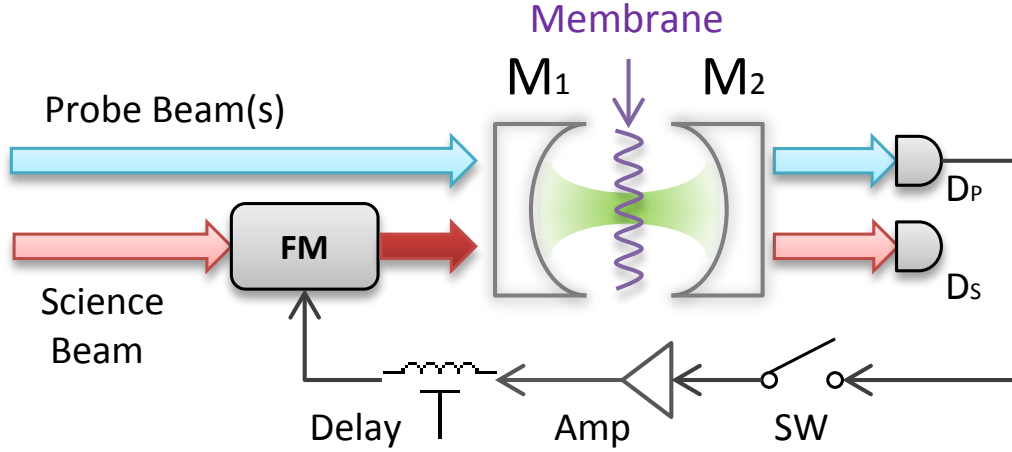
Figure 10.1: Conceptual diagram of the noise suppression scheme. $M_{1/2}$: cavity mirrors. $D_{P/S}$: photodetector for the probe field and the science field, respectively. SW: switch. FM: electro-optic frequency modulator.

[95, 96], these extraneous fluctuations can lead to noise heating as well as limit the precision of displacement measurement. To combat this challenge, we here propose and experimentally demonstrate a novel technique to actively suppress extraneous thermal noise in a cavity opto-mechanical system. A crucial requirement in this setting is the ability to sense and differentiate extraneous noise from intrinsic fluctuations produced by the oscillator's motion. To accomplish this, our strategy is to monitor the resonance frequency of multiple spatial modes of the cavity, each with different sensitivity to the oscillator's motion but comparable sensitivity to extraneous thermal motion [109]. We show how this information can be used to electro-optically imprint "anti-noise" onto the frequency of the incident laser field, resulting in suppression of noise on the instantaneous cavity-laser detuning. In the context of our particular system, based on a nano-mechanical membrane coupled to a Fabry-Pérot cavity, simulation and experimental results show that extraneous noise can be substantially suppressed without diminishing back action forces on the oscillator, thus enabling lower optical cooling base temperatures.

This chapter is organized as follows: in Section 10.2 we present an example of extraneous thermal noise in a cavity opto-mechanical system. In Sections 10.3 and 10.4 we propose and implement a method to suppress this noise using multiple cavity modes in conjunction with feedback to the laser frequency. In Section 10.5 we analyze how this feedback affects cavity back-action. Related issues are discussed in Section 10.6 and a summary is presented in Section 10.7. Details relevant to each section are presented in the appendix.

10.2 Extraneous Thermal Noise: Illustrative Example

Our experimental system is the same as reported in [14]. It consists of a high-Q nano-mechanical membrane (Chapter 4) coupled to a Fabry-Pérot cavity (Chapter 5, Figure 10.1) with a finesse of $\mathcal{F} \sim 10^4$ (using the techniques pioneered in [23, 7, 79]). Owing to the short length ($\langle L \rangle \simeq 0.74$ mm) and mode waist ($w_c \simeq 33\,\mu$m) of our cavity, thermal motion of the end-mirror substrates gives rise to large fluctuations of the cavity resonance frequency, ω_c.

To measure this "substrate noise", we monitor the detuning, Δ, between the cavity (with membrane removed) and a stable input field with frequency $\omega_0 = \omega_c + \Delta$. This can be done using the Pound-Drever-Hall technique ([54], Section 8.4), for instance, or by monitoring the power transmitted through the cavity off-resonance (Section 8.3). A plot of $S_\Delta(\Omega)$, the single-sided power spectral density of detuning fluctuations (Eq. 2.9), is shown in red in Figure 10.2. For illustrative purposes, we also express the noise as "effective cavity length" fluctuations $S_L^\Delta(\Omega) = (\langle L \rangle / \langle \omega_c \rangle)^2 S_\Delta(\Omega)$. The measured noise between 500 kHz and 5 MHz consists of a dense superposition of $Q \sim 700$ thermal noise peaks at the level of $\sqrt{S_\Delta(\Omega)} \sim 2\pi \times 10$ Hz$/\sqrt{\text{Hz}}$ ($\sqrt{S_L^\Delta(\Omega)} \sim 10^{-17}$ m$/\sqrt{\text{Hz}}$), consistent with the noise predicted from a finite element model of the substrate vibrational modes (Section 7.3.2), shown in blue.

The light source used for this measurement and all of the following reported in this chapter was a titanium-sapphire laser (Schwarz Electro-Optics) operating at a wavelength of $\lambda_0 = c/\omega_0 \approx 810$ nm. In the Fourier domain shown in Figure 10.2, an independent measurement of the power spectral density of ω_0 gives an upper bound of $\sqrt{S_{\omega_0}(\Omega)} \leq 2\pi \times 0.1$ Hz$/\sqrt{\text{Hz}}$ (Section 8.8.1.2), suggesting that laser frequency noise is not a major contributor to the inferred $S_\Delta(\Omega)$.

We can gauge the importance of the noise shown in Figure 10.2 by considering the cavity resonance frequency fluctuations produced by thermal motion of the intra-cavity mechanical oscillator: in our case a 0.5 mm $\times$ 0.5 mm $\times$ 50 nm high-stress (≈ 900 MPa) Si$_3$N$_4$ membrane with a physical mass of $m_p = 33.6$ ng [14]. The magnitude of $S_\Delta(\Omega)$ produced by a single vibrational mode of the membrane depends sensitively the spatial overlap between the vibrational mode-shape and the intensity profile of the cavity mode (Section 7.1.3).

In Figure 10.3 we show a numerical model of the multimode thermal noise produced by an optically damped membrane (using Eq. 7.28). In the model we assume that each vibrational mode (i, j) has a mechanical quality factor $Q_{ij} = 5 \times 10^6$ and that the optical mode is centered on the membrane, so that only odd-ordered vibrational modes ($i = 1, 3, 5...; j = 1, 3, 5...$) are opto-mechanically coupled to the cavity (Section 7.1.3.1). The power and detuning of the incident field have been chosen so that the $(i, j) = (3, 3)$ vibrational mode, with mechanical frequency of $\Omega_{33}/2\pi = 2.32$ MHz, is damped to a thermal phonon occupation number of $\overline{n}_{33} = 50$. Under these experimentally feasible conditions, we predict that the magnitude of $S_\Delta(\Omega)$ produced by membrane thermal
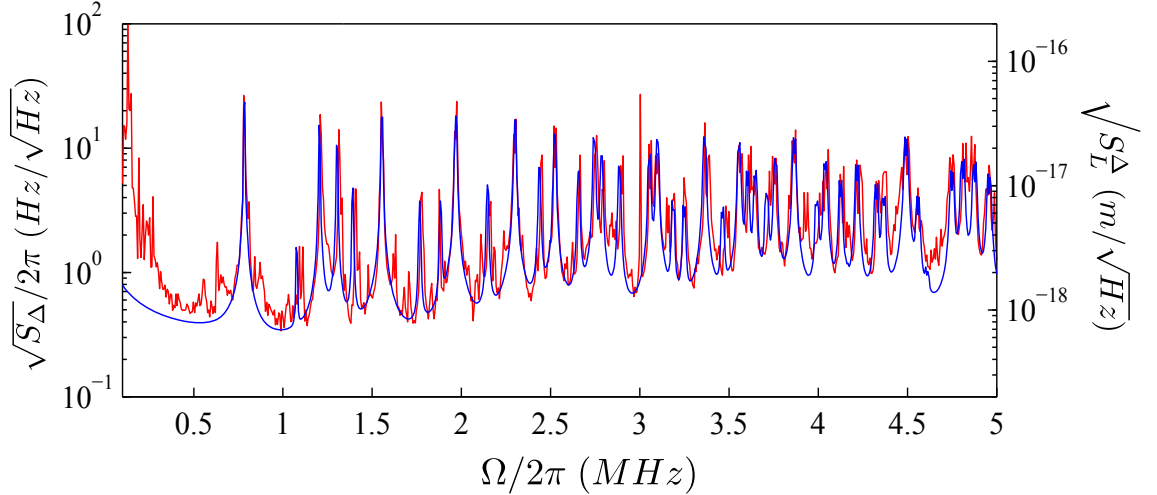
Figure 10.2: Measured spectrum of detuning fluctuations, $\sqrt{S_\Delta(\Omega)}$ (also expressed as effective cavity length fluctuations, $\sqrt{S_L^\Delta(\Omega)}$) for the Fabry-Pérot cavity described in Section 10.2 . The observed noise (red trace) arises from thermal motion of the end-mirror substrates, in agreement with the finite element model shown in blue. This "substrate noise" constitutes an extraneous background for the "membrane-in-the-middle" system conceptualized in Figure 10.1 and detailed in [14].

motion (blue curve) would be commensurate with the noise produced by substrate thermal motion (red curve). Substrate thermal motion therefore constitutes an important a roadblock to observing quantum behavior in our system [14].

10.3   Strategy to Suppress Extraneous Thermal Noise

Extraneous thermal motion manifests itself as fluctuations in the cavity resonance frequency, and therefore the detuning of an incident laser field. We now consider a method to suppress these detuning fluctuations using feedback. Our strategy is to electro-optically imprint an independent measurement of the extraneous cavity resonance frequency fluctuations onto the frequency of the incident field, with gain set so that this added "anti-noise" cancels the thermal fluctuations. To measure the extraneous noise, we monitor the resonance frequency of an auxiliary cavity mode which has nearly equal sensitivity to extraneous thermal motion but reduced (ideally no) sensitivity to thermal motion of the intracavity oscillator (further information could be obtained by simultaneously monitoring multiple cavity modes). The basis for this *"differential sensitivity"* is the spatial overlap between the cavity modes and the vibrational modes of the optomechanical system (as described in Section 7.1.3). We hereafter specialize our treatment to the experimental system described in Section 10.2, in which case extraneous thermal motion corresponds to mirror "substrate motion" and motion of the intracavity oscillator to "membrane motion", respectively.

A conceptual diagram of the feedback scheme is shown in Figure 10.1. The field used for mea-
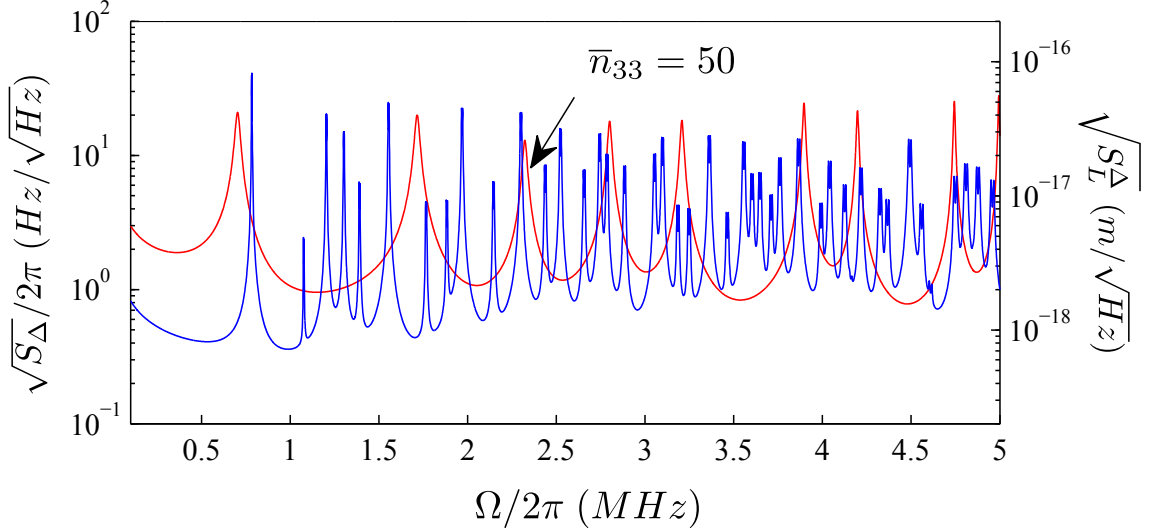
Figure 10.3: Model spectrum of detuning fluctuations arising from mirror substrate (blue trace) and membrane motion (red trace) for the system described in Section 10.2. The power and detuning of the cavity field are chosen so that the (3,3) membrane mode is optically damped to a thermal phonon occupation number of $\overline{n}_{33} = 50$. The substrates vibrate at room temperature.

surement of extraneous thermal noise is referred to as the "probe field". The incident field to which feedback is applied, and which is to serve the primary functions of the experiment, is referred to as the "science field". The frequencies of the probe and science fields are $\omega_0^{p,s} = \langle \omega_0^{p,s} \rangle + \delta\omega_0^{p,s}$, respectively. Each field is coupled to a single spatial mode of the cavity, referred to as the "probe mode" and the "science mode", respectively. Resonance frequencies of the probe mode, ω_c^p, and science mode, ω_c^s, both fluctuate in time as a consequence of substrate motion and membrane motion. We can represent these fluctuations, $\delta\omega_c^{p,s} \equiv \omega_c^{p,s} - \langle \omega_c^{p,s} \rangle$, as (Section 7.3)

$$\begin{aligned}
\delta\omega_c^p &= g_1 \delta z_1^p + g_2 \delta z_2^p + g_m \delta z_m^p \\
\delta\omega_c^s &= g_1 \delta z_1^s + g_2 \delta z_2^s + g_m \delta z_m^s.
\end{aligned} \tag{10.1}$$

Here $\delta z_{1,2,m}^{p,s}$ denotes the "effective displacement" of mirror substrate M1 ("1"), mirror substrate M2 ("2"), and the membrane ("m") with respect to the probe ("p") and science ("s") cavity modes, and $g_{1,2,m}$ denotes the "optomechanical coupling" of M1, M2, and the membrane, respectively. Effective displacement refers to the axial (along the cavity axis) displacement of the mirror or membrane surface averaged over the transverse intensity profile of the cavity mode (Section 7.3). Opto-mechanical coupling refers to the frequency shift per unit axial displacement if the entire surface were translated rigidly (Section 7.3.2.3). In the simple case for which the membrane is removed ($g_m = 0$), couplings $g_{1,2}$ take on the familiar values: $g_1 = -g_2 = \langle \omega_c^p \rangle / \langle L \rangle \simeq \langle \omega_c^s \rangle / \langle L \rangle$. Otherwise, all three are functions of the membrane's axial position relative to the intracavity standing
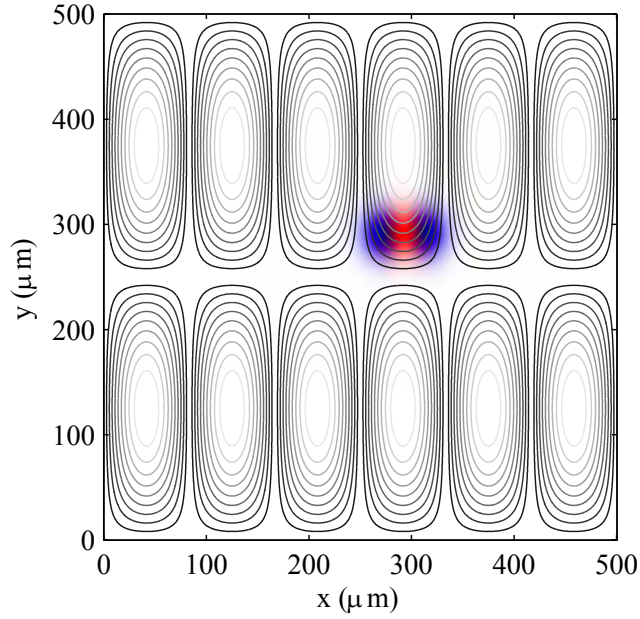
Figure 10.4: Location of the TEM_{00} (red) and TEM_{01} (blue) cavity modes relative to the membrane surface for experiments reported in Sections 10.4.2 – 10.4.4. Density plots of the intra-cavity intensity are displayed on top of a black contour plot representing the axial displacement of the (2,6) membrane mode. Averaging the displacement of the surface weighted by the intensity profile gives the "effective displacement" δz_m for membrane motion; in this case the effective displacement of the (2,6) mode is greater for the TEM_{00} mode than it is for TEM_{01} mode.

wave (Eq. 7.34).

To simplify the discussion of differential sensitivity, we confine our attention to a single vibrational mode of the membrane with generalized amplitude b (Section 7.1.1) and undamped mechanical frequency Ω_m. We will assume that cavity resonance frequencies ω_c^p and ω_c^s have different sensitivities to b but are equally sensitive to substrate motion at Fourier frequencies Ω near Ω_m. We can express these two conditions in terms of the Fourier transforms (Eq. 2.1) of the effective displacements as:

$$\delta z_m^{p,s}(\Omega) = \eta^{p,s} b(\Omega); \;\; \eta^p \neq \eta^s$$
$$\delta z_{1,2}^p(\Omega) \simeq \delta z_{1,2}^s(\Omega) \equiv \delta z_{1,2}(\Omega). \tag{10.2}$$

Factors $\eta^{p,s}$ characterize the "spatial overlap" between the vibrational mode and cavity modes p and s (Section 7.1.3). When referring to a specific vibrational mode (i,j), we will adopt the notation $\{b_{ij}, \Omega_{ij}, \eta_{ij}^{p,s}\}$ for the mode amplitude, frequency, and spatial overlap, respectively.

The first assumption of Eq. 10.2 is valid if the vibrational mode shape of the membrane varies rapidly on a spatial scale set by the cavity waist size, w_c. The latter assumption is valid if the opposite is true, i.e., we confine our attention to low-order substrate vibrational modes, whose shape varies slowly on a scale set by w_c. The substrate noise shown in Figure 10.2 fits this description, provided

that the cavity mode is also of low order, e.g., cavity modes TEM_{00} and TEM_{01} (Section 7.1.2). To visualize the differential sensitivity of TEM_{00} and TEM_{01}, in Figure 10.4 we plot the transverse intensity profile of each mode (Eq. 7.21b) atop contours representing the amplitude of the (2,6) drum vibration of the membrane (Eq. 7.21a), with waist size and position and the membrane dimensions representing the experimental conditions discussed in Section 10.4.2. Choosing TEM_{01} for the probe mode and TEM_{00} for the science mode gives $\eta_{26}^p/\eta_{26}^s \approx 0.6$ for this example.

To implement feedback, a measurement of the probe field detuning fluctuations $\delta\Delta_p \equiv \delta\omega_0^p - \delta\omega_c^p$ is electro-optically mapped onto the frequency of the science field with gain G. Combining Eqs. 10.1 and 10.2 and assuming that the laser source has negligible phase noise (i.e., $\delta\omega_0^p(\Omega) = 0$ and $\delta\omega_0^c(\Omega) = -G(\Omega)\delta\Delta_p(\Omega)$), we can express the fluctuations in the detuning of the science field, $\delta\Delta_s \equiv \delta\omega_0^s - \delta\omega_c^s$, as

$$
\begin{aligned}
\delta\Delta_s(\Omega) &= -\delta\omega_c^s(\Omega) - G(\Omega)\delta\Delta_p(\Omega) \\
&= -\left(g_1\delta z_1(\Omega) + g_2\delta z_2(\Omega)\right)\left(1 + G(\Omega)\right) - g_m\eta^s b(\Omega)\left(1 + (\eta^p/\eta^s)G(\Omega)\right).
\end{aligned}
\tag{10.3}
$$

Here we have ignored the effect of feedback on the physical amplitude, b (we consider this effect in Section 10.5).

The science field detuning in Eq. 10.3 is characterized by two components, an extraneous component proportional to $(1 + G(\Omega))$ and an intrinsic component proportional to $(1 + (\eta^p/\eta^s)G(\Omega))$. To suppress extraneous fluctuations, we can set the open loop gain to $G(\Omega) = -1$. The selectivity of this suppression is set by the "differential sensing factor" η^p/η^s. In the ideal case for which the probe measurement only contains information about the extraneous noise, i.e., $\eta^p/\eta^s \ll 1$, Eq. 10.3 predicts that only extraneous noise is suppressed.

For our open-loop architecture, noise suppression depends critically on the phase delay of the feedback. To emphasize this fact, we can express the open-loop gain as

$$
G(\Omega) = |G(\Omega)|e^{i\Omega\tau(\Omega)},
\tag{10.4}
$$

where $|G(\Omega)|$ is the magnitude and $\tau(\Omega) \equiv \text{Arg}[G(\Omega)]/\Omega$ is the phase delay of the open loop gain at Fourier frequency Ω. Phase delay arises from the cavity lifetime and latencies in detection and feedback, and becomes important at Fourier frequencies for which $\tau(\Omega) \gtrsim \pi/\Omega$. Since in practice we are only interested in fluctuations near the mechanical frequency of a single membrane mode, Ω_m, it is sufficient to achieve $G(\Omega_m) = -1$ by manually setting $|G(\Omega_m)| = 1$ (using an amplifier) and $\tau(\Omega_m) = \pi n/\Omega_m$ (using a delay cable), where n is an odd integer.

Two additional issues conspire to limit noise suppression. First, because substrate thermal motion is only partially coherent, noise suppression requires that $\tau(\Omega_m) \ll Q/\Omega_m$, where $Q \sim 700$ is the quality of the noise peaks shown in Figure 10.2. We achieve this by setting $\tau(\Omega_m) \sim \pi/\Omega_m$.

(a) Zoomed-out spectrum.

(b) Zoomed-in spectrum focusing on (3,3) membrane mode.
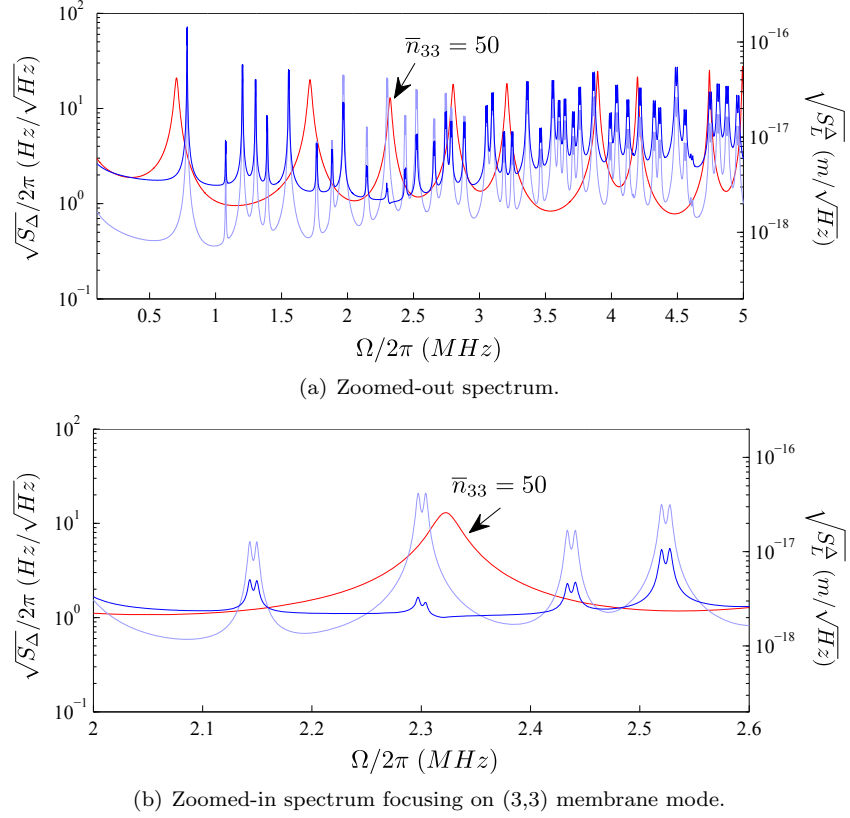
Figure 10.5: Predicted suppression of substrate detuning noise (dark blue) for the science field based on a feedback with ideal differential sensing, $\eta^p/\eta^s = 0$, for all modes, gain $G(\Omega) = e^{i\pi\Omega/\Omega_{33}}$, and measurement noise $S_{\omega_p^N}(\Omega) = 2\pi \times 1 \text{ Hz}^2/\text{Hz}$, where $\Omega_{33} = 2\pi \times 2.32$ MHz is the mechanical frequency of the (3,3) membrane mode. Unsuppressed substrate (light blue) and membrane noise (red) for the science field is taken from the model in Figure 10.3.

Another issue is that any noise process not entering the measurement of $\delta\Delta_p$ via Eq. 10.1 will be *added* onto the detuning of the science field via Eq. 10.3. The remaining extraneous contribution to $\delta\Delta_s$ will thus be non-zero even if $G(\Omega) = -1$. Expressing this measurement noise as an effective resonance frequency fluctuation $\delta\omega_c^N$, we can model the power spectrum of detuning fluctuations in the vicinity of Ω_m as

$$
\begin{aligned}
S_{\Delta_s}(\Omega) =& |1 + G(\Omega)|^2 \cdot (g_1{}^2 S_{x_1}(\Omega) + g_2{}^2 S_{x_2}(\Omega)) \\
& + |1 + (\eta^p/\eta^s)^2 G(\Omega)|^2 \cdot g_m^2 (\eta^p)^2 S_b(\Omega) + |G(\Omega)|^2 \cdot S_{\omega_c^N}(\Omega).
\end{aligned}
\tag{10.5}
$$

In Figure 10.5 we present an idealized model of our noise suppression strategy applied to the system described in Section 10.2. We assume an ideal differential sensing factor of $\eta^p/\eta^s = 0$ for all modes, a uniform gain magnitude of $|G(\Omega)| = 1$, and a uniform phase delay $\tau(\Omega) = \pi/\Omega_{33}$, where $\Omega_{33}/2\pi = 2.32$ MHz is the oscillation frequency of the (3,3) membrane mode. As in Figure 10.3, the detuning and power of the science field are chosen in order to optically damp the (3, 3) membrane
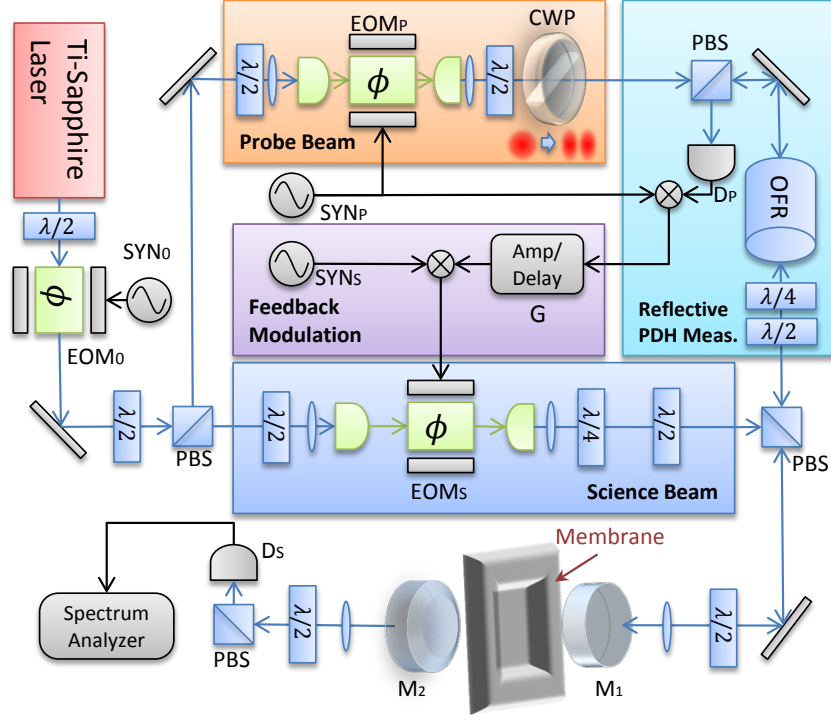
Figure 10.6: Experimental setup: $\lambda/2$: half wave plate. $\lambda/4$: quarter wave plate. PBS: polarizing beam splitter. $EOM_{0,P,S}$: electro-optical modulators for calibration and probe/science beams. CWP: split-π wave plate. OFR: optical Faraday rotator. $M_{1,2}$: cavity entry/exit mirrors. $D_{P,S}$: photodetectors for probe/science beams. $SYN_{0,P,S}$: synthesizers for driving $EOM_{0,P,S}$.

mode to a thermal phonon occupation of $\overline{n}_{33} = 50$. The probe measurement is also assumed to include extra noise at the level of $S_{\omega_c^N}(\Omega) = (2\pi)^2 \times 1 \; \mathrm{Hz}^2/\mathrm{Hz}$. Incorporating these assumptions into Eqs. 10.4 and 10.5 produces the science field detuning spectrum shown in Figure 10.5. In this idealized scenario, substrate noise near the $(3,3)$ membrane mode is reduced to a level more than an order of magnitude below the peak amplitude of the $(3,3)$ membrane mode.

10.4 Experiment

We have experimentally implemented the noise suppression scheme proposed in Section 10.3. Core elements of the optical and electronic set-up are illustrated in Figure 10.6. As indicated, the probe and the science fields are both derived from a common titanium-sapphire (ti-sapph) laser, which operates at a wavelength of $\lambda_0 \approx 810$ nm. The science field is coupled to the TEM_{00} cavity mode. The probe field is coupled to either the TEM_{00} or the TEM_{01} mode of the cavity. The frequencies of the science and probe fields are controlled by a pair of broadband electro-optic modulators ($EOM_{P,S}$ in Figure 10.6).

To monitor the frequency of the probe mode, ω_c^p, the reflected probe field is directed to pho-

todetector "D_P" and analyzed using the Pound-Drever-Hall (PDH) technique (Section 8.4). The low-frequency (< 1 kHz) portion of the PDH signal is used to stabilize slow drift of ω_p via piezo-electric feedback to one of the end-mirrors. The high-frequency portion of the PDH signal is used to generate the electro-optic (EO) feedback signal (Eq. 10.3). Feedback gain $G(\Omega)$ (Eq. 10.4) is controlled by passing the PDH signal through a control box ("Amp/Delay" in Figure 10.6) containing an amplifier and a delay line. The output of the control box, voltage V_{con}, is used to modulate the frequency of the science field using one of two methods. The first method involves coupling V_{con} to the frequency-modulation (FM) port of the synthesizer (SYN$_S$) driving EOM$_S$. The second method, not shown in Figure 10.6, involves passing the science beam through an AOM driven by a voltage-controlled-oscillator (VCO), which is modulated by V_{con}. Feedback modifies the instantaneous detuning of the science field, Δ_s, which we infer from the intensity of the transmitted field on photodetector "D_S".

We now develop several key aspects of the noise suppression scheme. In Section 10.4.1, we emphasize the performance of the feedback network by suppressing substrate noise with the membrane removed from the cavity. In Section 10.4.2, we introduce the membrane and study the combined noise produced by membrane and substrate motion. In Section 10.4.3, we demonstrate the concept of differential sensing by electronically subtracting dual measurements of the probe and science mode resonance frequencies. In Section 10.4.4, we combine these results to realize substrate noise suppression in the presence of the membrane. We use a detuned science field for this study, and record a significant effect on the radiation pressure pressure damping experienced by the membrane. This effect is explored in detail in Section 10.5.

10.4.1 Substrate Noise Suppression with the Membrane Removed

The performance of the feedback network is studied by first removing the membrane from the cavity, corresponding to $g_m = 0$ in Eqs. 10.1, 10.3, and 10.5. The feedback objective is to suppress the detuning noise on a science field coupled to the TEM$_{00}$ cavity mode, shown for example in Figure 10.2. Absent the membrane, it is not necessary to employ a different probe mode to monitor the substrate motion. For this example, both the science and probe field are coupled to the TEM$_{00}$ cavity mode. The science field is coupled to one of the (nearly linear) polarization eigen-modes of TEM$_{00}$ at a mean detuning $\langle\Delta_s\rangle = -\kappa$, where $\kappa \approx 2\pi \times 4$ MHz is the cavity amplitude decay rate at 810 nm. The probe field is resonantly coupled to the remaining (orthogonal) polarization eigen-mode of TEM$_{00}$. Detuning fluctuations $\delta\Delta_s$ are monitored via the transmitted intensity fluctuations on detector D_S. Resonance frequency fluctuations $\delta\omega_c^p$ are monitored via the PDH technique on detector D_P.

Feedback is implemented by directing the measurement of $\delta\omega_c^p$ to a VCO-controlled AOM in the science beam path (not shown in Figure 10.6). The feedback gain $G(\Omega)$ is tuned so that $S_{\Delta_s}(\Omega)$
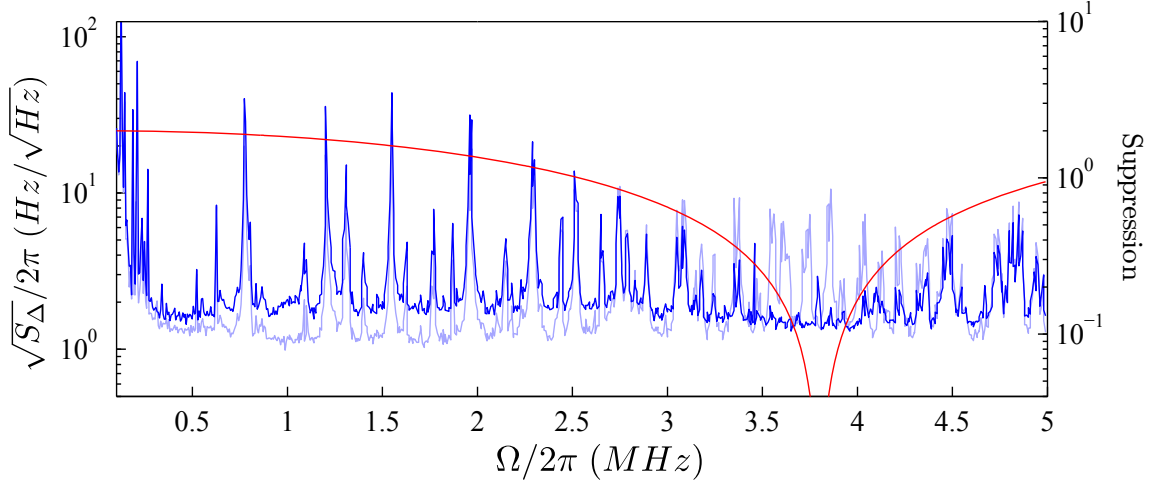
Figure 10.7: Substrate noise suppression implemented with the membrane removed. Gain is manually set to $G(\Omega_0 = 2\pi \times 3.8$ MHz$) \approx -1$ using an RF amplifier and a delay line. The ratio of the noise spectrum with (dark blue trace) and without (light blue trace) feedback is compared to the "suppression factor" $|1 + G(\Omega)|^2$ (red trace, right axis) with $G(\Omega) = e^{i\pi\Omega/\Omega_0}$.

(Eq. 10.5) is minimized at $\Omega = \Omega_0 \approx 2\pi \times 3.8$ MHz, corresponding in this case to $|G(\Omega_0)| \approx 1$ and $\tau(\Omega_0) = \pi/(\Omega_0)$. The magnitude of $S_{\Delta_s}(\Omega)$ over a broad domain with (dark blue) and without (light blue) feedback is shown in Figure 10.7. The observed suppression of $S_{\Delta_s}\Omega$ may be compared to the predicted value of $|1 + G(\Omega)|^2$ based on a uniform gain amplitude and phase delay: i.e. $|G(\Omega)| \approx 1$ and $\tau(\Omega) = \pi/\Omega_0$ (Eq. 10.4). In qualitative agreement with this model (red trace in Figure 10.7), noise suppression is observed over a 3 dB bandwidth of ~ 500 kHz. Noise suppression at target frequency Ω_0 is limited by shot noise in the measurement of $\delta\omega_c^p$, corresponding to $S_{\omega_c^N}(\Omega) \approx 2\pi \times 1$ Hz^2/Hz in Eq. 10.5; this value was used for the model in Figure 10.5.

10.4.2 Combined Substrate and Membrane Thermal Noise

With the science field coupled to the TEM$_{00}$ cavity mode at $\langle \Delta_s \rangle = -\kappa$, we now introduce the membrane oscillator (described in Section 10.2). We focus our attention on thermal noise in the vicinity of $\Omega_{26} = 2\pi \times 3.56$ MHz, the undamped frequency of the (2,6) vibrational mode of the membrane. To emphasize the dual contribution of membrane motion and substrate motion to fluctuations of ω_c^s, we axially position the membrane so that $g_m \sim 0.04 \cdot g_{1,2}$. This reduces the detuning fluctuations due to membrane motion, $g_m \delta z_m^s = g_m \eta^s b$ to near the level of the substrate noise $g_1 \delta z_1 + g_2 \delta z_2$. The location of the cavity mode relative to the displacement profile of the (2,6) mode has been separately determined, and is shown in Figure 10.4. For b coinciding with an antinode of the (2,6) vibrational node and the science mode coinciding with TEM$_{00}$, this location predicts a spatial overlap factor (Section 7.1.3.1) of $\eta_{26}^s \approx 0.4$.

A measurement of the science field detuning noise, $S_{\Delta_s}(\Omega)$ made with feedback turned off
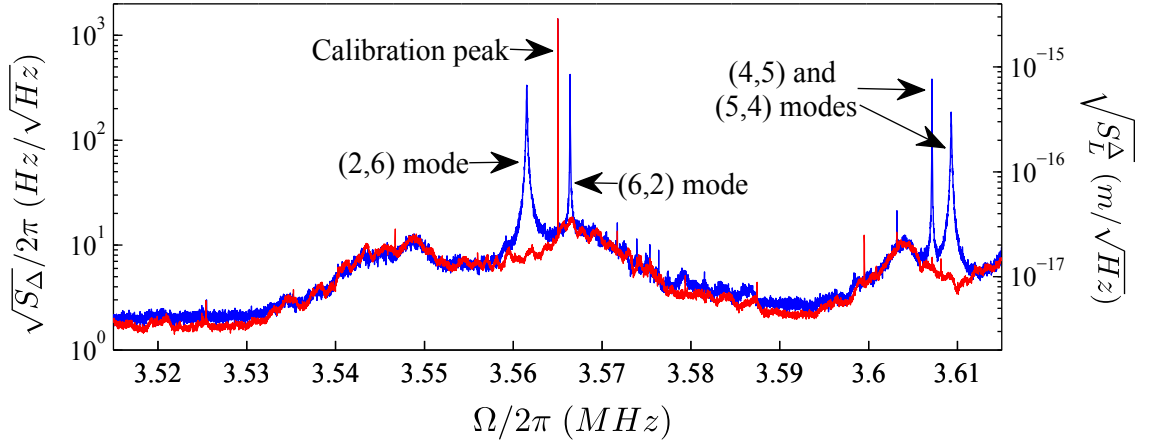
Figure 10.8: Combined membrane and substrate thermal noise (blue trace) in the vicinity of $\Omega_{26} = 2\pi \times 3.56$ MHz, the frequency of the (2,6) vibrational mode of the membrane. g_m has been set to approximately 4% of $g_{1,2}$ in order to emphasize the substrate noise component. For comparison, a measurement of the substrate noise with the membrane removed from the cavity is shown in red.

$(G(\Omega) = 0)$ is shown in Figure 10.8. The blue trace shows the combined contribution of substrate and membrane thermal noise. Note that the noise peaks associated with membrane motion are broadened and suppressed due to optical damping/cooling by the cavity field (Section 10.5). For comparison, we show an independent measurement made with the membrane removed (red trace). Both traces were calibrated by adding a small phase modulation to the science field (EOM$_0$ in Figure 10.6). We observe that the noise in the vicinity of Ω_{26} contains contributions from multiple membrane modes and substrate modes. The latter component contributes equally in both the blue and red traces, suggesting that substrate thermal motion indeed gives rise to the broad extraneous component in the blue trace. From the red curve, we infer that the magnitude of the extraneous noise at Ω_{26} is $S_{\Delta_s,e}(\Omega_{26}) \approx (2\pi)^2 \times 80$ Hz^2/Hz (hereafter subscript "e" signifies "extraneous"). The influence of this background on the vibrational amplitude b_{26} is discussed in Section 10.5.

10.4.3 Differential Sensing of Membrane and Substrate Motion

To "differentially sense" the noise shown in Figure 10.8, we use the probe field to monitor the resonance frequency of the TEM$_{01}$ mode. Coupling the science field to the TEM$_{00}$ mode (ω_s) and

Table 10.1: Differential sensing factor, η^p/η^s, for the (2,6) and (6,2) membrane modes, with TEM$_{00}$ and TEM$_{01}$ forming the science and probe modes, respectively. The values in this table are inferred from Figure 10.9 and the model discussed in the appendix.

Membrane mode	(2,6)	(6,2)
Determined from Figure 10.9	0.59	0.98
Calculated from Figure 10.4	0.61	0.96

(a) Zoomed-out spectrum.


(b) Zoomed-in spectrum.
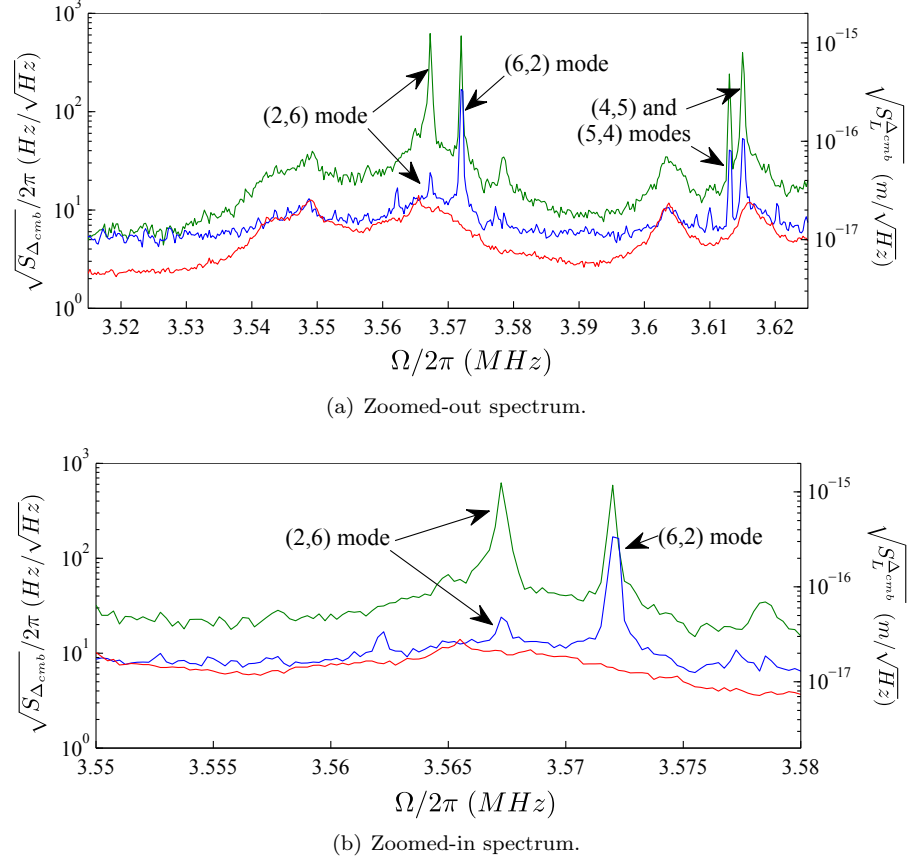
Figure 10.9: Characterizing differential sensitivity of the TEM_{00} (science) and TEM_{01} (probe) mode to membrane motion. Green and blue traces correspond the noise spectrum of electronically added (green) and subtracted (blue) measurements of $\delta\omega_c^p$ and $\delta\omega_c^s$. Electronic gain $G_0(\Omega)$ has been set so that subtraction coherently cancels the contribution from the (2,6) mode at the mechanical frequency of the (2,6) mode, $\Omega_{26} \approx 2\pi \times 3.568$ MHz. The magnitude of the gain implies that $\eta_{26}^p/\eta_{26}^s \approx 0.59$ for the (2,6) mode. The relatively small concomitant suppression of the nearby (6,2) noise peak at $\Omega_{62} \approx 2\pi \times 3.572$ MHz indicates that $\eta_{62}^p/\eta_{62}^s \approx 0.98$ for this mode. For comparison to earlier plots, on the right axis we convert the combined electronic noise, $S_{\Delta_{cmb}}(\Omega)$, as an effective cavity length noise, $S_L^{\Delta_{cmb}}(\Omega) \equiv g_0^{-2} S_{\Delta_{cmb}}(\Omega)$.

the probe field to the TEM_{01} mode (ω_p) requires displacing their frequencies by the transverse mode-splitting of the cavity, $\Delta_{tms} = \langle\omega_c^p\rangle - \langle\omega_c^s\rangle \approx 2\pi \times 11$ GHz (Δ_{tms} is set by the cavity length and the 5 cm radius of curvature of the mirrors). This is done by modulating EOM_S at frequency Δ_{tms}, generating a sideband (constituting the science field) which is coupled to the TEM_{00} mode when the probe field at the carrier frequency is coupled to the TEM_{01} mode. To spatially mode-match the incident Gaussian beam to the TEM_{01} mode, the probe beam is passed through a split π wave plate (CWP in Figure 10.6. (This plate was provided by Prof. Jun Ye's group.) This enables a mode-matching efficiency of $\approx 30\%$.

We can experimentally test the differential sensitivity (Eq. 10.2) of modes TEM_{00} and TEM_{01} by electronically adding and subtracting simultaneous measurements of $\delta\Delta_p$ and $\delta\Delta_s$. For this test,

both measurements were performed using the PDH technique (detection hardware for the science beam is not shown in Figure 10.6). PDH signals were combined on a RF combiner after passing the science signal through a RF attenuator and a delay line. The combined signal may be expressed as $\Delta_{\mathrm{cmb}}(\Omega) \equiv G_0(\Omega)\delta\Delta_s(\Omega) + \delta\Delta_p(\Omega)$, where $G_0(\Omega)$ represents the differential electronic gain.

The power spectral density of the combined electronic signal, $S_{\Delta_{\mathrm{cmb}}}(\Omega)$, is shown in Figure 10.9, again focusing on Fourier frequencies near Ω_{26}. In the blue ("subtraction") trace, $G_0(\Omega_{26})$ has been tuned in order to minimize the contribution from membrane motion, i.e., $G_0(\Omega_{26}) \approx -\eta_{26}^p/\eta_{26}^s$. In the green ("addition") trace, we invert this gain value. Also shown (red) is a scaled measurement of the substrate noise made with the membrane removed, corresponding to the red trace in Figure 10.8 (note that the elevated noise floor in the green and blue traces is due to shot noise in the PDH measurements, which combine incoherently). From the magnitude of the electronic gain, we can directly infer a differential sensing factor of $\eta_{26}^p/\eta_{26}^s = 0.59$ for the (2,6) membrane mode. By contrast, it is evident from the ratio of peak values in the subtraction and addition traces that neighboring membrane modes (6,2), (4,5), and (5,4) each have different differential sensing factors. For instance, the relative peak heights in Figure 10.9(b) suggest that $\eta_{62}^p/\eta_{62}^s = 0.98$. This difference relates to the strong correlation between $\eta^{p,s}$ and the location of the cavity mode on the membrane. In Table 10.1, we compare the inferred differential sensing factor for (2,6) and (6,2) to the predicted value based on the cavity mode location shown in Figure 10.4. These values agree to within a few percent.

10.4.4 Substrate Noise suppression With the Membrane Inside the Cavity

Building upon Sections 10.4.1– 10.4.3, we now implement substrate noise suppression with the membrane inside the cavity, which is the principal experimental result of this chapter. The science field is coupled to the TEM$_{00}$ cavity mode with $\langle\Delta_s\rangle = -\kappa$, and $\delta\Delta_s$ is monitored via the transmitted intensity fluctuations on D_S. The probe field is coupled to the TEM$_{01}$ cavity mode, and $\delta\Delta_p$ is monitored via PDH on detector D_P. Feedback is implemented by mapping the measurement of $\delta\Delta_p$ onto the frequency of the science field; this is done by modulating the frequency of the ≈ 11 GHz sideband generated by EOM$_S$ (via the FM modulation port of synthesizer SYN$_S$ in Figure 10.6). The feedback objective is to selectively suppress the substrate noise component of $S_{\Delta_s}(\Omega)$ near Ω_{26} — i.e., to subtract the red curve from the blue curve in Figure 10.8. To do this, the open-loop gain of the feedback is set to $G(\Omega_{26}) \approx -1$ (Eq. 10.5).

The magnitude of $S_{\Delta_s}(\Omega)$ with feedback on (orange) and off (blue) is shown in Figure 10.10. Comparing Figures 10.10 and 10.8, we infer that feedback enables reduction of the substrate noise component at Ω_{26} by a factor of $S_{\Delta_{s,e}}(\Omega_{26})|_{\mathrm{OFF}}/S_{\Delta_{s,e}}(\Omega_{26})|_{\mathrm{ON}} \approx 16$. The actual suppression is

(a) Zoomed-out spectrum.

(b) Zoomed-in spectrum focusing on (2,6) membrane mode.
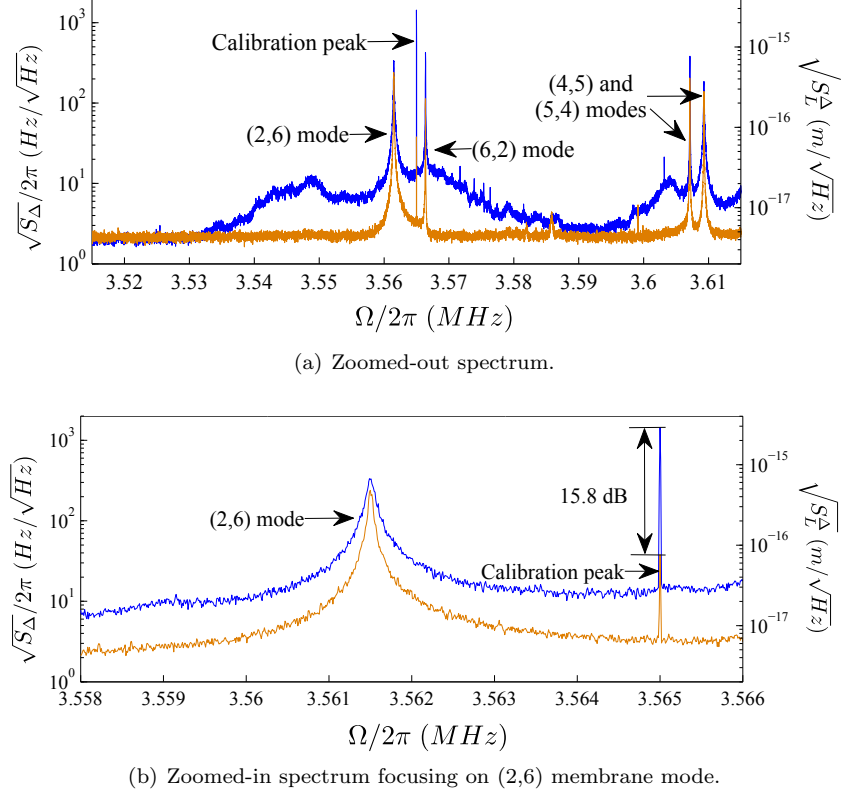
Figure 10.10: Substrate noise suppression with the membrane inside the cavity. Orange and blue traces correspond to the spectrum of science field detuning fluctuations with and without feedback, respectively. The open-loop gain of the feedback has been set to $G(\Omega_{26} \approx 2\pi \times 3.56 \text{ MHz}) = -1$ in order to suppress the substrate noise contribution near Ω_{26}. A common modulation on probe and science fields at 3.565 MHz ("calibration peak") is suppressed by 15.8 dB in amplitude with the feedback.

limited by two factors: drift in the open-loop gain and shot noise in the PDH measurement of $\delta\Delta_p$. The first effect was studied by applying a common FM tone to both the probe and science field (via EOM$_0$ in Figure 10.6; this modulation is also used to calibrate the measurements). Suppression of the FM tone, seen as a noise spike at frequency $\Omega_0 = 2\pi \times 3.565$ MHz in Fig. 10.10(b), indicates that the limit to noise suppression due to drift in $G(\Omega)$ is $S_{\Delta_s,e}(\Omega_0)|_{\text{OFF}}/S_{\Delta_s,e}(\Omega_0)|_{\text{ON}} \approx 1.4 \times 10^3$. The observed suppression of ≈ 16 is thus limited by shot noise in the measurement of $\delta\Delta_p$. This is confirmed by a small increase ($\sim 10\%$) in $S_\Delta(\Omega)$ around $\Omega = 2\pi \times 3.52$ MHz, and corresponds to $S_{\omega_c^N}(\Omega) \sim (2\pi)^2 \times 1 \text{ Hz}^2/\text{Hz}$ in Eq. 10.5. Note that the actual noise suppression factor is also partly obscured by shot noise in the measurement of $\delta\Delta_s$; this background is roughly $\sim (2\pi)^2 \times 4 \text{ Hz}^2/\text{Hz}$, coinciding with the level $S_{\Delta_s}(\Omega)|_{\text{OFF}}$ (blue trace) at $\Omega \approx 2\pi \times 3.52$ MHz in Figure 10.10(a).

In the following section, we consider the effect of electro-optic feedback on the membrane thermal noise component in Figure 10.10.

10.5 Extraneous Noise Suppression and Optical Damping: An Application

We now consider using a detuned science beam (as in Section 10.4.4) to optically damp the membrane. Optical damping here takes place as a consequence of the natural interplay between physical amplitude fluctuations, $b(\Omega)$, detuning fluctuations $-g_m\eta^s b(\Omega)$, and intracavity intensity fluctuations, which produce a radiation pressure force $\delta F_{\rm rad}(\Omega) = -\varphi(\Omega) \cdot g_m\eta^s b(\Omega)$ that "acts back" on $b(\Omega)$ (Section 10.8). The characteristic gain of this "back-action", $\varphi(\Omega)$, possesses an imaginary component due to the finite response time of the cavity; this results in a viscous radiation pressure force characterized by a mechanical damping rate $\Gamma_{\rm opt} \approx -{\rm Im}[\delta F_{\rm rad}(\Omega_m)/b(\Omega_m)]/(m\Omega_m)$ (See Section 9.1), where m is the effective mass of the b (Eq. 7.20).

In our noise suppression scheme, electro-optic feedback replaces the intrinsic detuning fluctuations, $-g_m\eta^s b(\Omega)$, with the modified detuning fluctuations, $-(1 + (\eta^p/\eta^s)G(\Omega))g_m\eta^p b(\Omega)$ (Eq. 10.3). The radiation pressure force experience by the membrane is thus modified by a factor of $(1 + (\eta^p/\eta^s)G(\Omega))$ (this reasoning is analytically substantiated in Section 10.8). Here we define a differential gain parameter $\mu \equiv (\eta^p/\eta^s)G(\Omega_m)$ (note that $\mu = 0$ corresponds to the absence of feedback). For purely real $G(\Omega_m)$, the modified optical damping rate as a function of μ has the relation (Eq. 10.23),

$$\frac{\Gamma_{\rm opt}(\mu)}{\Gamma_{\rm opt}(\mu = 0)} \approx 1 + \mu. \tag{10.6}$$

Associated with optical damping is "optical cooling", corresponding to a reduction of the vibrational energy (expressed as an amplitude variance $\langle b^2 \rangle$) from its equilibrium thermal value. $\langle b^2 \rangle$ is also as a function of μ. Following Section 9.1:

$$\langle b^2 \rangle(\mu) = \frac{\Gamma_m}{\Gamma_m + \Gamma_{\rm opt}(\mu)}\frac{k_B T_b}{m\Omega_m^2} = \frac{\Gamma_m}{\Gamma_{\rm eff}(\mu)}\frac{k_B T_b}{m\Omega_m^2}, \tag{10.7}$$

where k_B is the Boltzmann constant and T_b is the temperature of the thermal bath. Here $\Gamma_{\rm eff}(\mu) \equiv \Gamma_m + \Gamma_{\rm opt}(\mu)$ is the effective mechanical damping rate.

From Eqs. 10.6 and 10.7, we predict that if the probe is insensitive to membrane motion ($\eta^p = 0 \rightarrow \mu = 0$), then optical damping/cooling is unaffected by electro-optic feedback. In a realistic scenario for which $\eta^p/\eta^s > 0$ (e.q., Section 10.4), feedback with $G(\Omega_m) = -1$ (to suppress extraneous noise) results in a reduction of the optical damping rate and an increase in the vibrational energy of the oscillator. Remarkably, when $\eta^p/\eta^s < 0$, extraneous noise suppression can coincide with an increased optical damping rate and therefore a reduced vibrational energy. We elaborate on this subject in Section 10.6.2.

It is worth emphasizing that the effect described in Eq. 10.6 has much in common with active radiation pressure feedback damping, a.k.a "cold-damping", as pioneered in [89]. In the experiment

described in [89], feedback is applied to the position of a micro-mirror (in a Fabry-Pérot cavity) by modulating the intensity of an auxiliary laser beam reflected from the mirror's surface. This beam imparts a fluctuating radiation pressure force, which may be purely damping (or purely anti-damping) if the delay of the feedback is set so that the intensity modulation is in phase (or π out of phase) with the oscillator's velocity.

Our scheme differs from [89] in several important ways. In [89], the "probe" field is coupled to the cavity, but the intensity-modulated "science" field does not drive a cavity mode. By contrast, in our scheme, both the probe and science fields are coupled to independent spatial modes of the cavity. Moreover, instead of directly modifying the intensity of the incident science field, in our scheme we modify its detuning from the cavity, which indirectly modifies the *intra-cavity* intensity. The resulting radiation pressure fluctuations produce damping (or anti-damping) of the oscillator (in our case a membrane mode) if the detuning modulation is in phase (or π out of phase) with the oscillator's velocity. For the extraneous noise suppression result shown in Figure 10.10, the phase of the electro-optic feedback results in anti-damping of the membrane's motion. The reason why this is tolerable, and another crucial difference between our scheme and the "cold-damping" scheme of [89], is that the feedback force is super-imposed onto a strong cavity "back-action" force. In Figure 10.10, for example, the small amount of feedback anti-damping is negated by larger, positive back-action damping. The relative magnitude of these two effects depends on the differential sensing factor (η^p/η^s) for the two cavity modes.

To investigate the interplay of electro-optic feedback and optical damping, we now reanalyze the experiment described in Section 10.4.4. In that experiment, the science field was red-detuned by $\langle \Delta_s \rangle \approx -\kappa \approx -2\pi \times 4$ MHz, resulting in significant damping of the membrane motion. This damping is evident in a careful analysis of the width Γ_{eff} (FWHM in Hz^2/Hz units) and area $\langle \delta\Delta_s^2 \rangle \equiv \int_{\Omega_m} S_{\Delta_s}(\Omega) d\Omega/2\pi$ of the thermal noise peak centered near $\Omega_m = \Omega_{26}$ in Figure 10.10. We have investigated the influence of electro-optic feedback on optical damping by varying the magnitude of the feedback gain, $G(\Omega_{26})$, while monitoring $S_{\Delta_s}(\Omega)$ in addition to $S_{\Delta_p}(\Omega)$ (inferred from the probe PDH measurement). From the basic relations given in Eqs. 10.6 and 10.7, the ratio of the effective damping rate with and without electro-optic feedback is predicted to scale linearly with μ, i.e.,

$$R_{\Gamma_{\text{eff}}}(\mu) \equiv \frac{\Gamma_{\text{eff}}(\mu)}{\Gamma_{\text{eff}}(\mu = 0)} = 1 + \frac{\Gamma_{\text{eff}}(\mu = 0) - \Gamma_m}{\Gamma_{\text{eff}}(\mu = 0)}\mu. \tag{10.8}$$

Similarly, combining Eqs. 10.1 and 10.7 and ignoring substrate noise, we expect the mean-squared probe field detuning noise associated with the thermal peak centered at Ω_m, i.e., $\langle (\delta\Delta_p)^2 \rangle = \int_{\Omega_m} S_{\Delta_p}(\Omega) d\Omega/2\pi$, to have the property

$$R_{\Delta_p}(\mu) \equiv \frac{\langle (\delta\Delta_p)^2 \rangle(\mu = 0)}{\langle (\delta\Delta_p)^2 \rangle(\mu)} = R_{\Gamma_{\text{eff}}}(\mu). \tag{10.9}$$
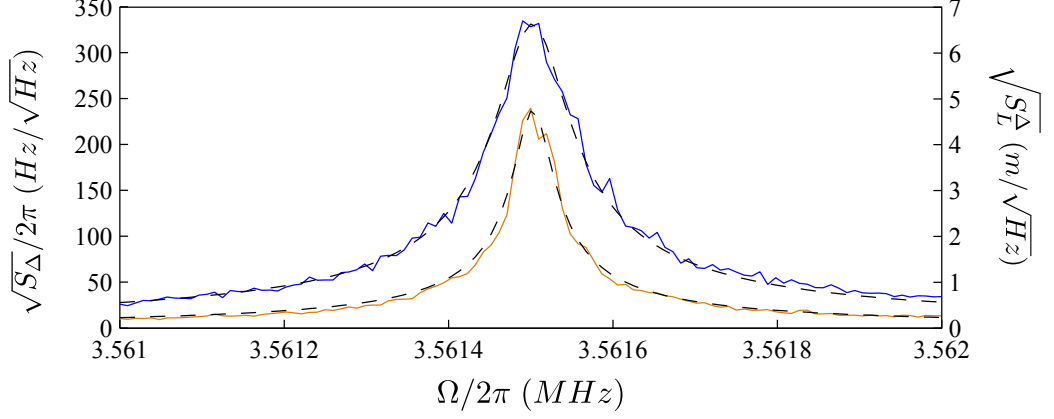
Figure 10.11: Lorentzian fits of the thermal noise peak near Ω_{26} in Figure 10.10, here plotted on a linear scale. Solid blue and orange traces correspond to science field detuning noise with noise suppression off and on, respectively. Dashed traces correspond to Lorentzian fits.

Finally, using Eq. 10.5, we expect the mean-squared science field detuning noise associated with the thermal peak centered at Ω_m, i.e., $\langle(\delta\Delta_s)^2\rangle = \int_{\Omega_m} S_{\omega_c^p}(\Omega)\mathrm{d}\Omega/2\pi$, to have the property

$$R_{\Delta_s}(\mu) \equiv \frac{\langle\delta\Delta_s^2\rangle(\mu=0)}{\langle\delta\Delta_s^2\rangle(\mu)} = \frac{R_{\Gamma_{\mathrm{eff}}}(\mu)}{(1-\mu)^2}. \tag{10.10}$$

To obtain values for Γ_{eff}, $\langle\delta\Delta_p^2\rangle$, and $\langle\delta\Delta_s^2\rangle$, we fit the noise peak near Ω_{26} in measurements of $S_{\Delta_p}(\Omega)$ and $S_{\Delta_s}(\Omega)$ to a Lorentzian line profile (Eq. 9.9). Two examples, corresponding to the noise peaks in Figure 10.10(b), are highlighted in Figure 10.11. The blue curve corresponds to $S_{\Delta_s}(\Omega)$ with $\mu = 0$ ($G(\Omega_{26}) = 0$) and the orange curve with $\mu = -\eta_{26}^p/\eta_{26}^s$ ($G(\Omega_{26}) = -1$). Values for Γ_{eff} and $\langle\delta\Delta_s^2\rangle$ inferred from these two fits are summarized in Table 10.2. Using these values and a separate measurement of $\Gamma_m = 2\pi \times 4.5$ Hz for the $(2,6)$ mode, we can test the model by comparing the differential sensing factor inferred from Eq. 10.8 and Eq. 10.10. From Eq. 10.8 we infer $\eta_{26}^p/\eta_{26}^s = 0.54$ and from Eq. 10.10 we infer $\eta_{26}^p/\eta_{26}^s \approx 0.61$. These values agree to within 10% of each other and the values listed in Table 10.1.

In Figure 10.12 we show measurements of $R_{\Gamma_{\mathrm{eff}}}$ (yellow circles) and R_{Δ_p} (blue squares) for several values of μ, varied by changing the magnitude of $G(\Omega_{26})$. The horizontal scale is calibrated by assuming $\eta_{26}^s/\eta_{26}^p = 0.6$. Both measured ratios have an approximately linear dependence on μ

Table 10.2: Parameters from Figures 10.8 and 10.11. $\mu = 0$ and $\mu = -\eta_{26}^p/\eta_{26}^s$ represents the noise suppression is off and on, respectively. Γ_{eff} and $\sqrt{\langle\delta\Delta_s^2\rangle}$ are inferred from the Lorentzian fits in Figure 10.11. $S_{\Delta_s,e}(\Omega_{26})$ with $\mu = 0$ and $\mu = -\eta_{26}^p/\eta_{26}^s$ are inferred from the red curve in Figure 10.8 and the orange curve in Figure 10.10, respectively.

| μ	$\Gamma_{\mathrm{eff}}/2\pi$ (Hz)	$\sqrt{\langle\delta\Delta_s^2\rangle}/2\pi$ (Hz)	$S_{\Delta_s,e}(\Omega_{26})/(2\pi)^2$ (Hz^2/Hz)
0	21	3.8×10^3	80
$-\eta_{26}^p/\eta_{26}^s$	12	2.1×10^3	5
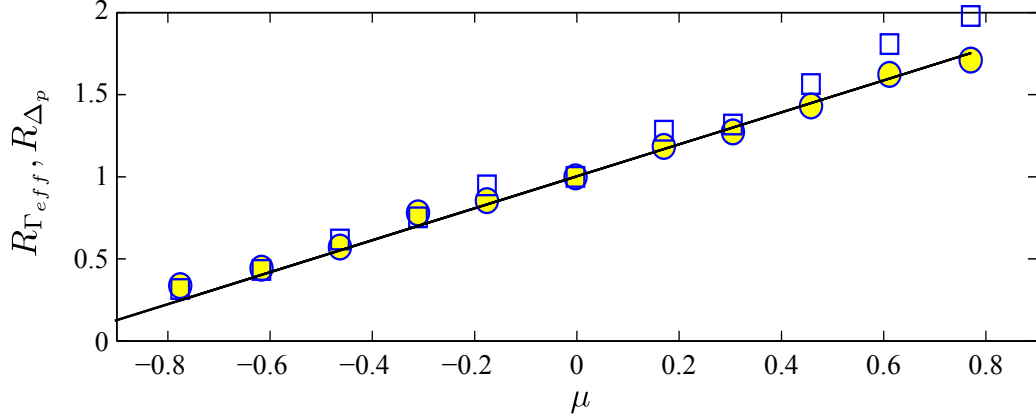
Figure 10.12: The impact of electro-optic feedback on optical damping/cooling of the (2,6) membrane mode with a red-detuned science field, as reflected in measured ratios $R_{\Gamma_{\text{eff}}}$ (yellow circles, Eq. 10.8) and R_{Δ_p} (blue squares, Eq. 10.9), as a function of feedback gain parameter μ. The model shown (black line) is for $\eta_{26}^s/\eta_{26}^p = 0.6$.

with a common slope that agrees with the prediction based on Eqs. 10.8 and 10.9 (black line).

10.6   Discussion

10.6.1   Optical Cooling Limits

Taking into account the reduction of extraneous noise (Section 10.4.4) and the effect of electro-optic feedback on optical damping (Section 10.5), we now estimate the base temperature achievable with optical cooling in our system. We base our estimate on the laser frequency noise heating model developed in [96], in which it was shown that the minimum thermal phonon occupation achievable in the presence of laser frequency noise with magnitude $S_{\omega_0}(\Omega)$ is given by

$$\bar{n}_{min} \simeq \frac{2\sqrt{\Gamma_0 S_{\omega_0}(\Omega_m)}}{g\delta z_{\text{zp}}} + \frac{\kappa^2}{\Omega_m^2}, \tag{10.11}$$

where $\Gamma_0 = k_B T_b/\hbar\Omega_m$ is the re-thermalization rate with the environment at temperature T_b and $g\delta z_{\text{zp}}$ is the cavity resonance frequency fluctuation associated with the zero-point motion of the oscillator.

We apply Eq. 10.11 to our system by replacing $S_{\omega_0}(\Omega_m)$ with extraneous detuning noise, $S_{\Delta_s,e}(\Omega_m)$, and $g\delta z_{\text{zp}}$ with feedback-modified zero-point fluctuations $g_m(1 - \eta^p/\eta^s)\eta^s b_{\text{zp}}$, where $b_{\text{zp}} = \sqrt{\hbar/(m\Omega_m)}$ and m are the zero-point amplitude and effective mass of amplitude coordinate b, respectively. We also assume that the membrane can be positioned so as to increase the opto-mechanical coupling to its maximal value $g_m^{\max} = 2|r_m|\langle\omega_c^s\rangle/\langle L\rangle$ (r_m is the membrane reflectively without effecting the magnitude of the suppressed substrate noise. Values for $S_{\Delta_s,e}(\Omega_{26})$ with feed-

back on and off are drawn from Table 10.2: $(2\pi)^2 \times 5$ Hz^2/Hz and $(2\pi)^2 \times 80$ Hz^2/Hz, respectively. Other parameters used are $\kappa = 2\pi \times 4$ MHz, $\Omega_m = \Omega_{26} = 2\pi \times 3.56$ MHz, $m = m_p/4 = 8.4$ ng, $|r_m| = 0.465$ ([23]), $g_m^{\max} = 2\pi \times 4.6 \times 10^5$ MHz/μm (for $\langle L \rangle = 0.74$ mm), $\eta_{26}^p = 0.24$, and $\eta_{26}^s = 0.4$ (from Figure 10.4). With and without feedback, we obtain values of $\overline{n}_{\min}^{(2,6)} = 128$ and 206, respectively, for the $(2,6)$ vibrational mode.

The improvement from $\overline{n}_{\min}^{(2,6)} = 206$ to 128 is modest and derives from the use of a relatively large and positive differential sensing factor, $\eta_{26}^p/\eta_{26}^s \approx 0.6$, as well as shot noise in the probe measurement, which sets a lower bound for the extraneous detuning fluctuations ($S_{\Delta_s,e}(\Omega_{26}) \approx S_{\omega_c^N}(\Omega_{26}) \approx (2\pi)^2 \times 5$ Hz^2/Hz in Figure 10.10). Paths to reduce or even change the sign of the differential sensing factor are discussed in Section 10.6.2. Reduction of shot noise requires increasing the technically accessible probe power; as indicated in Section 10.4.4, we suspect that significant reduction of $S_{\Delta_s,e}(\Omega_{26})$ can be had if this improvement were made.

Note that the above values of $\overline{n}_{\min}^{(2,6)}$ are based on an estimate of the maximum obtainable opto-mechanical coupling $g_m^{\max}$. For the experiment in Section 10.4, however, we have set the opto-mechanical coupling coefficient $g_m \ll g_m^{\max}$ in order to emphasize the substrate noise. From the data in Figure 10.10, we infer g_m to be

$$g_m = \frac{2\pi\Omega_{26}\sqrt{\langle\delta\Delta_s^2\rangle}}{\eta_{26}^s}\sqrt{\frac{m\Gamma_{\text{eff}}}{k_B T_b \Gamma_m}} = 2\pi \times 2.1 \times 10^4 \text{ MHz/}\mu\text{m}, \tag{10.12}$$

which is $\approx 4.6\%$ of $g_m^{\max}$. Thus for experimental parameters specific to Figure 10.10, the cooling limit is closer to $\overline{n}_{\min}^{(2,6)} = 2800$.

10.6.2 "Negative" Differential Sensing

It is interesting to consider the consequences of realizing a *negative* differential sensing factor, $\eta^p/\eta^s < 0$. Eq. 10.3 implies that in this case electro-optic feedback can be used to suppress extraneous noise ($G(\Omega_m) < 0$) without diminishing sensitivity to intrinsic motion (i.e., $(\eta^p/\eta^s)G(\Omega_m) > 0$). As a remarkable corollary, Eqs. 10.5 and 10.6 imply that extraneous noise suppression can coincide with *enhanced* optical damping, i.e., $\mu = (\eta^p/\eta^s)G(\Omega_m) > 0$, if $\eta^p/\eta^s < 0$. Using electro-optic feedback in this fashion to simultaneously enhance back-action while suppressing extraneous noise seems appealing from the standpoint of optical cooling.

Achieving $\eta^p/\eta^s < 0$ requires an appropriate choice of cavity and mechanical mode shapes and their relative orientation. In the context of the "membrane-in-the-middle" geometry, we can identify two ways of achieving a negative differential sensing factor. The first involves selecting a mechanical mode with a nodal spacing comparable to the cavity waist. Consider the arrangement shown in Figure 10.13, in which the TEM$_{00}$ and TEM$_{01}$ cavity modes are centered on the central antinode of the $(1,5)$ membrane mode (a 1D slice through the midline of the membrane is shown). The ratio
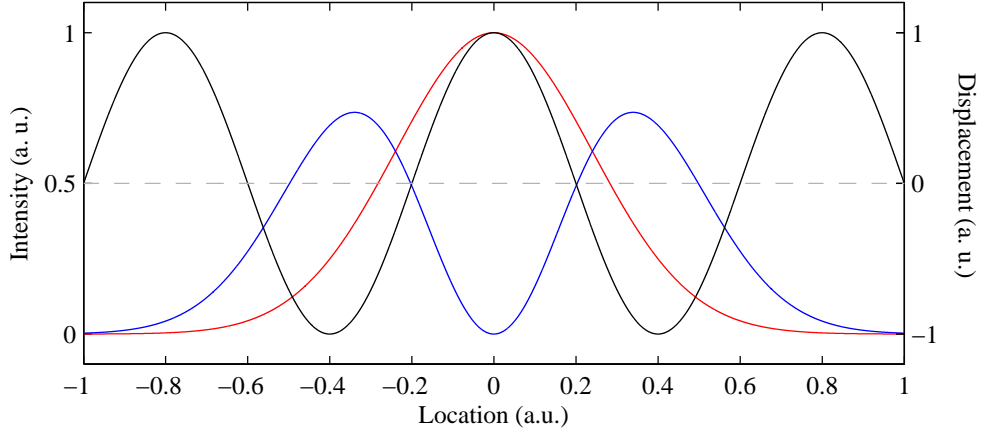
Figure 10.13: Visualization of "negative" differential sensing. The transverse displacement profile of the (1,5) membrane mode is shown in black (a 1D slice along the midline of the membrane is shown). Red and blue curves represent the transverse intensity profile of TEM_{00} and TEM_{01} cavity modes, both centered on the membrane. The cavity waist size is adjusted so that the displacement averaged over the intensity profile is negative for TEM_{01} and positive for TEM_{00}.

of the ($1/e^2$ intensity) cavity waist, w_c, and the nodal spacing, w_{node}, has been adjusted so that the distance between antinodes of the TEM_{01} cavity mode roughly matches w_{node}; in this case, $w_c/w_{\mathrm{node}} = 0.88$. It is intuitive to see that the displacement profile averaged over the blue (TEM_{01}) and red (TEM_{00}) intensity profiles is negative in the first case and positive in the second. Using TEM_{01} as the probe mode and TEM_{00} as the science mode in this case gives $\eta_{15}^p = -0.34$, $\eta_{15}^s = 0.37$, and $\eta_{15}^p/\eta_{15}^s = -0.92$.

Another possibility is to center the cavity mode near a vibrational *node* of the membrane. In this situation, numerical calculation shows that rotating the TEM_{01} (probe) mode at an appropriate angle with respect to the membrane can give $\eta^p/\eta^s < 0$ (with TEM_{00} as the science mode), albeit at the cost of reducing the absolute magnitudes of η^p and η^s. We have experimentally observed this effect in our system by positioning the cavity modes near the geometric center of the membrane, which is a node for all of the even-order vibrational modes (modes (i,j) with i or j even). As in Section 10.4.3, we electronically added and subtracted simultaneous measurements of $\delta\omega_c^p$ and $\delta\omega_c^s$ in order to assess their differential sensitivity. A measurement of the noise near the mechanical frequencies of the $(2,3)$ and $(3,2)$ membrane modes is shown in Figure 10.14. We found for this configuration that *adding* the signal with the appropriate gain (black trace) leads to enhancement of the (2,3) mode (left peak) and suppression of the (3,2) mode (right peak), in contrast to the results in Figure 10.9, for which all modes are either suppressed or enhanced. This suggests that $\eta_{23}^p/\eta_{32}^s < 0$.
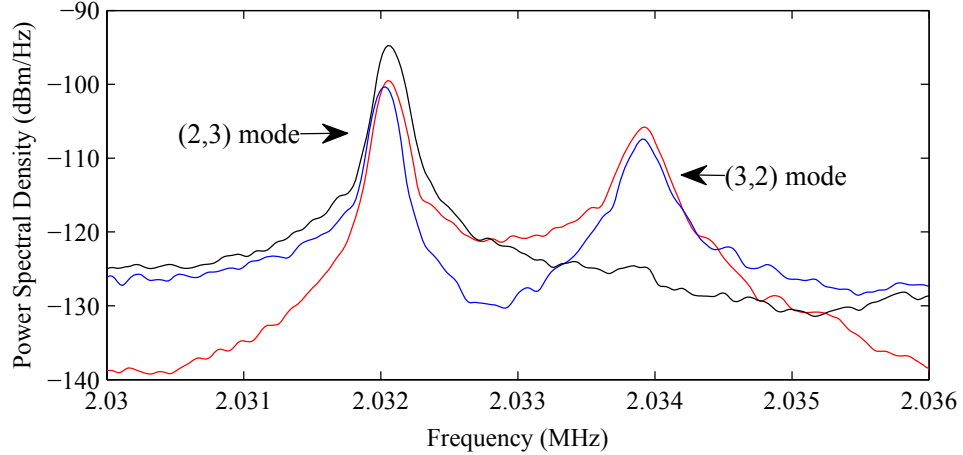
Figure 10.14: Realization of "negative" differential sensing for the (3,2) membrane mode. The TEM_{00} (science) and TEM_{01} (probe) modes are positioned near the center of the membrane. Measurements of $\delta\omega_c^p$ (blue) and $\delta\omega_c^s$ (red) are combined electronically on an RF splitter with positive gain, $G_0 = \eta_{32}^p/\eta_{32}^s$, as discussed in Section 10.4.3. The power spectrum of the electronic signal before (blue and red) and after (black) the splitter (here in raw units of dBm/Hz) is shown. The (2,3) noise peak in the combined signal is amplified while the (3,2) noise peak is supressed, indicating that $\eta_{23}^p/\eta_{23}^s > 0$ and $\eta_{32}^p/\eta_{32}^s < 0$.

10.7   Summary and Conclusions

We have proposed and experimentally demonstrated a technique to suppress extraneous thermal noise in a cavity optomechanical system. Our technique (Section 10.3) involves mapping a measurement of the extraneous noise onto the frequency of the incident laser field, delayed and amplified so as to stabilize the associated laser-cavity detuning. To obtain an independent measurement of the extraneous noise, we have proposed monitoring the resonance frequency of an auxiliary cavity mode with reduced sensitivity to the intracavity oscillator but similar sensitivity to the extraneous thermal motion.

To demonstrate the viability of this strategy, we have applied it to an experimental system consisting of a nanomechanical membrane coupled to a short Fabry-Pèrot cavity (Sections 10.2 and 10.4). We have shown that in this system, operating at *room temperature*, thermal motion of the end-mirror substrates can give rise to large laser-cavity detuning noise (Figure 10.2). Using the above technique, with primary ("science") and auxiliary ("probe") cavity modes corresponding to TEM_{00} and TEM_{01}, we have been been able to reduce this "substrate" detuning noise by more than an order of magnitude (Figures 10.7 and 10.10). We've also investigated how this noise suppression scheme can be used to "purify" a red-detuned field used to optically damp the membrane (Section 10.5). We found that optical damping is effected by residual coupling of the auxiliary cavity mode to the membrane, producing feedback which modifies the intrinsic cavity "back-action" (Figure 10.12). We argued that this effect is akin to "cold-damping" [89], and that it need not significantly

limit, and could even enhance, the optical cooling, if an appropriate auxiliary cavity mode is used (Section 10.6.2). Current challenges include increasing the shot noise sensitivity of the auxiliary probe measurement and reducing or changing the "sign" (Section 10.6.2) of the coupling beteen the auxiliary cavity mode and the membrane.

It is worth noting that our technique is applicable to a broader class of extraneous fluctuations that manifest themselves in the laser-cavity detuning, including laser phase noise, radial oscillation of optical fibers, and seismic/acoustic vibration of the cavity structure. The concept of "differential sensitivity" (Eq. 10.2) central to our technique is also applicable to a wide variety of optomechanical geometries.

10.8   Appendix: Radiation Pressure Stiffening/Damping with Electro-Optic Feedback

Here we consider a simple model for the dynamics of a vibrating membrane (or equivalently, a vibrating mirror) linearly coupled to an optical cavity driven by a frequency-modulated laser. We focus on a single vibrational mode of the membrane with amplitude $b(t)$. The cavity exhibits a fluctuating resonance frequency $\delta\omega_c(t) = g_m\eta^s b(t)$, where g_m is the optomechanical coupling and η^s the spatial overlap factor between the cavity mode and the vibrational mode (Section 10.3). Fluctuations $\delta\omega_c(t)$ give rise to intracavity intensity fluctuations, which alter the dynamics of $b(t)$ through the radiation pressure force. Superimposed onto this back-action is the effect of electro-optic feedback, which we model by assuming a definite phase relationship between $b(t)$ and the modulated frequency of the incident field.

Following Section 9.1.2.2, we adopt the following coupled differential equations to describe vibrational amplitude $b(t)$ and intracavity field amplitude, $a(t)$ (here expressed in the frame rotating at the frequency of the drive field, $\langle\omega_0\rangle = \langle\omega_c\rangle + \langle\Delta\rangle$, and normalized so that $|a(t)|^2 = U_c(t)$ is the intracavity energy):

$$\ddot{b}(t) + \Gamma_m\dot{b}(t) + \Omega_m^2 b(t) = F_{\text{ext}}(t) + \delta F_{\text{rad}}(t) \tag{10.13a}$$

$$\dot{a}(t) + \kappa + i(\langle\Delta\rangle - \delta\omega_c(t)))a(t) = \sqrt{2\kappa_1}E_0 e^{2i\phi(t)}. \tag{10.13b}$$

Eq. 10.13a describes the motion of a velocity-damped harmonic oscillator driven by an external force $F_{\text{ext}}(t)$ in addition to a radiation pressure force $F_{\text{rad}}(t) = \langle F_{\text{rad}}\rangle + \delta F_{\text{rad}}(t)$. We define b relative to its equilibrium position with the cavity field excited, thus we ignore the static part of the radiation pressure force. We adopt the following expression for the radiation pressure force based on energy conservation (Section 2.4): $F_{\text{rad}} = -\partial U_c/\partial b = -g_m\eta U_c/\langle\omega_c\rangle$.

Eq. 10.13b is based on the standard input-output model for a low-loss, two-mirror resonator [110].

Here E_0 and $|E_0|^2$ represent the amplitude and power of the incident field, $\phi(t)$ the instantaneous phase of the incident field, and $\kappa = \kappa_1 + \kappa_2 + \kappa_L$ the total cavity (amplitude) decay rate, expressed as the sum of the decay rates through mirror 1, mirror 2, and due to internal losses, respectively. Recall that in the "membrane-in-the-middle" system, $\kappa_{1,2,L}$ all depend on the membrane's axial position with respect to the intracavity standing wave (Section 8.2).

Using this notation, the instantaneous frequency and detuning of the input field are given by:

$$\delta\omega_0(t) = \dot{\phi}(t) \tag{10.14a}$$

$$\delta\Delta(t) = \dot{\phi}(t) - \delta\omega_c(t) = \dot{\phi}(t) - g_m\eta^s b(t). \tag{10.14b}$$

We seek solutions to Eq. 10.13 by expressing $a(t)$ as a small fluctuation around its respective steady-state solution, $a(t) = \langle a \rangle + \delta a(t)$. In this case the radiation pressure force is given by

$$\delta F_{rad}(t) = -\frac{g_m\eta}{\omega_c}(\langle a \rangle^* \delta a(t) + \langle a \rangle \delta a^*(t)). \tag{10.15}$$

An equation of motion for $\delta a(t)$ is obtained from Eq. 10.13 with the assuption that $\delta a(t) \ll \langle a \rangle$, $\phi(t) \ll 1$, and $\delta\omega_c(t) \ll \langle \Delta \rangle$. This approximation gives

$$\delta\dot{a}(t) + (\kappa + i(\langle\Delta\rangle))\delta a(t) - \kappa\delta\omega_c(t)\langle a \rangle = i\sqrt{2\kappa_1}E_0\phi(t), \tag{10.16}$$

where

$$\langle a \rangle = E_0 \frac{\sqrt{2\kappa_1}}{\kappa + i\langle\Delta\rangle}. \tag{10.17}$$

Applying the Fourier transform (Eq. 2.1) to both sides of Eq. 10.16, we obtain the following expression for the spectrum of intracavity amplitude fluctuations:

$$\delta a(\Omega) = \frac{i\langle a \rangle}{\kappa + i(\langle\Delta\rangle + \Omega)}\left(\delta\omega_c(\Omega) + (\kappa + i\langle\Delta\rangle)\phi(\Omega)\right). \tag{10.18}$$

Combining expressions for $\delta a(\Omega)$ and $[\delta a^*](\Omega)$ (the Fourier transform of $\delta a^*(t)$, which obeys the complex conjugate of Eq. 10.16), we obtain the following expression for the spectrum of radiation pressure force fluctuations:

$$\delta F_{rad}(\Omega) = -\frac{g_m\eta|\langle a \rangle|^2}{\omega_c}\left(\frac{i}{\kappa + i(\langle\Delta\rangle + \Omega)} - \frac{i}{\kappa - i(\langle\Delta\rangle - \Omega)}\right)(\delta\omega_c(\Omega) - i\phi(\Omega)/\Omega). \tag{10.19}$$

Using Eq. 10.17 and identifying $\delta\omega_c(\Omega) - i\phi(\Omega)/\Omega = -\delta\Delta(\Omega)$ as the instantaneous laser-cavity detuning, we infer the following relationship between detuning and the radiation pressure force

fluctuations:

$$\delta F_{\rm rad}(\Omega) = \frac{g_m \eta}{\langle \omega_c \rangle} |E_0|^2 \frac{2\kappa_1}{\kappa^2 + \langle \Delta \rangle^2} \left(\frac{i}{\kappa + i(\langle \Delta \rangle + \Omega)} - \frac{i}{\kappa - i(\langle \Delta \rangle - \Omega)} \right) \delta\Delta(\Omega) \qquad (10.20a)$$

$$\equiv \varphi(\Omega)\delta\Delta(\Omega) = -\varphi(\Omega) g_m \eta^s b(\Omega)(1 + \mu(\Omega)) \qquad (10.20b)$$

where $\mu(\Omega) = -(\eta^p/\eta^s)G(\Omega)$ is the electro-optic feedback gain as defined in Eq. 10.3.

Eq. 10.20 suggests that radiation pressure force fluctuations associated with thermal motion can be suppressed by using electro-optic feedback to stabilize the associated laser-cavity detuning fluctuations. The effect of $\delta F_{\rm rad}$ on the dynamics of b in Eq. 10.16a may be expressed as a modified mechanical susceptibility, $\chi_{\rm eff}(\Omega) \equiv b(\Omega)/F_{\rm ext}(\Omega)$. Applying the Fourier transform to both sides of Eq. 10.13a and using Eq. 10.20 gives:

$$\chi_{\rm eff}(\Omega)^{-1} = \chi_m(\Omega)^{-1} - \delta F_{\rm rad}(\Omega)/b(\Omega) \qquad (10.21a)$$

$$= \left(\Omega_m^2 - \Omega^2 + i\Omega\Gamma_m \right) m + \varphi(\Omega) g_m \eta^s (1 + \mu(\Omega)). \qquad (10.21b)$$

For sufficiently weak radiation pressure, the mechanical susceptibility near resonance can be approximated

$$\chi_{\rm eff}(\Omega)^{-1} \approx \left((\Omega_m + \Delta\Omega_{\rm opt})^2 - \Omega^2 + i\Omega(\Gamma_m + \Gamma_{\rm opt}) \right) m \qquad (10.22)$$

where

$$\Gamma_{\rm opt} \equiv -\frac{1}{\Omega_m m} {\rm Im} \left(\frac{F_{\rm rad}(\Omega_m)}{b(\Omega_m)} \right) = \frac{g_m \eta^s}{\Omega_m m} {\rm Im} \left((1 + \mu(\Omega_m))\varphi(\Omega_m) \right) \qquad (10.23a)$$

$$\Delta\Omega_{\rm opt} \equiv -\frac{1}{2\Omega_m m} {\rm Re} \left(\frac{F_{\rm rad}(\Omega_m)}{b(\Omega_m)} \right) = \frac{g_m \eta^s}{2\Omega_m m} {\rm Re} \left((1 + \mu(\Omega_m))\varphi(\Omega_m) \right). \qquad (10.23b)$$

From this expression and the Fluctuation-Dissipation theorem (Eq. 9.8b) we infer the modified membrane thermal noise spectrum (equivalent to 9.9 but in this case expressions for $\{\Gamma_{\rm opt}, \Delta\Omega_{\rm opt}\}$ are both modified by electro-optic feedback):

$$S_b(\Omega) = |\chi_{\rm eff}(\Omega)|^2 \cdot 4k_B T_b \Gamma_m \Omega = \frac{4k_B T_{bath} \Gamma_m/m}{((\Omega_m + \Delta\Omega_{\rm opt})^2 - \Omega^2)^2 + \Omega^2(\Gamma_m + \Gamma_{\rm opt})^2}. \qquad (10.24)$$

Bibliography

[1] T.J. Kippenberg and K.J. Vahala. Cavity opto-mechanics. *Optics Express*, 15(25):17172–17205, 2007.

[2] F. Marquardt. Optomechanics: Push towards the quantum limit. *Nature Physics*, 4(7):513–514, 2008.

[3] A. Cleland. Optomechanics: Photons refrigerating phonons. *Nature Physics*, 5(7):458–460, 2009.

[4] R. Riviere, S. Deleglise, S. Weis, E. Gavartin, O. Arcizet, A. Schliesser, and T.J. Kippenberg. Optomechanical sideband cooling of a micromechanical oscillator close to the quantum ground state. *Physical Review A*, 83(6):063835, 2011.

[5] S. Gröblacher, K. Hammerer, M.R. Vanner, and M. Aspelmeyer. Observation of strong coupling between a micromechanical resonator and an optical cavity field. *Nature*, 460(7256):724–727, 2009.

[6] J. Chan, T.P.M. Alegre, A.H. Safavi-Naeini, J.T. Hill, A. Krause, S. Gröblacher, M. Aspelmeyer, and O. Painter. Laser cooling of a nanomechanical oscillator into its quantum ground state. *Nature*, 478(7367):89–92, 2011.

[7] J.D. Thompson, B.M. Zwickl, A.M. Jayich, F. Marquardt, S.M. Girvin, and J.G.E. Harris. Strong dispersive coupling of a high-finesse cavity to a micromechanical membrane. *Nature*, 452(7183):72–75, 2008.

[8] S. Gröblacher, J.B. Hertzberg, M.R. Vanner, G.D. Cole, S. Gigan, KC Schwab, and M. Aspelmeyer. Demonstration of an ultracold micro-optomechanical oscillator in a cryogenic cavity. *Nature Physics*, 5(7):485–488, 2009.

[9] O. Arcizet, R. Rivière, A. Schliesser, G. Anetsberger, and T.J. Kippenberg. Cryogenic properties of optomechanical silica microcavities. *Physical Review A*, 80(2):021803, 2009.

[10] A.D. O'Connell, M. Hofheinz, M. Ansmann, R.C. Bialczak, M. Lenander, E. Lucero, M. Neeley, D. Sank, H. Wang, M. Weides, et al. Quantum ground state and single-phonon control of a mechanical resonator. *Nature*, 464(7289):697–703, 2010.

[11] M. Eichenfield, J. Chan, A.H. Safavi-Naeini, K.J. Vahala, and O. Painter. Modeling dispersive coupling and losses of localized optical and mechanical modes in optomechanical crystals. *Optics Express*, 17(22):20078–20098, 2009.

[12] G.D. Cole, I. Wilson-Rae, K. Werbach, M.R. Vanner, and M. Aspelmeyer. Phonon-tunnelling dissipation in mechanical resonators. *Nature Communications*, 2:231, 2011.

[13] B.M. Zwickl, W.E. Shanks, A.M. Jayich, C. Yang, B. Jayich, J.D. Thompson, and J.G.E. Harris. High quality mechanical and optical properties of commercial silicon nitride membranes. *Applied Physics Letters*, 92(10):103125–103125, 2008.

[14] D.J. Wilson, C.A. Regal, S.B. Papp, and H.J. Kimble. Cavity optomechanics with stoichiometric sin films. *Physical Review Letters*, 103(20):207204, 2009.

[15] JD Teufel, T. Donner, D. Li, JW Harlow, MS Allman, K. Cicak, AJ Sirois, JD Whittaker, KW Lehnert, and RW Simmonds. Sideband cooling of micromechanical motion to the quantum ground state. *Nature*, 475(7356):359–363, 2011.

[16] C. Genes, D. Vitali, P. Tombesi, S. Gigan, and M. Aspelmeyer. Ground-state cooling of a micromechanical oscillator: Comparing cold damping and cavity-assisted cooling schemes. *Physical Review. A*, 77(3):033804, 2008.

[17] I. Wilson-Rae, N. Nooshi, W. Zwerger, and T.J. Kippenberg. Theory of ground state cooling of a mechanical oscillator using dynamical backaction. *Physical Review Letters*, 99(9):093901, 2007.

[18] M. Aspelmeyer, S. Gröblacher, K. Hammerer, and N. Kiesel. Quantum optomechanics—throwing a glance [invited]. *Journal of the Optical Society of America B, Optical Physics*, 27:189, 2010.

[19] T. Rocheleau, T. Ndukum, C. Macklin, J.B. Hertzberg, A.A. Clerk, and K.C. Schwab. Preparation and detection of a mechanical resonator near the ground state of motion. *Nature*, 463(7277):72–75, 2009.

[20] P. Treutlein, D. Hunger, S. Camerer, T.W. Hänsch, and J. Reichel. Bose-einstein condensate coupled to a nanomechanical resonator on an atom chip. *Physical review letters*, 99(14):140403, 2007.

[21] K. Hammerer, M. Wallquist, C. Genes, M. Ludwig, F. Marquardt, P. Treutlein, P. Zoller, J. Ye, and H.J. Kimble. Strong coupling of a mechanical oscillator and a single atom. *Physical Review Letters*, 103(6):63005, 2009.

[22] K. Hammerer, M. Aspelmeyer, E.S. Polzik, and P. Zoller. Establishing einstein-poldosky-rosen channels between nanomechanics and atomic ensembles. *Physical review letters*, 102(2):20501, 2009.

[23] A.M. Jayich, J.C. Sankey, B.M. Zwickl, C. Yang, J.D. Thompson, S.M. Girvin, A.A. Clerk, F. Marquardt, and J.G.E. Harris. Dispersive optomechanics: a membrane inside a cavity. *New Journal of Physics*, 10:095008, 2008.

[24] F. Marquardt, J.P. Chen, A.A. Clerk, and S.M. Girvin. Quantum theory of cavity-assisted sideband cooling of mechanical motion. *Physical Review Letters*, 99(9):93902, 2007.

[25] W.B. Davenport and W.L. Root. *An introduction to the theory of random signals and noise*, volume 11. McGraw-Hill, New York, 1958.

[26] H.A. Haus. *Waves and fields in optoelectronics*, volume 1. Prentice-Hall, New Jersey, 1984.

[27] J. Sólnes. *Stochastic processes and random vibrations: theory and practice.* John Wiley & Sons, 1997.

[28] H.B. Callen and T.A. Welton. Irreversibility and generalized noise. *Physical Review*, 83(1):34–40, 1951.

[29] P.R. Saulson. Thermal noise in mechanical experiments. *Physical Review D*, 42(8):2437, 1990.

[30] E. Hecht. *Optics.* Oldenbourg, 3rd edition, 2001.

[31] A.E. Siegman. *Lasers.* University Science Books, 1986.

[32] M.J. Lawrence, B. Willke, M.E. Husman, E.K. Gustafson, and R.L. Byer. Dynamic response of a fabry–perot interferometer. *Journal of the Optical Society of America B*, 16(4):523–532, 1999.

[33] H.A. Macleod. *Thin-film optical filters.* Taylor & Francis, 2001.

[34] http://www.norcada.com/.

[35] M. Gad-el Hak. *MEMS: design and fabrication*, volume 2. CRC Press, 2006.

[36] P.E. Barclay, K. Srinivasan, O. Painter, B. Lev, and H. Mabuchi. Integration of fiber-coupled high-q sin microdisks with atom chips. *Applied Physics Letters*, 89:131108, 2006.

[37] C.J. Hood, HJ Kimble, and J. Ye. Characterization of high-finesse mirrors: Loss, phase shifts, and mode structure in an optical cavity. *PHYSICAL REVIEW A Phys Rev A*, 64:033804.

[38] RG DeVoe, C. Fabre, K. Jungmann, J. Hoffnagle, and RG Brewer. Precision optical-frequency-difference measurements. *Physical review A*, 37(5):1802, 1988.

[39] S.S. Verbridge, J.M. Parpia, R.B. Reichenbach, L.M. Bellan, and H.G. Craighead. High quality factor resonance at room temperature with nanostrings under high tensile stress. *Journal of Applied Physics*, 99:124304, 2006.

[40] S.S. Verbridge, H.G. Craighead, and J.M. Parpia. A megahertz nanomechanical resonator with room temperature quality factor over a million. *Applied Physics Letters*, 92:013112, 2008.

[41] D.R. Southworth, R.A. Barton, SS Verbridge, B. Ilic, A.D. Fefferman, H.G. Craighead, and J.M. Parpia. Stress and silicon nitride: A crack in the universal dissipation of glasses. *Physical review letters*, 102(22):225503, 2009.

[42] T. Corbitt, Y. Chen, E. Innerhofer, H. Müller-Ebhardt, D. Ottaway, H. Rehbein, D. Sigg, S. Whitcomb, C. Wipf, and N. Mavalvala. An all-optical trap for a gram-scale mirror. *Physical Review Letters*, 98(15):150802, 2007.

[43] C.A. Regal, J.D. Teufel, and K.W. Lehnert. Measuring nanomechanical motion with a microwave cavity interferometer. *Nature Physics*, 4(7):555–560, 2008.

[44] H.O. Pierson. *Handbook of chemical vapor deposition (CVD): principles, technology, and applications.* William Andrew, 1999.

[45] W.H. Chuang, T. Luger, R.K. Fettig, and R. Ghodssi. Mechanical property characterization of lpcvd silicon nitride thin films at cryogenic temperatures. *Journal of Microelectromechanical Systems*, 13(5):870–879, 2004.

[46] O. Tabata, K. Kawahata, S. Sugiyama, and I. Igarashi. Mechanical property measurements of thin films using load-deflection of composite rectangular membranes. *Sensors and Actuators*, 20(1-2):135–141, 1989.

[47] A. Kaushik, H. Kahn, and A.H. Heuer. Wafer-level mechanical characterization of silicon nitride mems. *Microelectromechanical Systems, Journal of*, 14(2):359–367, 2005.

[48] L.D. Landau and E.M. Lifshitz. *Theory of Elasticity.* Oxford, UK, 1986.

[49] W. Weaver, S. Timoshenko, and D.H. Young. *Vibration problems in engineering.* Wiley-Interscience, 1990.

[50] S.S. Rao. *Mechanical vibrations.* Addison-Wesley Reading, MA, 1990.

[51] M. Pinard, Y. Hadjar, and A. Heidmann. Effective mass in quantum effects of radiation pressure. *The European Physical Journal D–Atomic, Molecular, Optical and Plasma Physics*, 7(1):107–116, 1999.

[52] A. Gillespie and F. Raab. Thermally excited vibrations of the mirrors of laser interferometer gravitational-wave detectors. *Physical Review D*, 52(2):577, 1995.

[53] N. Wax. *Selected Papers on Noise and Stochastic Processes*. Dover, June 1954.

[54] E. Black. Notes on pound-drever-hall technique. *LIGO Technical Notes*, 1998.

[55] C.J. Hood, T.W. Lynn, A.C. Doherty, A.S. Parkins, and H.J. Kimble. The atom-cavity microscope: single atoms bound in orbit by single photons. *Science*, 287(5457):1447, 2000.

[56] Agilent. Agilent application note pn 4395/96-1: "how to measure noise accurately using the agilent combination analyzers".

[57] Agilent. Agilent application note 1303: "agilent spectrum and signal analyzer measurements and noise".

[58] I. Wilson-Rae, R.A. Barton, S.S. Verbridge, D.R. Southworth, B. Ilic, H.G. Craighead, and J.M. Parpia. High-q nanomechanics via destructive interference of elastic waves. *Physical Review Letters*, 106(4):47205, 2011.

[59] K.L. Ekinci and M.L. Roukes. Nanoelectromechanical systems. *Review of Scientific Instruments*, 76:061101, 2005.

[60] R. Lifshitz and M.L. Roukes. Thermoelastic damping in micro- and nanomechanical systems. *Physical Review B*, 61(8):5600, 2000.

[61] Private correspondence with group of J.E. Harris.

[62] S.S. Verbridge, D.F. Shapiro, H.G. Craighead, and J.M. Parpia. Macroscopic tuning of nanomechanics: substrate bending for reversible control of frequency and quality factor of nanostring resonators. *Nano Letters*, 7(6):1728–1735, 2007.

[63] R.L. Miller. *Characterization and control of a strongly-coupled atom-cavity system*. PhD thesis, California Institute of Technology, 2009.

[64] A.D. Boozer, A. Boca, R. Miller, T.E. Northup, and H.J. Kimble. Reversible state transfer between light and a single trapped atom. *Physical review letters*, 98(19):193601, 2007.

[65] T.E. Northup. *Coherent control in cavity QED*. PhD thesis, California Institute of Technology, 2008.

[66] A. Boca. *Experiments in cavity QED: Exploring the interaction of quantized light with a single trapped atom.* PhD thesis, California Institute of Technology, 2005.

[67] K.M. Birnbaum. *Cavity QED with multilevel atoms.* PhD thesis, California Institute of Technology, 2005.

[68] J. McKeever. *Trapped atoms in cavity QED for quantum optics and quantum information.* PhD thesis, California Institute of Technology, 2004.

[69] J.R. Buck. *Cavity QED in microsphere and Fabry-Perot cavities.* PhD thesis, California Institute of Technology, 2003.

[70] T.W. Lynn. *Measurement and control of individual quanta in cavity QED.* PhD thesis, California Institute of Technology, 2003.

[71] C.J. Hood. *Real-time measurement and trapping of single atoms by single photons.* PhD thesis, California Institute of Technology, 2000.

[72] D.W. Vernooy. *Cold atoms in cavity QED for quantum information processing.* PhD thesis, California Institute of Technology, 2000.

[73] Q.A. Turchette. *Quantum optics with single atoms and single photons.* PhD thesis, California Institute of Technology, 1997.

[74] D. Alexson and D.D. Smith. Characterization of attocube nanopositioners for vibration. Technical report, DTIC Document, 2010.

[75] S.M. Spillane, T.J. Kippenberg, K.J. Vahala, K.W. Goh, E. Wilcut, and H.J. Kimble. Ultrahigh-q toroidal microresonators for cavity quantum electrodynamics. *Physical Review A*, 71(1):013817, 2005.

[76] J.C. Snowdon. *Vibration and shock in damped mechanical systems.* J. Wiley, 1968.

[77] O. Carnal, Q.A. Turchette, and H.J. Kimble. Near-field imaging with two transmission gratings for submicrometer localization of atoms. *Physical Review A*, 51(4):3079, 1995.

[78] N.S. Harris. *Modern vacuum practice.* McGraw-Hill, 1989.

[79] J.C. Sankey, C. Yang, B.M. Zwickl, A.M. Jayich, and J.G.E. Harris. Strong and tunable nonlinear optomechanical coupling in a low-loss system. *Nature Physics*, 6(9):707–712, 2010.

[80] Comsol multiphysics. *www.comsol.com.*

[81] A.B. Comsol. Comsol multiphysics – structural mechanics module. *User's Guide. Comsol, Inc.*, 2008.

[82] R.W.P. Drever, J.L. Hall, F.V. Kowalski, J. Hough, G.M. Ford, A.J. Munley, and H. Ward. Laser phase and frequency stabilization using an optical resonator. *Applied Physics B: Lasers and Optics*, 31(2):97–105, 1983.

[83] A.F. Harvey and M. Cerna. The fundamentals of fft-based signal analysis and measurement in labview and labwindows. *Application Note*, 41, 1993.

[84] M.L. Gorodetsky, A. Schliesser, G. Anetsberger, S. Deleglise, and T.J. Kippenberg. Determination of the vacuum optomechanical coupling rate using frequency noise calibration. *Optics Express*, 18(22):23236–23246, 2010.

[85] W.T. Eadie and F. James. *Statistical methods in experimental physics*. World Scientific, 2006.

[86] K.J. Williams, A. Dandridge, A.D. Kersey, J.F. Weller, A.M. Yurek, and A.B. Tveten. Interferometric measurement of low-frequency phase noise characteristics of diode laser-pumped nd: Yag ring laser. *Electronics Letters*, 25(12):774–776, 1989.

[87] F. Marquardt, A.A. Clerk, and S.M. Girvin. Quantum theory of optomechanical cooling. *Journal of Modern Optics*, 55(19):3329–3338, 2008.

[88] A. Dorsel, J.D. McCullen, P. Meystre, E. Vignes, and H. Walther. Optical bistability and mirror confinement induced by radiation pressure. *Physical Review Letters*, 51:1550, 1983.

[89] P.F. Cohadon, A. Heidmann, and M. Pinard. Cooling of a mirror by radiation pressure. *Physical Review Letters*, 83(16):3174–3177, Oct 1999.

[90] V.B. Braginsky, A.B. Manukin, and M.Y. Tikhonov. Investigation of dissipative ponderomotive effects of electromagnetic radiation. *Soviet Journal of Experimental and Theoretical Physics*, 31:829, 1970.

[91] F. Marquardt and S.M. Girvin. Optomechanics (a brief review). *Physics*, 2:40, 2009.

[92] G. Anetsberger, R. Rivière, A. Schliesser, O. Arcizet, and T.J. Kippenberg. Ultralow-dissipation optomechanical resonators on a chip. *Nature Photonics*, 2(10):627–633, 2008.

[93] T. Carmon, T.J. Kippenberg, L. Yang, H. Rokhsari, S. Spillane, and K. Vahala. Feedback control of ultra-high-q microcavities: application to micro-raman lasers and microparametric oscillators. *Optics Express*, 13:3558, 2005.

[94] L. Diósi. Laser linewidth hazard in optomechanical cooling. *Physical Review A*, 78(2):021801, 2008.

[95] G.A. Phelps and P. Meystre. Laser phase noise effects on the dynamics of optomechanical resonators. *Physical Review A*, 83(6):063838, 2011.

[96] P. Rabl, C. Genes, K. Hammerer, and M. Aspelmeyer. Phase-noise induced limitations on cooling and coherent evolution in optomechanical systems. *Physical Review A*, 80(6):063819, 2009.

[97] G.M. Harry, H. Armandula, E. Black, D.R.M. Crooks, G. Cagnoli, J. Hough, P. Murray, S. Reid, S. Rowan, P. Sneddon, M.M. Fejer, R. Route, and S.D. Penn. Thermal noise from optical coatings in gravitational wave detectors. *Applied Optics*, 45(7):1569–1574, 2006.

[98] H. J. Butt and M. Jaschke. Calculation of thermal noise in atomic force microscopy. *Nanotech.*, 6:1, 1995.

[99] K. Numata, A. Kemery, and J. Camp. Thermal-noise limit in the frequency stabilization of lasers with rigid cavities. *Physical Review Letters*, 93(25):250602, 2004.

[100] A.N. Cleland and M.L. Roukes. Noise processes in nanomechanical resonators. *Journal of Applied Physics*, 92(5):2758–2769, 2002.

[101] T.B. Gabrielson. Mechanical-thermal noise in micromachined acoustic and vibration sensors. *IEEE Transactions on Electronic Devices*, 40(5):903–909, 1993.

[102] V.B. Braginsky, V.P. Mitrofanov, V.I. Panov, K.S. Thorne, and C. Eller. *Systems with small dissipation*. University of Chicago Press, 1986.

[103] S.D. Penn, A. Ageev, D. Busby, G.M. Harry, A.M. Gretarsson, K. Numata, and P. Willems. Frequency and surface dependence of the mechanical loss in fused silica. *Physics Letters A*, 352(1):3–6, 2006.

[104] D.H. Santamore and Y. Levin. Eliminating thermal violin spikes from ligo noise. *Physical Review D*, 64(4):042002, 2001.

[105] M. Poggio, C.L. Degen, H.J. Mamin, and D. Rugar. Feedback cooling of a cantilever's fundamental mode below 5 mk. *Physical Review Letters*, 99(1):017201, Jul 2007.

[106] B.S. Sheard, M.B. Gray, B.J.J. Slagmolen, J.H. Chow, and D.E. McClelland. Experimental demonstration of in-loop intracavity intensity-noise suppression. *IEEE Journal of Quantum Electronics*, 41(3):434–440, 2005.

[107] C.H. Metzger and K. Karrai. Cavity cooling of a microlever. *Nature*, 432(7020):1002–1005, 2004.

[108] V.B. Braginsky and S.P. Vyatchanin. Low quantum noise tranquilizer for fabry-perot interferometer. *Physics Letters A*, 293(5):228–234, 2002.

[109] J. Ye and P. Zoller, private discussion.

[110] D.F. Walls and G.J. Milburn. *Quantum optics*. Springer Verlag, 2008.